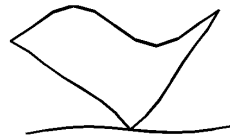
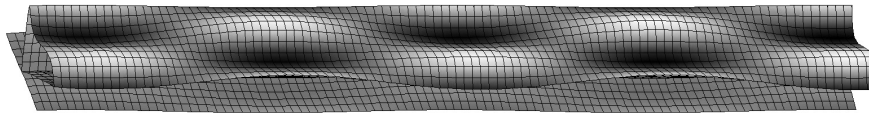




WAVE PROPAGATION IN LIGHT WEIGHT PLATES WITH TRUSS-LIKE CORES



vorgelegt von

Dipl.-Ing. Torsten Kohrs

Von der Fakultät V - Verkehrs- und Maschinensysteme
der Technischen Universität Berlin

zur Erlangung des akademischen Grades
Doktor der Ingenieurwissenschaften (Dr.-Ing.)
genehmigte

D i s s e r t a t i o n

Promotionsausschuss:

Vorsitzender:	Prof. Dr.-Ing. Markus Hecht
Gutachter:	Prof. Dr.-Ing. Michael Möser
Gutachter:	Prof. Dr. David J. Thompson
Betreuer:	Prof. Dr. sc. B. A. T. Petersson

Tag der wissenschaftlichen Aussprache: 19.06.2008

Berlin 2008

D83

Acknowledgements

I would like to thank my supervisor Prof. Björn A. T. Petersson for his support and guidance during the years. His door was always open for questions and discussions. I would like to thank the examiners Prof. David Thompson and Prof. Michael Möser for the interest and willing take-over of this role for my thesis.

I appreciate the initial financial support of Bombardier which was made possible by the convincing efforts of Dr. Alexander Orellano. The cooperation simplified the access to real light weight plate structures which were essential for the experimental part of the work. The financial support of the German Research Foundation (DFG) within the project 'Körperschall typischer Leichtbaustrukturen' is especially acknowledged.

Throughout the years many people supported me in two pleasant working environments at the Institute of Fluid Mechanics and Mechanical Engineering, the former ITA, and at Bombardier in Hennigsdorf. The critical and interested attitude of Karl-Richard Fehse for all acoustical topics was always a motivation to learn and try to understand new concepts. Carsten Hoever supported me with his quick and substantiated thesis-work on the experimental part which wouldn't have been possible without the help of the ITA workshop.

Special thanks are devoted to Silje Korte, who thoroughly read my thesis draft and had to spend a large amount of free time on this.

Finally, I would like to express my gratitude to my parents and especially to Yvonne, who always approved the time and effort I spent to finalize the thesis.

Abstract

Wave propagation in light weight plates with truss-like cores is investigated in this thesis.

In a first step, a simplified two-dimensional strip model based on analytic beam functions is established and validated experimentally. This model is also valid for line force excitation and response in the direction parallel to the intermediate webs. The model is employed to investigate the wave propagation in light weight profile strips with truss-like cores. A study using different core geometries with and without diagonal stiffeners reveals significant differences. Periodic system effects are clearly visible, most pronounced for the case of solely vertical webs. A stiffening effect of the fillets at the joints is identified, whereas their additional mass is of minor importance.

The wavenumber content of periodic light weight profile strips is investigated by using the theory of wave propagation in multi-coupled periodic systems to extract the dispersion characteristics of typical configurations. Solving the transfer matrix eigenvalue problem forms a basis for understanding the wave propagation in (infinite) strips; six characteristic waves traveling in each direction arise, either propagating, decaying or complex. Each characteristic wave consists of multiple wavenumbers of different amplitude, forming the so called "space harmonic" series. Typical wave forms of characteristic waves are shown and form the basis for identifying their relative contributions in the space harmonic series.

Based on the dynamic stiffness matrix of a single subelement of the periodic system the forced response is calculated for infinite, light weight profile strips. The characteristic wave amplitudes for selected force excitations in combination with the corresponding wavenumber spectra form the basis for structural acoustic investigations. Input mobilities for the infinite strip are presented demonstrating the typical pass- and stop-band behaviour. A brief study of the influence of periodicity perturbations reveals that for typical profiles, even quite high random length variations up to about 5% have a limited effect on the structural dynamics of the strip.

The second part of the work extends the two-dimensional strip model to

a full three-dimensional model of the investigated light weight plates.

For the generic light weight plates with periodicity in the lateral dimension the wavenumber content is characterized by strong directional wave propagation and resulting wave beaming in some frequency bands, where local vibrations are of primary concern. In the low frequency region, where global plate waves dominate, the vibrational behaviour can be reduced to equivalent plate models. For profiles with inclined webs, global orthotropicity is limited and global bending wave dispersion is similar irrespective of direction. For profiles with solely vertical webs, strong orthotropicity with significantly higher wavenumbers in lateral direction, normal to the webs, is demonstrated.

The strong periodic pass- and stop-band behaviour detected in the strip investigation is transformed into a spatial stop- and pass-band distribution of high and low vibration zones. As a result, the stop-bands of the two-dimensional investigation are weakened for point excitation of full plates, represented by a rising real part of the input mobilities. In these lateral stop-bands the imparted power is transmitted mainly in the longitudinal direction, parallel to the webs of the inner core.

Different methods for the extraction of theoretical and experimental dispersion characteristics are applied and discussed. Theoretical dispersion characteristics and mobilities are validated on a regional train floor section which serves as an application example.

Zusammenfassung

Die vorliegende Arbeit beschäftigt sich mit der Körperschallausbreitung in Leichtbauprofilen mit fachwerkähnlichem Kern. Der erste Teil der Arbeit widmet sich der Untersuchung eines vereinfachten, zweidimensionalen Modells, das auf gekoppelten, analytisch zu beschreibenden Balken beruht. Es repräsentiert einen schmalen Streifen der Leichtbauplatte oder kann als Modell für Linienkrafteerregung parallel zu den inneren Stegen verwendet werden. Nach der Modellentwicklung und der experimentellen Validierung wird es für die Untersuchung der Wellenausbreitung in Leichtbau-Plattenstreifen verwendet. Eine Studie unter Berücksichtigung unterschiedlicher grundsätzlicher Fachwerkstrukturen mit schrägen und geraden Versteifungen zeigt deutliche, prinzipielle Unterschiede. Typische Effekte periodischer Systeme werden nachgewiesen, insbesondere für Profilstreifen mit ausschließlich vertikalen Versteifungen. Die fertigungsbedingten radialen Übergänge an den Verbindungsstellen angrenzender Stege führen zu einer deutlichen Versteifung, während die zusätzliche Masse an diesen Stellen von untergeordneter Bedeutung ist.

Der Wellenzahl-Inhalt von periodischen Leichtbauprofilstreifen wird unter Verwendung der Theorie mehrfach gekoppelter periodischer Systeme ermittelt, wobei die Dispersionseigenschaften typischer Profilgeometrien untersucht werden. Die Lösung des Eigenwertproblems für die Transfermatrizen bildet die Grundlage für das Verständnis der Wellenausbreitung in (unendlichen) Profilstreifen. Sechs charakteristische Wellen in jede Richtung werden identifiziert, die entweder ausbreitungsfähig, abklingend oder schwingend abklingend (komplex) sind. Jede charakteristische Welle enthält mehrere Wellenzahlkomponenten mit unterschiedlicher Amplitude, welche die so genannte 'Space harmonic series' bilden. Die ermittelten charakteristischen Wellenformen bilden die Grundlage für die Bestimmung der relativen Anteile in der 'Space harmonic series'.

Mit Hilfe der dynamischen Steifigkeitsmatrix eines einzelnen Grundelements des periodischen Systems wird die Schwingungsantwort für unendliche Leichtbauprofilstreifen ermittelt. Die charakteristischen Wellenamplituden

für ausgewählte Kraftanregungen in Verbindung mit den zugehörigen Wellenzahlspektren bilden die Grundlage für strukturakustische Untersuchungen. Die ermittelten Eingangsmobilitäten demonstrieren das typische Durchlass- und Sperrbandverhalten periodischer Systeme. Eine kurze Betrachtung des Einflusses von Periodizitätsabweichungen verdeutlicht, dass recht hohe, zufällige Längenänderungen der Grundelemente bis zu ca. 5 % nur einen geringen Einfluss auf die Strukturodynamik der Plattenstreifen haben.

Im zweiten Teil der Arbeit wird das Modell des zweidimensionalen Profilstreifens auf ein volles dreidimensionales Modell der Leichtbauplatte erweitert.

Für die untersuchten Leichtbauprofile mit einer Periodizität in nur einer, der seitlichen Richtung, sind die Dispersionseigenschaften geprägt von einer frequenzabhängigen, stark gerichteten Wellenausbreitung, die im höheren Frequenzbereich in Erscheinung tritt. In diesen Bereichen sind lokale Schwingungsmuster von entscheidender Bedeutung. Für tiefe Frequenzen, in denen globale Plattenwellen vorherrschen, kann die Leichtbauplatte zu äquivalenten Platten reduziert werden. Für Profile mit Diagonalversteifung ist die globale Orthotropizität begrenzt und eine globale Biegewellenausbreitung ohne signifikante Richtungsabhängigkeit tritt auf. Für Profile, die ausschließlich vertikale Versteifungen aufweisen, kann ein stark orthotropes Verhalten mit deutlich höheren Wellenzahlen in lateraler Richtung, senkrecht zu den Versteifungen, beobachtet werden.

Das stark periodische Verhalten, das für die Profilstreifen beobachtet wird, wird in eine räumliche Verteilung von Sperr- und Durchlassbereichen überführt. Daraus ergibt sich, dass die Sperrbänder der zweidimensionalen Betrachtung für punkterregte Leichtbauplatten an Bedeutung verlieren. Dies manifestiert sich in steigenden Realteilen der Eingangsmobilitäten im Bereich der lateralen Sperrbänder. In diesen Frequenzbereichen wird die eingespeiste Körperschalleistung hauptsächlich in longitudinaler Richtung entlang der Versteifungen transportiert.

Unterschiedliche Methoden für die Extraktion der theoretischen und experimentellen Dispersionseigenschaften werden angewendet und die Ergebnisse diskutiert. Die theoretischen Dispersionseigenschaften und Mobilitäten werden für die Leichtbau-Bodenplatte eines Regionalzuges ermittelt und durch Messungen validiert.

Contents

1	Introduction	14
1.1	Previous work	17
1.2	Thesis overview	19
2	Profile strips: Theory and experimental validation	20
2.1	Introduction	20
2.2	Calculation method	20
2.2.1	Dynamic stiffness matrix assembly	21
2.2.2	Dynamic stiffness matrix for a typical subsystem	21
2.2.3	Model benchmarking and extensions	23
2.3	Influence of web geometry on input and transfer mobility	23
2.4	Point masses influence	27
2.5	Experimental validation	29
2.6	Concluding remarks	35
3	Profile strips: Wavenumber content	36
3.1	Introduction	36
3.2	Dispersion characteristics of profile strips	36
3.2.1	Multi-coupled periodic systems	38
3.2.2	Dispersion characteristics using spatial DFT	41
3.2.3	Dispersion characteristics using transfer matrix	44
3.3	Characteristic waves	47
3.4	Wavenumber content in characteristic waves	52
3.4.1	Theory	52
3.4.2	Results	54
3.5	Concluding remarks	62
4	Profile strips: Forced response	63
4.1	Introduction	63
4.2	Forced response of infinite profile strip	64
4.2.1	Theory of forced response using dyn. stiffness matrix	64

CONTENTS

4.2.2	Results for forced wave propagation of infinite strips . . .	65
4.3	Aperiodicity	74
4.3.1	Influence on wave propagation	74
4.3.2	Influence on deflection shapes and mobilities	76
4.4	Concluding remarks	78
5	Free wave prop. in light weight plates	82
5.1	Introduction	82
5.2	Dispersion characteristics using DFT	84
5.2.1	Discrete spatial Fourier Transform	85
5.2.2	Frequency dependent dispersion from DFT	91
5.3	Dispersion characteristics using phase constant surfaces	97
5.3.1	Theory	97
5.3.2	Numerical results	99
5.4	Dispersion characteristics using WFE	108
5.4.1	Theory	108
5.4.2	Wave propagation in single subelement profiles	110
5.4.3	Wave propagation in multiple subelement profiles	115
5.4.4	Influence of dyn. reduction on dispersion characteristics	122
5.5	Concluding remarks	124
6	Forced response of light weight plates	125
6.1	Introduction	125
6.2	Theory	125
6.3	Numerical results	126
6.4	Forced response with reduced wave basis	134
6.5	Forced response using dynamic reduction methods	138
6.6	Concluding remarks	139
7	Application example: Train floor	142
7.1	Free wave propagation	143
7.2	Forced Response - Calculation and experimental results	146
7.2.1	Calculated and measured mobility results	150
7.2.2	Dispersion characteristics	152
7.2.3	Impulse propagation	156
7.3	Concluding remarks	165
8	Summary and Outlook	166
A	Slope deflection method and subs. dyn. stiffness matrix	177
B	Measured and calculated deflection shapes of profile strip	181

CONTENTS

C	Profile strip spatial Fourier transform results	187
D	WFE forced response benchmark results	190
E	Inhomogeneous wave correlation method	198
F	Regional train floor section results	200
F.1	Measured and calculated displacement fields	200
F.2	Measured and calculated dispersion characteristics	205
F.3	Time-frequency content	210
F.4	Mobility Tests on regional train floor plate	214
F.4.1	Test setup	214
F.4.2	Mass calibration	214
F.4.3	Support influence	214
F.4.4	Input mobility for stiffener excitation	216
F.4.5	Input mobility for plate field excitation	216
F.4.6	Comparison of input mobilities	217
F.4.7	Transfer mobilities	217
F.4.8	Mean square velocity	229
F.5	Comparison Calculation - Measurement	231
F.5.1	Stiffener Excitation	231
F.5.2	Plate Field Excitation	237

List of symbols

a	Acceleration
d_i	Normalization factor for eigenvectors
f	Frequency
j	$\sqrt{-1}$
k	Wavenumber
l_x	Length of subelement
m	Mass (Section 2.4)
m'	Mass per unit length
m, n, p, q	Integer values
t	Thickness
u	x-displacement
v	y-displacement (Section 2.2)
v	Velocity
v_{free}	Free velocity
$A_{i,n}$	Amplitudes of components in space harmonic series
A, B, C	Labels for investigated generic profiles
C_f	Coupling function
E_0	Young's modulus
F	Force
F_i	Kolousek beam functions (Appendix A)
I	Cross sectional moment of inertia (Appendix A)
L	Length of finite strips $A-C$
L_e	Periodic length
L_v	Velocity level
M	Moment
N	Number of sampling points
Q	Complex structure-borne power
S	Source descriptor (Chapter 1)
S	Cross sectional area (Appendix A)
V	Velocity spectrum (wavenumber domain)
W	Active structure-borne power
X	Force in x -direction (Section 2.2)
Y	Force in y -direction (Section 2.2)
Y	Mobility
Y_R	Receiver mobility
Y_S	Source mobility
Y_T	Transmission element mobility

LIST OF SYMBOLS

0	Zero matrix or vector
A, B	Reduction matrices
F	Force vector
I	Identity matrix
K	Dynamic stiffness matrix
L	Wave amplitudes of left travelling waves
M	Mass matrix
P	Topology matrix
R	Wave amplitudes of right travelling waves
S	Stiffness matrix
T	Transfer matrix
W	Wave transfer matrix / Reduction matrix
Y	Mobility matrix
α	Web angle
ϵ	Phase constant
η	Loss factor
δ	Attenuation constant
λ	Eigenvalue
μ	Propagation constant
ν	Poisson's ratio
ω	Circular frequency
ϕ, φ	Rotational angle
ρ	Mass density
ξ	Displacement
Λ	Helmholtz number for bending waves
Ψ	Helmholtz number for longitudinal waves
ϕ	Right eigenvector
ψ	Left eigenvector
ξ	Displacement vector
Φ	Eigenvector
Λ	Diagonal matrix of eigenvalues
$\Phi_{\mathbf{R}}$	Right eigenvector matrix
Ψ^{-}	Eigenvector matrix of left (negative) travelling waves
Ψ^{+}	Eigenvector matrix of right (positive) travelling waves
Ψ	Left eigenvector matrix
$\Psi_{\mathbf{R}}$	Right eigenvector matrix
$\Psi_{\mathbf{R}}$	Right eigenvector matrix

LIST OF SYMBOLS

Indexes

b	Back
e	Element
f	Front
i	Index
i	Inner (Section 4.2)
l	Left
r	Right
sub	Subsystem
x	x -direction
y	y -direction
z	z -direction
B	Bending wave

Superscripts

-1	Matrix inverse
T	Matrix transpose
H	Matrix Hermetian transpose (complex conjugate and transpose)

Chapter 1

Introduction

Light weight profiles are extensively used in different industrial applications. In a world where sustainability should be the main focus for economic and social behaviour, consumption of energy and raw materials have to be minimized in all sectors. Light weight design, driven historically mainly by technological and economic constraints in the aeronautics and astronautics is nowadays commonplace and essential in all industrial branches.

Typical light weight plates are designed of outer face plates in connection with a core of a variety of materials and geometries, e.g. foams, honeycomb structures or inclined as well as straight webs. The latter design is investigated in this thesis (see Fig. 1.1). These types of profiles are often made of aluminium and formed in an extrusion process, so that nearly arbitrary lengths of the profiles can be manufactured. In this thesis the term "length" is related to the extension parallel to the intermediate plates (z -direction), "width" the extension crossing the web connections (x -direction) and "height" the dimension corresponding to the thickness of the light weight plate (y -direction).

The thesis focusses on the wave propagation in such structures, which comprise a high static stiffness in combination with low mass. Often there are two thin outer plates connected via inclined or upright stiffeners.

In the railcar industry carriage design from extruded aluminium profiles is commonplace and can assist in achieving light weight rail vehicles. In addition to the light weight there are several advantages of these profiles, e.g. the high water- and air-tightness that are possible through the line-welding process to connect the profiles and the quite simple production process by extrusion. Moreover, the profiles are easier to handle than big sheet metal plates which are needed alternatively. Furthermore, curvature of the complete structure can be included fairly simply and exactly by including the radius in the design of each profile [1]. One of the drawbacks of these light

weight profiles is the low sound transmission loss of the bare profiles in comparison to single wall mass law behaviour [2].

With regard to interior acoustic comfort not only the airborne transmission is of importance, but also the structure-borne sound transmission can dominate in some frequency bands, mainly expected in the low frequency regime up to about 500 – 1000 Hz. The reduced mass of the carriage tends to increase the structure-borne contribution due to higher structural mobilities and increased radiation in the global vibrational regime. The latter is a consequence of the low mass in connection with high static bending stiffness, resulting in critical frequencies of about 200 Hz [2]. The reduction of lead time and costs in the vehicle manufacturing process is accompanied by the abandoning of prototyping in the railcar industry. Hence, the industry demands reliable and manageable prediction processes, which have to be founded on a profound physical basis in order to assure acoustical quality without 'trial and error' modifications on production vehicles or prototypes.

For appropriate design of rail vehicles with respect to structure-borne sound one has to cope with the complex vibro-acoustic process sketched in Fig. 1.2.

The structure-borne sound power transmitted from the source to the receiving structure, in this case the carriage, depends not only on the source, but also on the mobilities of the source and the receiving structure. This fact which is strictly true also, but usually neglected, for airborne sound sources, hinders the separate optimization of source and receiver. An overview of the concept of structure-borne sound source characterization and structural power transmission is given in [3]. For a proper source characterization source activity (free velocity / blocked force) and source mobility have to be evaluated. Besides the source characterization, which is an ongoing research and development task, the structure-borne sound characteristics of the receiving structure are essential. They influence not only the transmission process, but

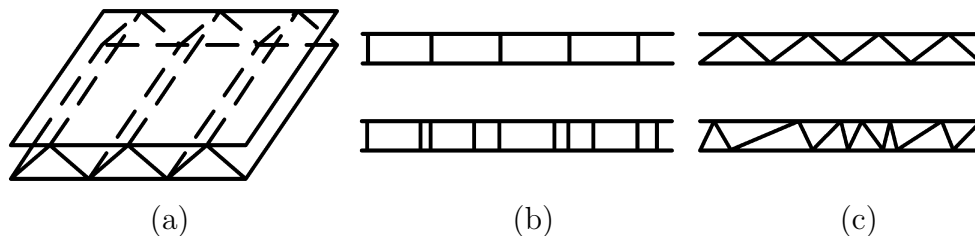


Figure 1.1: (a) Periodic light weight plate (b) cross sections with vertical webs (c) cross sections with inclined webs

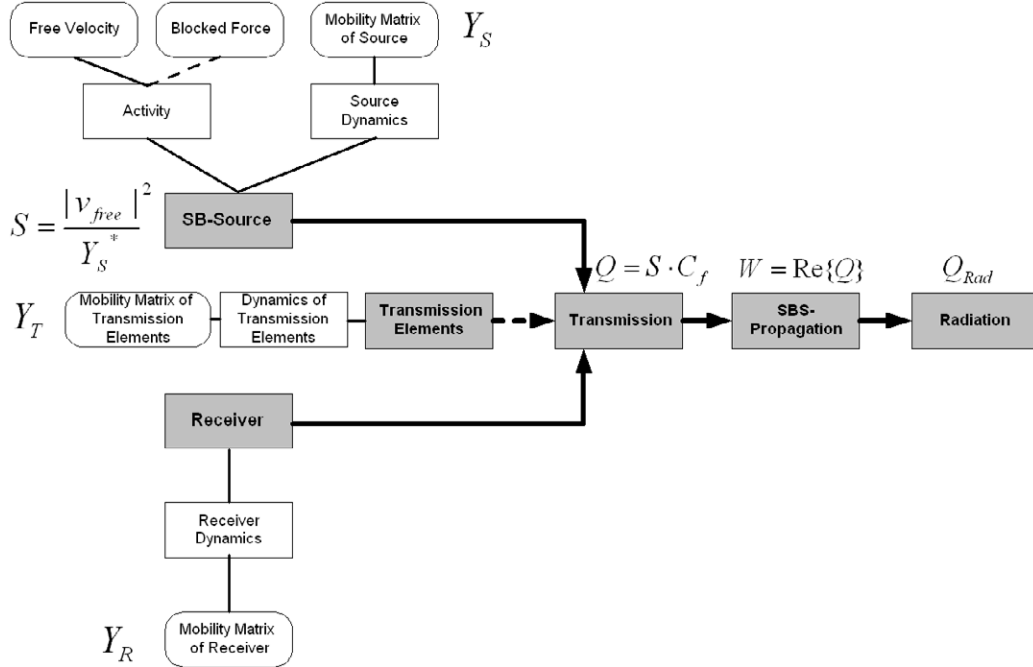


Figure 1.2: Complete vibro-acoustic process

form the basis for structure-borne sound propagation and radiation. In this thesis, the latter is of concern and therefore the wave propagation in typical light weight plates is investigated. The focus is on the physical understanding of the inherent wave propagation. Once the dispersion characteristics of the light weight profiles are sufficiently understood, generic carriage models like box or cylinder models can be established to calculate the structure-borne sound propagation and radiation due to vibrational force or moment excitations at the source - carriage connection points. In [4, 5] an example of a generic cylinder model of a classical steel carriage is published and deals with exterior sound radiation from structure-borne excited train carriages.

In the automotive industry there is a tendency for increased usage of extruded aluminium profiles in car bodies, e.g Audi uses the *AudiSpaceFrame* technology as a mixture of cast aluminium, aluminium profiles, aluminium and iron sheets [6].

As typical light weight profiles are often periodic or nearly periodic a central question is the existence of periodic system effects like pass- and stop-bands.

Besides these technical light weight plates, periodic systems are significant also in biological systems, e.g. honeycombs of bees, where structure-borne

sound transmission seems to be a major means of communication inside the hive [7]. Measurements and observations indicate that the bees optimize the honeycombs for transmission in certain frequency bands, probably related to periodic pass-band effects, where part of the communication takes place. These effects are not investigated in this work but shall highlight the significance of periodic vibrational systems also in other scientific domains.

1.1 Previous work

Structural-acoustic investigations of light weight plates as sketched in Fig. 1.1 for mid- and high frequency applications are rare. A short overview of the related work is given in this section.

Often the lightweight structures are periodic or nearly periodic. This is especially true for industrial standard profiles, designed for a variety of applications. The details of the structural loads are unknown or locally varying and hence no specific (static) design is performed, reinforcing for example the load carrying regions. Periodic structures show some characteristic effects which have been studied extensively in the past (cf. e.g. [8, 9, 10, 11, 12, 13, 14, 15, 16]). The periodic nature simplifies the calculation procedure as only one periodic subsystem has to be analysed. The wave propagation of a complete profile strip can be deduced from the subsystem results.

The most important feature of the wave propagation in periodic structures is the existence of pass- and stop-bands, where unhindered and strongly suppressed wave propagation appears respectively. Hence, the wave propagation undergoes a mechanical bandpass filtering [17].

Different approaches to describe the structural-acoustic characteristics of light weight profiles can be found in literature. The global behaviour of the profile, dominating in the low frequency regime, is investigated using a sandwich approach by Lok and Cheng [18, 1]. The structure is treated as an equivalent orthotropic plate. For higher frequencies, where local vibrations of the structural members appear, different approaches are necessary. Statistical methods are applied by Geissler and Neumann [19] and Xie et. al. [20, 21]. Xie et. al. demonstrate that for a typical railway carriage profile the local vibrations dominate at frequencies above 500 Hz and introduce a statistical model as a combination of global and local subsystems. Global vibrations are characterized by wavelength which are significantly larger than the distance between the webs, whereas local vibrations arise in web sections enclosed between the web joints. The modal density of the extruded panels is estimated in [22] and verified by the modal density extracted from an

FE-model of the section. The coupling between global and local modes is described by the coupling between a travelling global wave and uncorrelated local waves. Presented results for radiation efficiency and level difference of the face plates are promising for mechanical excitation but less satisfactory for acoustical excitation.

Pezerat and Guyader [23] use an analytical modal approach to describe the structural acoustic characteristics of light weight profiles, whereas El-Raheb [24] uses a transfer matrix approach. Both studies do not focus on the wave propagation and dispersion characteristics and hence, the physical insight in the inherent processes is limited.

Pang [25] uses both spectral finite element calculations to extract dispersion characteristics and commercial SEA-software to investigate the structural-acoustic behaviour of extruded aluminium profiles. Investigation of dispersion characteristics using spectral finite element calculations reveals some insights in the wave propagation mechanisms involved and local cut-on phenomena are detailed. The main focus of that work is the calculation of structural acoustic parameters, e.g. the transmission loss, for acoustically excited panels by the development of appropriate SEA-models.

Nilsson and Jones introduce a coupled waveguide finite and boundary element method for calculating the sound transmission through an extruded profile section [26]. The presented approach is more efficient than full standard 3D FE/BE calculation and can be used for transmission loss prediction of panels with large extension in the rib direction. This dimension is assumed to be infinite in the model. The sensitivity of the calculated transmission loss to inherent damping is mainly addressed to power transmission in the vicinity of the cut-on frequencies, where the injected power is proportional to the slope of the dispersion curves.

Cross sections of the profile plates can be treated as plane truss frameworks which have been investigated extensively in the past, e.g. by Signorelli and von Flotow [27] who deal with the wave propagation in periodic truss beams in detail. Characteristic waves are extracted and the periodic system effects are investigated. As only the translational degrees of freedom at the joints are included, results are strictly valid only for the special case of suppressed rotations at the joints. Emaci et. al. [28] deal with truss structures of similar shapes and identify the characteristic waves for the periodic system. In the first part, they use the complete formulation including rotational components at the joints. No detailed investigation of the wavenumber content is included so that the results are not applicable for sound radiation phenomena. This is indeed not intended for the investigated structures there. Ruzzene [29] investigates the dynamics and sound radiation of sandwich beams with honeycomb truss core and also with a 'square' core, similar to one of the

geometries investigated here. The calculation is based on the spectral finite element method and results are presented for finite strip configurations. No use is made of periodic system theory and the wave propagation is not investigated. Sound radiation is treated and a comparison with a unit cell analysis with special guided boundary condition agree principally with the results for the complete strip, at least for the investigated average response for normally incident pressure wave excitation.

The published work on truss-core light weight plates does not focus on the wave propagation mechanisms in the mid- to high-frequency regime, where local vibrations are of major significance so that the physical insight in the structural-acoustic behaviour is limited. This thesis shall shed some light on the dispersion characteristics of such systems and investigate some of the major scientific questions in this area:

- Which wave types can propagate freely in the light weight plates?
- Are periodic system effects like pass- and stop-band behaviour of significance? If so, how much periodicity perturbations can be allowed to maintain these effects?
- Which methods can be used to investigate the wave propagation?

1.2 Thesis overview

The thesis starts with the investigation of two-dimensional models of strips of the light weight profile plates in chapters 2 to 4. This simplification enables the use of analytical beam elements to calculate the behaviour of the profile strips. The three-dimensional investigation of the full light weight profiles starts in chapter 5 with the free wave propagation. The thesis continues with forced response calculations in chapter 6, an experimental validation on a regional train floor section in chapter 7 and concludes with a summary and an outlook in chapter 8.

Chapter 2

Light weight profile strips: Theory, modelling and experimental validation

2.1 Introduction

In this chapter an analytical approach is chosen to investigate the wave propagation in the light weight structures. At first, a two-dimensional model is established, describing the wave propagation and the resulting mobilities of a profile strip or the wave propagation for line force excited profile plates, where the line force extends parallel to the interconnecting plates. The inherent wave propagation phenomena for periodic strips are investigated and constitute together with an experimental validation the central issues in this chapter. In chapters 3 and 4 the dispersion characteristics of periodic strips, the forced response and the influence of periodicity perturbations are treated.

2.2 Calculation method

Starting point to handle the complex structure is a two-dimensional model of a profile cross section (see Fig. 1.1(b) and (c)). The structural dynamic behaviour of such a section can be investigated by using the methods for plane truss networks. An analytical description using beam functions for the bending and longitudinal vibrations of the members can be gained following the so called "slope-deflection method" [30, 31], see also Appendix A. Euler-Bernoulli bending theory is used in this study as the material thickness of typical light weight profile members is small in comparison with the governing wavelengths. The inclusion of longitudinal waves is mandatory as

wave conversion phenomena arise at the joints. Small vibration amplitudes are postulated so that linear vibration theory and the superposition principle apply.

2.2.1 Dynamic stiffness matrix assembly

For built-up systems comprising similar, successive elements it is helpful to divide the complete system in subsystems of similar shape. Therefore, only the subsystem dynamic stiffness matrix has to be assembled using e.g. the "slope-deflection method". The resulting system of equations for a subsystem can be written in a condensed matrix form using the subsystem dynamic stiffness matrix \mathbf{K}_{sub} , displacement vector $\boldsymbol{\xi}$ and force vector \mathbf{F} ,

$$\mathbf{K}_{\text{sub}}\boldsymbol{\xi} = \mathbf{F}. \quad (2.1)$$

The complete system dynamics can be developed by connecting the subsystems side by side. This can be done for the dynamic stiffness matrix approach by just adding the influence of the directly connected elements at the same global degree of freedom using a topology matrix \mathbf{P} ,

$$\mathbf{K}_{\text{strip}} = \mathbf{P}^T \mathbf{K}_{\text{sub}} \mathbf{P}. \quad (2.2)$$

2.2.2 Dynamic stiffness matrix for a typical subsystem

For profiles with inclined webs a subsystem can be defined as shown in Fig. 2.1. Using this subsystem and the corresponding mirrored one is sufficient to assemble the complete dynamic stiffness matrix of all profile strips shown in Fig. 1.1 (c). This profile with inclined members is the typical situation in train carriage applications. In the case of webs normal to the outer faces, the subsystem can be developed in a similar way which is not outlined explicitly here for the sake of brevity.

The arrangement of the translational and rotational degrees of freedom in the vectors and matrices is based on the convention that point after point is treated with its three degrees of freedom (rotation around z-axis (φ_g), translation in x -direction (u_g) and translation in y -direction (v_g)). This results in

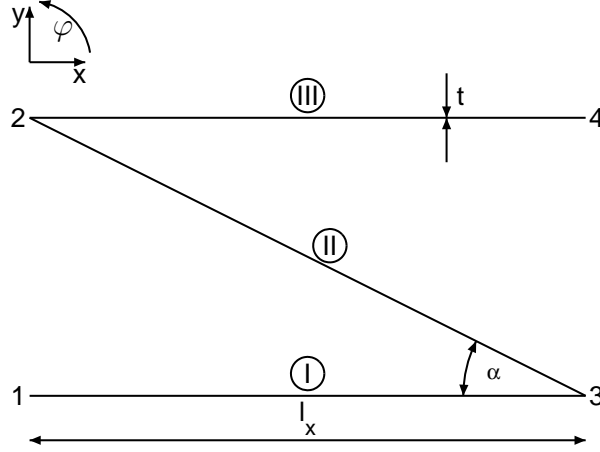


Figure 2.1: Subsystem element with inclined web including nomenclature and coordinate system

the following definition of the dynamic stiffness matrix \mathbf{K} ,

$$\begin{pmatrix}
 k_{1,1} & k_{1,2} & k_{1,3} & k_{1,4} & \dots & k_{1,12} \\
 k_{2,1} & k_{2,2} & k_{2,3} & k_{2,4} & \dots & k_{2,12} \\
 k_{3,1} & k_{3,2} & k_{3,3} & k_{3,4} & \dots & k_{3,12} \\
 \dots & & & & & \\
 & \dots & & & & \\
 & & \dots & & & \\
 & & & \dots & & \\
 & & & & \dots & \\
 & & & & & \dots \\
 k_{11,1} & k_{11,2} & k_{11,3} & k_{11,4} & \dots & k_{11,12} \\
 k_{12,1} & k_{12,2} & k_{12,3} & k_{12,4} & \dots & k_{12,12}
 \end{pmatrix} \cdot \begin{pmatrix} \varphi_1 \\ u_1 \\ v_1 \\ \varphi_2 \\ u_2 \\ v_2 \\ \varphi_3 \\ u_3 \\ v_3 \\ \varphi_4 \\ u_4 \\ v_4 \end{pmatrix} = \begin{pmatrix} M_1 \\ X_1 \\ Y_1 \\ M_2 \\ X_2 \\ Y_2 \\ M_3 \\ X_3 \\ Y_3 \\ M_4 \\ X_4 \\ Y_4 \end{pmatrix} \quad (2.3)$$

For the sake of brevity, only the non-zero elements of the \mathbf{K} -matrix are given in Eqs. (A.4) in Appendix A. Because of reciprocity, evaluation of the upper (or lower) off-diagonal elements is sufficient and hence the notation is restricted to the upper off-diagonal terms.

The solution for a forced response of the finite strip can be calculated by inverting the \mathbf{K} -matrix or by a different solution algorithm, e.g. Gauss elimination for each frequency. Moreover, it is possible to calculate the mobility

matrix \mathbf{Y} from the dynamic stiffness matrix by¹

$$\mathbf{Y} = j\omega \cdot \mathbf{K}^{-1} . \quad (2.4)$$

2.2.3 Model benchmarking and extensions

The model is extended to encompass also straight vertical stiffeners using the same approach as described above. Damping is included in the model by using a complex Young's modulus $E = E_0(1 + j\eta)$ with loss factor η . In order to check the implementation, different benchmark calculations are performed with a standard Finite Element code. The equality of mobility results is strikingly good. Only at higher frequencies a slight frequency shift exists due to the Euler-Bernoulli beam theory applied, which assumes infinite shear stiffness, whereas finite shear stiffness is employed in the FE-calculations. For the sake of brevity, no results are presented here, but results of an FE-calculation including point masses are found in Figs. 2.6 and 2.7. No need for a model extension to compensate this shift is identified as the deviations are negligible for practical profile geometries in reasonable frequency ranges.

2.3 Influence of web geometry on input and transfer mobility

In order to investigate the influence of different geometries on the structure-borne sound characteristics of the profile strips, the input and transfer mobilities are studied for three periodic aluminium profiles with different inner webs, shown in Fig. 2.2. The parameters are listed in Tab. 2.1. In order to make the results comparable in a light weight design sense, the thickness of all inner webs is adjusted to maintain a constant profile mass of 83 kg per unit width. It is expected that the behaviour of the strip can be characterized by global vibrations at low frequencies below the first bending eigenfrequencies of the webs. Hence, it is appropriate to compare the resulting mobilities with that of an equivalent beam. The equivalent homogeneous bending beam is defined here by using the cross sectional second area moment of the dominating outer plates, calculating an equivalent thickness according to this second area moment and adjusting the mass density in order to maintain the same total mass. The equivalent parameters are included in Tab. 2.1.

A resulting ordinary transfer mobility magnitude from force excitation in y -direction at the left end to the response at the right end in the same direction is plotted in Fig. 2.3 for profiles A,B and C versus Helmholtz number,

¹The time base $e^{+j\omega t}$ is consistently used in this thesis.

CHAPTER 2. PROFILE STRIPS: THEORY AND EXPERIMENTAL
VALIDATION

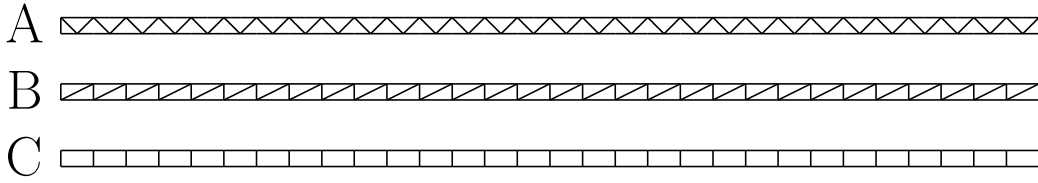


Figure 2.2: Profile strips used for the study on web geometry. The thickness of the inner webs is adjusted to maintain constant total mass of the profile strip.

Table 2.1: Calculation parameters for study of profiles A, B, C and the definition of equiv. beam (see Fig. 2.1 for nomenclature)

Profile	A	B	C	Equivalent beam
t_{outer}, t_{eq} [mm]	3.0	3.0	3.0	34.0
t_{inner} [mm]	3.0	2.6	8.5	-
α [°]	45.0	26.6 / 90.0	90.0	-
l_x [mm]	50	100	100	-
Total length L [mm]	3000	3000	3000	3000
E_0 [N/m ²]	$7.2 \cdot 10^{10}$	$7.2 \cdot 10^{10}$	$7.2 \cdot 10^{10}$	$7.2 \cdot 10^{10}$
η [-]	0.01	0.01	0.01	0.01
ρ [kg/m ³]	2700	2700	2700	812.5
Total mass per unit width [kg/m]	83	83	83	83

$k_B L$, of the equivalent beam. The corresponding mobility for the equivalent beam is also included. All mobilities are given for a force per unit width in z -direction and free boundary conditions. The real part of the input mobility, which is proportional to the input power is plotted in Fig. 2.4. It is obvious that the equivalent beam is capable of capturing the dynamic behaviour of the profiles A and B with sufficient accuracy in the low frequency regime up to a Helmholtz number of about 15. The match for beam A is good up to slightly higher frequencies. At high frequencies, where local vibrations and periodic system effects govern the structure-borne sound propagation, the equivalent beam model naturally fails to represent the inherent characteristics. For profile C the equivalent bending beam is nowhere an adequate model in the complete investigated frequency range, except for the rigid body behaviour at very low frequencies. The C-beam exhibits a higher modal density for global vibrations which can be explained by the shorter global wavelength extractable from the mode shapes or the dispersion characteristics presented

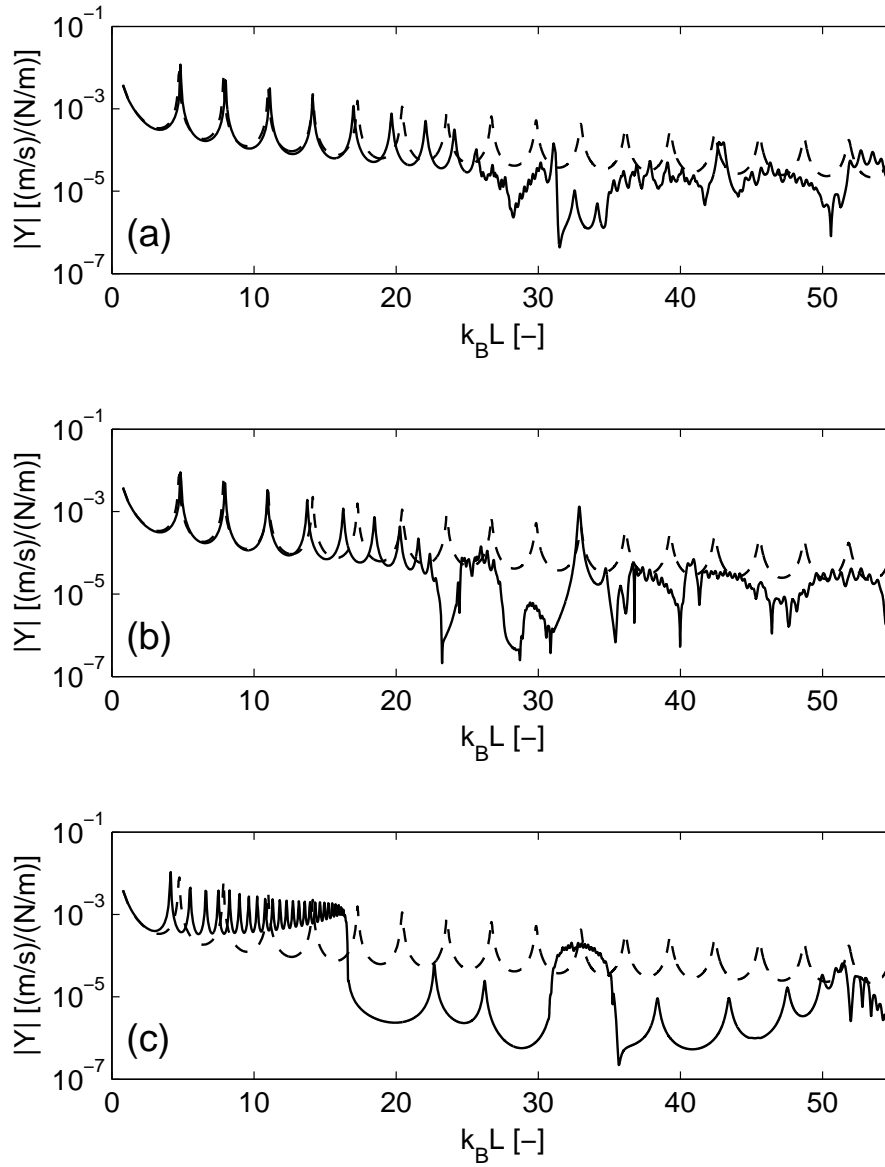


Figure 2.3: Magnitude of transfer mobility (F_y, v_y) of strip (a) A, (b) B and (c) C in comparison to equivalent bending beam (— strip A, B, C; -- equivalent bending beam)

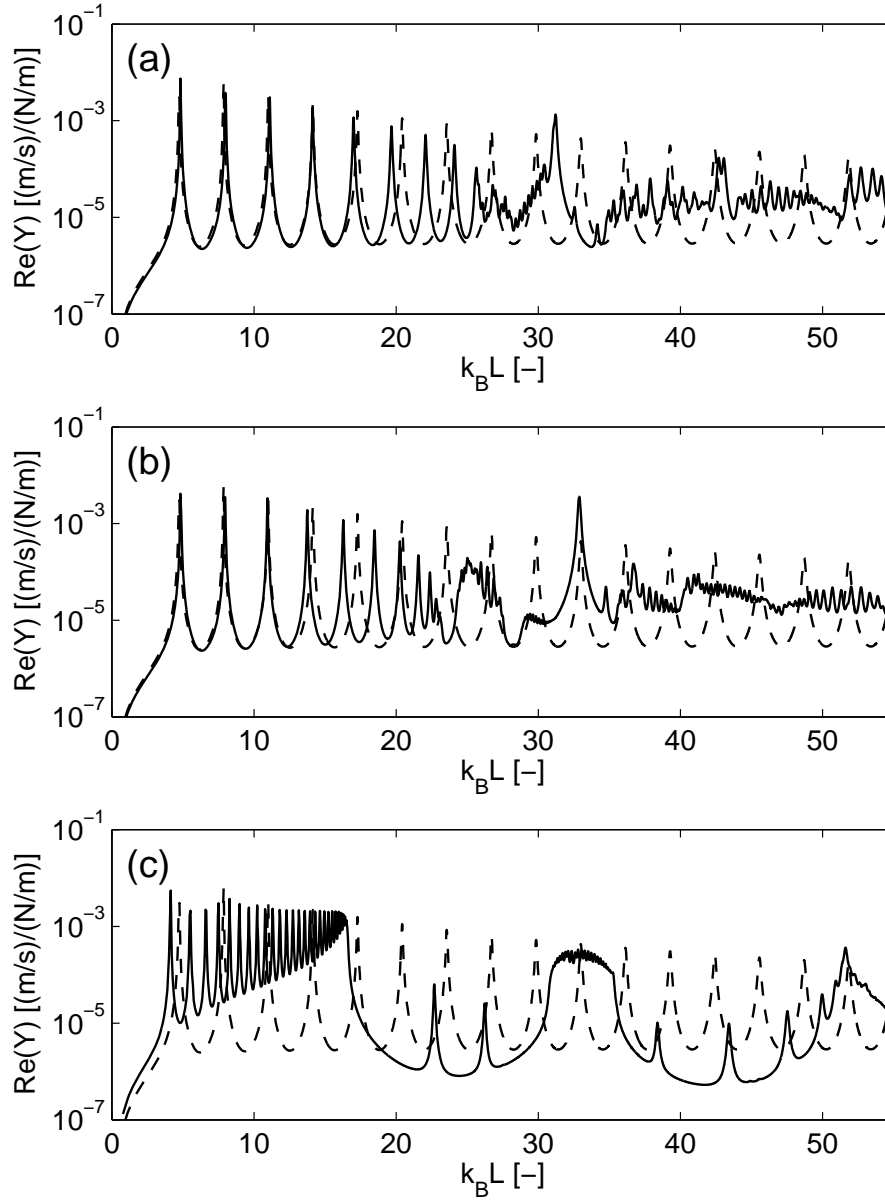


Figure 2.4: Real part of input mobility (F_y, v_y) (a) A, (b) B and (c) C in comparison to equivalent bending beam (— strip A, B, C; - - equivalent bending beam)

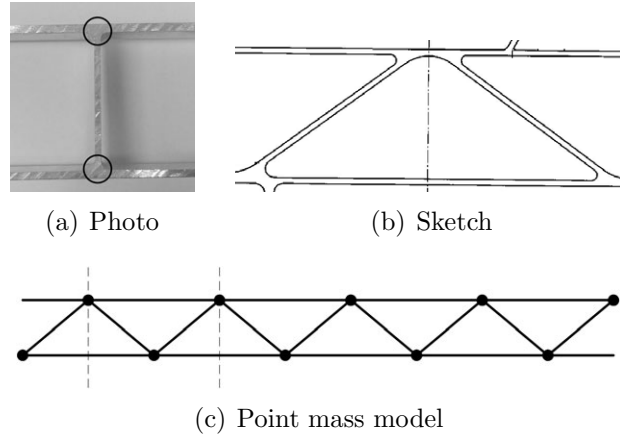


Figure 2.5: Fillets at joints of extruded profiles and point mass approximation

in chapter 3.

A kind of 'shear' deformation arises, where the vertical webs mainly translate in y -direction without overall rotation and only the outer beams perform local bending vibration. For profiles with diagonal webs, this kind of global vibration is suppressed by the longitudinal stiffness of the diagonal members. Starting with $k_B L = 17$, clear periodic system effects arise for the C-beam. In contrast to mono-coupled periodic beams, where in alternation stop- and pass-bands arise, the C-beam shows wide stop-bands between the pass-bands. Only one pass-band between Helmholtz numbers 31 and 35 is prominent. The stop-bands are interrupted by narrow single resonances, resulting from finite strip end reflections.

The periodic system effects are less pronounced for the profiles with inclined webs (A and B). This is due to 'weaker' wave conversions at the joints (see e.g. [32, p. 401]) smearing the pass- and stop-bands. Nonetheless, stop-bands are visible, e.g. between 32 and 35 for profile A and between 27 and 28 for profile B. For these profiles the real part of the input mobilities (Fig. 2.4) exhibits a distinct peak for frequencies above the first periodic system effects.

2.4 Point masses influence

In order to investigate the significance of welding spots and fillets at the end of each web (see Fig. 2.5), point masses are introduced at the connection points of the webs.

The additional inertia forces resulting from these masses have to be added to the total dynamic stiffness matrix at the appropriate location. For point masses, i.e. assuming no extension of the mass, the mass moment of inertia

is zero and hence no moment reaction forces appear. Starting from Newton's second law, $F = m \cdot a$, the dynamic stiffness of the mass reads

$$K_{\text{pointmass}} = \frac{F}{\xi} = -\omega^2 \cdot m_{\text{pointmass}}, \quad (2.5)$$

which has to be added for the x - and y -translational degrees of freedom in the global dynamic stiffness matrix \mathbf{K} .

The influence of increased web thickness at the joints of real profiles is investigated by the inclusion of additional point masses in the calculation model as described above. This is done by adding 1%, 5% and 10% of the complete profile mass as additional point masses localized to the joints.

The results show that point mass influence is small and hence, only the results for the highest additional masses (10%) are shown in Fig. 2.6 and Fig. 2.7 for profile A. The effect of the additional point masses is a slight shift of the resonance frequencies to lower frequencies and small modifications at high frequencies, where local motion emerges. Moreover the results of an FE-calculation using beam elements (length= 10 mm) are presented to check the implementation of the calculation model. The limiting frequency according to the six elements per wavelength criterion for bending waves is approximately 7800 Hz and hence sufficient for the investigated frequency range up to 5000 Hz. The agreement of FE-calculation and analytical solution is very good. Only at high frequencies, small deviations come into effect, due to the Euler-Bernoulli beam theory used in the analytical approach assuming infinite shear stiffness. In the FE-model, the effects of finite shear stiffness are included and hence, the resonances are shifted slightly downwards. The differences are very limited and do not influence the general characteristics suggesting that the current model using Euler-Bernoulli theory is adequate.

The results for profiles B and C are not presented here, but show the same general trends as described for profile A.

As expected from the theoretical results, the experimental investigation reveals that the influence of the fillets is not dominated by the mass, but by a stiffening effect related to a frequency shift in the measured mobilities (see section 2.5 for details).

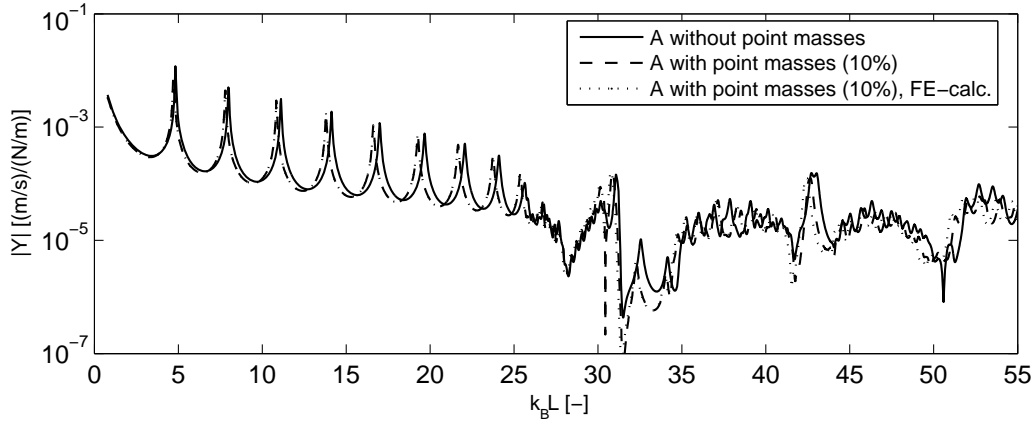


Figure 2.6: Magnitude of transfer mobility (F_y, v_y) with and without additional point masses (10% of total profile mass) and results of FE-calculation for profile A

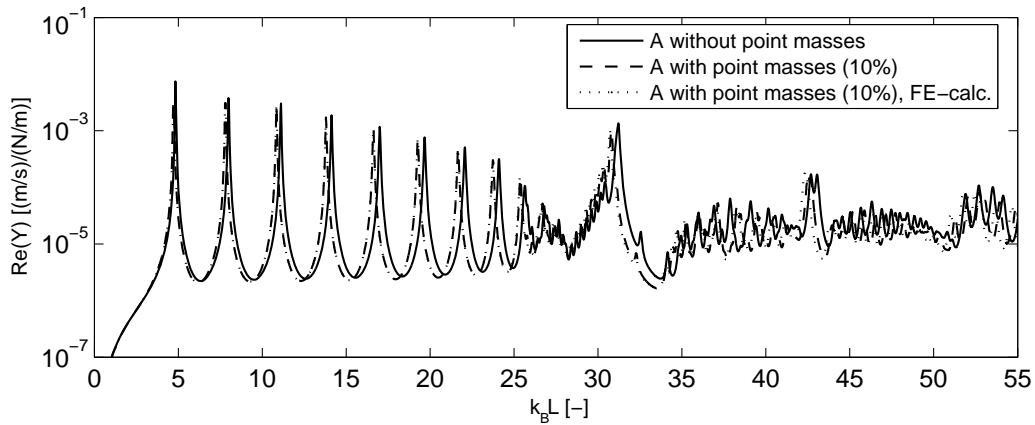


Figure 2.7: Real part of input mobility (F_y, v_y) with and without additional point masses (10% of total profile mass) and results of FE-calculation for profile A

2.5 Experimental validation

The theoretical results are compared with those obtained in an experimental investigation. A strip is considered of a typical extruded aluminium profile with vertical webs between the outer plates. The strip has a width of about 2 cm so that the two-dimensional beam model should be adequate up to about 14.5 kHz, where half the bending wavelength approaches the strip width. For brevity, no details of the geometry are given, but the overall

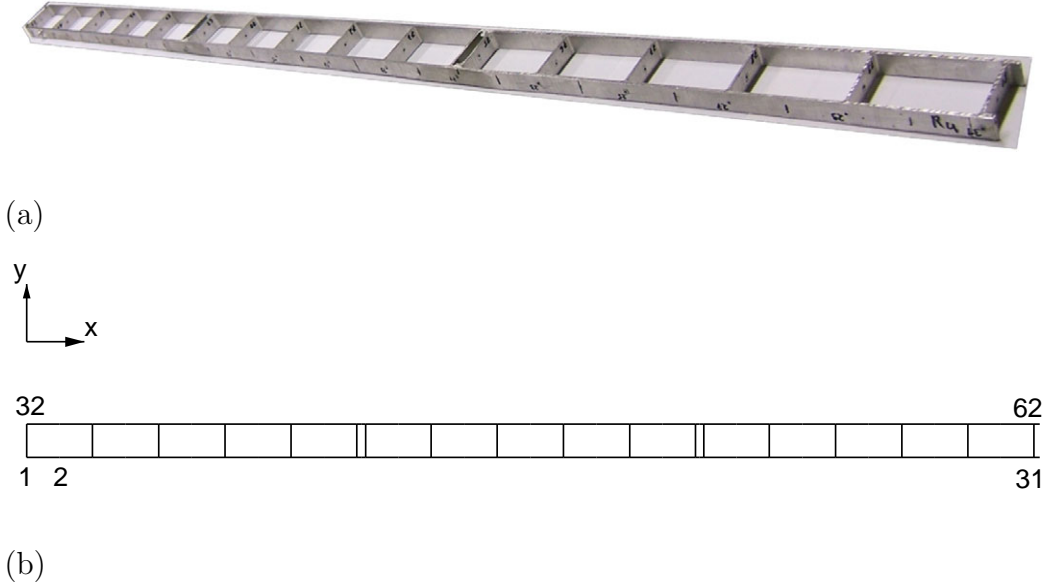


Figure 2.8: (a) Photo and (b) sketch of calculation model of the extruded profile test object including node numbering

length is 1765 mm, the height is 60 mm, the distance of the inner webs is about 110 mm and the thicknesses of the webs as well as outer flanges are in the range of 2.5 – 3.5 mm resulting in a total profile mass of 0.873 kg. The strip is shown in Fig. 2.8. Mobility measurements are performed on the strip using white noise force excitation in y -direction at one end. Results are compared with calculated ones for response measurements at the excitation position (input mobility), node 1 and 2, and at remote positions (transfer mobility). Moreover, rotational response components are measured using two laser vibrometers at closely spaced measurement positions (10 mm distance).

The comparison of calculated and measured results for the force input mobility in the y -direction at node 2 is shown in Fig. 2.9. The measured results are in agreement with the calculated curves in the complete investigated frequency range. Global vibrations arise mainly up to about 500 Hz, where the periodic system effects come into play with the lowest stop-band. A systematic difference between measurement and calculation is detected at low frequencies, where the measured eigenfrequencies are shifted slightly towards higher frequencies. This observation can be referred to an effect of the fillets at the joints. It is dominated by the additional stiffening of the web ends (see Fig. 2.5) and not by the additional mass loading. A calculation with slightly higher thickness of the webs demonstrates that the shift

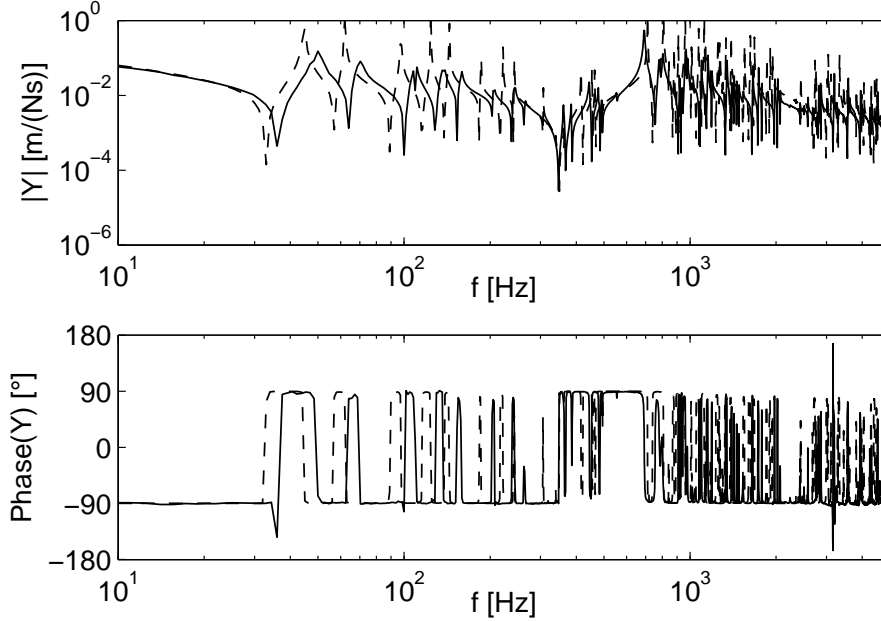


Figure 2.9: Comparison of measured (—) and calculated (---) y -force input mobility of extruded profile strip at node 2

of the resonances towards higher frequencies is sensitive to this parameter. A drawback of simply using the higher web thickness is a deviation at high frequencies.

The calculation is performed assuming a constant loss factor of $\eta = 0.001$. This is in contrast to results of damping tests of the profile, where it is observed that the loss factor is higher at low frequencies up to about 200 Hz and diminishes towards higher frequencies. Such a frequency dependency explains the broader resonance peaks in the measured mobilities at low frequencies. The transfer mobility from force excitation at node 1 in y -direction to the response at node 62 is shown in Fig. 2.10. The transfer mobility demonstrates the existence of periodic system effects in the high frequency range with stop-bands between 600 and 900 Hz as well as between 2000 and 2600 Hz, bounded by pass-bands. The lowest frequency where local vibrations come into play is associated with the lowest bending eigenfrequency of an outer member. Postulating simply supported boundary conditions for the web beams, this frequency is approximately 580 Hz, coinciding with the beginning of the lowest stop-band. This is not in accordance with the results for mono-coupled periodically simply supported single beams [16], where the pass-bands start with the eigenfrequency of the simply supported beam section and ends with

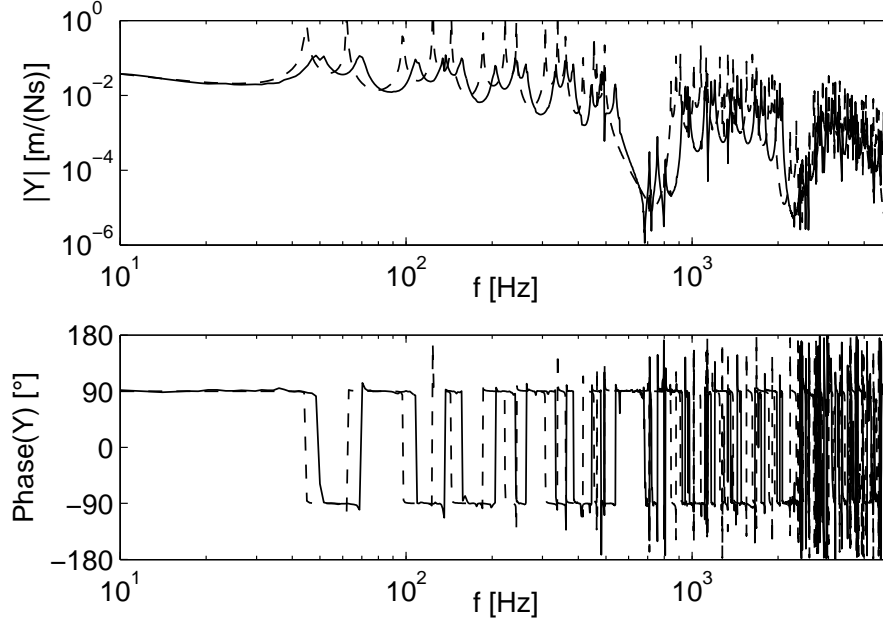


Figure 2.10: Comparison of measured (—) and calculated (---) y -force transfer mobility of extruded profile strip (y -force at node 1, y -response at node 62)

the clamped eigenfrequency. For multi-coupled systems, a thorough investigation is necessary to identify the possibly overlapping limits of pass- and stop-bands (see theory of multi-coupled periodic systems in chapter 3).

The cross transfer mobility from force excitation at node 1 to rotational velocity at node 61 is included in Fig. 2.11 and corroborates the reliability of the calculation model also for the rotational components.

From the complex transfer functions to all measured positions along the strip, the operational deflection shapes are developed and some examples are presented in Figs. 2.12 to 2.14 together with the calculated ones. The matching of measured and calculated shapes is good at low frequencies when the above mentioned slight frequency shift is considered, and remains reasonable at high frequencies. Figs. 2.12 and 2.13 correspond to resonances of the strip in the global regime whereas Fig. 2.14 illustrates wave propagation slightly above the first stop-band. Additional deflection shapes are included in Appendix B.

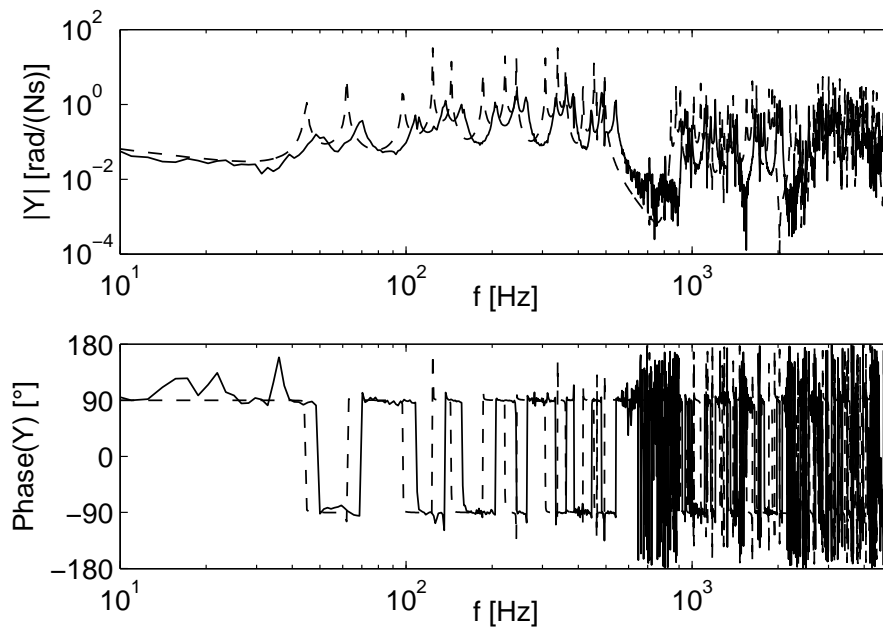


Figure 2.11: Comparison of measured (—) and calculated (---) cross transfer mobility of extruded profile strip (y -force at node 1, rotational velocity response at node 61)

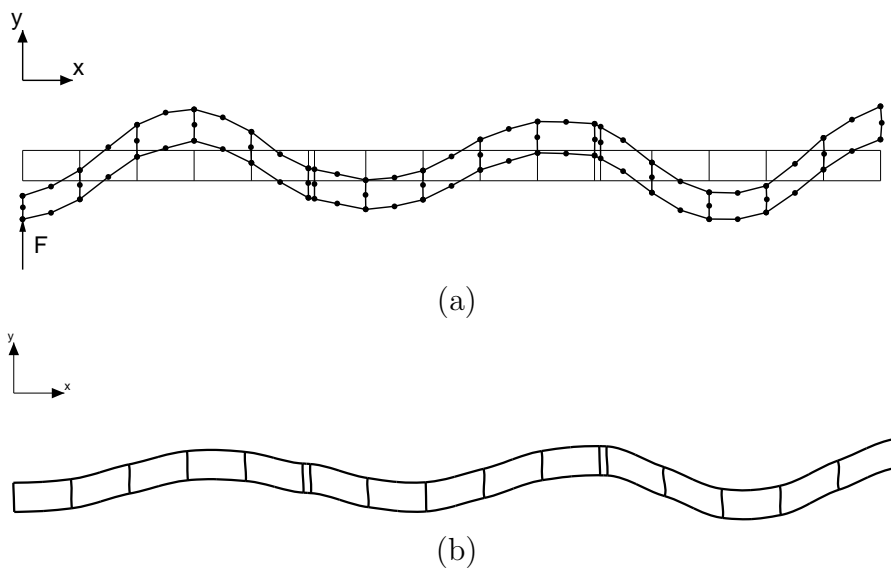


Figure 2.12: Comparison of (a) measured and (b) calculated deflection shapes ($f_{meas} = 139$ Hz, $f_{calc} = 130$ Hz, y -force at node 1)

CHAPTER 2. PROFILE STRIPS: THEORY AND EXPERIMENTAL VALIDATION

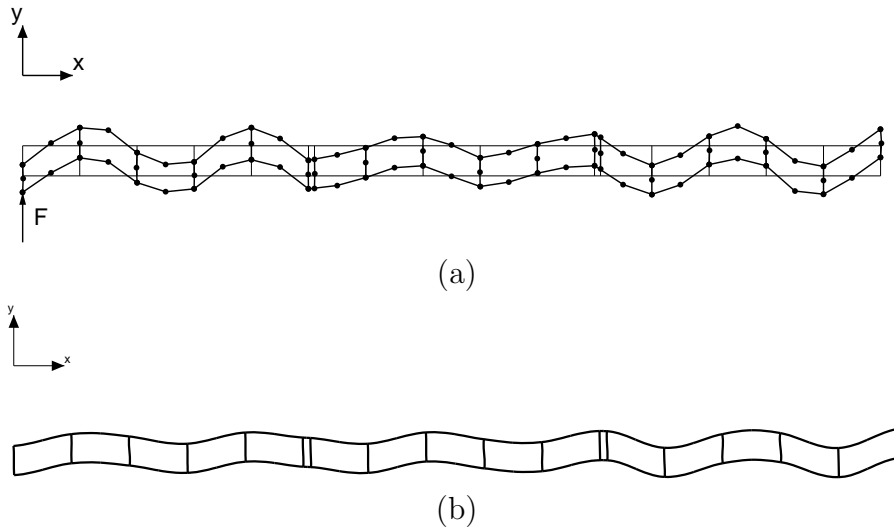


Figure 2.13: Comparison of a) measured and b) calculated deflection shapes ($f_{meas} = 364$ Hz, $f_{calc} = 345$ Hz, y -force at node 1)

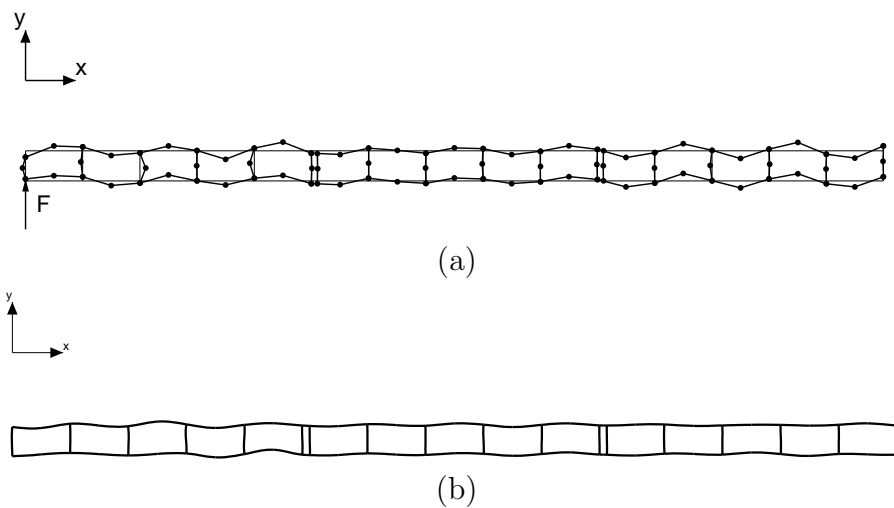


Figure 2.14: Comparison of a) measured and b) calculated deflection shapes ($f_{meas} = 950$ Hz, $f_{calc} = 950$ Hz, y -force at node 1)

2.6 Concluding remarks

A calculation model for cross sections of typical light weight profiles based on beam vibrations is established and experimentally validated for a profile strip with vertical webs. Parameter studies on periodic systems with straight and inclined webs between the outer faces show that typical periodic system pass- and stop-band behaviour is most pronounced in the case of solely vertical stiffeners. These effects are also present for the profiles with inclined members. The periodic effects are also clearly visible in the experimental results.

The influence of welds and thicker ends of the webs at the joints is mainly characterized by a stiffening effect, manifested by an eigenfrequency shift towards high frequencies. The additional mass is of minor importance. Details of the geometry of the inner profile webs influence the dynamic behaviour explicitly so that any sandwich approach, neglecting the details, is inappropriate.

The wave propagation at low frequencies (global vibrations) can be approximated for profiles with inclined members by an equivalent bending beam. For the case of solely vertical stiffeners, however, the global vibrations are not well represented by an equivalent bending beam since the wavelength at low frequencies is significantly shorter than with inclined stiffeners here which is shown in chapter 3. At high frequencies the detailed description of the dynamics for both configurations with and without inclined webs is inevitable.

Chapter 3

Light weight profile strips: Wavenumber content

3.1 Introduction

In order to get a better understanding of the structure-borne sound characteristics of typical light weight profiles, the wave propagation in different strips is investigated. The objective is to identify the characteristic waves that propagate or decay in the strips. The wavenumber content of the outer plates forms the basis for treating sound radiation problems. Based on the calculation model established and validated in chapter 2, the wavenumber content and the wave forms of the characteristic waves in the infinite light weight structures are investigated in this chapter.

Often the light weight profiles are periodic or nearly periodic so that periodic structure theory can be exploited to investigate the dispersion characteristics. A general theory for the wave propagation in mono- and multi-coupled structural periodic systems has been developed by Mead [9, 10]. Mono-coupled periodic systems are connected by only one displacement variable in contrast to multi-coupled systems. The light weight profiles investigated here are typical members of the multi-coupled case for which a general theory is thoroughly presented in [10].

3.2 Dispersion characteristics of profile strips

For the profiles A to C introduced in chapter 2 the wavenumber content of the characteristic waves is investigated using three different methods. The first one uses the determinantal equation resulting from multi-coupled periodic system theory, the second one is the spatial Fourier transform and the third

one is the solution of the transfer matrix eigenvalue problem. The complete set of procedures is illustrated in Fig. 3.1. In order to capture the wave propagation in the profile strips without the influence of end reflections, the calculation is performed on prolonged strips or based on infinite strip theory.

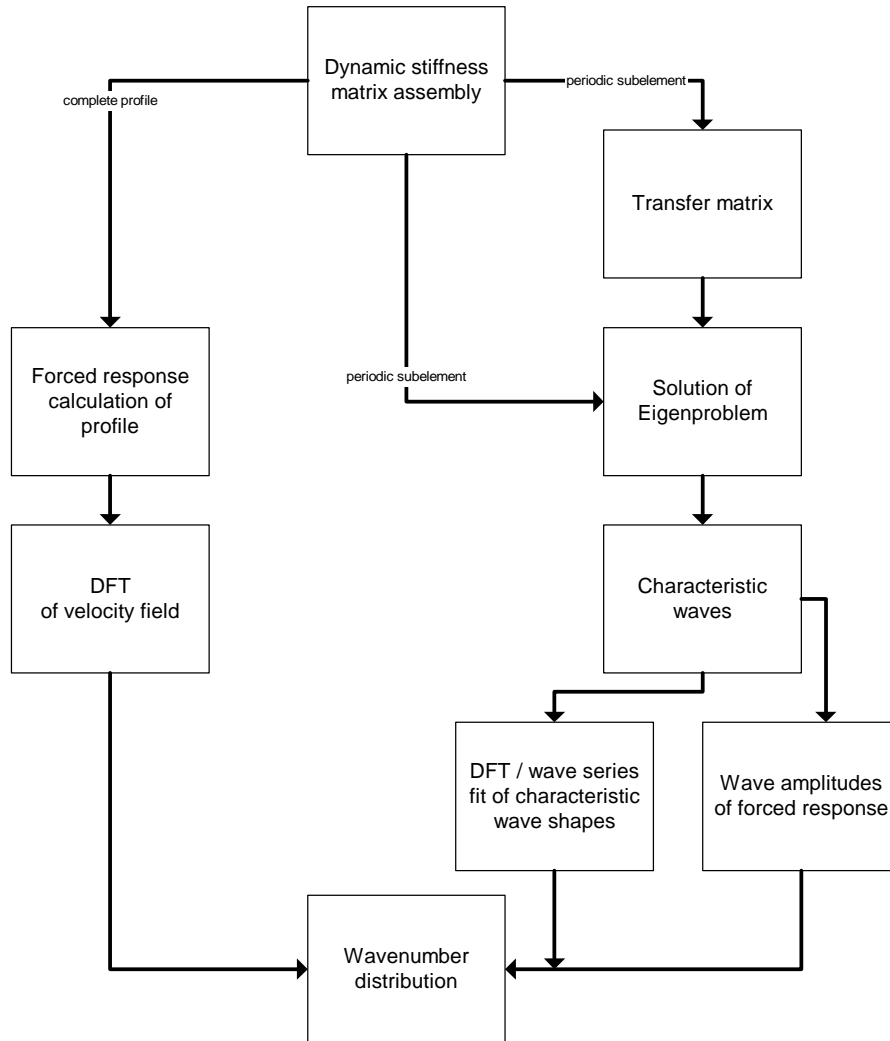


Figure 3.1: Principal ways to determine dispersion characteristics (quantitative wavenumber distribution) of profile strip

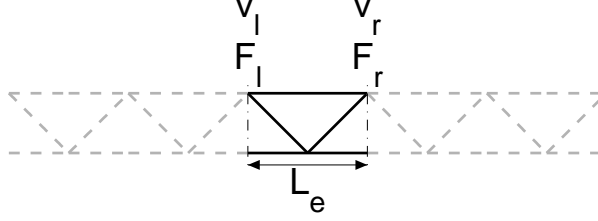


Figure 3.2: Subelement in periodic chain, illustrated for profile A

3.2.1 Multi-coupled periodic systems and determinantal equation

The subelements of the light weight profile strips under study are connected at each edge by two points with three degrees of freedom each, resulting in a multi-coupled periodic system with six coupling coordinates (see Fig. 3.2). No detailed review of the theory for multi-coupled periodic systems will be given, but some main features shall be highlighted.

A single subsystem of the periodic system is coupled to the adjacent subsystems by n degrees of freedom (DOFs), which can be arbitrarily translational or rotational DOFs. Hence, the mobility matrix of a subsystem including the left and right connection points can be formulated using a $(2n) \times (2n)$ mobility matrix \mathbf{Y}

$$\begin{Bmatrix} \mathbf{v}_l \\ \mathbf{v}_r \end{Bmatrix} = \mathbf{Y} \begin{Bmatrix} \mathbf{F}_l \\ \mathbf{F}_r \end{Bmatrix} = \begin{bmatrix} \mathbf{Y}_{ll} & \mathbf{Y}_{lr} \\ \mathbf{Y}_{rl} & \mathbf{Y}_{rr} \end{bmatrix} \begin{Bmatrix} \mathbf{F}_l \\ \mathbf{F}_r \end{Bmatrix}. \quad (3.1)$$

Here, index l represents quantities on the left hand side of the element and index r represents the quantities on the right. The vectors \mathbf{v} and \mathbf{F} may contain translational and rotational quantities.

Assuming now that the quantities on the left are always related to the quantities on the right by an exponential factor (Bloch's theorem), one may write the following relation using the complex propagation constant $\mu = -\delta \pm j\epsilon$,

$$\begin{aligned} \mathbf{v}_r &= e^\mu \mathbf{v}_l = e^{jkL_e} \mathbf{v}_l \\ \mathbf{F}_r &= -e^\mu \mathbf{F}_l = -e^{jkL_e} \mathbf{F}_l. \end{aligned} \quad (3.2)$$

δ is the attenuation constant and ϵ is the phase constant [33, p. 187]. The complex wavenumber k with the real part defining the phase difference per unit length and the imaginary part the attenuation per unit length, is included in Eq. (3.2) in conjunction with the periodic length L_e .

Using the exponential ansatz of Eq. (3.2) in Eq. (3.1) and performing some algebraic transformations results in a homogeneous matrix equation which has a non-trivial solution when the determinant of the matrix vanishes,

$$|\mathbf{Y}_{ll} + \mathbf{Y}_{rr} - e^{\mu}\mathbf{Y}_{lr} - e^{-\mu}\mathbf{Y}_{rl}| = 0. \quad (3.3)$$

At any frequency, up to $2n$ different values of μ can exist.

The phase constant related to propagating waves is multi-valued. If ϵ_0 is a solution between 0 and π , then $\epsilon_n = \epsilon_0 + 2\pi n$ ($n = 0, \pm 1, \pm 2, \pm 3 \dots$) is also a solution of Eq. (3.3).

The phase constant has a distinct relation to the wavenumber as it represents the difference in phase of the motion in the periodic system at points separated by the periodic distance L_e . The corresponding phase difference per unit length (wavenumber k_n) is ϵ_n/L_e .

$$k_n = \pm(\epsilon_0 + 2n\pi)/L_e \quad (3.4)$$

In analogy to the wavenumber definition for travelling waves, an imaginary wavenumber component for the decaying waves can be defined by

$$k_{decay} = \pm j \delta/L_e. \quad (3.5)$$

In contrast to the multi-valued solution for the travelling waves, the decaying waves are single valued.

As a result of the multi-valued travelling components, an infinite series of waves with the given wavenumbers exists in the periodic system. The positive and negative wavenumbers are related to left- and rightwards travelling waves, respectively.

From the solution of the determinantal Eq. (3.3) the wavenumbers can be directly calculated but the solution for propagating waves (imaginary μ) is multi-valued with a periodicity of 2π . For decaying waves (real μ) distinct solutions exist. For each characteristic wave the distribution is fixed between the principal value ($n = 0$) and the higher and lower values of μ or k . Nonetheless, the overall wavenumber content for a certain excitation depends not only on the structure itself but also on the amplitudes of the excited characteristic waves. Each characteristic wave contributes to the overall wavenumber spectrum through its definite wavenumber content, weighted with its wave amplitude. This definite wavenumber content is detailed in section 3.4.

Herein, the solution of the determinantal Eq. (3.3) is limited to purely real or imaginary wavenumbers. Hence, only the purely propagating and decaying waves are shown in Fig. 3.3 for strip A (see Fig. 2.2). Complex waves are not included.

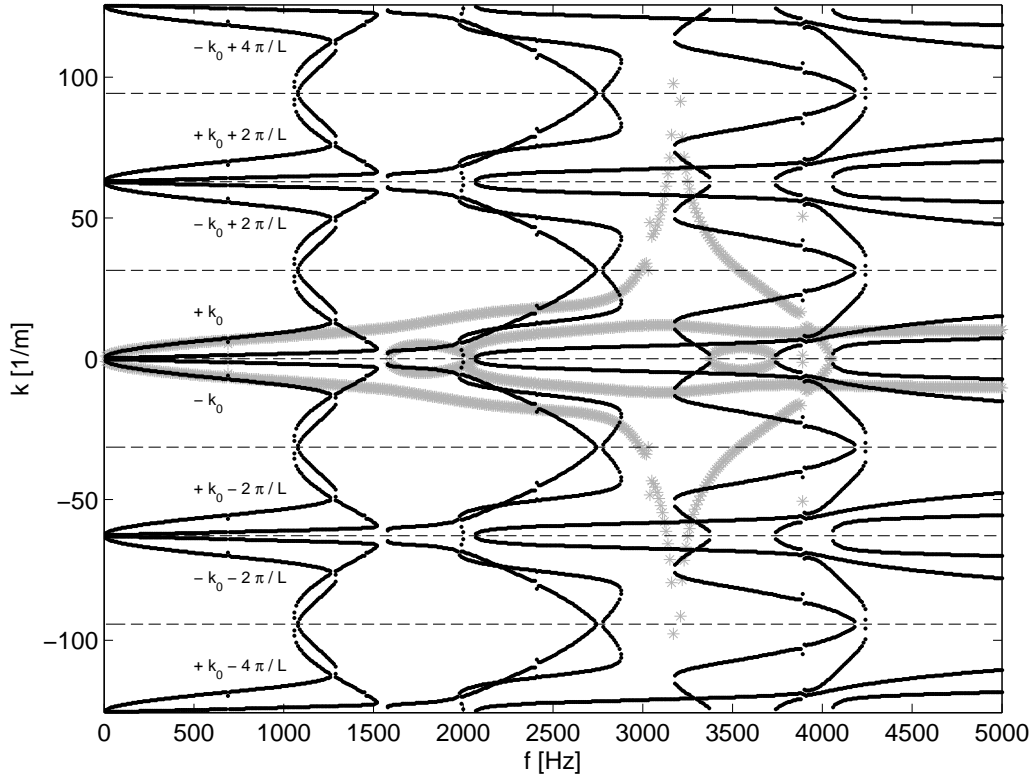


Figure 3.3: Wavenumber dispersion plot for periodic profile strip A including positive, negative travelling waves and decaying waves (* (grey): decaying waves, ... (black) propagating waves)

As the wavenumber is periodically repeated with $2n\pi/L_e$, only a fraction of the complete dispersion diagram can be shown and indeed, there is no benefit of plotting more than $\pm k_0$ except for the decaying part, plotted in grey, which is not periodic (imaginary wavenumber).

In order to illustrate the periodic character of the propagating waves the plot is extended beyond the principal values. Regions in the plot indicate (repeated) rightward or leftward travelling waves.

A drawback of the approach with the determinantal equation is that the solutions for μ need not be purely real or imaginary but can also be complex. This means that the wave comprises a propagating and a decaying part. It is quite a laborious task to find the complex roots of the determinantal equation for each frequency. Hence, for the complete picture including complex waves, the approach using the transfer matrix presented later is favourable.

The dispersion plotted in Fig. 3.3 reveals that for profile A global wave behaviour is expected for frequencies up to 1100 Hz, where local waves start to propagate with significantly higher wavenumbers. Between 1500 and 2000 Hz a stop-band can be identified, followed alternately by pass- and stop-bands. Even so, there are some propagating waves remaining in the stop-bands which are related to mainly longitudinal wave motion with low wavenumbers.

3.2.2 Dispersion characteristics using spatial Fourier transform

For this approach a spatial sampling at discrete points is necessary, resulting in the discrete Fourier transform (DFT). For a profile of length L with N equally distributed spatial sampling points, $v_n = v(n\Delta x)$; $n = 1, 2, 3, \dots, N$, results in the following transformation

$$\begin{aligned} V_m = V(m\Delta k) &= \Delta x \sum_{n=1}^N v_n e^{-j2\pi \frac{mn}{N}}, \quad m = 1, 2, 3, \dots, N \\ &= \Delta x \sum_{n=1}^N v_n e^{-jm\Delta k x_n}, \quad \Delta k = \frac{2\pi}{L} = \frac{2\pi}{N\Delta x}. \end{aligned} \quad (3.6)$$

To satisfy the Nyquist criterion, the maximum wavenumber, which can be unambiguously identified, is given by $k_{max} = \frac{\pi}{\Delta x}$. Therefore, it has to be assured that there is only negligible spectral content above this wavenumber. This can only be done by choosing a high resolution so that the critical wavenumber is above the highest occurring wavenumber.

The advantage of the DFT-approach is that it is easy to implement, standard FFT algorithms can be used and it is applicable to all profile structures independent of periodicity. The disadvantage is that it is computationally quite demanding as the complete vibration field of the profile has to be calculated and the FFT with high resolution has to be performed. One problem for finite structures is that the wavenumber resolution depends only on the investigated profile length L . For an adequate resolution a long profile strip has to be calculated enlarging the computational effort involved.

Another feature of this approach is that the energy distribution in the periodic wavenumber series is readily obtained. This gives some remarkable insight for the given excitation conditions as the excitation of different wave types can be identified. On the other hand, it should be pointed out that this can also give misleading results when trying to extract the general wave propagation features. Not all the wave types which are possible in the structure have to be excited by a certain force or moment excitation. At least,

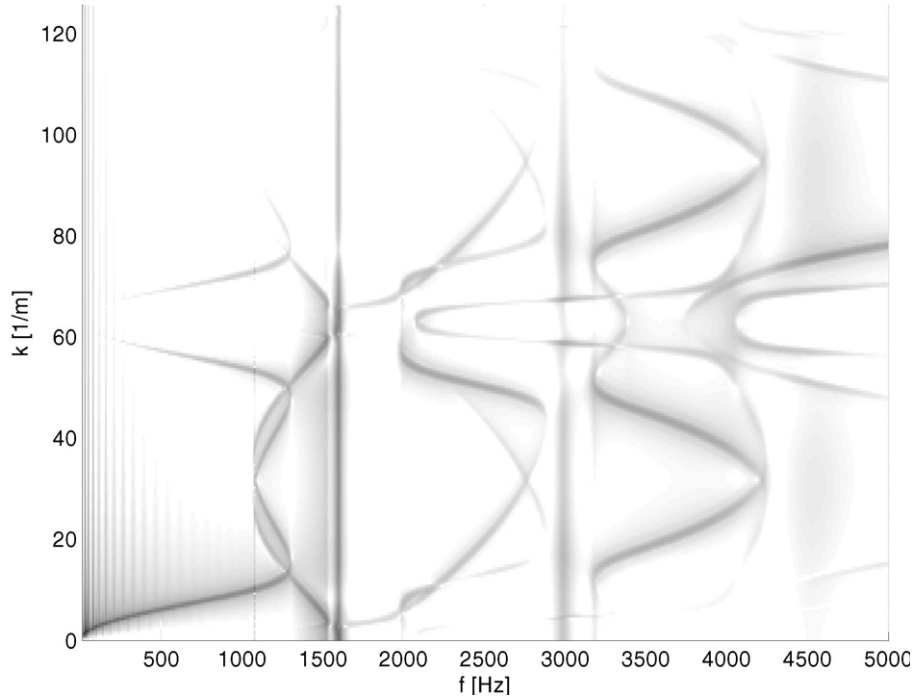


Figure 3.4: DFT plot of lower plate profile strip A, unit y -force excitation at left lower side, shading limits $L_{v,DFT}$: 10 (white) ... 90 (black) dB re. 5×10^{-8} m/s

different excitation mechanisms should be applied and the results compared to get a more general picture.

The dispersion characteristics of the profile strip A, using the DFT approach, are shown in Figs. 3.4 and 3.5 for force and moment excitation respectively. The excitation is located at the left end of the profile strip, the right end is damped with gradually increasing loss factor in order to simulate a non-reflective boundary comparable to a semi-infinite strip. The DFT is performed over a 6 m long section from the left end in order to achieve a good resolution.

For the DFT, the normal velocity distribution of the lower edge is calculated and interpolated to give a uniform spatial sampling by using a spline interpolation function.

The result of the spatial Fourier transform is given by the two-sided spectrum V of the velocity distribution. For plotting the logarithmic value of the magnitude $L_{v,DFT} = 20 \log [|V|/(5 \times 10^{-8} \text{ m/s})]$ is used.

Despite the simulated non-reflective boundary on the right, reflections arise in the low frequency regime and hence, modes are visible manifested by

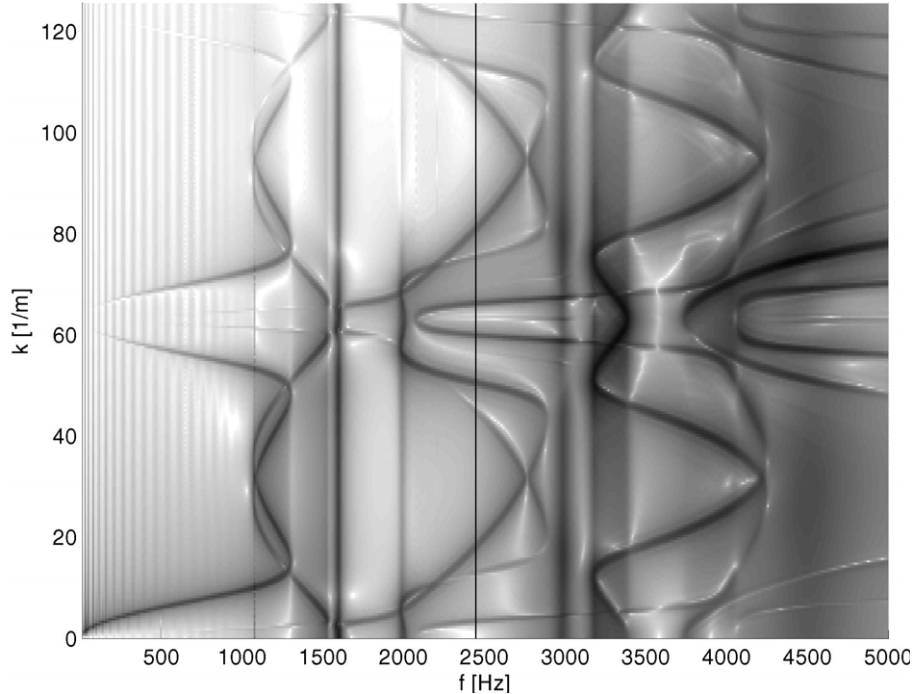


Figure 3.5: DFT plot of lower plate profile strip A, unit moment excitation at left lower side, shading limits $L_{v,DFT}$: 10 (white) ... 90 (black) dB re. 5×10^{-8} m/s

faint vertical lines up to about 1000 Hz.

The periodic nature of the wavenumber content is visible when using the DFT, where the energy is distributed in a characteristic way between the principal value and the 'side bands'. At low frequencies the principal value with a wavenumber similar to global equivalent bending wave behaviour dominates the wave propagation. Starting with about 1000 Hz, alternating pass- and stop-bands emerge for profile A. The different excitations (force and moment) lead to slightly different quantitative distributions in the excited waves, but do not modify the overall dispersion characteristics. The response for unit moment excitation exceeds the unit force excitation. The DFT-results for profiles B and C are included in Appendix C, where profile C exhibits the most significant periodic system effects and shows also a significant difference in excited wave types for force and moment excitation respectively.

The decaying waves cannot be found in the DFT-result as they decay too rapidly and do not contribute significantly to the velocity spectrum of the complete strip. They can be extracted using the determinantal equation or by solving the eigenvalue problem. This gives a clearer picture of the

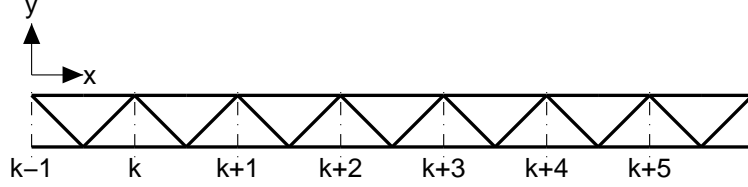


Figure 3.6: The positions along the periodic chain are labelled in the given way

characteristic waves, but the energy distribution cannot be extracted directly.

3.2.3 Dispersion characteristics using transfer matrix eigenvalue problem

As an alternative for finding the wave types in the periodic structure, the transfer matrix \mathbf{T} of a single subsystem can be used.

The notation for the positions along the periodic chain is shown in Fig. 3.6:

Starting with the definition of the T-matrix

$$\begin{Bmatrix} \mathbf{v}_{k+1} \\ \mathbf{F}_{k+1} \end{Bmatrix} = \mathbf{T} \begin{Bmatrix} \mathbf{v}_k \\ \mathbf{F}_k \end{Bmatrix} \quad (3.7)$$

and invoking Bloch's theorem, Eq. (3.2), the state vectors on both sides of the periodic subsystem can be related by

$$\begin{Bmatrix} \mathbf{v}_{k+1} \\ \mathbf{F}_{k+1} \end{Bmatrix} = \lambda \begin{Bmatrix} \mathbf{v}_k \\ \mathbf{F}_k \end{Bmatrix}, \text{ where } \lambda = e^{\mu}. \quad (3.8)$$

Combining Eqs. (3.7) and (3.8) results in an eigenvalue problem, where the identity matrix \mathbf{I} is introduced,

$$[\mathbf{T} - \lambda \mathbf{I}] \begin{Bmatrix} \mathbf{v}_k \\ \mathbf{F}_k \end{Bmatrix} = \mathbf{0}. \quad (3.9)$$

From this equation it is obvious that λ are the eigenvalues of the \mathbf{T} -matrix. The number of eigenvalues is two times the number of coupling coordinates. Routines for the solution of the complex eigenvalue problem are available and can be used to find all the eigenvalues and related propagation constants of the periodic system including the complex waves.

The only disadvantage of the approach, apart from the multi-valued solution, is the fact that numerical instabilities can arise in the solution of the

eigenvalue problem. The multi-valued solution exists not only for the purely propagating waves, but also for the complex waves as $e^{\mu_{complex}} = e^{\mu_{complex} + 2n\pi j}$, n being an arbitrary integer.

Due to the nature of the \mathbf{T} -matrix, the eigenvalues are generally complex and occur in reciprocal pairs $(\lambda_i, 1/\lambda_i)$. Assuming no internal damping, a purely propagating wave exists if $|\lambda_i| = 1$, corresponding to pass-bands for the wave. In a stop band, the eigenvalues are real valued. An eigenvalue inside the unit circle represents a positive (right) going wave, whereas an eigenvalue outside the unit circle represents a negative (left) going wave.¹ Complex eigenvalues can occur only in groups of four and hence are only possible for systems with more than one coupling coordinate as there are only two eigenvalues for mono-coupled transfer matrices (2×2).

To each eigenvalue a certain eigenvector exists, defining the wave form of the wave type. The complete vibration of the profile can be set up by adding the contributions of all wave types

$$\begin{Bmatrix} \mathbf{v}_k \\ \mathbf{F}_k \end{Bmatrix} = \Phi_R^T \begin{Bmatrix} \mathbf{L}_k \\ \mathbf{R}_k \end{Bmatrix}^T. \quad (3.11)$$

As there are $2m$ independent waves, the first m columns of the matrix Φ_R are the eigenvectors of the transfer matrix corresponding to the left travelling waves ($\lambda_i, i = 1, \dots, m, \lambda_i \geq 1$) and the last m columns to the right-going waves ($1/\lambda_i, i = 1, \dots, m, \lambda_i \geq 1$). m defines the number of coupling coordinates with corresponding orthogonal eigenvectors, excluding the pass-band bounding frequencies, where double eigenvalues occur.

The vector \mathbf{L}_k contains the amplitudes of the left-going waves and the vector \mathbf{R}_k contains those of the right-going waves. The wave amplitudes at adjacent bays are related by

$$\begin{Bmatrix} \mathbf{L}_{k+1} \\ \mathbf{R}_{k+1} \end{Bmatrix} = \mathbf{W} \begin{Bmatrix} \mathbf{L}_k \\ \mathbf{R}_k \end{Bmatrix} \quad \text{where} \quad \mathbf{W} = \Phi_R^{-1} \mathbf{T} \Phi_R. \quad (3.12)$$

Since Φ_R is the (right) eigenvector matrix of \mathbf{T} , the matrix \mathbf{W} is the diagonal matrix of the eigenvalues of \mathbf{T} and is called the wave transfer matrix,

¹This distinction is not possible for undamped systems, where in the pass-bands $|\lambda| = 1$. In this case the distinction can be based on the following rule provided $e^{j\omega t}$,

$$\begin{aligned} \text{Im}(\lambda) > 0 &\rightarrow k \text{ positive} \rightarrow \text{negative (left) travelling wave} \\ \text{Im}(\lambda) = 0 &\rightarrow k = 0 \rightarrow \text{standing wave} \\ \text{Im}(\lambda) < 0 &\rightarrow k \text{ negative} \rightarrow \text{positive (right) travelling wave} \end{aligned}$$

$$\mathbf{W} = \begin{bmatrix} \mathbf{\Lambda} & \mathbf{0} \\ \mathbf{0} & \mathbf{\Lambda}^{-1} \end{bmatrix} \quad \text{where} \quad \mathbf{\Lambda} = \text{diag}(\lambda_1, \dots, \lambda_m). \quad (3.13)$$

Solving the eigenvalue problem in Eq. (3.9) results in a complete picture of free wave propagation in the strip. The eigenvalues can be directly linked to wavenumbers and the eigenvectors establish the wave form of each characteristic wave. Knowing the wave amplitudes at a certain position makes it possible to calculate the complete wave amplitudes at all other positions along an infinite strip using the wave transfer matrix containing the eigenvalues. In practice it is necessary to get the wave amplitudes for a certain excitation (forced response). This is treated in chapter 4.

The major task after the solution of the transfer matrix eigenvalue problem is the identification of the different characteristic wave types, i.e. the unique separation of the wave types over the whole investigated frequency range. Different algorithms are tried in the complex plane for the propagation constants, but fail mainly at the points where different wave types join. A unique separation at these points is difficult (or perhaps not possible) if the structural damping is set to zero. Nonetheless, it is possible to follow each characteristic wave in the complex plane by adding a small amount of structural damping ($\eta = 0.01$). The eigenvalues are identified as complex conjugate pairs and only the eigenvalues with modulus smaller than unity are taken for the identification procedure. The sorted frequency dependent wavenumber content for the right-travelling waves 7 to 12 is shown for strips A, B and C in Figs. 3.7 to 3.9.

It is obvious that the profiles with inclined members (A and B) exhibit a more involved wave propagation. Low frequency bending wave dispersion for the equivalent beam can be identified for waves 11 (A) and 10 (B) up to about 1000 Hz. For strip A, longitudinal wavenumbers can be identified in wave 8 in the range 2000 to 4000 Hz. Wave 10 exhibits longitudinal character for strip B between 1000 and 2500 Hz. Hence, it is clear that the character of a wave can change with frequency. For strip C this kind of change does not occur; waves 11 and 12 stay longitudinal in the frequency range up to 4000 Hz. Wave 7 of strips A and B is a purely decaying wave having a wavenumber outside the plotted range. This marked decaying process (or growing process in the other direction) leads to numerical instability, clearly visible in the high frequency regime. For Profile C waves 7 to 10 exhibit a strong decaying component in wide frequency ranges. Wave 10 propagates only in some frequency bands, whereas wave 9 only around 1500 Hz. Above 4000 Hz both are propagating. Only the mainly longitudinal waves 11 and 12 are propagating in almost the complete frequency range.

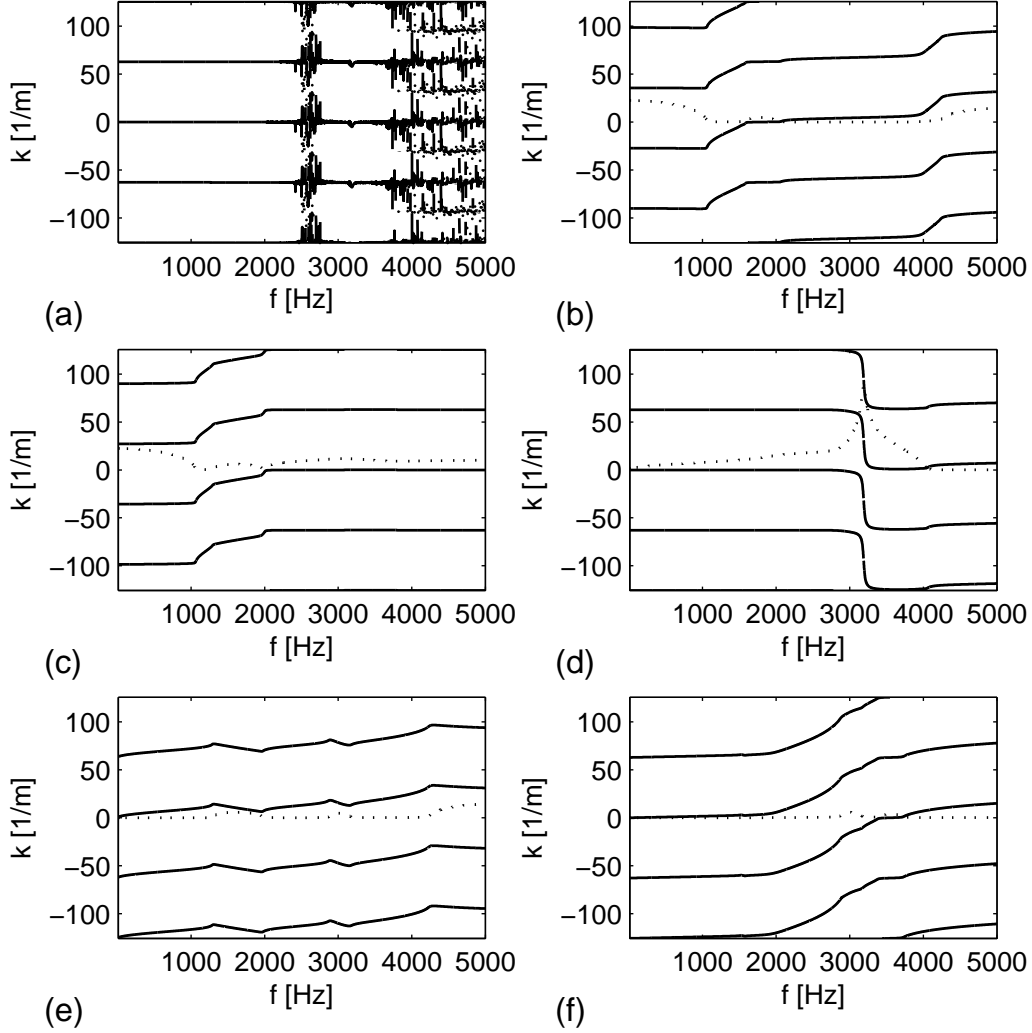


Figure 3.7: Wavenumbers of characteristic waves of profile A extracted using T-matrix, (a) Wave 7, (b) Wave 8, (c) Wave 9, (d) Wave 10 (e) Wave 11, (f) Wave 12, — propagating, - - decaying

3.3 Characteristic waves

In order to plot the wave forms, the eigenvectors, including the end point velocities and forces, are used to calculate the complete velocity pattern of the intermediate beams. For subelements without internal joints, this can be done straightforwardly. For others, the transfer matrix of a part of the element has to be adopted to calculate the intermediate state vectors from which the complete pattern can be reconstructed.

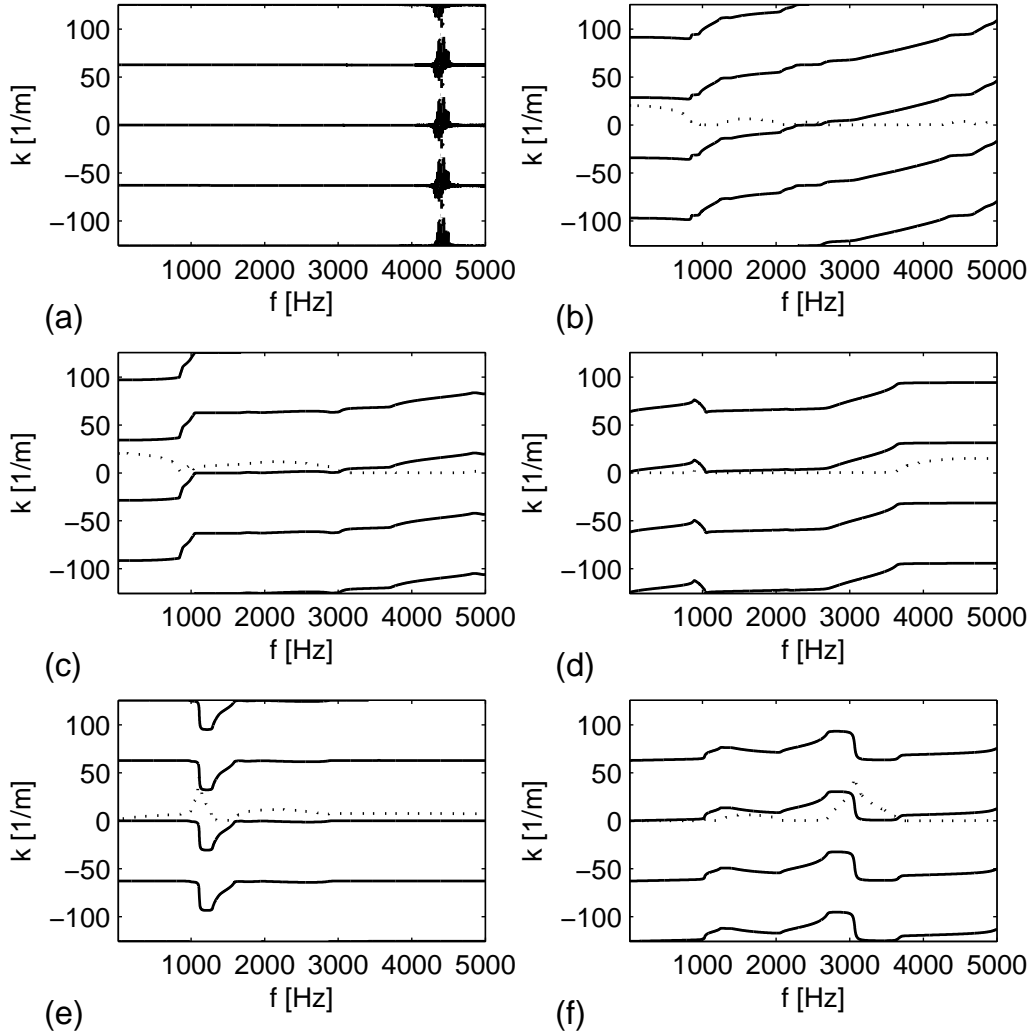


Figure 3.8: Wavenumbers of characteristic waves of profile B extracted using T-matrix, (a) Wave 7, (b) Wave 8, (c) Wave 9, (d) Wave 10 (e) Wave 11, (f) Wave 12, — propagating, - - decaying

The resulting characteristic waves are shown in Figs. 3.10 to 3.12 for a frequency of 1000 Hz. For profile A the waves 11 and 12 are propagating whilst the other wave types are either purely decaying or complex. For practical applications, the propagating waves will dominate the overall vibration of the profile strips. Wave 11, which can be characterized mainly by a form of bending vibration, shows a clear mixture of global and local displacements. Wave 12 is a propagating compressional wave that also contains long and short wavelength components.

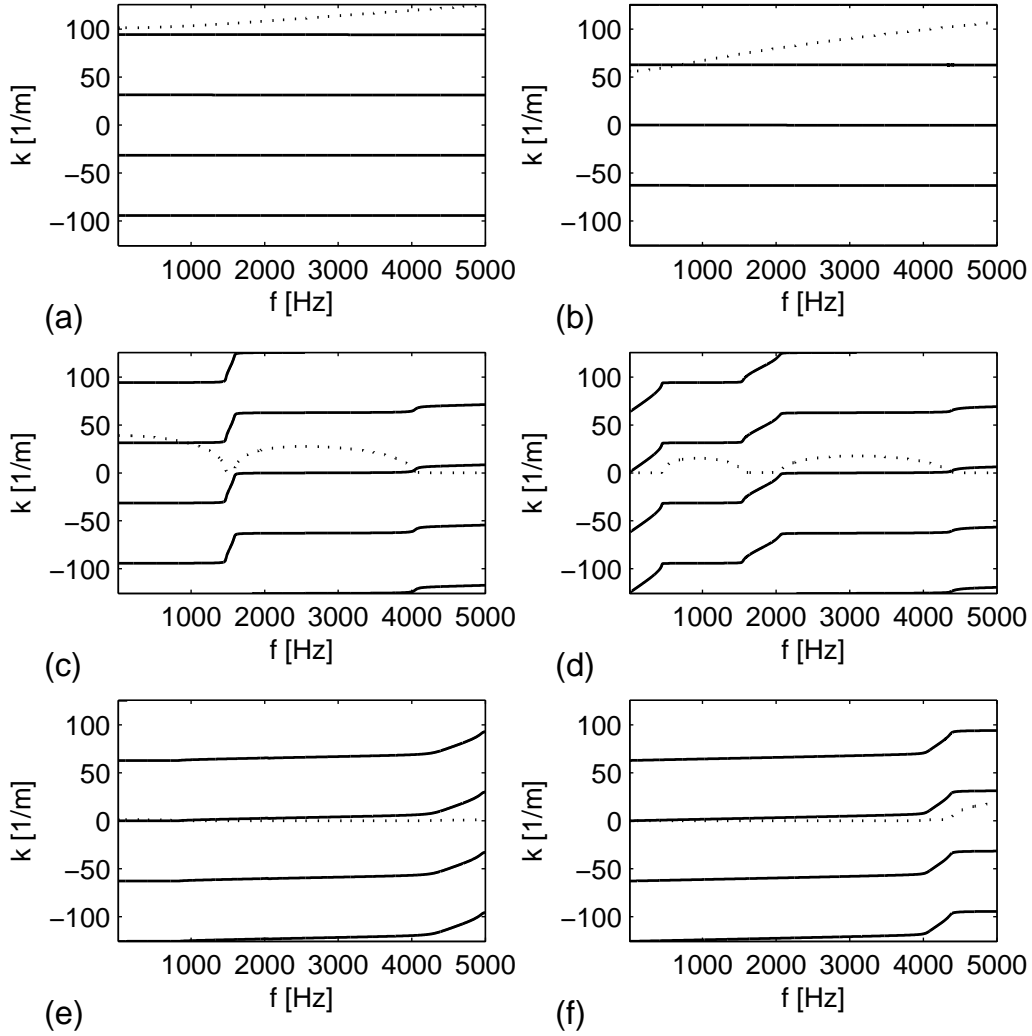


Figure 3.9: Wavenumbers of characteristic waves of profile C extracted using T-matrix, (a) Wave 7, (b) Wave 8, (c) Wave 9, (d) Wave 10 (e) Wave 11, (f) Wave 12, — propagating, - - decaying

For profile B wave types 8 and 12 are mainly propagating. Wave 8 is of compressional character and wave 12 is a mixture of long wave bending and compressional wave.

The propagating waves of profile C at 1000 Hz are number 11 (rotational wave) and 12 (compressional wave).

It should be kept in mind, that no strict classification of the wave types over the complete frequency range can be achieved as e.g. wave number 8 of profile A starts as a decaying wave at low frequencies, then reaches a

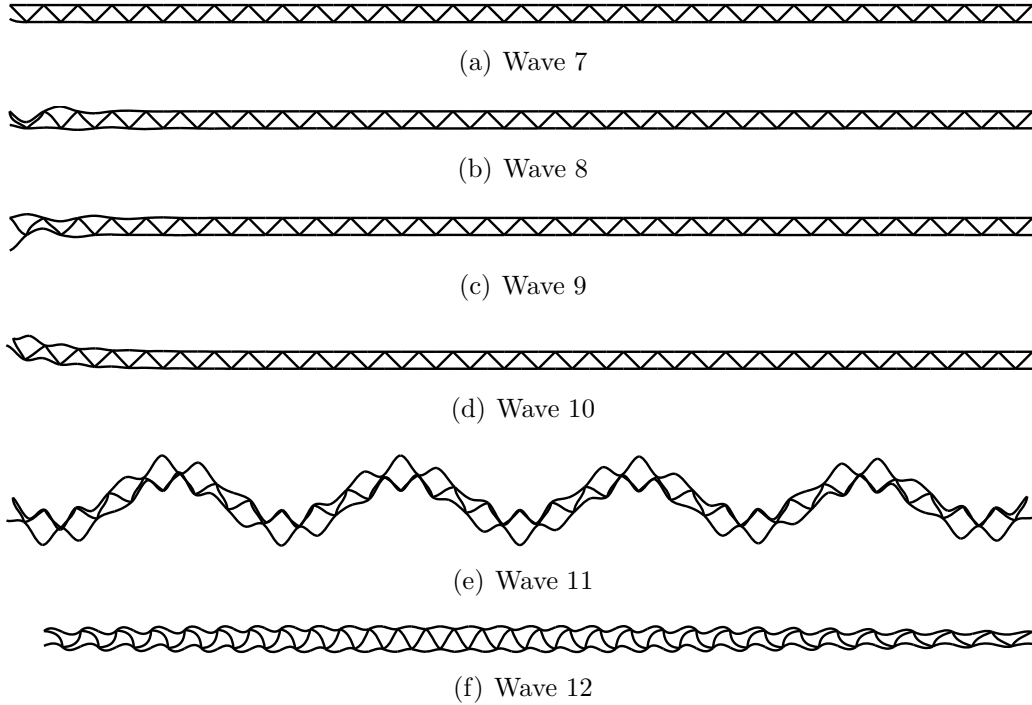


Figure 3.10: Wave forms of characteristic right-travelling waves for profile A ($f = 1000$ Hz)

propagation zone with bending character, is complex again, turns into a compressional wave that passes over in a bending type wave, and finally gets complex again in the investigated frequency range up to 5000 Hz (see Fig. 3.7).

The identification of the characteristic waves realizes the opportunity to simplify the wave propagation in the profile strips. It is reasonable, that the decaying and complex waves do not contribute significantly to the overall vibration of the panel, at least if there is a limited number of excitation points such that the waves can decay.

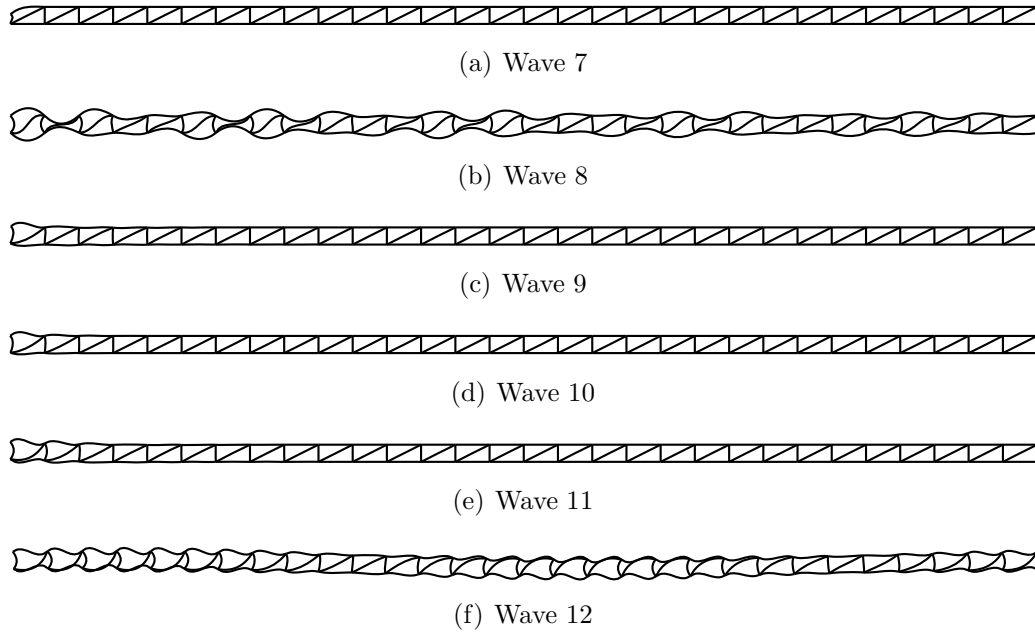


Figure 3.11: Wave forms of characteristic right-travelling waves for profile B ($f = 1000$ Hz)

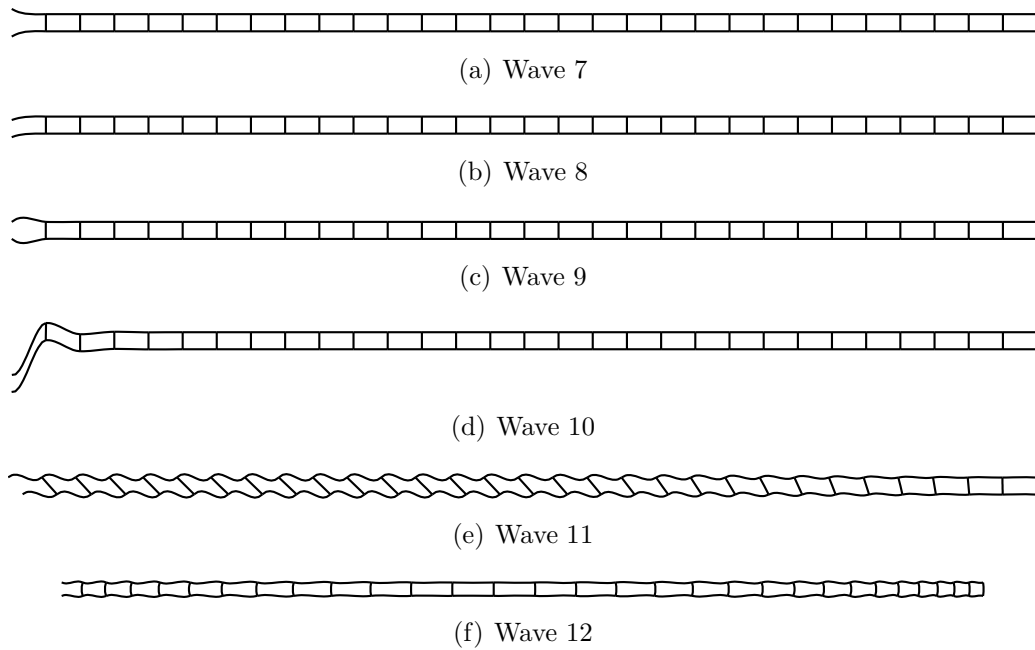


Figure 3.12: Wave forms of characteristic right-travelling waves for profile C ($f = 1000$ Hz)

3.4 Wavenumber content in characteristic waves

3.4.1 Theory

When looking at the wave forms of the profile strips it is obvious that the non-uniqueness of the wavenumbers, resulting from the solution of the eigenvalue problem, is only part of the truth. It establishes a set of *possible* wavenumbers that mathematically fulfil the periodic system condition. The distribution among these wave set components is fixed and can be extracted for each characteristic wave.

The mathematical non-uniqueness for the wavenumbers (periodicity of $2\pi/L_e$) can be explained by the limited spatial resolution of the real physical process. It is not possible to distinguish - with a spatial sampling of L_e - if in between two neighbouring endpoints of the subsystem e.g. one or two wavelengths exist. For a general phase shift ϵ from point to point this means that adding 2π does not change the results at the sampling points $e^{j\epsilon} = e^{j(\epsilon+n2\pi)}$. In terms of wavenumbers $k_n = k_0 + 2\pi n/L_e$.

In contrast to this mathematical ambiguity the physical wavenumber distribution on the structure has to be definite, which means that the energy distribution among the corresponding possible wavenumbers is fixed. It is reasonable that for each characteristic wave such a wavenumber distribution can be determined regardless of the excitation mechanism. The excitation only determines the characteristic wave amplitudes and not the distribution of wavenumbers in each characteristic wave. Hence, it is possible to calculate the fixed wavenumber distribution in each characteristic wave from a characteristic wave form.² Summing up the contributions of all excited characteristic waves results in a unique wavenumber spectrum of the strip that can be used e.g. for the calculation of sound radiation.

One option to extract the frequency dependent wavenumber content, distributed in the set of wavenumbers is to perform a discrete fourier transform of the characteristic wave forms. Though this approach is straight forward and easy to implement, there are some drawbacks:

- To obtain a high wavenumber resolution it is necessary to calculate the DFT over a long distance of the profile. Hence, the calculation effort rises.

²The distribution depends not only on the characteristic wave itself but also on the component of motion of interest. For sound radiation to the exterior the normal velocity of the outer plates is sought. The wavenumber distribution for vibrations in the x -direction will probably be significantly different!

- It is only possible to extract the propagating waves (and perhaps some portion of the complex waves). The decaying waves will vanish too fast to be extractable.
- The quantitative portions for complex waves form a kind of mean value for the investigated range and hence the amplitudes depend strongly on the length of the transformed section. It is more desirable to get the wave amplitudes at a characteristic point ($x = 0$). With this information the displacement at any arbitrary position can be recalculated quite simply.

To circumvent the drawbacks mentioned, it is possible for the periodic system to use another method. This is possible since some information about the wavenumbers and the inherent waves is available. The possible wavenumbers are known to be a series of wavenumbers, extracted from the transfer matrix eigenvalue problem. It is quite reasonable to assume that this series will converge rapidly since the main contributions will be in the range where the free wavenumbers arise in a simple homogeneous member. This is easily seen also from the calculation results presented later. Hence, another option is just to use the extracted wavenumber series as basis functions with unknown amplitudes. The amplitudes are estimated from the solution of a linear system of equations, which can be overdetermined, by projecting the real displacement pattern on this wavenumber basis.

The displacement ξ_i for each characteristic wave form at any point on the profile strip can be written as a series of 'space harmonics',

$$\xi_i(x) = \sum_{n=-\infty}^{\infty} A_{i,n} \varphi_i e^{-jk_{i,n}x} \quad \text{with} \quad k_{i,n} = k_0 + \frac{2\pi n}{L_e}. \quad (3.14)$$

In a reduced form considering only one direction, Eq. (3.14) holds also for the y -component, which is the relevant for the radiation,

$$\xi_{y,i}(x) = \sum_{n=-\infty}^{\infty} A_{i,n} e^{-jk_{i,n}x}. \quad (3.15)$$

The magnitude of the y -component in the eigenvector φ_i is neglected. This magnitude only affects the result with a constant factor, which is unimportant for the relative contributions of $k_{i,n}$. The correct scaling can be achieved by weighting the space harmonic amplitudes in accordance with these relative contributions.

When truncating the series at M terms and using K positions for the displacement evaluation, Eq. (3.15) can be written in matrix form

$$\begin{aligned}
 \begin{Bmatrix} \xi_{y,1} \\ \xi_{y,2} \\ \dots \\ \xi_{y,K} \end{Bmatrix} &= \begin{bmatrix} e^{-jk_{-M}x_1} & e^{-jk_{(-M+1)}x_1} & \dots & e^{-jk_Mx_1} \\ e^{-jk_{-M}x_2} & e^{-jk_{(-M+1)}x_2} & \dots & e^{-jk_Mx_2} \\ \dots & \dots & \dots & \dots \\ \dots & \dots & \dots & \dots \\ e^{-jk_{-M}x_K} & e^{-jk_{(-M+1)}x_K} & \dots & e^{-jk_Mx_K} \end{bmatrix} \begin{Bmatrix} A_{-M} \\ A_{-M+1} \\ \dots \\ A_M \end{Bmatrix} \quad (3.16a) \\
 (K, 1) &= \quad \quad \quad (K, 2M + 1) \quad \quad \quad \times (2M + 1, 1).
 \end{aligned}$$

The number of displacement positions K must be greater or equal to $2M + 1$, i.e. the number of desired wave series amplitudes. If the number is greater, the system is overdetermined and can be solved using a least square solution routine. The spacing of the K displacement points is arbitrary but has to be chosen fine enough to ensure a resolution necessary to represent the smallest occurring wavelength. It should be pointed out that the space harmonic amplitudes as well as the displacements ξ_y are complex. Initially only the real part of ξ_y was used but then the method became unstable in some cases.

3.4.2 Results

The relative space harmonic amplitudes of profile A for the characteristic waves travelling to the right (waves 7 to 12) are shown in Fig. 3.13 to 3.18 for a frequency of 1000 Hz. For the results presented, the y -displacement of the upper outer beams is used and the amplitudes are normalized by the maximum amplitude. In order to check the implementation and the robustness of the method, a comparison is performed of real displacement shapes and reconstructed displacement shapes using the estimated amplitudes of the space harmonic series.

It is clear that the method is robust in finding the relative space harmonic amplitudes; the matching between the calculated displacement and the space harmonic series fit is that precise that the curves are hardly distinguishable in the plots. Moreover it can be stated, that in the investigated frequency range, $-5 \leq n \leq 5$ is sufficient to represent the wave forms. For the propagating waves, $-2 \leq n \leq 2$ could be sufficient as well. The amplitudes are only symmetric for waves with symmetric wavenumber content in the space harmonic series, i.e. for $Re(k_0) = 0$. For the presented results this is the case for waves 7 and 10.

A comparison is also made of the space harmonic identification method and the DFT method. For the propagating waves, the wavenumber spectra are quite similar as is seen in Fig. 3.19 but the discrepancy in amplitudes

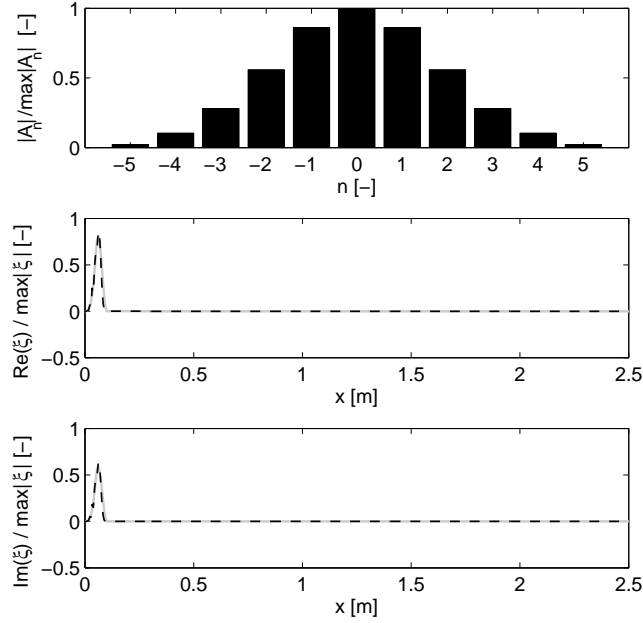


Figure 3.13: Amplitudes of space harmonic series (Profile A, $f = 1000$ Hz, wave 7, — calculated displacement (grey) - - wave series fit (black))

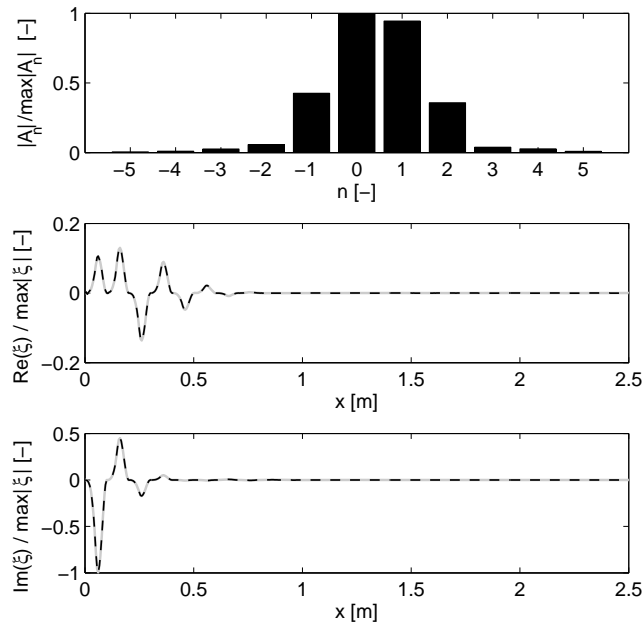


Figure 3.14: Amplitudes of space harmonic series (Profile A, $f = 1000$ Hz, wave 8, — calculated displacement (grey) - - wave series fit (black))

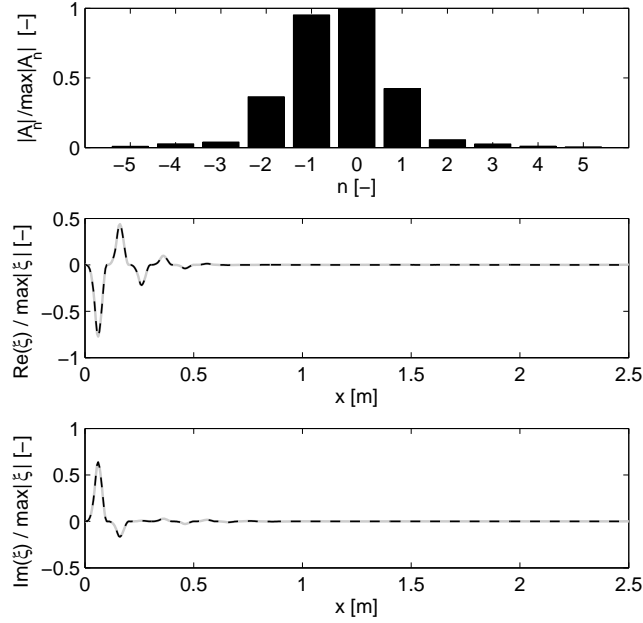


Figure 3.15: Amplitudes of space harmonic series (Profile A, $f = 1000$ Hz, wave 9, — calculated displacement (grey) - - wave series fit (black))

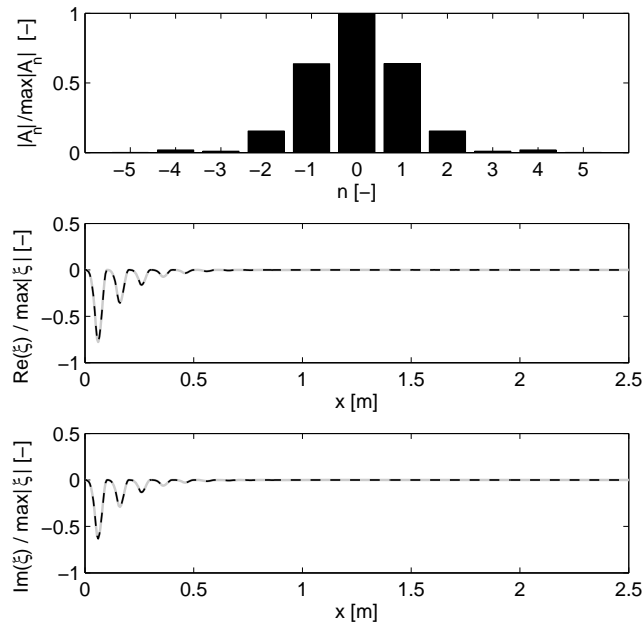


Figure 3.16: Amplitudes of space harmonic series (Profile A, $f = 1000$ Hz, wave 10, — calculated displacement (grey) - - wave series fit (black))

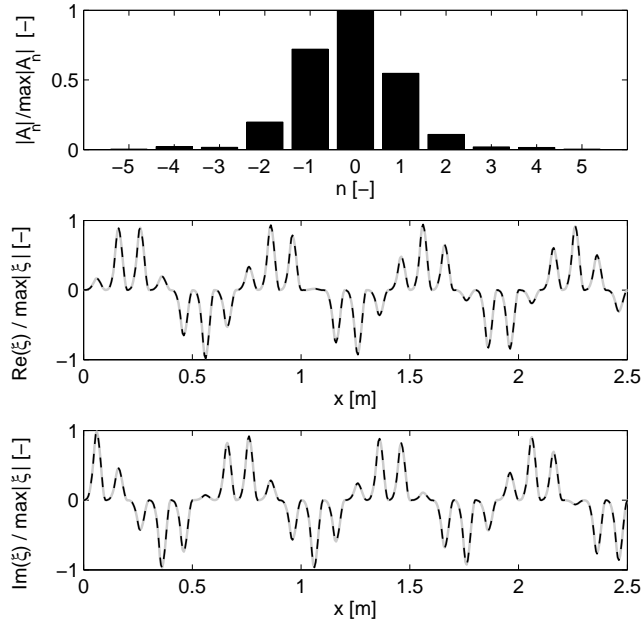


Figure 3.17: Amplitudes of space harmonic series (Profile A, $f = 1000$ Hz, wave 11, — calculated displacement (grey) - - wave series fit (black))

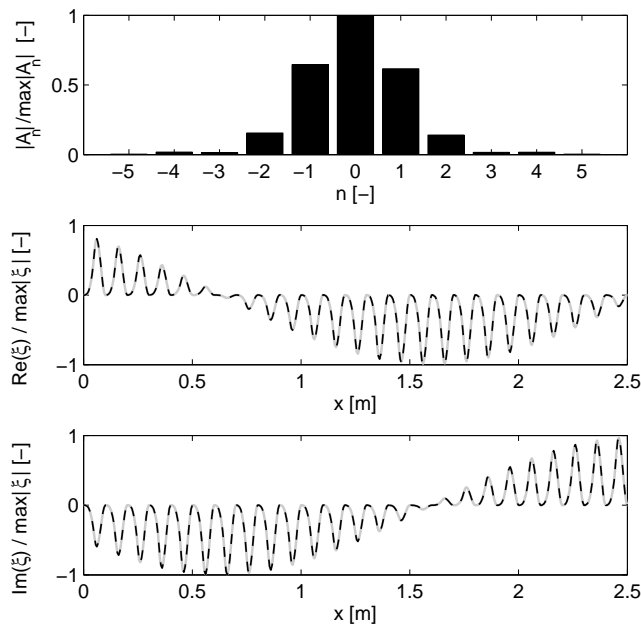


Figure 3.18: Amplitudes of space harmonic series (Profile A, $f = 1000$ Hz, wave 12, — calculated displacement (grey) - - wave series fit (black))

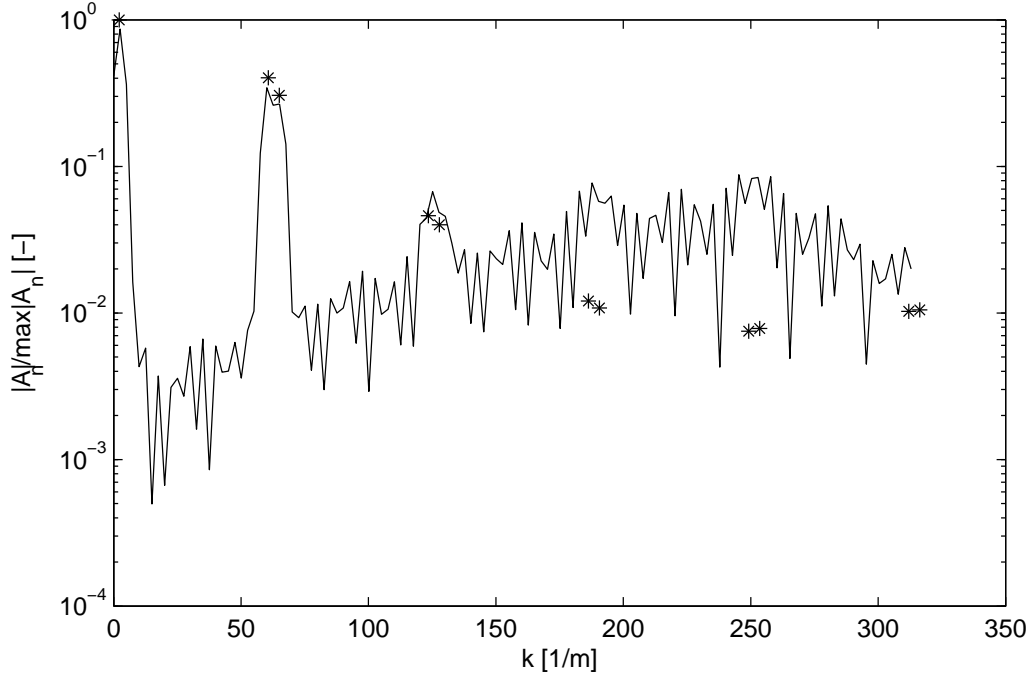


Figure 3.19: Amplitudes of space harmonic series (*) in comparison with DFT result (—) (Profile B, $f = 1000$ Hz, wave 12). The occurring pairs for the space harmonics result from the values for $\pm n$.

increases with wavenumber. For complex waves, the correct wavenumbers are found in the DFT, but the amplitude is underestimated because of the decaying process.

The results up to now show only relative space harmonic amplitudes for a frequency of 1000 Hz. In order to get an overview what happens in the complete frequency regime, shaded figures are created indicating the distribution of space harmonics for each wave. The plots are normalized by the maximum amplitude for each frequency and wave. These scaled results, in combination with the wave amplitudes for a forced response (see chapter 4), lead to the quantitative space harmonic amplitudes for each wave and as a sum, the complete wavenumber distribution. The results for the waves propagating to the right (waves 7 to 12) are shown in the Figs. 3.20 to 3.22.

It is obvious, that not only for 1000 Hz as shown previously, but also in the complete investigated frequency regime, the wavenumber content is localized between -150 and 150 m^{-1} .³ Higher and lower wavenumbers contribute only

³Remarkable high wavenumber components are present only for strongly decaying waves, e.g. wave 7.

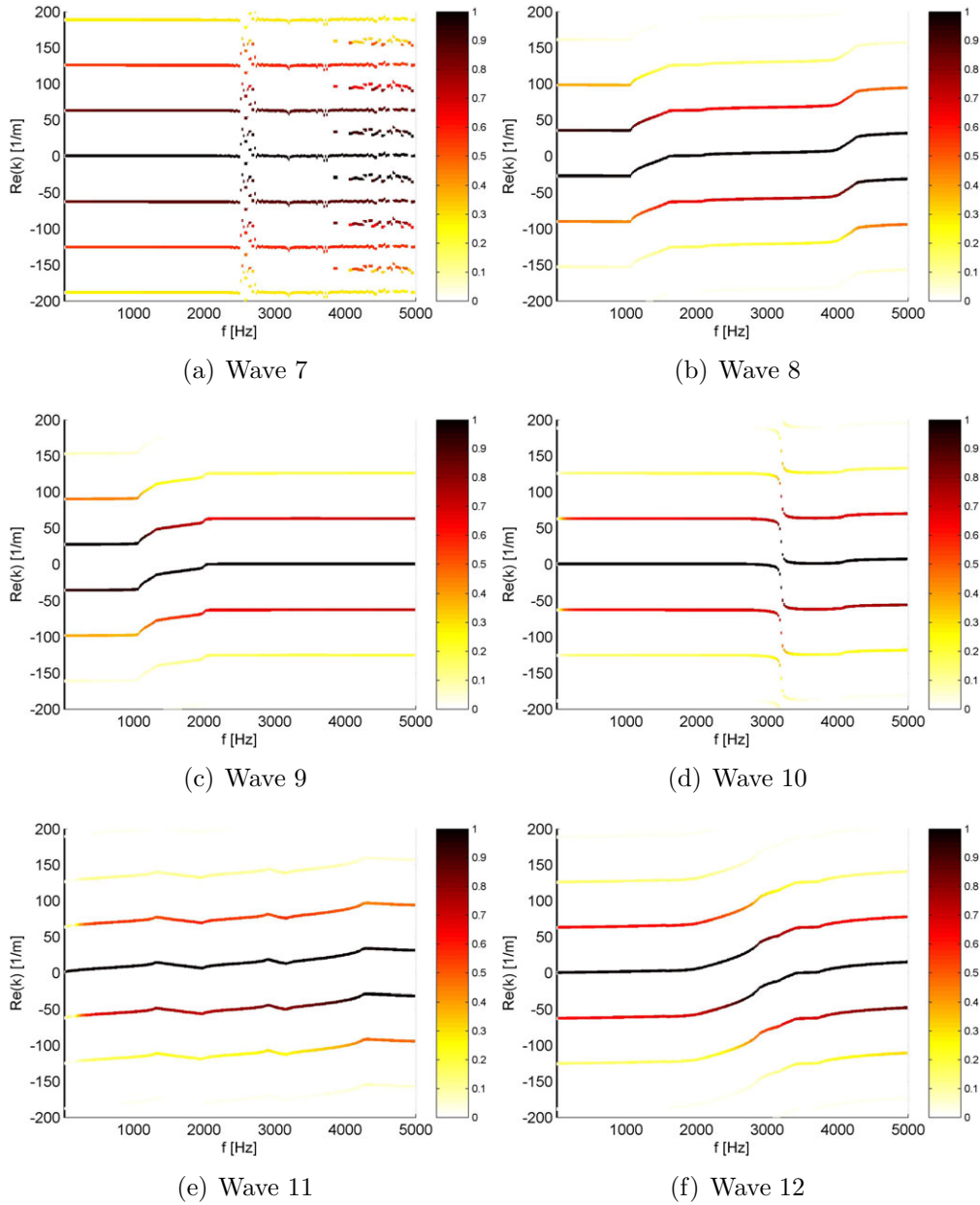


Figure 3.20: Normalized amplitudes of space harmonic series for right-travelling characteristic waves (Profile A)

CHAPTER 3. PROFILE STRIPS: WAVENUMBER CONTENT

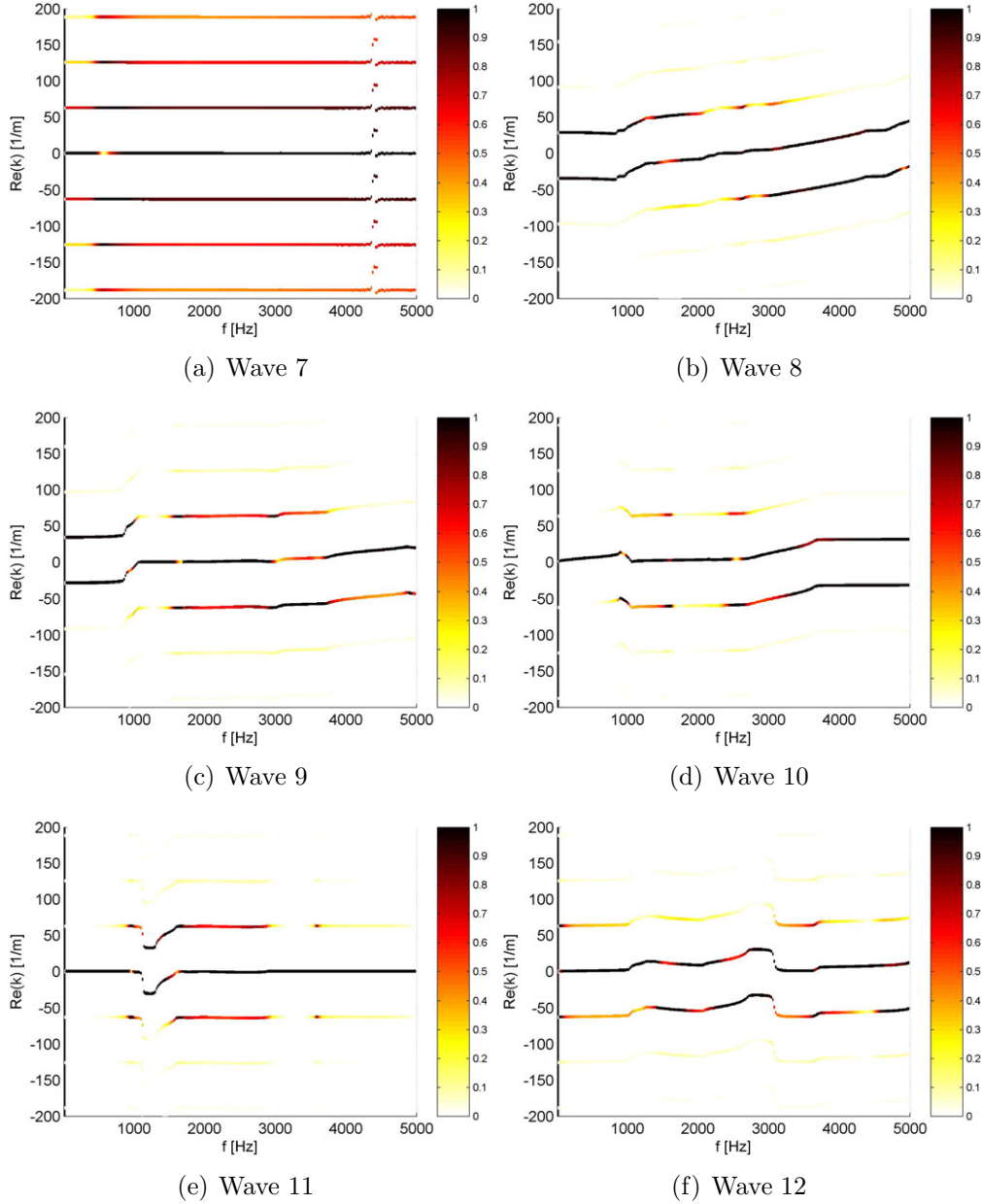


Figure 3.21: Normalized amplitudes of space harmonic series for right-travelling characteristic waves (Profile B)

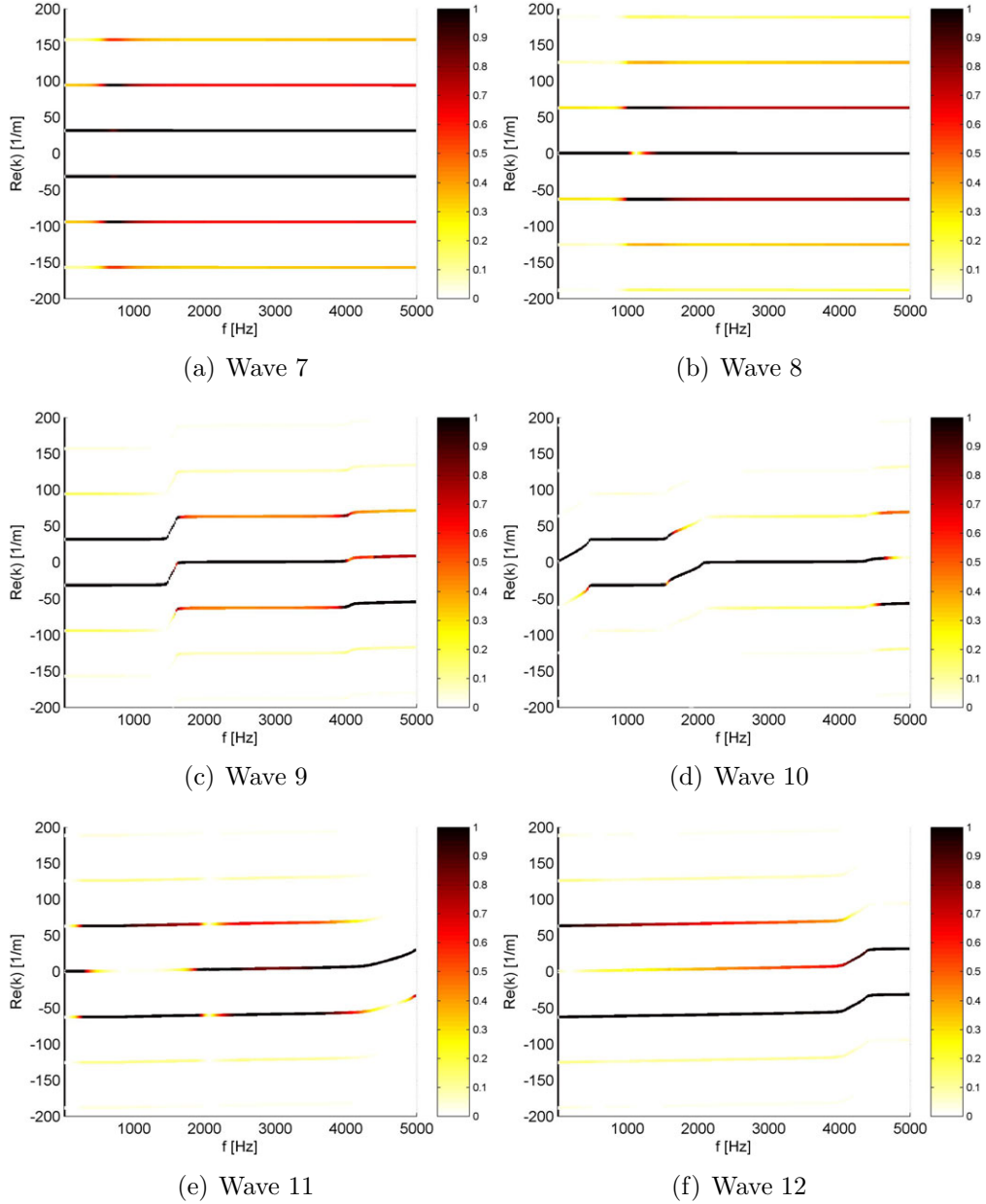


Figure 3.22: Normalized amplitudes of space harmonic series for right-travelling characteristic waves (Profile C)

minutely to the overall result. It is expected that the significant wavenumber group will gradually drift to larger values, if the behaviour were investigated for higher frequencies beyond 5000 Hz. For the presented positive travelling waves the group velocity is mainly positive (positive slope of the curves), also for the components with negative phase speed (negative wavenumber). This means that the space harmonic series gives a positive travelling characteristic wave (energy flow in positive direction) as a sum. However, there are some components with negative phase speed included, induced by the reflections at the joints. There are, indeed, some characteristic waves with negative group velocity in some frequency ranges, e.g. wave 11 of profile A between 1400 and 2000 Hz. The wavenumbers are complex in these regions, so that this phenomenon is related to backflow of nearfield energy, which can be explained by the necessarily pairwise occurrence of complex nearfields, see e.g. [34].

3.5 Concluding remarks

The complete picture of propagating, decaying and complex waves can be gained by solving the transfer-matrix eigenvalue problem. For the profiles considered, up to six characteristic waves can be identified, travelling in each direction. The wavenumber content in each characteristic wave is formed of several "space harmonics", realising a periodic wavenumber spectrum. The relative contributions in the wavenumber series are fixed for each characteristic wave and can be identified from the complete characteristic wave forms. The extraction of the characteristic waves establishes means to simplify the wave propagation in the light weight profile strips. Provided there is a limited number of excitation points, the decaying and complex waves will not contribute significantly to the overall vibration of the strip.

Chapter 4

Light weight profile strips: Forced response and influence of periodicity perturbations

4.1 Introduction

In chapter 2 a calculation model for light weight profile strips was established and three different geometries were investigated. The wave amplitudes of the characteristic waves presented in chapter 3 depend on the applied excitation. This is studied for infinite profile strips in this chapter. Moreover, the influence of structural periodicity perturbations on the behaviour of the strip is discussed briefly.

According to Engels [35] the forced response of an infinite or semi-infinite periodic structure can be calculated based on the eigenvalues and eigenvectors of the transfer matrix. An alternative is the direct use of the dynamic stiffness matrix of the subsystem, outlined by Thompson [36] to calculate the wavenumbers and forced response of a structure, applied and extended also in [37]. For the present study, the employed slope-deflection method directly establishes the dynamic stiffness matrix. Hence, this alternative is selected for the eigenvalue problem.

As in reality strict periodicity cannot be achieved, e.g. because of manufacturing tolerances, the influence of these perturbations is investigated briefly using periodic subelements with random length variations.

4.2 Forced response of infinite profile strip

For structural acoustic investigations in the mid and high Helmholtz number regime, theoretical infinite systems are of great value. In those regimes the influence of boundary effects for finite structures diminishes such that the corresponding infinite structure can be used to estimate the behaviour of the former. Hence, forced excitation of infinite strips is investigated here.

4.2.1 Theory of forced response using dynamic stiffness matrix

For the infinite periodic strip, forced response can be developed by using the dynamic stiffness matrix of a single subsystem [36]. If the periodic subsystem contains inner degrees of freedom which are not connected to the left or right side, it is necessary to build a new reduced dynamic stiffness matrix as the matrix elements depend on the chosen degrees of freedom (blocked assumptions). In contrast, the mobility enables arbitrary degrees of freedom to be eliminated without changing the remaining matrix elements. For the case with inner degrees of freedom, where no force excitation is assumed, the reduction starts with the definition of dynamic stiffness submatrices $\tilde{\mathbf{K}}$ where index i indicates inner degrees of freedom, l the left and r the right ones,

$$\begin{bmatrix} \tilde{\mathbf{K}}_{ll} & \tilde{\mathbf{K}}_{li} & \tilde{\mathbf{K}}_{lr} \\ \tilde{\mathbf{K}}_{il} & \tilde{\mathbf{K}}_{ii} & \tilde{\mathbf{K}}_{ir} \\ \tilde{\mathbf{K}}_{rl} & \tilde{\mathbf{K}}_{ri} & \tilde{\mathbf{K}}_{rr} \end{bmatrix} \begin{Bmatrix} \xi_l \\ \xi_i \\ \xi_r \end{Bmatrix} = \begin{Bmatrix} \mathbf{F}_l \\ \mathbf{0} \\ \mathbf{F}_r \end{Bmatrix}. \quad (4.1)$$

The inner DOFs can be eliminated by using the relation

$$\xi_i = -\tilde{\mathbf{K}}_{ii}^{-1} (\tilde{\mathbf{K}}_{il}\xi_l + \tilde{\mathbf{K}}_{ir}\xi_r). \quad (4.2)$$

After some simple algebraic manipulations the new dynamic stiffness matrix can be assembled as

$$\begin{bmatrix} \mathbf{K}_{ll} & \mathbf{K}_{lr} \\ \mathbf{K}_{rl} & \mathbf{K}_{rr} \end{bmatrix} \begin{Bmatrix} \xi_l \\ \xi_r \end{Bmatrix} = \begin{Bmatrix} \mathbf{F}_l \\ \mathbf{F}_r \end{Bmatrix} \quad (4.3)$$

with

$$\begin{aligned} \mathbf{K}_{ll} &= \tilde{\mathbf{K}}_{ll} - \tilde{\mathbf{K}}_{li}\tilde{\mathbf{K}}_{ii}^{-1}\tilde{\mathbf{K}}_{il} & \mathbf{K}_{lr} &= \tilde{\mathbf{K}}_{lr} - \tilde{\mathbf{K}}_{li}\tilde{\mathbf{K}}_{ii}^{-1}\tilde{\mathbf{K}}_{ir} \\ \mathbf{K}_{rl} &= \tilde{\mathbf{K}}_{rl} - \tilde{\mathbf{K}}_{ri}\tilde{\mathbf{K}}_{ii}^{-1}\tilde{\mathbf{K}}_{il} & \mathbf{K}_{rr} &= \tilde{\mathbf{K}}_{rr} - \tilde{\mathbf{K}}_{ri}\tilde{\mathbf{K}}_{ii}^{-1}\tilde{\mathbf{K}}_{ir}. \end{aligned} \quad (4.4)$$

Based on Bloch's theorem Thompson gives the following eigenvalue problem $(\mathbf{B} + \lambda\mathbf{C})\boldsymbol{\Psi} = \mathbf{0}$ using the submatrices given in Eq. (4.4)

$$\left(\begin{bmatrix} \mathbf{K}_{rl} & \mathbf{K}_{rr} \\ \mathbf{0} & \mathbf{I} \end{bmatrix} + \lambda \begin{bmatrix} \mathbf{K}_{ll} & \mathbf{K}_{lr} \\ -\mathbf{I} & \mathbf{0} \end{bmatrix} \right) \begin{Bmatrix} \boldsymbol{\xi}_l \\ \boldsymbol{\xi}_r \end{Bmatrix} = \mathbf{0} . \quad (4.5)$$

After solving the eigenvalue problem for the eigenvalues λ and eigenvectors $\boldsymbol{\Psi}$, the solution can be arranged in a way such that the eigenvectors of right travelling waves are put into one submatrix $\boldsymbol{\Psi}^+$ containing the corresponding eigenvectors and another submatrix $\boldsymbol{\Psi}^-$ containing the left travelling components. Within each there are displacement degrees of freedom for the left part $\boldsymbol{\Psi}_l^{+/-}$ and the right part $\boldsymbol{\Psi}_r^{+/-}$ of the excited subsystem.¹

The following equation relates the excitation forces at an arbitrary element within an infinite periodic structure to the wave amplitudes of the right travelling waves \mathbf{R} .²

$$\mathbf{F} = \left(\mathbf{K}_{ll}\boldsymbol{\Psi}_l^+ + \mathbf{K}_{lr}\boldsymbol{\Psi}_r^+ + \mathbf{K}_{rl}\boldsymbol{\Psi}_r^-\boldsymbol{\Psi}_l^{-1}\boldsymbol{\Psi}_l^+ + \mathbf{K}_{rr}\boldsymbol{\Psi}_r^+ \right) \mathbf{R} \quad (4.6)$$

This can be solved for the desired wave amplitudes \mathbf{R} in the special excitation case by an inversion process once the excitation is specified.

The wave amplitudes of the left-travelling components can be deduced from the right-travelling amplitudes since [36]:

$$\mathbf{L} = (\boldsymbol{\Psi}_l^-)^{-1} \boldsymbol{\Psi}_l^+ \mathbf{R} \quad (4.7)$$

These wave amplitudes in combination with the wavenumber content in each wave gives a quantitative description of the wavenumber content for a given excitation of an infinite profile strip.

4.2.2 Results for forced wave propagation of infinite strips

In this section, the outlined theory is used to extract the wave amplitudes of the characteristic waves for a given force (or moment) excitation of an infinite strip. The first step is the solution of the eigenvalue problem, in this case based on the dynamic stiffness matrix of the corresponding subsystem. The eigenvectors, which are in this case not velocity, but displacement based, are normalized with the vector (column) norm. After extracting the wave

¹Note that the eigenvectors and the eigenvalue problem are defined here on a displacement basis. No forces are included in the eigenvectors.

²This is the version used and given by Thompson. In the equation given by Brown the first two $\boldsymbol{\Psi}$ matrices in the third term are interchanged.

amplitudes for the left- and right-travelling normalized waves, the velocities at the excitation point can be calculated by using Eq. (3.11) of chapter 3, resulting in the input mobility of the infinite strip. The same profiles used previously in chapter 2 for the finite strips A to C are used as infinite profiles. Moreover, in order to benchmark the results, an approximate, infinite profile strip is investigated by directly assembling the complete dynamic stiffness matrix. This means that a weakly damped interior part (2.5 m, $\eta = 0.01$) is enclosed between two end parts where damping is slightly increased to form non-reflective ends. The end parts are both 2.5 m and with the loss factor η increasing gradually from 0.01 to 0.25.

The resulting wave amplitudes for the positive (right)-travelling waves are shown in the Figs. 4.1, 4.4 and 4.7. The calculation is done for all three profiles and for two excitation components ($F_{1,x}; F_{1,y}$) at node 1 (see Fig. 2.1). The corresponding input mobilities are shown in Figs. 4.2, 4.3, 4.5, 4.6, 4.8 and 4.9.

The mobilities for the infinite profile strips resemble those of the approximate, infinite strips at sufficiently high frequencies. Because of the longer wavelength for the longitudinal wave components, which are excited stronger by axial force excitation, the deviations are larger than for transversal force excitation.

The contribution of the longitudinal waves is much higher in the low frequency regime for axial excitation and all profiles than for transversal excitation (see e.g. wave 12 in Figs. 4.1 and 4.4). Because of the transition between the wave types this dominance is reduced at high frequencies. For the transversal excitation the 'bending' type waves are dominant in the passbands.

It is anticipated that the wave amplitudes are changing along the profile, at least for decaying and complex waves. Wave amplitudes shown in Figs. 4.1, 4.4 and 4.7 are given for the point of excitation. Two examples of the wave amplitudes along the strip are shown for profiles A and B in Figs. 4.10 and 4.11. Depending on the type of wave, the wave amplitudes decay strongly for complex and decaying waves and very limited for propagating waves, where only the small structural damping attenuates the wave amplitudes.

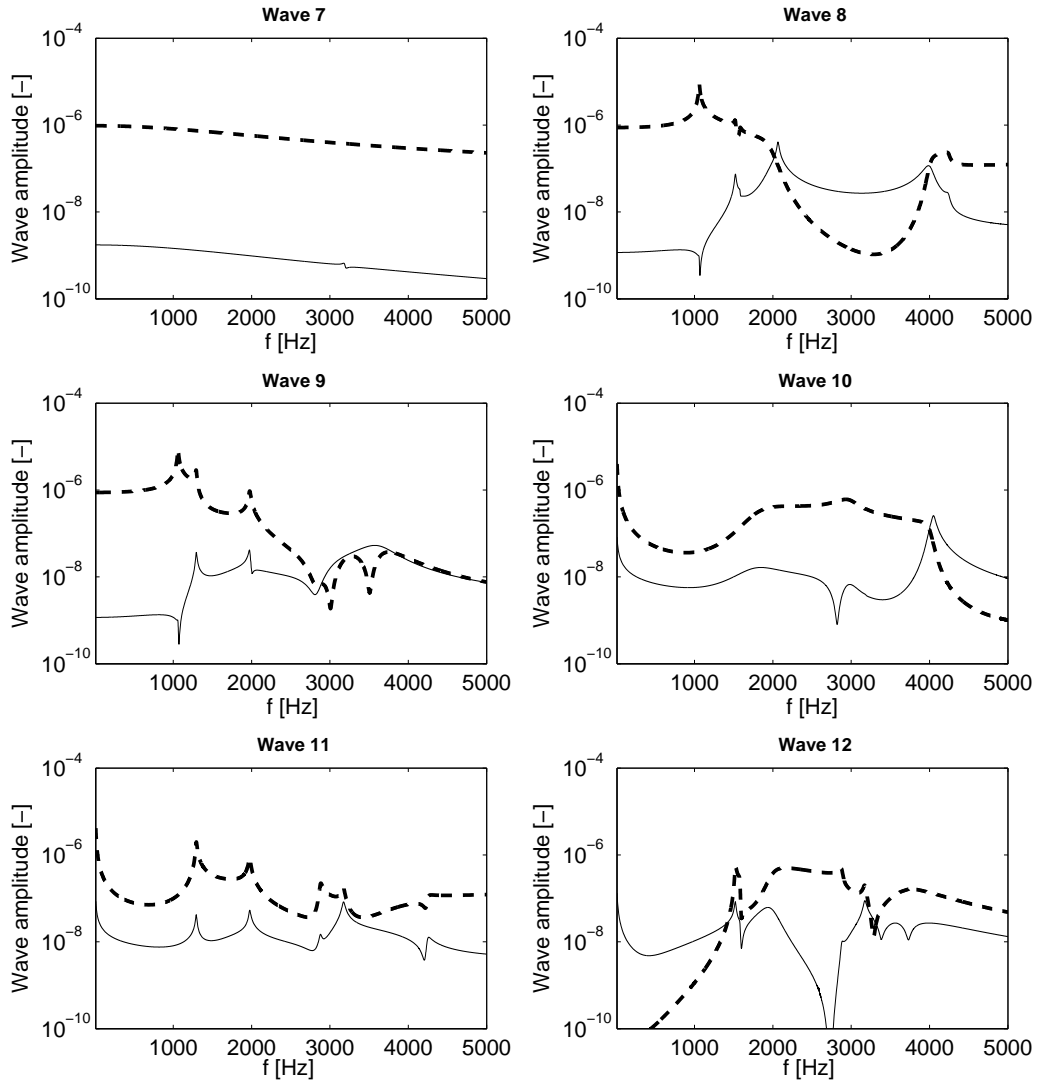


Figure 4.1: Wave amplitudes of right-travelling characteristic waves for force excited profile strip A, ($- F_{1,x}$, $--$ (thick) $F_{1,y}$)

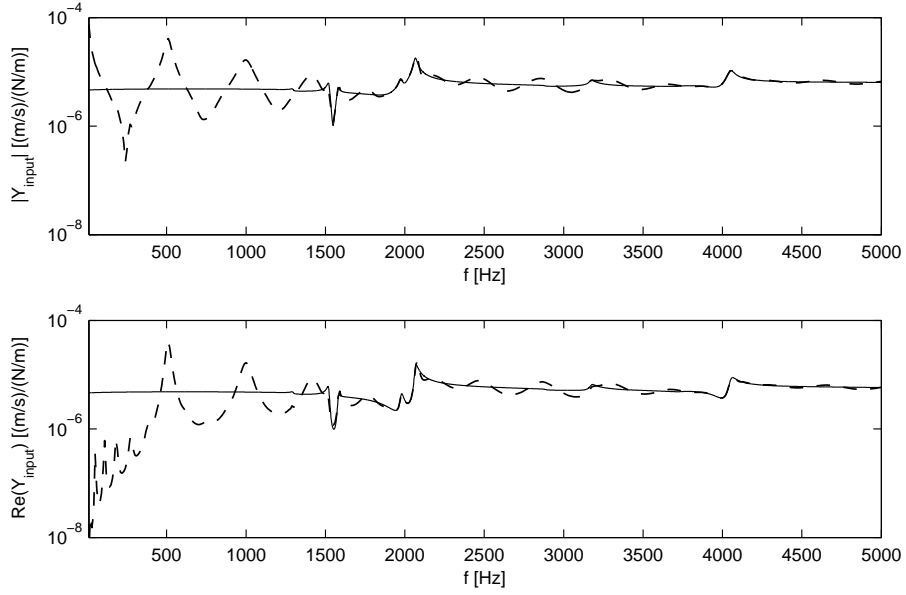


Figure 4.2: Input mobility, profile strip A, $F_{1,x}$, (— infinite, -- approximately infinite)

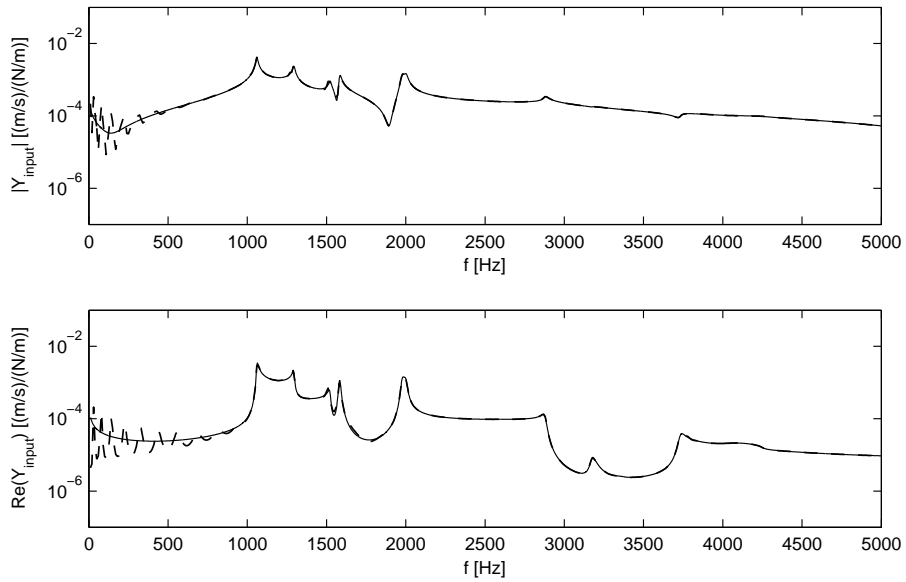


Figure 4.3: Input mobility, profile strip A, $F_{1,y}$, (— infinite, -- approximately infinite)

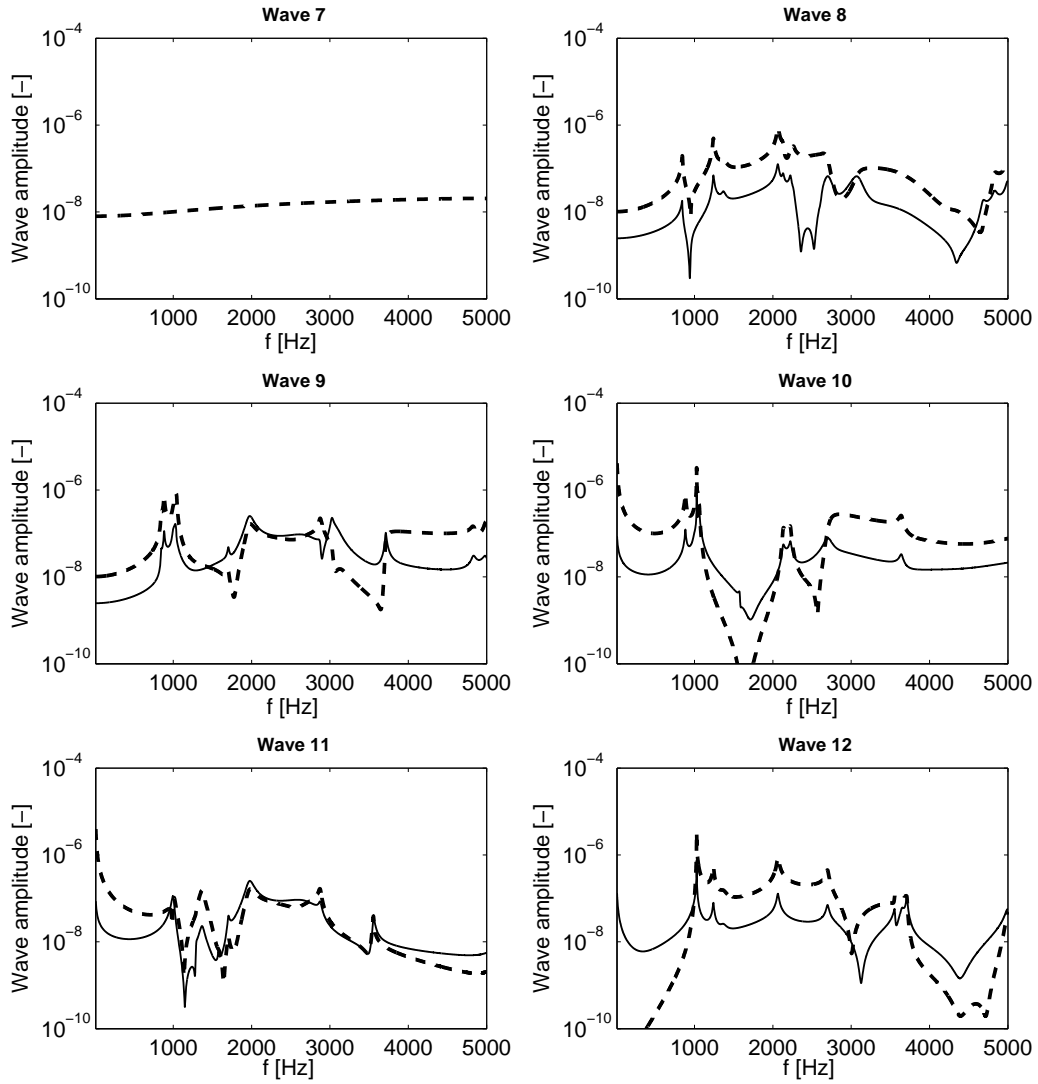


Figure 4.4: Wave amplitudes of right-travelling characteristic waves for force excited profile strip B, ($- F_{1,x}$, $--$ (thick) $F_{1,y}$)

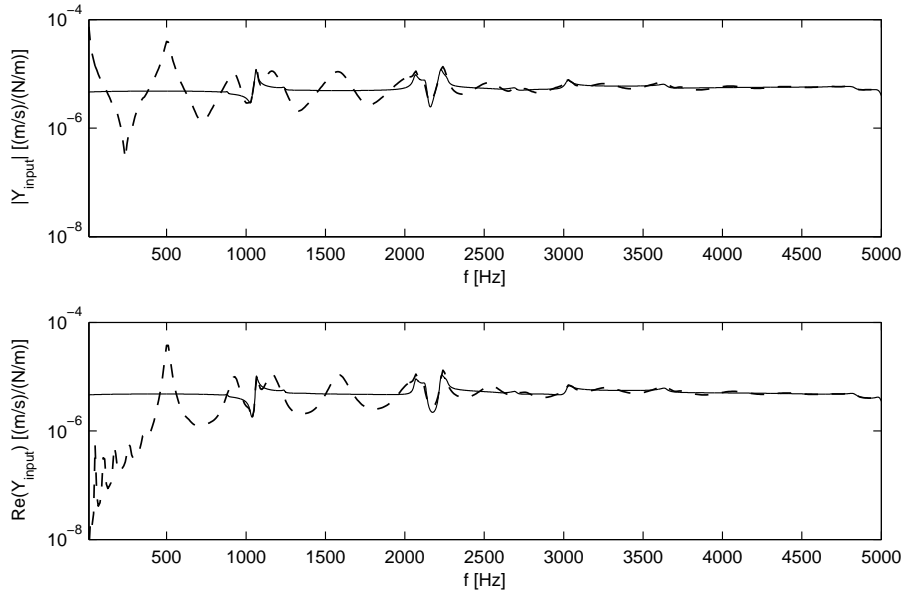


Figure 4.5: Input mobility, profile strip B, $F_{1,x}$, (— infinite, -- approximately infinite)

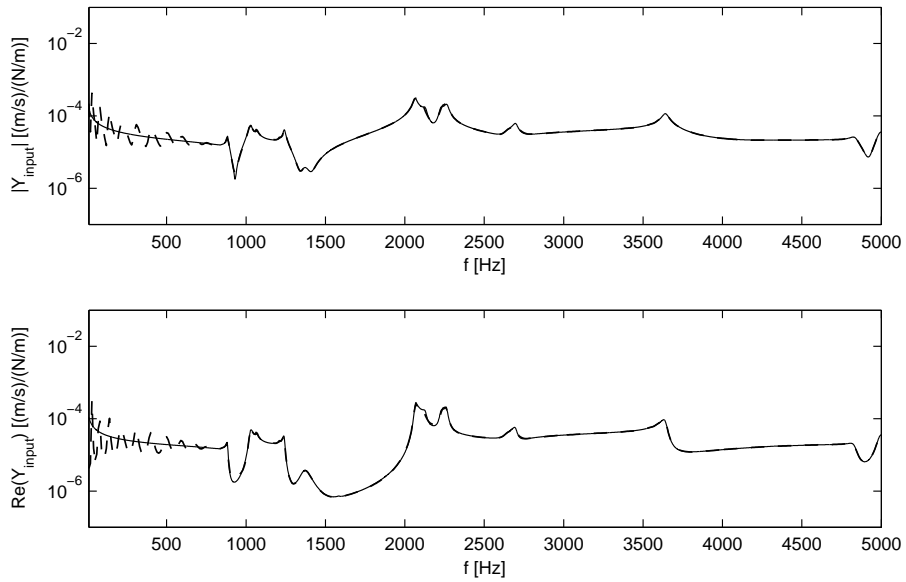


Figure 4.6: Input mobility, profile strip B, $F_{1,y}$, (— infinite, -- approximately infinite)

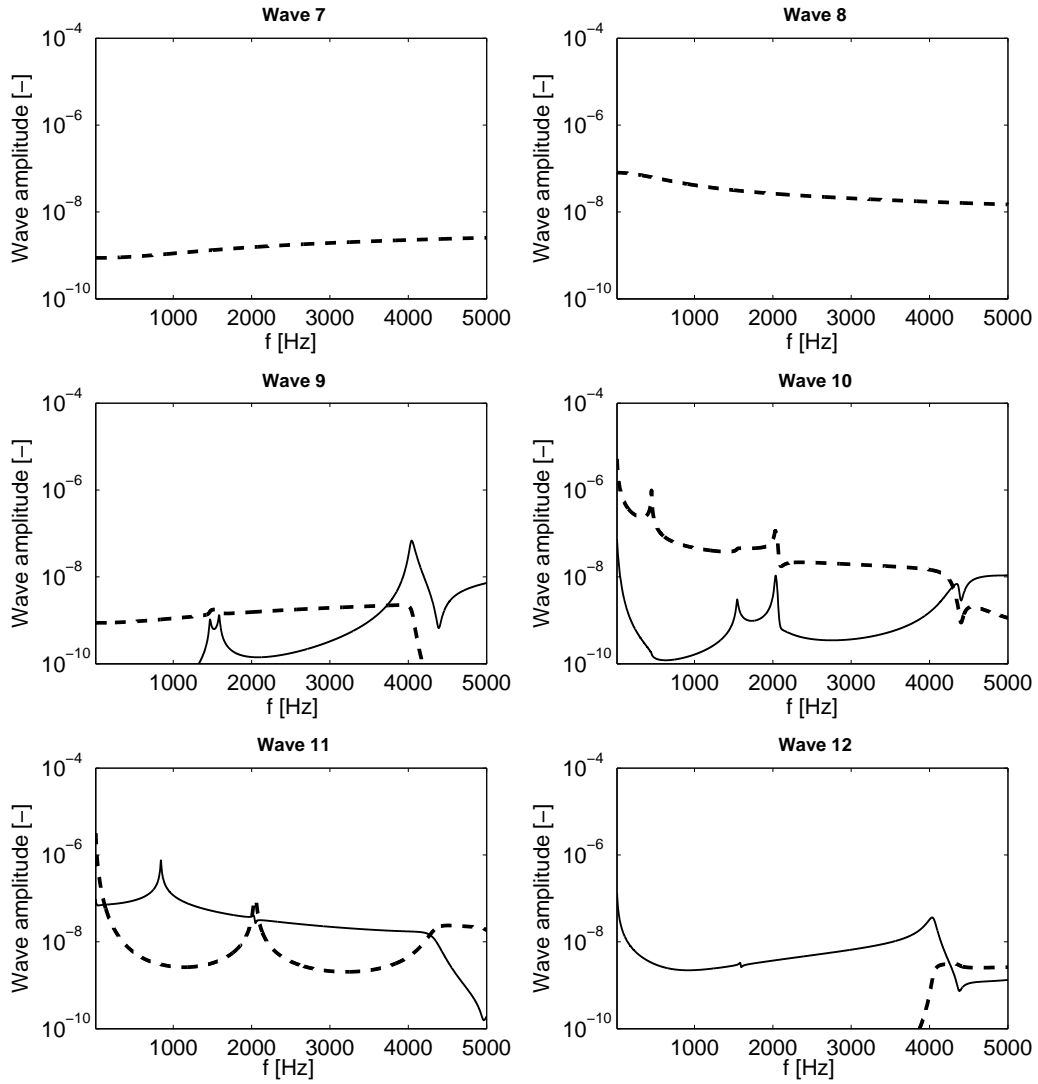


Figure 4.7: Wave amplitudes of right-travelling characteristic waves for force excited profile strip C, ($- F_{1,x}$, $--$ (thick) $F_{1,y}$)

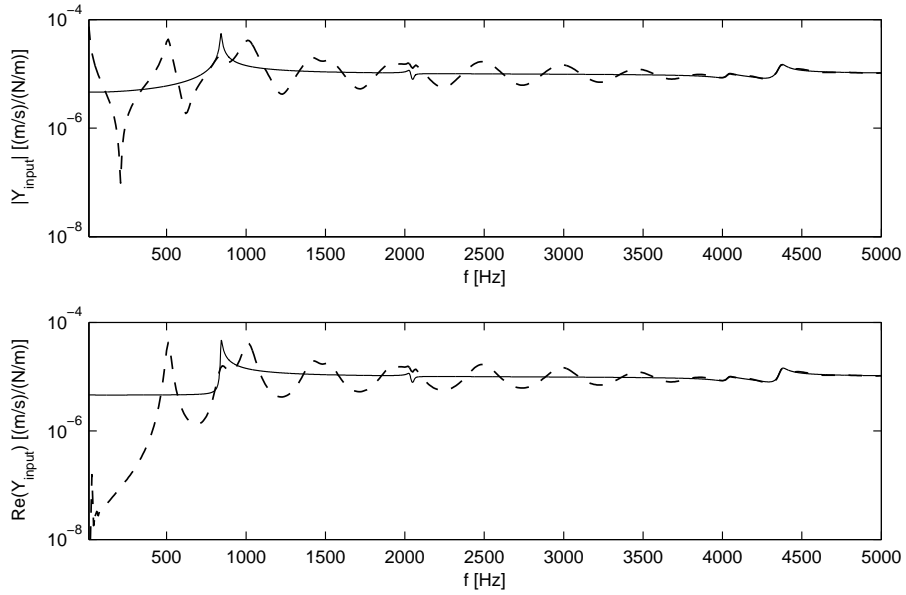


Figure 4.8: Input mobility, profile strip C, $F_{1,x}$, (— infinite, -- approximately infinite)

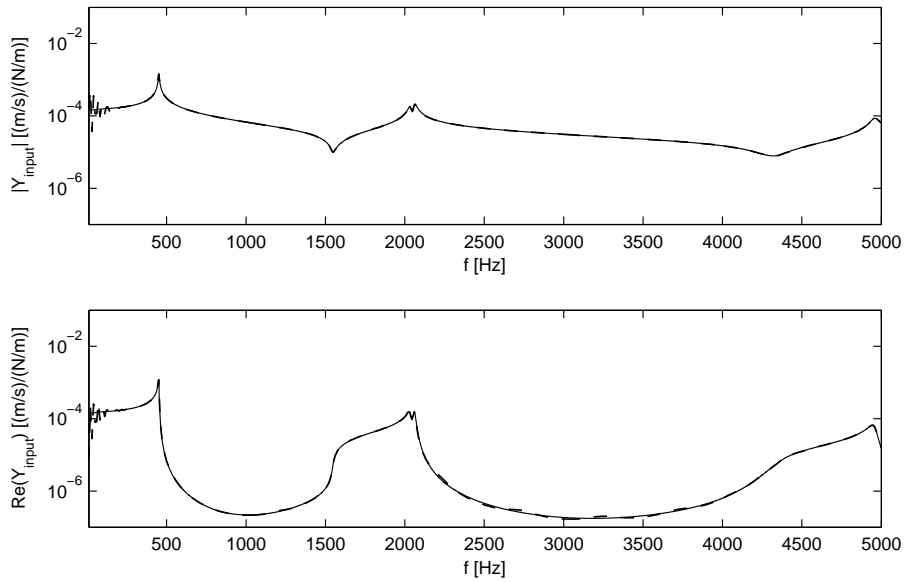


Figure 4.9: Input mobility, profile strip C, $F_{1,y}$, (— infinite, -- approximately infinite)

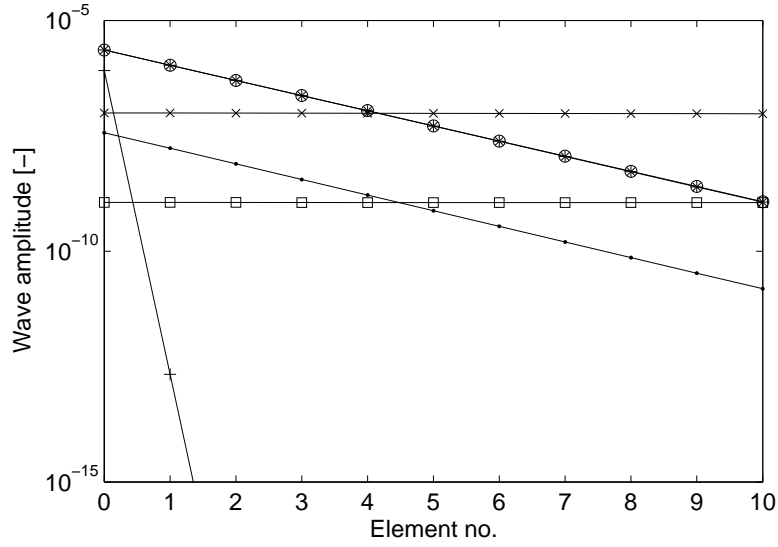


Figure 4.10: Wave amplitudes of right-travelling waves along profile strip (Profile A) for $F_{1,y}$ force excitation at element number 0, $f = 1000$ Hz, (+ Wave 7, o Wave 8, * Wave 9, • Wave 10, x Wave 11, □ Wave 12)

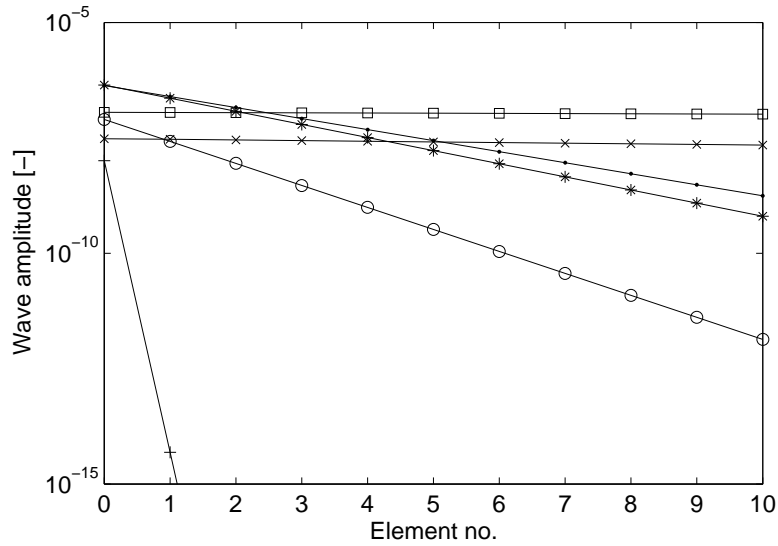


Figure 4.11: Wave amplitudes of right-travelling waves along profile strip (Profile B) for $F_{1,y}$ force excitation at element number 0, $f = 1000$ Hz, (+ Wave 7, o Wave 8, * Wave 9, • Wave 10, x Wave 11, □ Wave 12)

4.3 Aperiodicity

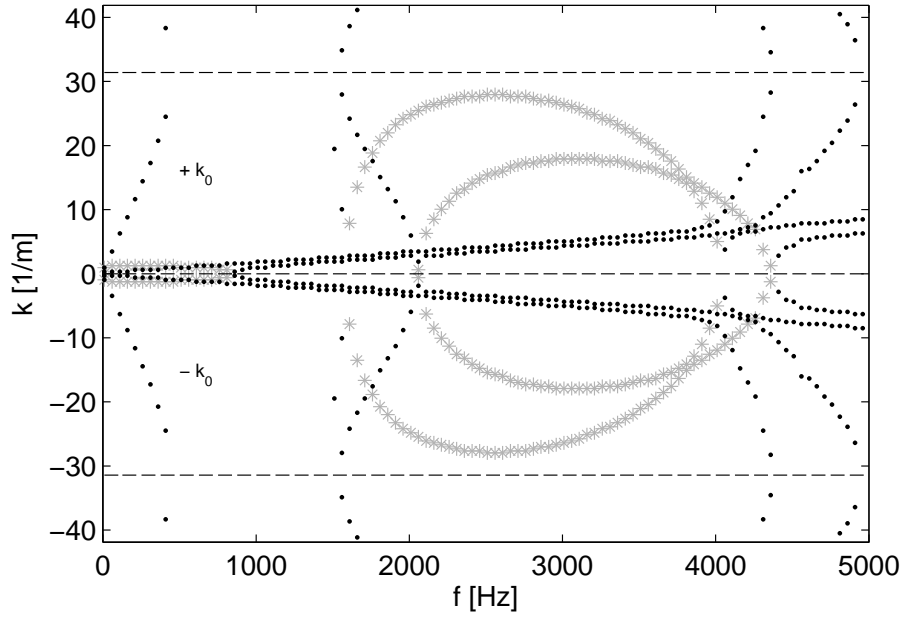
4.3.1 Influence of periodicity perturbations on wave propagation

Apart from the DFT, the presented approaches in chapter 3 for wavenumber extraction are only applicable to periodic profiles. As industrial profiles always have periodicity perturbations, it is of interest to investigate the influence of these perturbations on the dispersion characteristics.

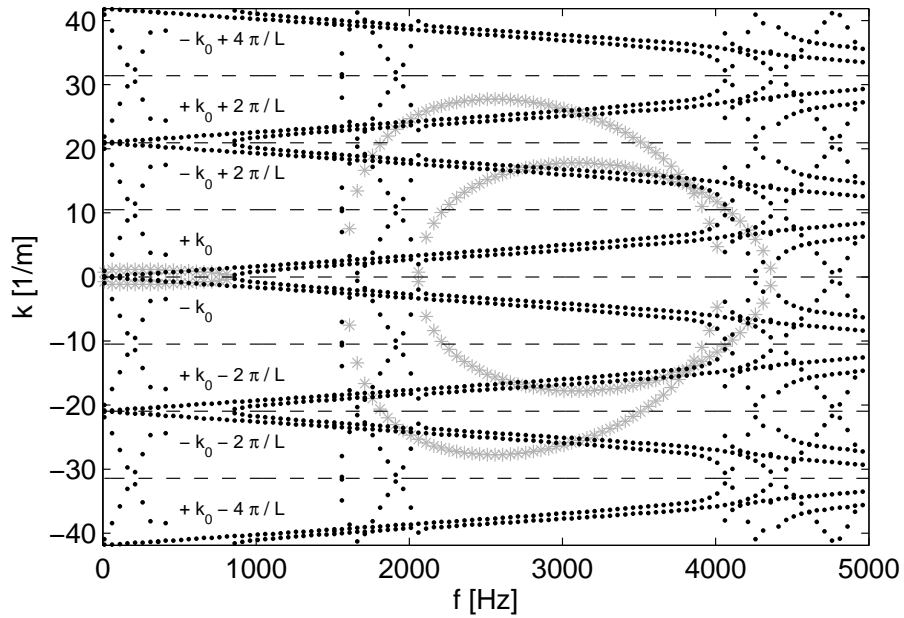
One option is to assume that the periodic element is not part of the profile but is formed by the complete aperiodic profile, it should be possible to use the same tools as outlined for strictly periodic systems. In practice this would mean that one calculates the complete mobility matrix of the profile strip and uses the result in the determinantal equation to find the propagating waves. The problem of solving the determinantal equation for multiple subelements is illustrated for the case of three subelements. By using the mobility matrix of the three coupled subelements the same wavenumber content can be extracted as for one subelement but additionally, there are other spurious waves coming into play. Fig. 4.12 illustrates the resulting spectrum for three subsystems in comparison with only one subsystem. The additional wavenumbers in the plots can be linked to the original ones by mirroring the original values at the periodic lines ($\pi/L_e + 2\pi n/L_e$). The periodicity of the wavenumber spectrum with period $2\pi/L_e$ introduces these additional spurious waves as L_e increases if more than one element is used. Due to this fact the results using the complete aperiodic strip will not give real insight into the wave propagation characteristics as the periodicity 'hides' the dominating wavenumbers.

The solution of the transfer matrix eigenvalue problem for multiple subelements could be used as an alternative. However, this is not practicable because no stable transfer matrix can be calculated for large systems. Moreover, the same problems as for the determinantal equation are expected. Upon solving the eigenvalue problem of the three-subelement T-matrix, the results, not included here for the sake of brevity, show the strong numerical instabilities arising. No meaningful results can be obtained for more than two subelements.

As the methods for strictly periodic systems fail, the only feasible alternative is the application of the DFT method. The problem here is the low resolution if a short profile strip shall be investigated. One possibility to get a higher resolution is the use of a repeated strip. Moreover, the wavenumbers are smeared by the aperiodic features (see Fig. 4.13 for introducing random length variations to form aperiodic profiles based on profile A). For a ran-



(a)



(b)

Figure 4.12: Wavenumber plot extracted using determinantal equation based on (a) one element and (b) three elements for profile C (* (grey): decaying waves, ... (black) propagating waves)

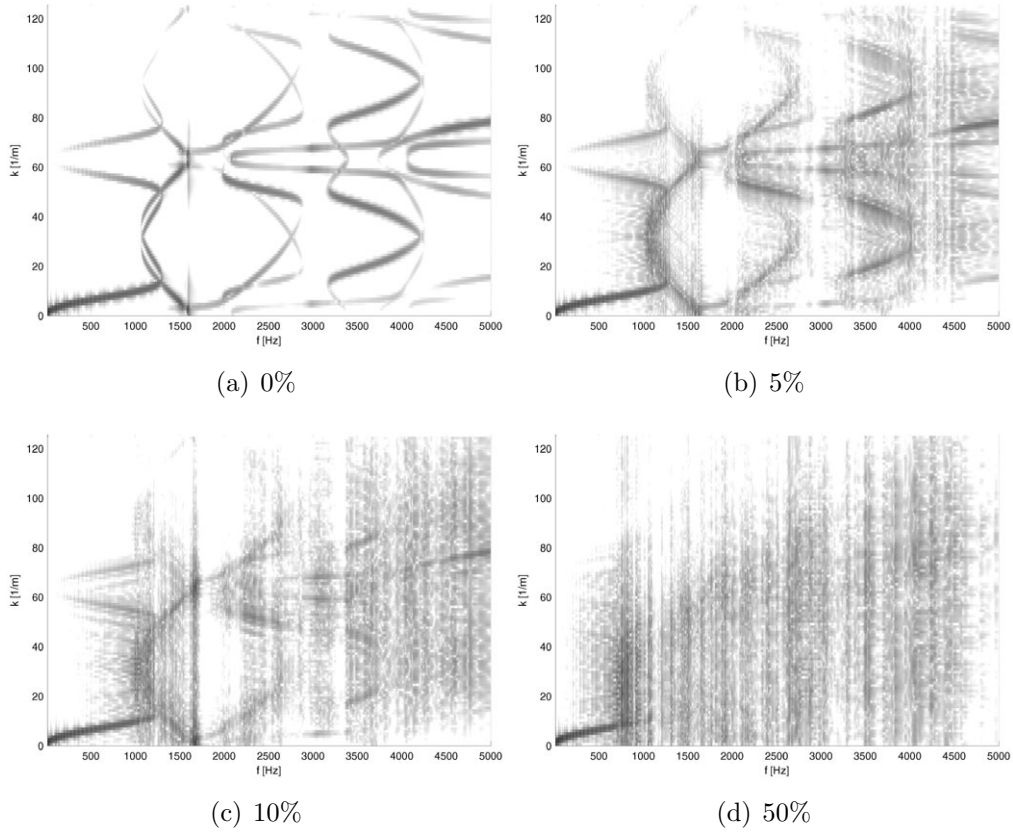


Figure 4.13: Wavenumber plots using DFT of strip A introducing maximum random length variations (force excitation $F_{1,y}$)

domization level of 5%, the characteristic wave distribution is conserved, for higher randomness, only the low frequency behaviour is maintained whereas the high frequency wavenumber components are smeared.

4.3.2 Influence of periodicity perturbations on deflection shapes and mobilities

One objective of this study is the determination of an acceptable criterion for the perturbations up to which the influence is of minor importance. Therefore, different calculations with the generic finite profiles presented in chapter 2 are performed with random perturbations. In this case, the length of each subsystem is varied with a uniformly distributed random number on an interval set by the maximum deviation (in percent) from the original periodic length. Values in the range from 1 % to 50 % are used and results for deflection shapes are shown in Fig. 4.14.

A more general investigation of this topic requires e.g. Monte-Carlo simulations with different random deviations. This is not done in detail here because of the inherent computational and evaluation effort involved. Only one random sample is considered. This can provide an informative basis for the influence of periodicity perturbations.

For profile A the forced deflection shapes (excitation F_y at left end) are shown in a pass-band (2500 Hz) in Fig. 4.14. The phenomenon of 'Anderson localization' reveals that the disorder induces a kind of damping, where the vibration amplitudes are 'localized' in the excitation region. Hence, the typical undamped wave propagation in the pass-bands is reduced by introducing the irregularity. The question posed here is if and when such a behavior can be demonstrated also for the investigated generic profile strips.

From the calculated deflection shapes no strict 'localization' can be deduced. 1 % randomness does not alter the deflection form, the 5 % realization reduces the vibration levels on the complete strip significantly. Only for 50 % random length variation the vibration is localized in some regions. However, this is not the classical 'localization' as it is not restricted to the left end excitation region.

The influence on the input and transfer mobility is plotted for profile A in Figs. 4.15 and 4.16 for force excitation at the left end in y -direction and response at a joint approximately at the centre of the finite strip, also in y -direction. The corresponding plots for profile B are shown in Figs. 4.17 and 4.18 and for profile C in Figs. 4.19 and 4.20. As in chapter 2 the results are again plotted for a force F_y per unit z -length. In order to increase legibility, the 1% variation case is suppressed. It is obvious that only large perturbations in the structure have significant influence on the mobilities. For profile C, where distinct pass- and stop-bands are present, the random length variations have only a small effect on the general trends. The influence on the transfer mobilities is more pronounced than for the real part of the input mobility. For the low frequency behaviour, the influence of periodicity perturbations is less pronounced than for higher frequencies, where significant distortion of the pattern is more commonplace.

These results suggest that periodic effects will not disappear by small perturbations, at least for the investigated geometries. Hence, it seems to be possible to design structures in a way to use e.g. the stop-band behaviour for noise control purposes.

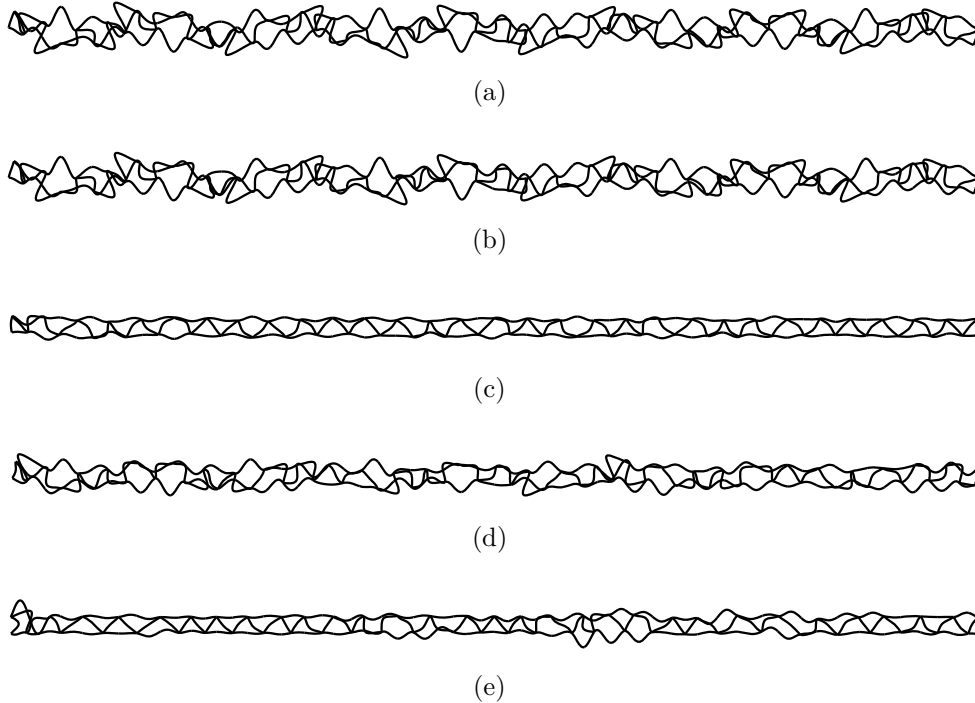


Figure 4.14: Deflection shapes of (a) strictly periodic profile strip A, (b) maximum 1%, (c) 5%, (d) 10%, (e) 50% random length variation. Force excitation F_y at left end, 2500 Hz. Same scaling is maintained for all subplots.

4.4 Concluding remarks

The amplitudes of the characteristic waves for forced vibrations of infinite profile strips and resulting mobilities can be calculated by using the dynamic stiffness matrix of a single periodic subsystem. The amplitudes and the wavenumber content of each characteristic wave form the basis for a quantitative wavenumber distribution on the profile faces, which can be used for structure-borne sound and radiation problems.

A brief study on irregularity effects shows that the influence is limited. The general dynamic behaviour of the periodic profiles is conserved even for high random length variations of up to 5%.

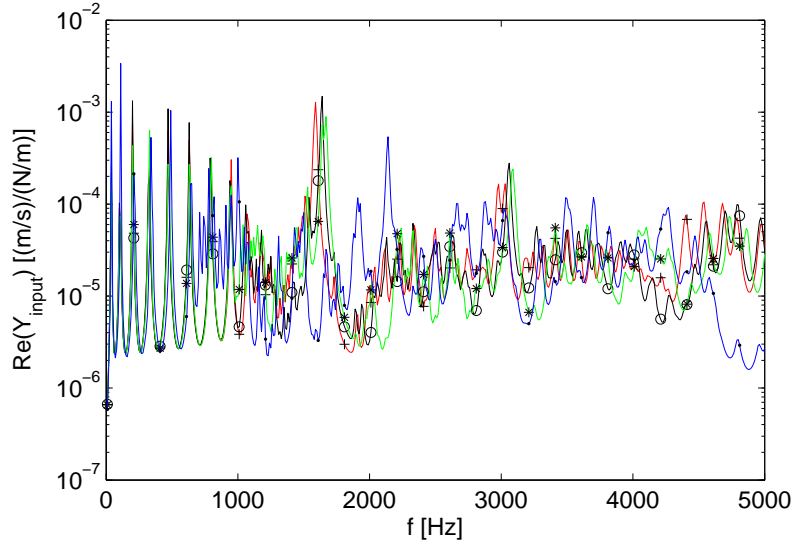


Figure 4.15: Input mobility for randomly varied profile strip A. (force excitation in y-direction at left end) +(red) strictly periodic, o(black) 5 %, *(green) 10%, •(blue) 50 % random length variations of subsystems

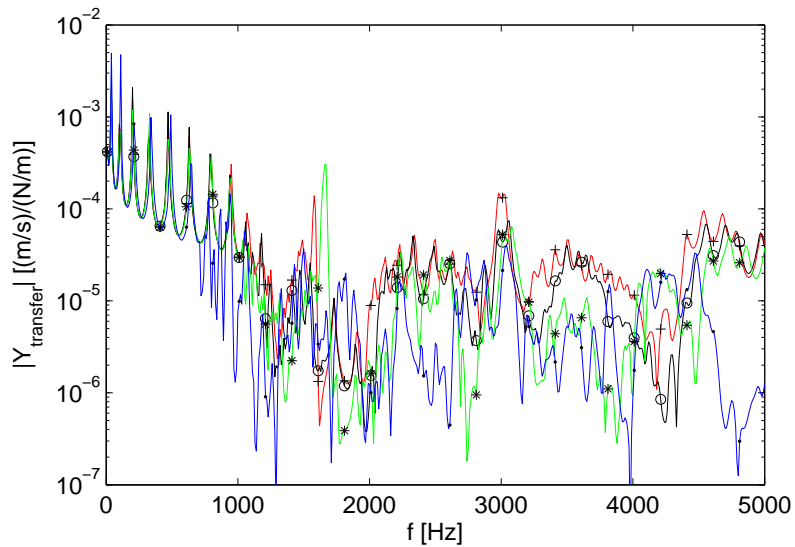


Figure 4.16: Transfer mobility for randomly varied profile strip A. (force excitation in y-direction at left end, response in y-direction approximately at centre of strip) +(red) strictly periodic, o(black) 5 %, *(green) 10%, •(blue) 50 % random length variations of subsystems

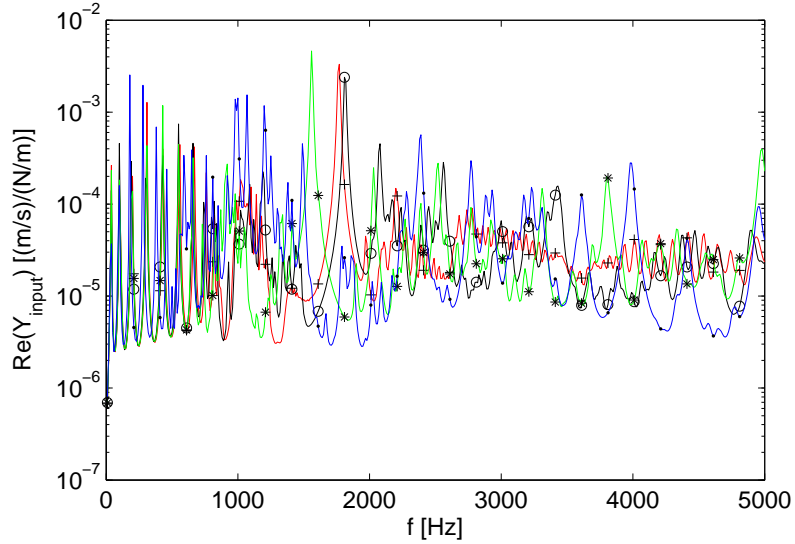


Figure 4.17: Input mobility for randomly varied profile strip B. (force excitation in y-direction at left end) +(red) strictly periodic, o(black) 5%, *(green) 10%, •(blue) 50 % random length variations of subsystems

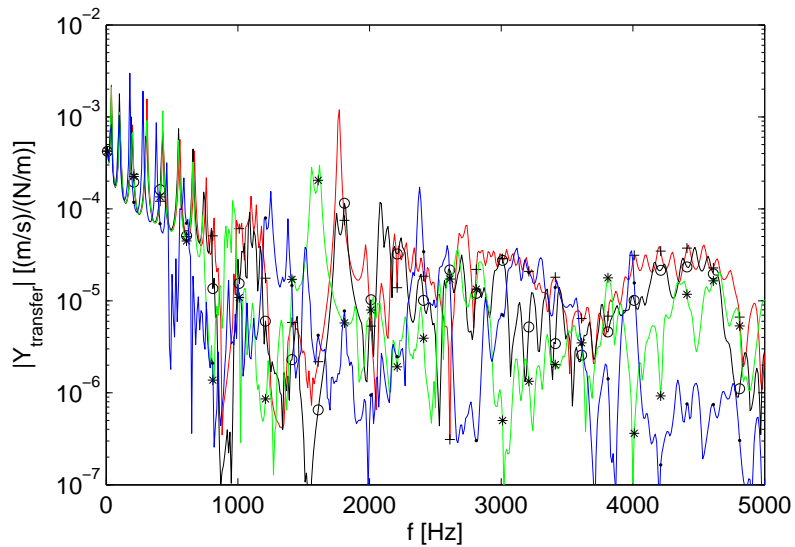


Figure 4.18: Transfer mobility for randomly varied profile strip B. (force excitation in y-direction at left end, response in y-direction approximately at centre of strip) +(red) strictly periodic, o(black) 5 %, *(green) 10%, •(blue) 50 % random length variations of subsystems

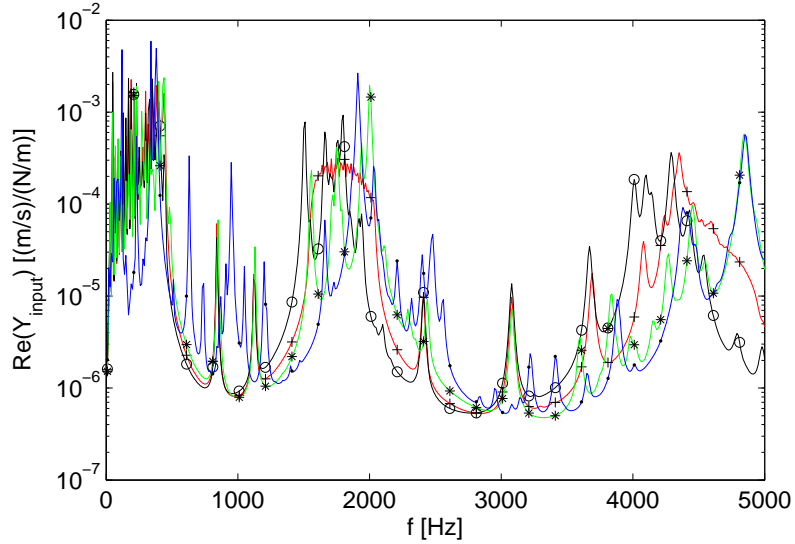


Figure 4.19: Input mobility for randomly varied profile strip C. (force excitation in y-direction at left end) +(red) strictly periodic, o(black) 5 %, *(green) 10%, •(blue) 50 % random length variations of subsystems

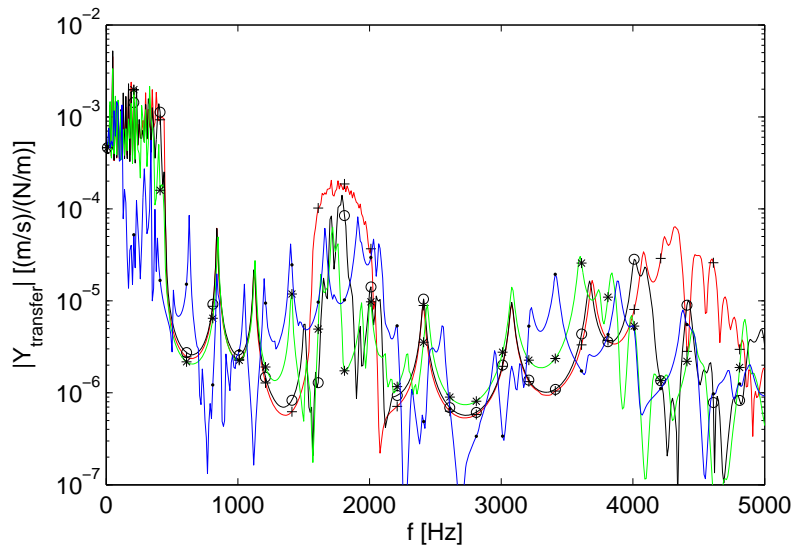


Figure 4.20: Transfer mobility for randomly varied profile strip C. (force excitation in y-direction at left end, response in y-direction approximately at centre of strip) +(red) strictly periodic, o(black) 5 %, *(green) 10%, •(blue) 50 % random length variations of subsystems

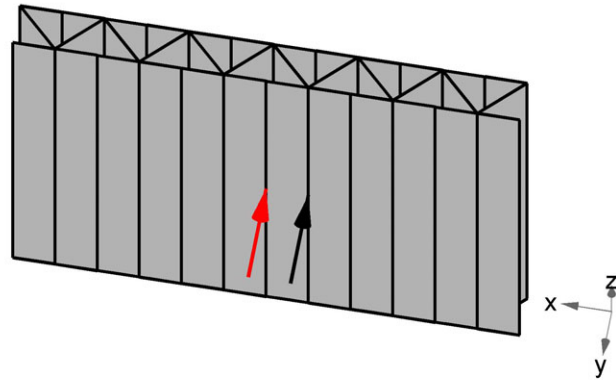
Chapter 5

Free wave propagation in light weight profile plates

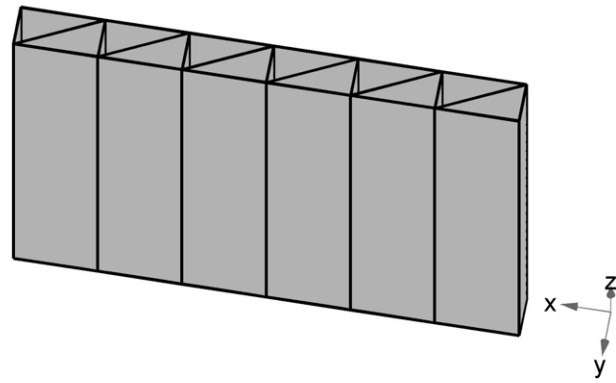
5.1 Introduction

The wave propagation in light weight profile strips with different truss-like core geometries is thoroughly investigated in chapters 2 to 4 and typical periodic system effects like pass- and stop-band behaviour are identified. The results presented there are valid also for plates with line force excitation perpendicular to the strip plane in z -direction. For structure-borne sound applications the loads are often concentrated to small areas where e.g. machine footings are attached to the light weight plate. As long as the wavelength is larger than the contact dimension they can be treated as point contacts.

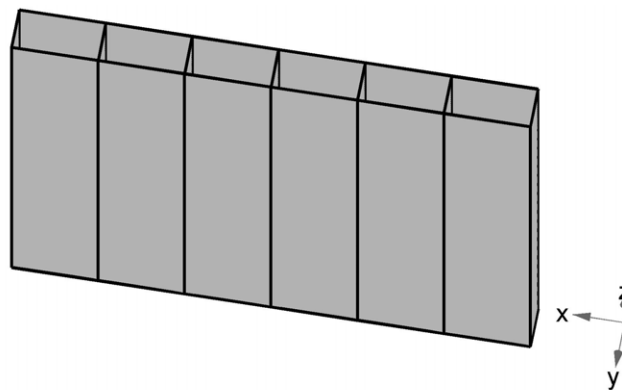
In this chapter the wave propagation in the light weight plates illustrated in Fig. 5.1 is investigated. For the case of point force excitation the wave propagation spreading from the excitation point is treated in sections 5.2 and 5.3. One of the questions posed is if the pass- and stop-band effects are also distinct for point excited plate configurations. Langley and Bardell show in [38] that for two-dimensional periodic systems (beam grillages), the wave propagation can be highly directional. Similar results are reported by Ruzzene et. al. in [39]. It is investigated here if such a phenomenon also exists for a two-dimensional structure with periodicity only in one direction. Therefore the forced response of typical profiles is calculated using standard Finite Element techniques. For a physical understanding and interpretation of the wave propagation in the light weight profiles the two-dimensional wavenumber content is extracted from the calculated vibration fields. Results of the spatial Fourier-transform method are shown and reveal the wave beaming effects for the investigated light weight plates. As an alternative to the spatial



(a) Profile A



(b) Profile B



(c) Profile C

Figure 5.1: Investigated generic light weight profiles. Arrows in (a) indicate extreme normal force excitation positions (left arrow at centre of plate strip and right arrow at a stiffener position)

Fourier transform the dispersion characteristics of propagating waves can be extracted from a single subelement, repeated in both directions, resulting in the so-called phase constant surfaces. Results are compared with DFT and reveal the enhanced resolution capabilities of the subelement approach for periodic profiles. For profiles of finite width the wavenumber content in z -direction is extracted using the waveguide finite element technique (WFE), [40, 41]. A narrow slice of the complete waveguide is modelled with standard FE methods and periodic system theory delivers the characteristic waves propagating in z -direction in the infinite light weight plate section.

5.2 Dispersion characteristics using DFT

In order to understand the wave propagation in the light weight profiles, the wavenumber content for propagation in x - and z -direction is sought (see Fig. 5.1). There are several options to extract the wavenumber content from measured or calculated data. A lot of work in the area of one-dimensional wavenumber estimation has been published, see e.g. [42, 43, 44]. For two-dimensional extraction procedures details can be found in [45], [46] and [47]. Mainly for usage with experimental data a Correlation method [46] and the Inhomogeneous Wave Correlation method (IWC) [45, 48] are introduced. Both are intended to overcome some limitations of the standard spatial discrete Fourier Transform technique when only limited and possibly noisy (experimental) data is available. For this study calculated vibration fields with high resolution are available so that the spatial Discrete Fourier Transform (DFT) technique is applicable. A clearer picture of the two-dimensional wave propagation can be gained with the evaluation of the phase constant surfaces from the 2D-periodic subelement. This is compared with the DFT-results in section 5.3. If the system can be handled as a waveguide, in which wave propagation is of primary concern only along the waveguide, i.e. parallel to the inner webs of the profile, the dispersion characteristics for this direction can be investigated e.g. with spectral or waveguide finite element techniques, see e.g. [26, 41, 40]. From these methods the properties of characteristic waves propagating in the waveguide direction can be deduced. For profiles of finite width this approach is favourable for general investigations of wave propagation in the waveguide direction. This approach is chosen for the investigation in section 5.4. The IWC method is applied for the experimental dispersion investigation of a train floor in section 7.2.2 and results are related to the DFT results.

5.2.1 Discrete spatial Fourier Transform

For the application of the DFT-method, a spatial sampling at points on a discrete two-dimensional grid is necessary, resulting in the two-dimensional discrete fourier transform (2D-DFT). Having a profile section of dimensions L_x and L_z with $N_x \times N_z$ equally distributed spatial sampling points $v_{n_x, n_z} = v(n_x \Delta x, n_z \Delta z)$, $n_x = 1, 2, 3, \dots, N_x$; $n_z = 1, 2, 3, \dots, N_z$, results in the following transformation:

$$V_{p,q} = V(p\Delta k_x, q\Delta k_z) = \Delta x \Delta z \sum_{n_x=1}^{N_x} \sum_{n_z=1}^{N_z} v_{n_x, n_z} e^{-j p \Delta k_x x_p} e^{-j q \Delta k_z z_q}$$

$$\Delta k_x = \frac{2\pi}{L_x}, \quad \Delta k_z = \frac{2\pi}{L_z} \quad (5.1)$$

This is a direct extension of the one-dimensional Fourier transform introduced in section 3.2.2, where limitations and practical aspects of the method and its application are discussed.

As stated already for the one-dimensional case the DFT-approach is beneficial for a specific forced excitation, as it directly results in the energy distribution among different waves for this excitation. On the other hand this can be a limitation if a more general understanding of possible wave propagation in the light weight plates is sought. It cannot be directly assured that all the important wave types are excited and hence can be extracted. For a more general investigation, the WFE method or the phase constant surface evaluation presented later on are favoured.

The velocity field data on a regular spaced grid is calculated using standard FE-modeling techniques using MSC NASTRAN ¹. In order to suppress reflections from the model boundaries, the edge regions (0.5 m width) are highly damped (loss factor 0.1). For a reduced calculation effort, symmetry is exploited and only a quarter model with symmetry boundary conditions is established. The principal geometries of the investigated profiles are shown in Fig. 5.1. Details of geometric dimensions and material properties are listed in Tab. 5.1. The thickness of the inner webs of profiles B and C is adjusted to maintain constant total mass per unit area.

As shown already in chapter 3 the vibrations of truss-like light weight objects can be divided in global and local wave motion. The global waves dominate at lower frequencies whereas at higher frequencies global and local vibrations are of significance.

¹CQUAD4 shell elements, element length 12.5 mm, frequency limit according to six elements per (bending) wavelength criterion is about 5300 Hz, direct frequency response calculation method (SOL 108) is used.

Table 5.1: Geometry and material properties of investigated profiles (see Fig. 2.1 for nomenclature)

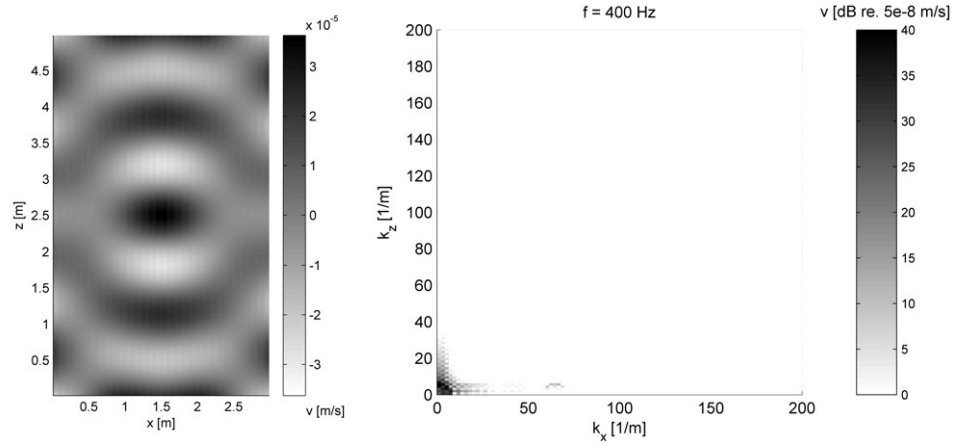
Profile	A	B	C
t_{outer} [mm]	3.0	3.0	3.0
t_{inner} [mm]	3.0	2.6	8.5
Web angle α [°]	45.0	26.6 / 90.0	90.0
Periodic length l_x [mm]	100	100	100
Total length L_x [mm]	3000	3000	3000
Total length L_z [mm]	5000	5000	5000
E_0 [N/m ²]	$7.2 \cdot 10^{10}$	$7.2 \cdot 10^{10}$	$7.2 \cdot 10^{10}$
ν [-]	0.34	0.34	0.34
η [-]	0.01/0.1	0.01/0.1	0.01/0.1
ρ [kg/m ³]	2700	2700	2700
Total mass per unit area [kg/m ²]	27.7	27.7	27.7

The geometry of the truss-like light weight profiles is highly orthotropic as the intermediate plates are orientated only in the z -direction. Despite this geometrical orthotropy, the global vibrations for profiles of type A are mainly isotropic as shown in [2]. The static and low frequency bending stiffnesses are dominated by the face plates which do not comprise any orthotropy. The following investigation shall shed some light on the influence of generic geometry (A, B, C) on vibrational orthotropy.

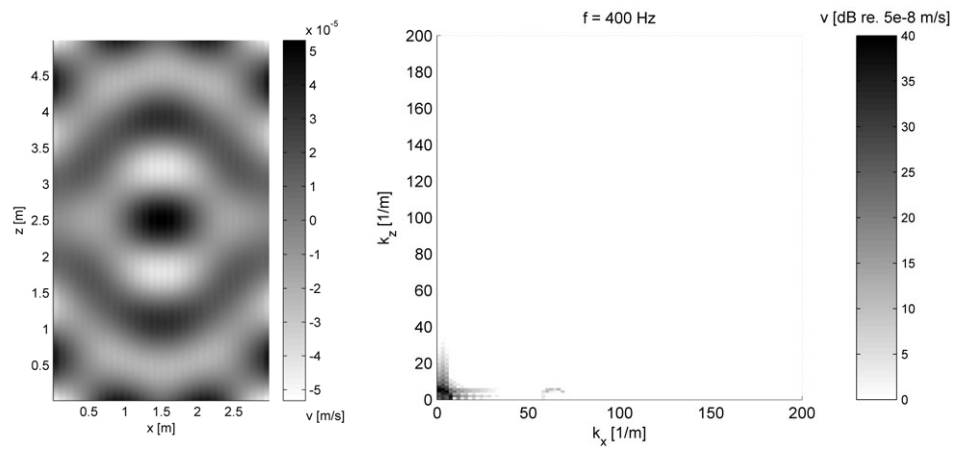
Representative for the global wave region, the 400 Hz results of all three profile types are presented in Fig. 5.2. The wavenumber content is displayed on a logarithmic grey scale and strong contributions are dark shaded. The results presented correspond to unit normal point force excitation at the centre of a plate field (A and C) or an excitation at a stiffener position (B). The normal velocity of the outer plate of the excited side is selected for the evaluation. The influence of excitation position is treated in [49] and section 5.2.2 and can be summarized by a quantitative variation in the wavenumber content, but the inherent waves are similar.

The results in Fig. 5.2 show the dominance of the global, low wavenumber waves for all profiles at 400 Hz. The response of A and B is similar, the wavenumber content displaying the isotropic nature of the wave propagation with a quarter circle at very low wavenumbers. In contrast to this the velocity field for profile C comprises much shorter wavelength in x -direction ($k_x = 30 \text{ m}^{-1}$, $k_z = 8 \text{ m}^{-1}$, see Fig. 5.2(c)). This is directly linked to the elliptical wavenumber curve in the DFT-result with a higher wavenumber for k_x .

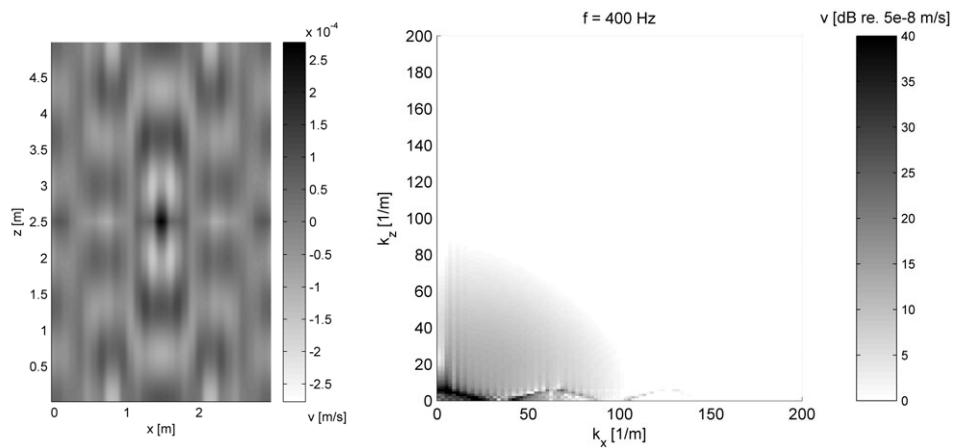
Although the global waves dominate the vibration, there are also higher



(a) Profile A (left: velocity field, right: wavenumber content), plate field excitation



(b) Profile B (left: velocity field, right: wavenumber content), stiffener excitation

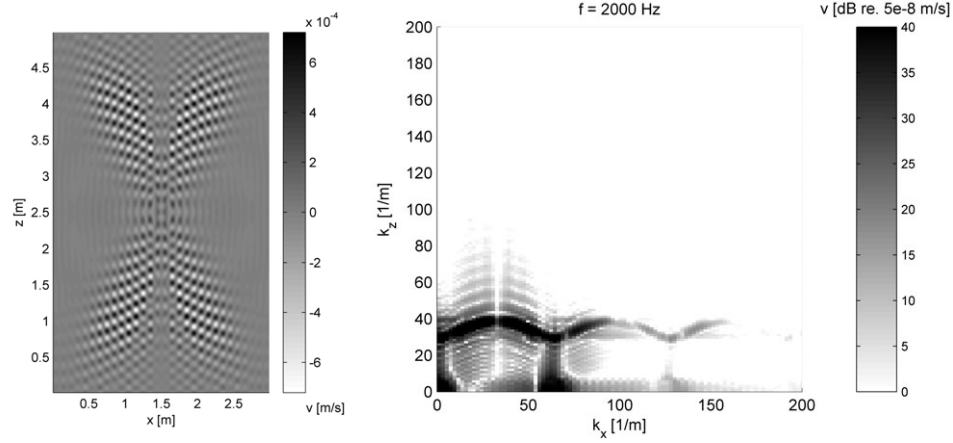


(c) Profile C (left: velocity field, right: wavenumber content), plate field excitation

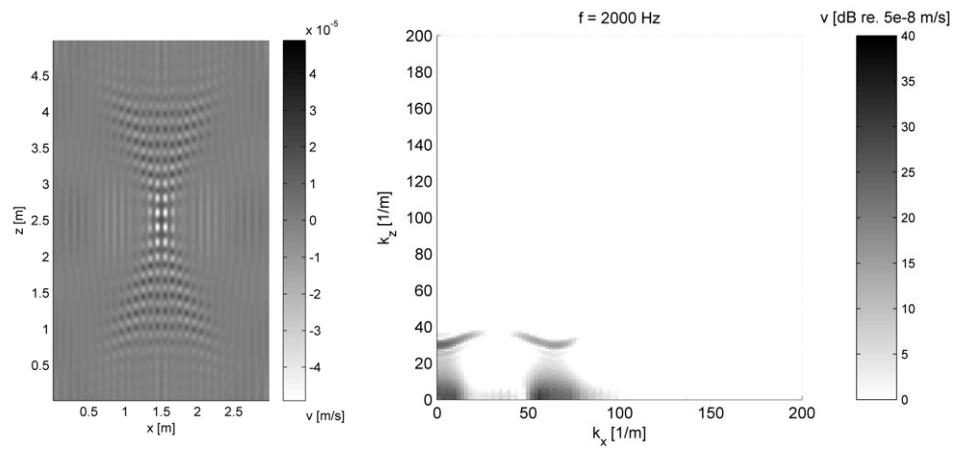
Figure 5.2: Velocity fields for normal force excitation and DFT wavenumber content ($f = 400$ Hz)

wavenumber components included, representing some local behaviour. For the periodicity in x -direction, a higher wavenumber component is present with a separation of $2\pi/l_x = 62.8 \text{ m}^{-1}$ to the global waves, where l_x is the periodic length of 0.1 m in x -direction. For higher frequencies the significance of the global waves decreases (Fig. 5.3) and the velocity field is dominated by high wavenumber (short wavelength) components. These wave components comprise an interesting feature, they propagate only in the direction of a limited angular segment, which is related to strong wave beaming effects most clearly visible for types A and C. For profile A the main direction is oblique, whereas for profile C the lobes are orientated mainly in z -direction. This kind of wave beaming is similar to the results presented by Langley [50, 38] for point excited periodic beam grillages. This means that wave beaming is not only existing for structures with periodicity in both directions, but also for structures comprising periodicity only in one direction.

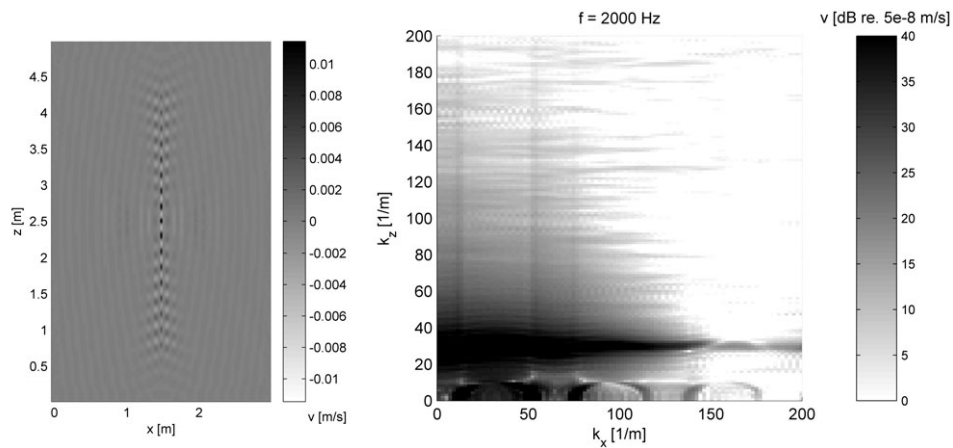
Going higher in frequency the wave propagation characteristics shown in Fig. 5.4 for 5000 Hz arise. For profile A strong wave beaming effects are still visible. The wave propagation in profile C arises mainly along the excited plate strip in z -direction. Nonetheless, some less pronounced waves with periodic wavenumber content propagate also in x -direction, clearly visible in the wavenumber domain.



(a) Profile A (left: velocity field, right: wavenumber content), plate field excitation

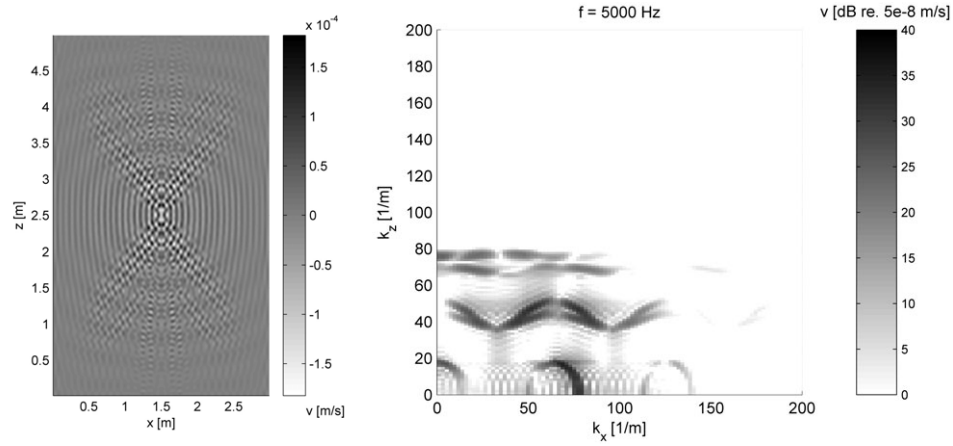


(b) Profile B (left: velocity field, right: wavenumber content), stiffener excitation

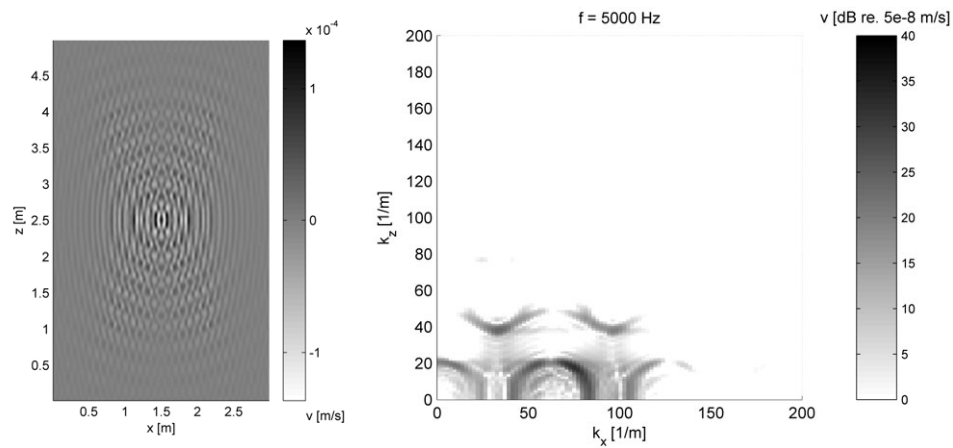


(c) Profile C (left: velocity field, right: wavenumber content), plate field excitation

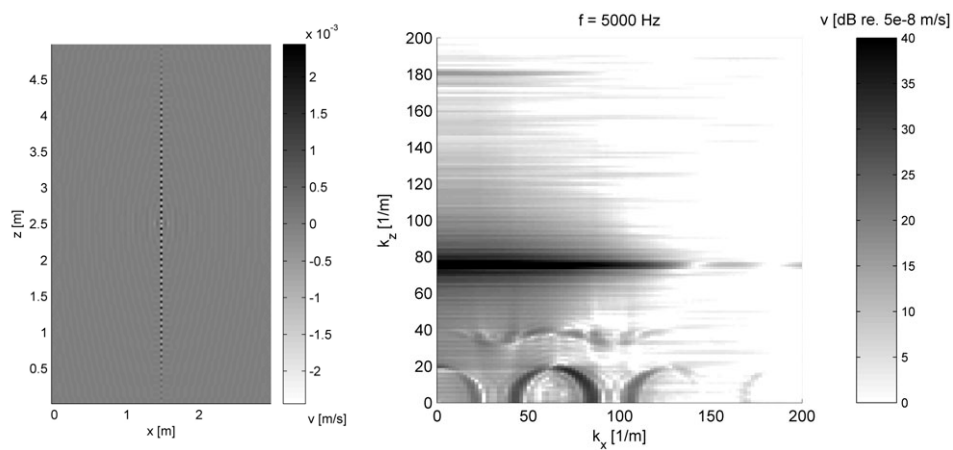
Figure 5.3: Velocity fields for normal force excitation and DFT wavenumber content ($f = 2000$ Hz)



(a) Profile A (left: velocity field, right: wavenumber content), plate field excitation



(b) Profile B (left: velocity field, right: wavenumber content), stiffener excitation



(c) Profile C (left: velocity field, right: wavenumber content), plate field excitation

Figure 5.4: Velocity fields for normal force excitation and DFT wavenumber content ($f = 5000$ Hz)

5.2.2 Frequency dependent dispersion from DFT

In order to get insight into the frequency dependent behaviour and for comparison with WFE and phase constant surface results, the wavenumbers in the main directions x and z are extracted from the 2D-DFT results. The extraction procedure is performed with a frequency increment of 50 Hz and results are shown in Figs. 5.5 to 5.9 for the different generic profiles and excitation positions.

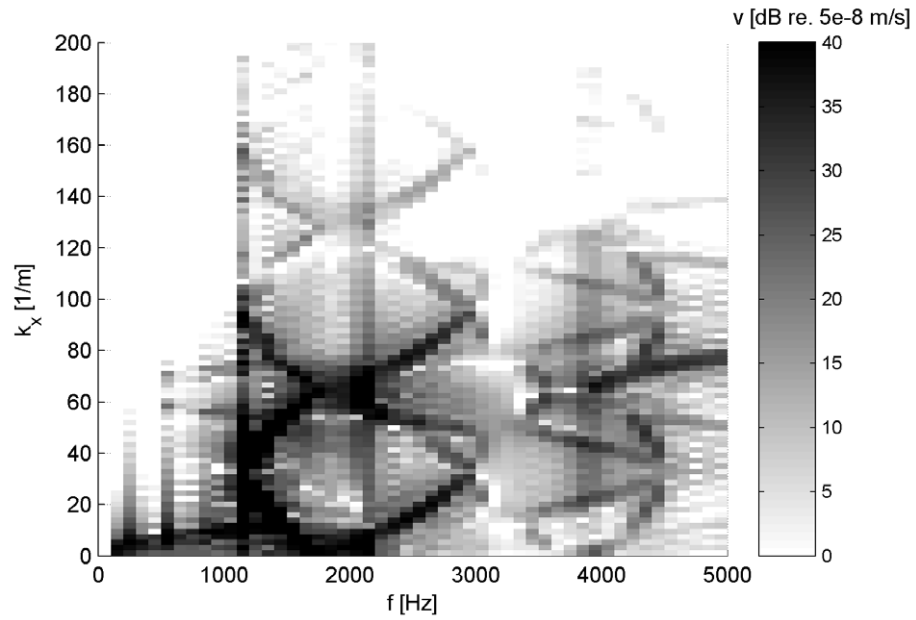
As expected the dispersion in x -direction is very similar to the characteristics obtained from the two-dimensional strip investigation, chapter 3. The periodic stop- and pass-band behaviour is distinct especially for profile C with two wide stop-bands. Moreover the periodic wavenumber content with spacing $2\pi/l_x$ is clearly visible in the pass-bands.

The influence of force position is demonstrated with Figs. 5.5 and 5.6. The same waves are inherent in the structure independent of excitation position but with different amplitudes. The plate field excitation tends to excite higher wavenumbers, i.e. local waves, especially in the range 1100-3000 Hz. For this excitation an additional dispersion curve appears for wave propagation in z -direction cutting on at approximately 1000 Hz.

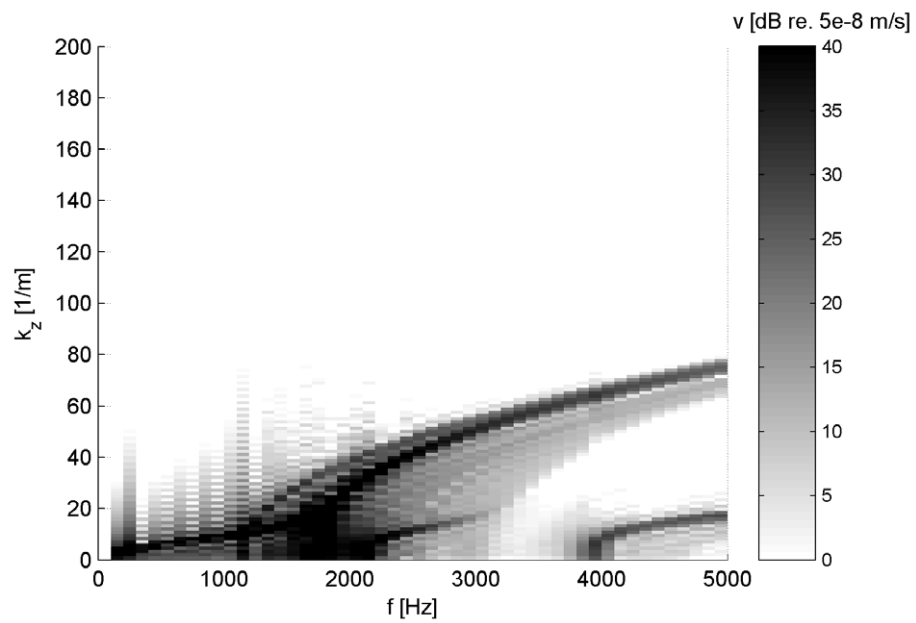
Figs. 5.7 and 5.8 demonstrate the wavenumber content of the velocity field of face $y = 0.05$ m for the excitation on lower ($y = 0$) and upper plate face ($y = 0.05$ m). The wavenumber content is very similar on both sides with some quantitative differences of the inherent waves.

As expected by the plate geometries, wave propagation in x -direction is highly influenced by the structural periodicity and to different extent stop- and pass-band behaviour is observed. Wave propagation in z -direction parallel to the intermediate plates is much more distinct and exists in the complete frequency range, starting with global bending wave behaviour at low frequencies and a transition to local plate strip bending wave behaviour at higher frequencies, similar e.g. to dispersion in cylinders, where global torsional and bending waves of the complete cylinder dominate at low frequencies and change to bending dispersion of the hull at high frequencies.

The limited resolution of the DFT-results makes the interpretation somewhat difficult. The WFE method and the phase constant surface results shall give some further insight into the wave propagation in z -direction and the corresponding characteristic waves.

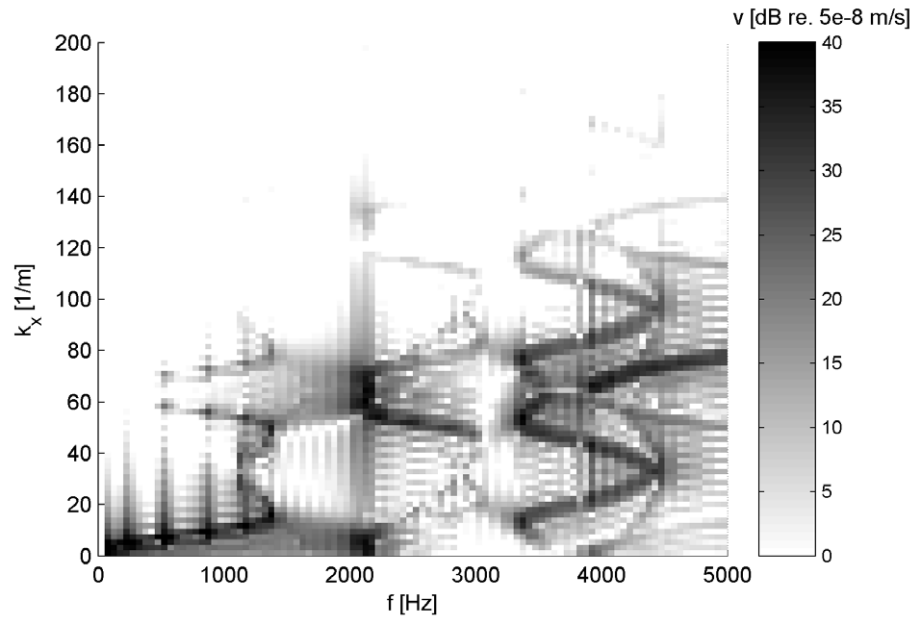


(a) k_x ($k_z = 0$)

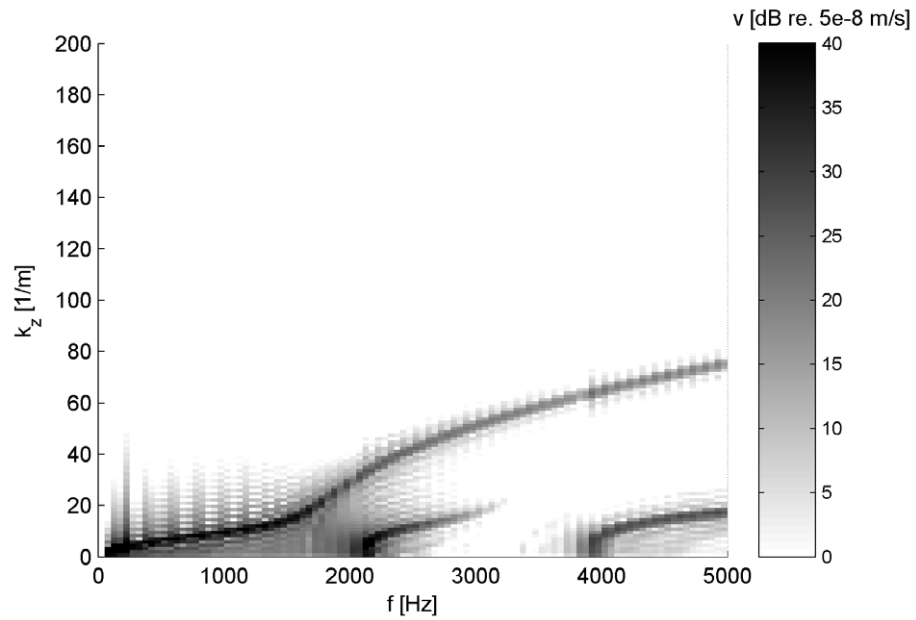


(b) k_z ($k_x = 0$)

Figure 5.5: Dispersion characteristics of profile A in x - and z -direction extracted from 2D-DFT results, plate field excitation

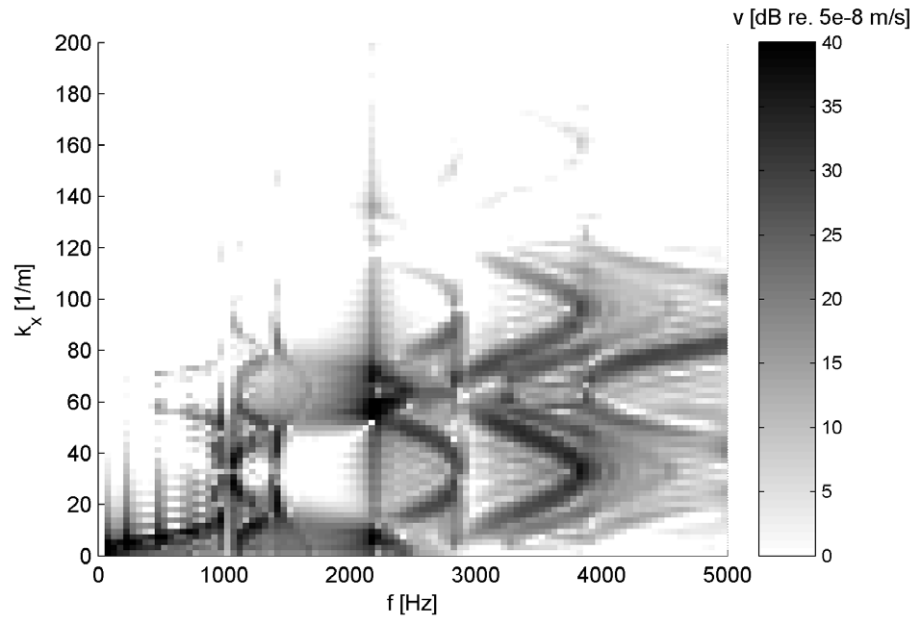


(a) k_x ($k_z = 0$)

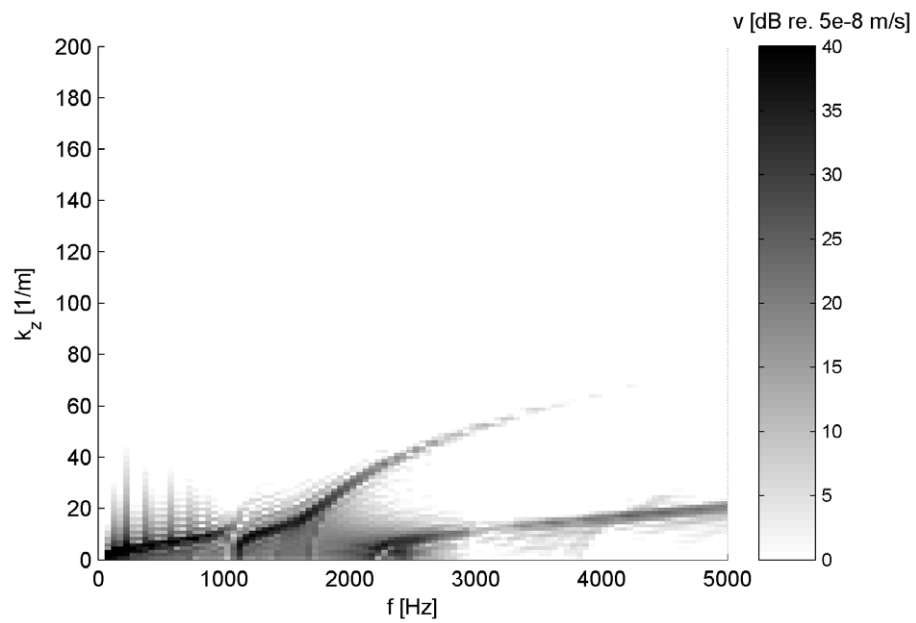


(b) k_z ($k_x = 0$)

Figure 5.6: Dispersion characteristics of profile A in x - and z -direction extracted from 2D-DFT results, stiffener excitation

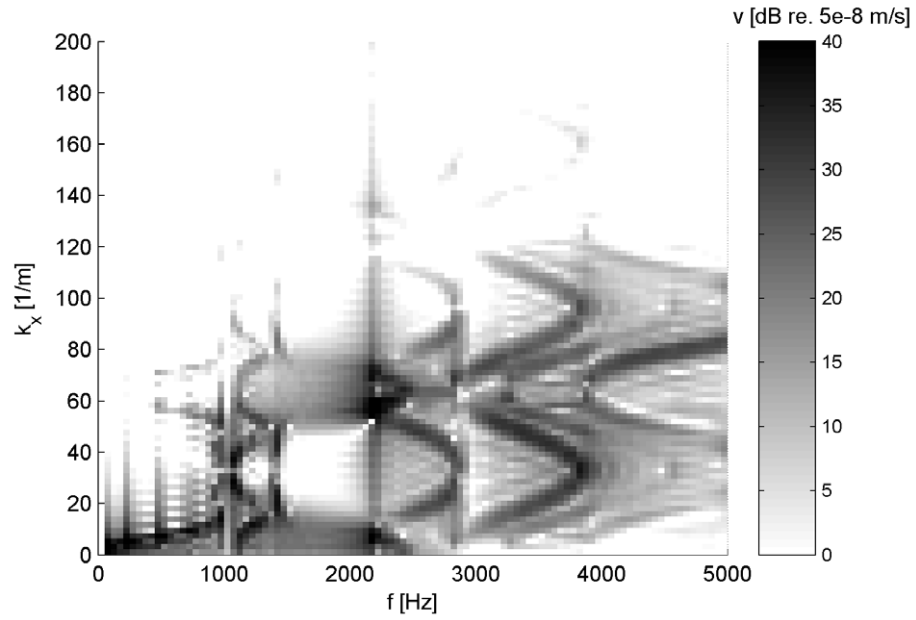


(a) k_x ($k_z = 0$)

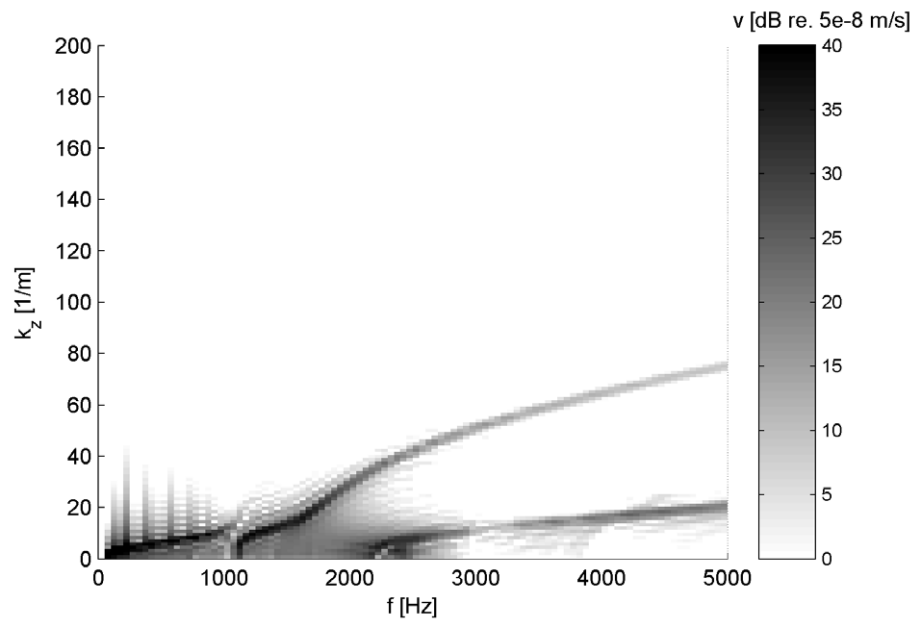


(b) k_z ($k_x = 0$)

Figure 5.7: Dispersion characteristics of profile B in x - and z -direction extracted from 2D-DFT results, stiffener excitation, $y = 0$

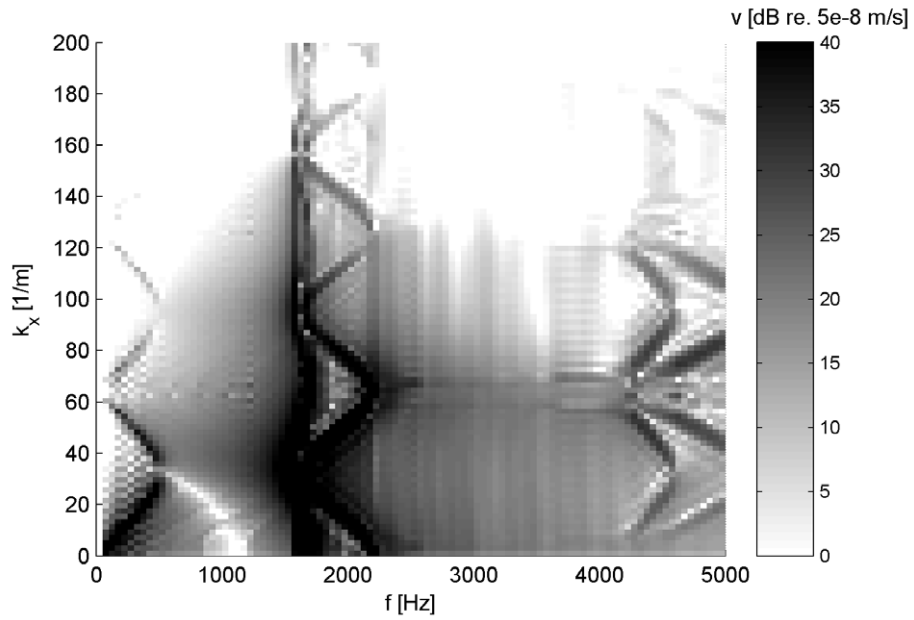


(a) k_x ($k_z = 0$)

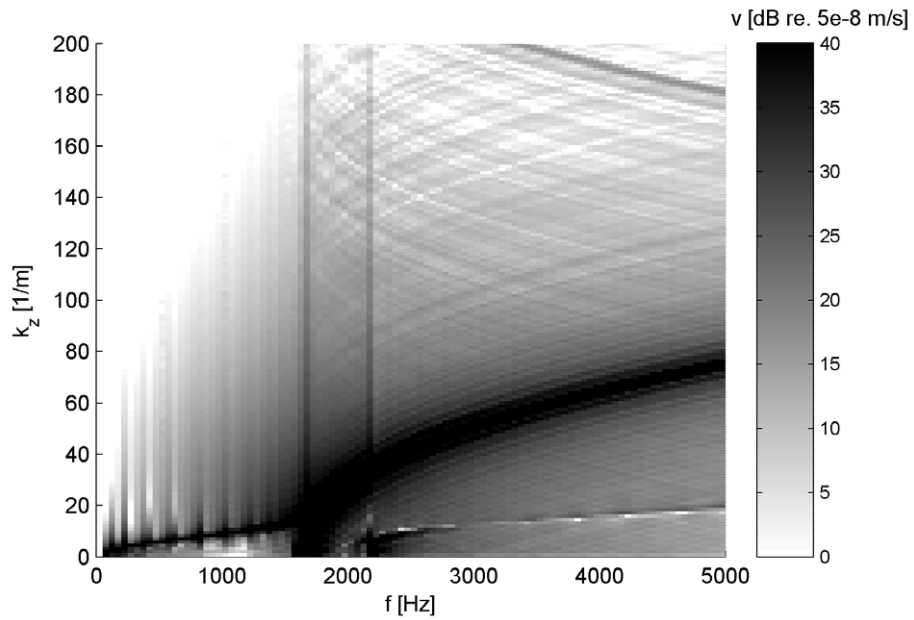


(b) k_z ($k_x = 0$)

Figure 5.8: Dispersion characteristics of profile B in x - and z -direction extracted from 2D-DFT results, stiffener excitation, $y = 0.05$ m, velocity field of face $y = 0.05$ m



(a) k_x ($k_z = 0$)



(b) k_z ($k_x = 0$)

Figure 5.9: Dispersion characteristics of profile C in x - and z -direction extracted from 2D-DFT results, plate field excitation

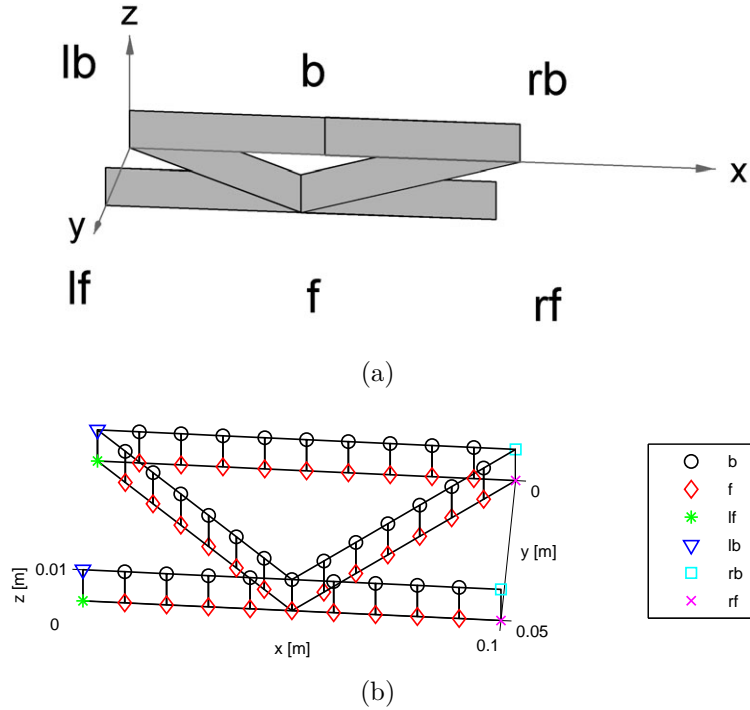


Figure 5.10: Naming conventions of the periodic subelement for dispersion extraction in x - and z -direction exemplified for profile A. (a) general illustration, (b) detailed assignment of FE-nodes

5.3 Dispersion characteristics using phase constant surfaces

5.3.1 Theory

Based on 2D-periodic system theory the so-called phase constant surfaces can be extracted from a reduced eigenvalue problem of the 2D-periodic subelement [51, 38, 52].

The naming convention for the subelement used for extraction of the phase constant surfaces is shown in Fig. 5.10. In contrast to the formulation by Mead et. al. [51], no inner degrees of freedom and no degrees of freedom solely related to left and right boundaries are present. This is due to the fact that the extension in z -direction is intended to be very small (10 mm) in order to achieve in this direction, which does not comprise classical periodicity, a high limiting wavenumber.

Starting with the definition of the displacement and force vectors,

$$\boldsymbol{\xi} = [\boldsymbol{\xi}_b \boldsymbol{\xi}_f \boldsymbol{\xi}_{lf} \boldsymbol{\xi}_{lb} \boldsymbol{\xi}_{rb} \boldsymbol{\xi}_{rf}]^T \quad (5.2)$$

$$\mathbf{F} = [\mathbf{F}_b \mathbf{F}_f \mathbf{F}_{lf} \mathbf{F}_{lb} \mathbf{F}_{rb} \mathbf{F}_{rf}]^T \quad (5.3)$$

the undamped equations of motion with stiffness matrix \mathbf{S} and mass matrix \mathbf{M} read:

$$(\mathbf{S} - \omega^2 \mathbf{M}) \boldsymbol{\xi} = \mathbf{F} \quad (5.4)$$

Using Bloch's theorem relating displacement and forces at the boundaries of the periodic subelement, the equations of motion can be condensed in the case of free wave propagation. The detailed Bloch conditions read:

$$\begin{aligned} \boldsymbol{\xi}_b &= e^{\mu z} \boldsymbol{\xi}_f \\ \boldsymbol{\xi}_{lb} &= e^{\mu z} \boldsymbol{\xi}_{lf} \\ \boldsymbol{\xi}_{rb} &= e^{\mu_x + \mu z} \boldsymbol{\xi}_{lf} \\ \boldsymbol{\xi}_{rf} &= e^{\mu_x} \boldsymbol{\xi}_{lf} \end{aligned} \quad (5.5)$$

$$\begin{aligned} \mathbf{F}_b &= -e^{\mu z} \mathbf{F}_f \\ \mathbf{F}_{lb} &= -e^{\mu z} \mathbf{F}_{lf} \\ \mathbf{F}_{rb} &= +e^{\mu_x + \mu z} \mathbf{F}_{lf} \\ \mathbf{F}_{rf} &= -e^{\mu_x} \mathbf{F}_{lf} \end{aligned} \quad (5.6)$$

Using these conditions, reduced vectors can be used

$$\boldsymbol{\xi}_{red} = [\boldsymbol{\xi}_f \boldsymbol{\xi}_{lf}]^T \quad (5.7)$$

$$\mathbf{F}_{red} = [\mathbf{F}_f \mathbf{F}_{lf}]^T. \quad (5.8)$$

From the reduced vectors the full vectors can be calculated using the Bloch conditions in matrix form,

$$\boldsymbol{\xi} = \mathbf{A} \boldsymbol{\xi}_{red} \quad \text{with} \quad \mathbf{A} = \begin{pmatrix} \mathbf{I}_b e^{\mu z} & \mathbf{0} \\ \mathbf{I}_f & \mathbf{0} \\ \mathbf{0} & \mathbf{I}_{lf} \\ \mathbf{0} & \mathbf{I}_{lb} e^{\mu z} \\ \mathbf{0} & \mathbf{I}_{rb} e^{\mu_x + \mu z} \\ \mathbf{0} & \mathbf{I}_{rf} e^{\mu_x} \end{pmatrix} \quad (5.9)$$

$$\mathbf{F} = \mathbf{B} \mathbf{F}_{red} \quad \text{with} \quad \mathbf{B} = \begin{pmatrix} -\mathbf{I}_b e^{\mu_z} & \mathbf{0} \\ \mathbf{I}_f & \mathbf{0} \\ \mathbf{0} & \mathbf{I}_{lf} \\ \mathbf{0} & -\mathbf{I}_{lb} e^{\mu_z} \\ \mathbf{0} & +\mathbf{I}_{rb} e^{\mu_x + \mu_z} \\ \mathbf{0} & -\mathbf{I}_{rf} e^{\mu_x} \end{pmatrix}. \quad (5.10)$$

Introducing the reduced force and velocity vectors in equation (5.4) and pre-multiplying with \mathbf{A}^H results in a reduced eigenvalue problem with reduced mass and stiffness matrices \mathbf{M}_{red} and \mathbf{S}_{red} .

$$(\mathbf{S}_{red} - \omega^2 \mathbf{M}_{red}) \boldsymbol{\xi}_{red} = \mathbf{0} \quad (5.11)$$

$$\text{with } \mathbf{S}_{red} = \mathbf{A}^H \mathbf{S} \mathbf{A}, \quad \mathbf{M}_{red} = \mathbf{A}^H \mathbf{M} \mathbf{A}$$

The right side of Eq. (5.11) is $\mathbf{0}$ for purely imaginary propagation constants, i.e. purely propagating waves without losses. For each combination of purely imaginary μ_x, μ_z several real eigenvalue solutions for ω^2 exist. The resulting triples μ_x, μ_z, ω form the so called phase constant surfaces representing the dispersion characteristics of the infinite profile formed by repeated subelements in x - and z -direction.

5.3.2 Numerical results

Phase constant surfaces are calculated from FE-subelement models of profiles A, B and C with a mesh size of 10 mm (see Fig. 5.19). Some examples for the first four phase constant surfaces in the frequency range up to 5000 Hz are presented in Fig. 5.11. In the x -direction with a periodic subelement length of $L_e = 0.1$ m wavenumbers are multi-valued with the periodicity given in Eq. (3.4), forming the space harmonic series.

Only the first phase constant surface of Fig. 5.11 starts at very low frequencies and represents the global wave behaviour. All others cut on with propagating waves in the phase constant surface at higher frequencies.

As the phase constant surfaces are difficult to interpret directly, contours for selected frequencies are presented in Figs. 5.12 to 5.14. The contour lines represent the wavenumber content for these selected frequencies. Periodicity in x -direction is accounted for in the plotted results by including higher space harmonics up to $k_x = 200 \text{ m}^{-1}$. For comparison, the DFT results presented in section 5.2.1 are included by colour shading in the plots, while the contour lines are included with blue full lines. The agreement between DFT results and contour lines is high. The comparison of the phase constant surface dispersion results with the spatial Fourier transform results reveals

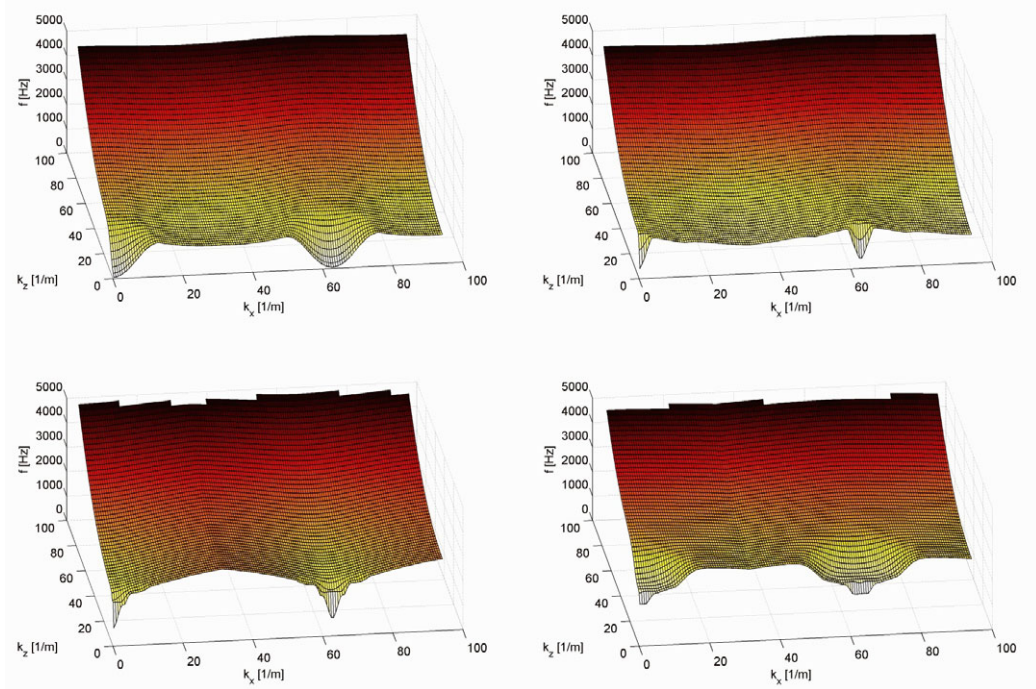


Figure 5.11: First four phase constant surfaces of profile A subelement, higher order space harmonics included in x -direction for clarity. The wavenumber periodicity is $k_x = 62.8 \text{ m}^{-1}$.

the strength of the former to identify clearly the possible inherent propagating waves. The drawback is that the energy distribution among the different components of the space harmonics and the different wave types is not readily given for a specific excitation. This is particularly the case for the periodic x -direction. Wave beaming plays a dominant role in some frequency bands, as expected already from the DFT results. For low frequencies global waves are prominent. With increasing frequency new wave types cut on, increasing the complexity of the wavenumber content. For profile C in particular, the distinct pass- and stop-band behaviour for bending wave propagation in x -direction is obvious. Significant lateral wave propagation is possible only in the pass-bands 1500-2200 Hz and beyond 4200 Hz, see Figs. 5.14(c) and 5.17(a).

CHAPTER 5. FREE WAVE PROP. IN LIGHT WEIGHT PLATES

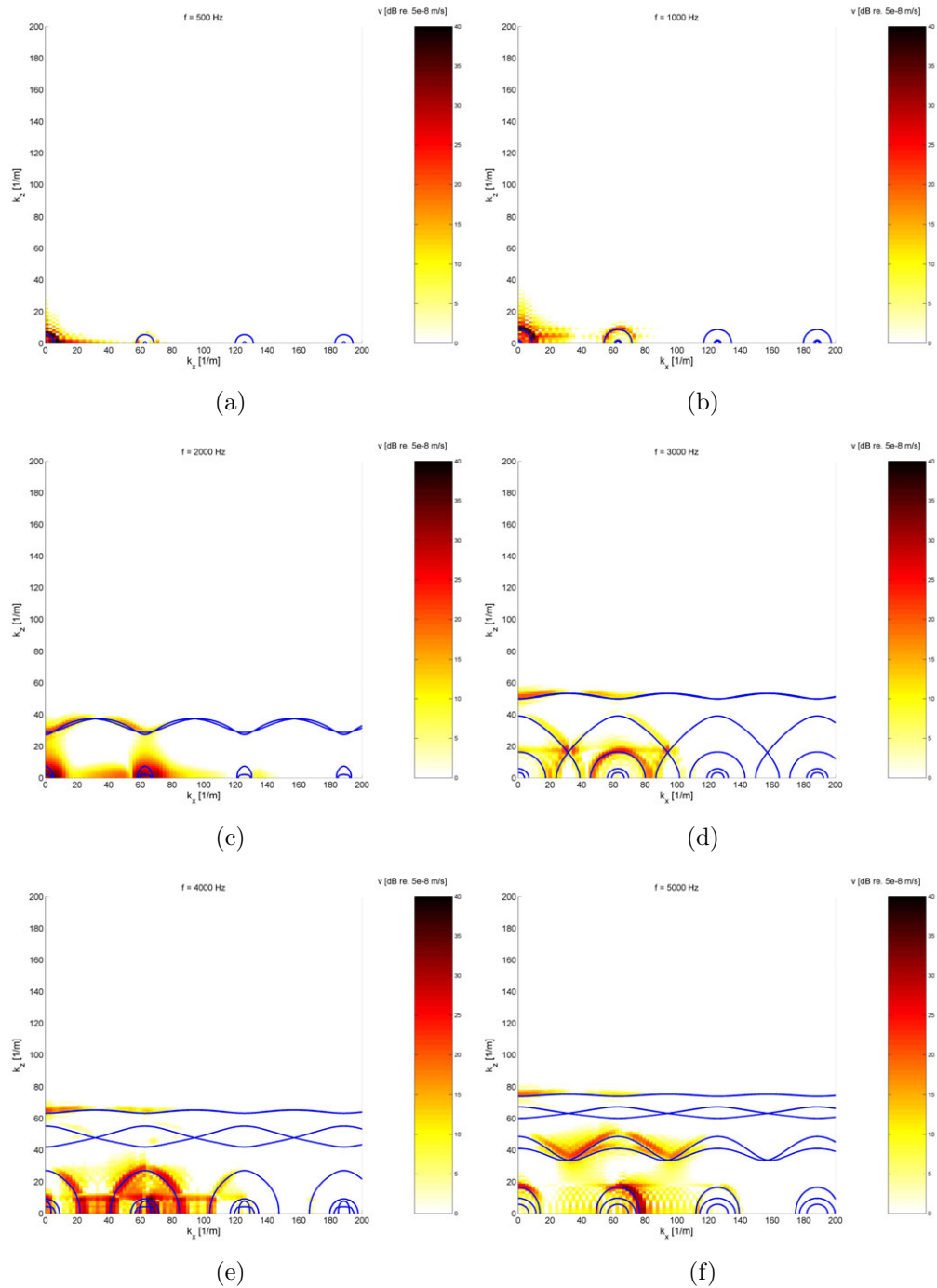


Figure 5.12: Wavenumber content of profile A for selected frequencies (DFT results using colour shading and phase constant surface results in blue)

CHAPTER 5. FREE WAVE PROP. IN LIGHT WEIGHT PLATES

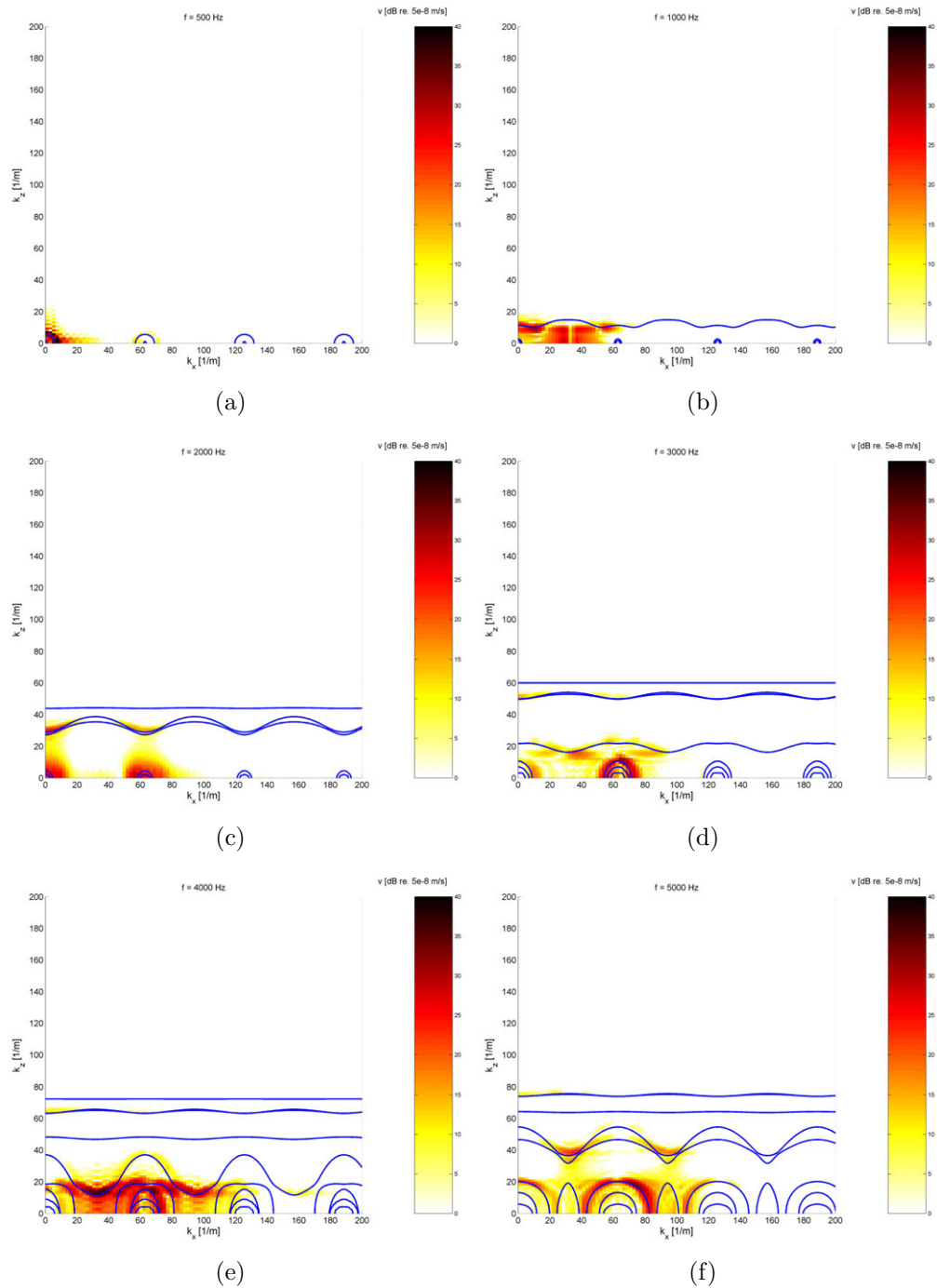


Figure 5.13: Wavenumber content of profile B for selected frequencies (DFT results using colour shading and phase constant surface results in blue)

CHAPTER 5. FREE WAVE PROP. IN LIGHT WEIGHT PLATES

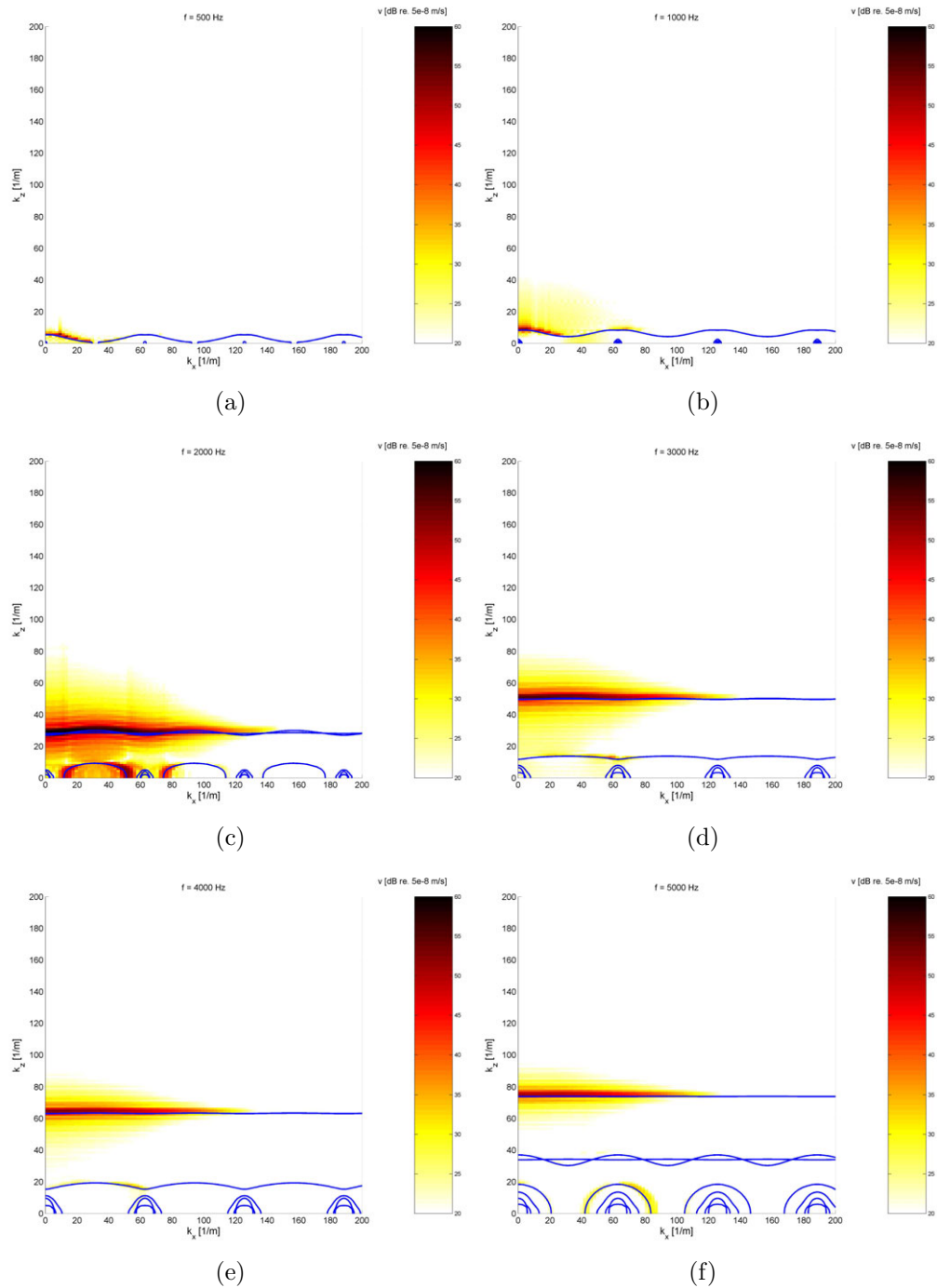
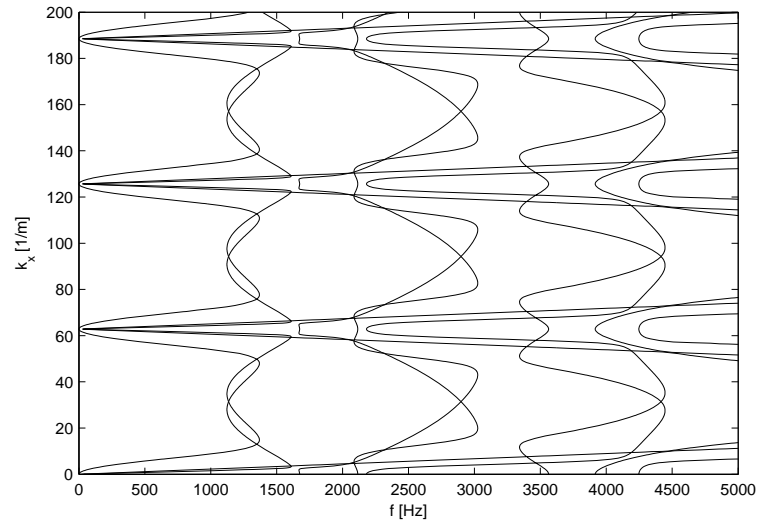


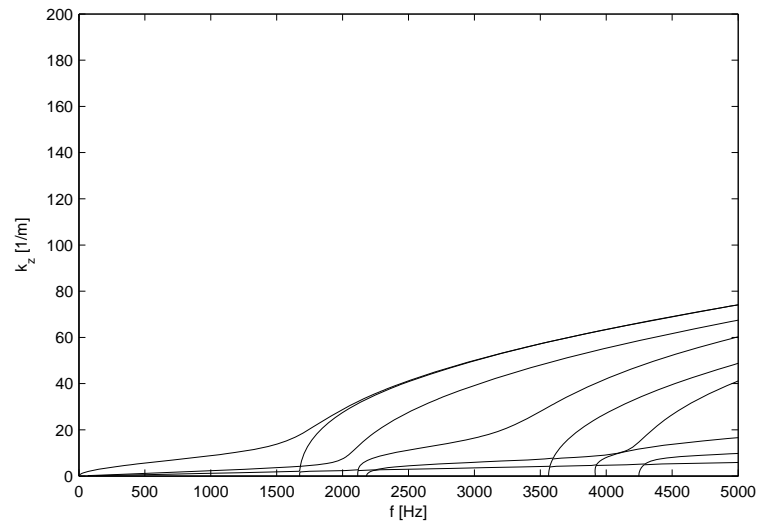
Figure 5.14: Wavenumber content of profile C for selected frequencies (DFT results using colour shading and phase constant surface results in blue)

For propagation in the x - and z -direction the frequency dependent dispersion curves extracted in Fig. 5.15 for profile A, Fig. 5.16 for profile B and Fig. 5.17 for profile C are shown. The dispersion curves for k_x agree, as expected, with the results of the two-dimensional investigation presented in chapter 3.

The two-dimensional wave propagation results corroborate the DFT results presented in Figs. 5.5 to 5.9 with much clearer pictures of the inherent possible waves. Moreover, the calculation and modelling effort is drastically reduced in comparison with the spatial Fourier transform approach as only one single periodic FE-subelement has to be modelled and calculated.

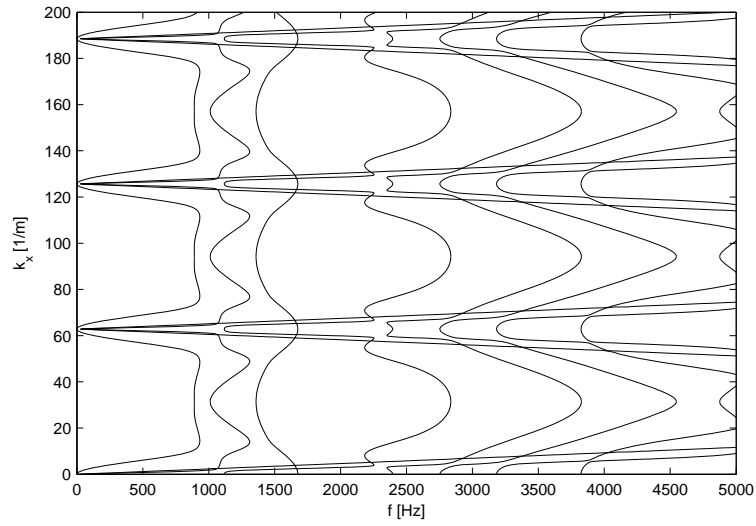


(a) k_x ($k_z = 0$)

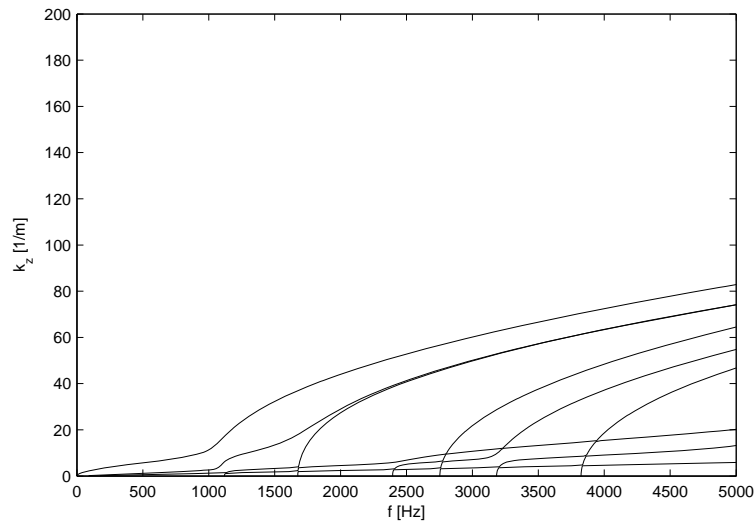


(b) k_z ($k_x = 0$)

Figure 5.15: Dispersion characteristics of profile A extracted from phase constant surfaces in x - and z -direction

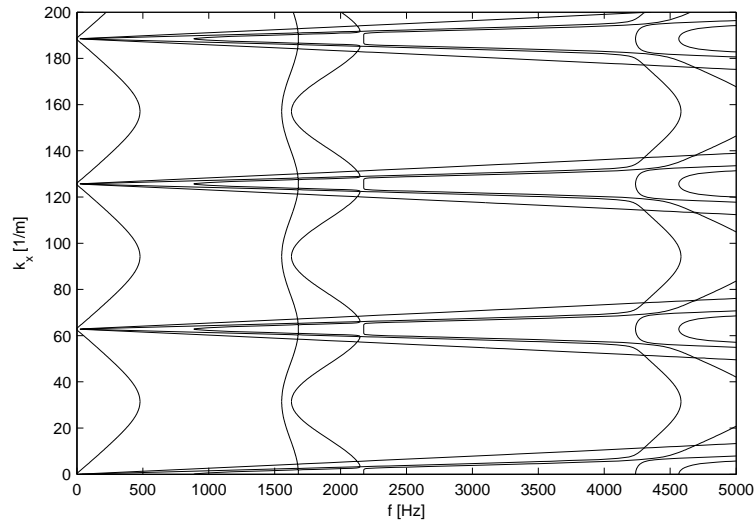


(a) k_x ($k_z = 0$)

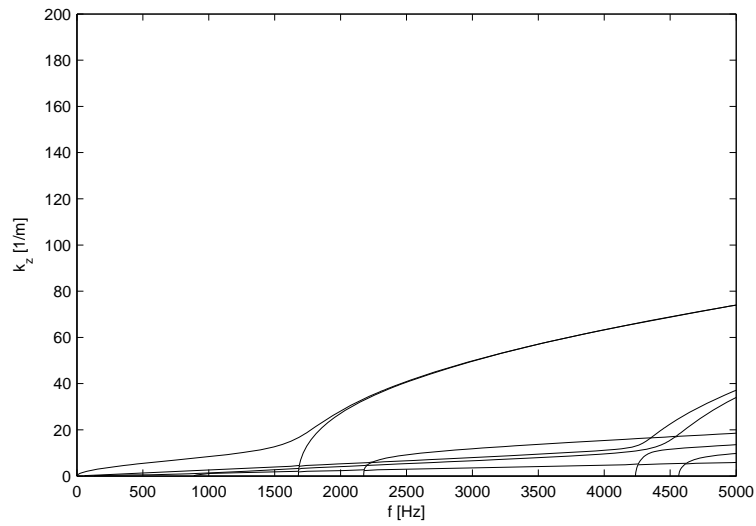


(b) k_z ($k_x = 0$)

Figure 5.16: Dispersion characteristics of profile B extracted from phase constant surfaces in x - and z -direction



(a) k_x ($k_z = 0$)



(b) k_z ($k_x = 0$)

Figure 5.17: Dispersion characteristics of profile C extracted from phase constant surfaces in x - and z -direction

5.4 Dispersion characteristics using Waveguide Finite Element technique

It is not directly possible to identify the wave shapes of the inherent waves in the profile from the full 3D-FE-calculations or the phase constant surface results. These wave shapes are useful to gain insight in the wave propagation process. Moreover, full 3D-modelling and FE-calculation of the light weight profiles is quite demanding with regard to computer resources and evaluation time. Therefore, a different approach is aimed at in order to investigate the wave propagation in the light weight profiles. In many applications, e.g. in train carriages the extension of the profiles along the carriage can be quite long, so that the structure-borne sound propagation is similar to an infinite extension in this direction whereas it is finite in the lateral direction.

The option is then to model only a cross section of the complete profile and to use Waveguide Finite Element technique for the infinite extension in the z -direction. In contrast to the spectral finite element formulation introduced by Finnveden [53], there is no need to create new element types for the calculation. Standard FE-libraries and packages can be used to create the dynamic stiffness matrix of a cross section. This greatly enhances the applicability for general use so that complex geometries can be modelled easily.

5.4.1 Theory

The waveguide FE approach models a section of the strip in z -direction by conventional FE-methods using shell elements. An example of such a strip is shown in Fig. 7.1(b).² This technique results in quite small FE-models as only a small part of a complete plate has to be modelled. For periodic strips in x -direction it is sufficient to model only one subelement (see e.g. Fig. 5.19). Extended sections in x -direction can be assembled from these subelements by using standard FE-assembling methods. In analogy to the case of multi-coupled periodic elements, it is assumed that this section is not only assembled in x -direction, but repeated in z -direction also to form an infinite plate in the latter direction (see Fig. 5.18). Now the wave propagation in the z -direction can be investigated in analogy to multi-coupled periodic systems. Defining the edges of the section in z -direction as front and back end of the periodic element and assembling the transfer matrix offers the op-

²In chapters 2 to 4 the investigated strip is similar in shape, but in that case no extension in z -direction is modelled and beam elements are used to calculate the wave propagation in x -direction only.

portunity to solve the transfer matrix eigenvalue problem directly or based on the dynamic stiffness matrix. This approach has been used for rails to predict the wave propagation along the rail by calculating a small section of the rail, see e.g. [36, 54, 55]. One problem for a complete profile strip is that a high number of coupling nodes is introduced enlarging the transfer matrix involved. In some cases the method can become unstable, but this instability can be circumvented by using appropriate FE-elements and a stable implementation to solve the eigenvalue problem. For details see e.g. [56, 57, 58]. The same technique is also used for investigations of wave propagation in ultrasonics, e.g. [59, 60].

The WFE-calculation is based on a standard FE-model of a subelement marked in black in Fig. 5.18. Using the subelement mass and stiffness matrices \mathbf{M} and \mathbf{S} , the equation of motion for harmonic excitation using time base $e^{j\omega t}$ and structural damping with loss factor η reads:

$$(-\omega^2\mathbf{M} + (1 + j\eta)\mathbf{S})\boldsymbol{\xi} = \mathbf{F} \quad (5.12)$$

The *dynamic* stiffness matrix \mathbf{K} is defined and partitioned in front (f) and back (b) degrees of freedom (DOF), see Fig5.10.³

$$\mathbf{K}\boldsymbol{\xi} = \begin{bmatrix} \mathbf{K}_{ff} & \mathbf{K}_{fb} \\ \mathbf{K}_{bf} & \mathbf{K}_{bb} \end{bmatrix} \begin{Bmatrix} \boldsymbol{\xi}_f \\ \boldsymbol{\xi}_b \end{Bmatrix} = \begin{Bmatrix} \mathbf{F}_f \\ \mathbf{F}_b \end{Bmatrix} \quad (5.13)$$

A wave basis can be established based on the solution of the eigenvalue problem of the transfer matrix \mathbf{T} , relating front and back edges of the subelement. The transfer matrix reads:

$$\mathbf{T} \begin{Bmatrix} \boldsymbol{\xi}_f \\ \mathbf{F}_f \end{Bmatrix} = \begin{Bmatrix} \boldsymbol{\xi}_b \\ -\mathbf{F}_b \end{Bmatrix} \quad (5.14)$$

The transfer matrix can be established from the partitioned dynamic stiffness matrix.

$$\mathbf{T} = \begin{bmatrix} -\mathbf{K}_{fb}^{-1}\mathbf{K}_{ff} & \mathbf{K}_{fb}^{-1} \\ -\mathbf{K}_{bf} + \mathbf{K}_{bb}\mathbf{K}_{fb}^{-1}\mathbf{K}_{ff} & -\mathbf{K}_{bb}\mathbf{K}_{fb}^{-1} \end{bmatrix} \quad (5.15)$$

Based on Bloch's theorem, relating the front and back edges of all the connected elements with a constant amplitude and phase shift λ , the eigenproblem for free wave propagation can be defined as

$$\mathbf{T} \begin{Bmatrix} \boldsymbol{\xi}_f \\ \mathbf{F}_f \end{Bmatrix} = \lambda \begin{Bmatrix} \boldsymbol{\xi}_f \\ \mathbf{F}_f \end{Bmatrix}, \quad \lambda = e^{jk_z L_e}. \quad (5.16)$$

³For the applications used here no inner DOFs are used in the subelement model so that the dynamic stiffness matrix contains only front and back DOFs. Otherwise the inner DOFs have to be condensed.

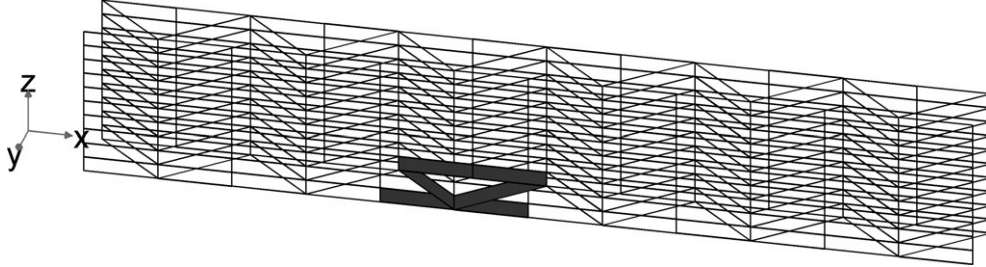


Figure 5.18: Artificial periodic subelement (marked in black) as part of a complete light weight plate

Thence, the wavenumber k_z can be related directly to the eigenvalues λ with the periodic length L_e in z -direction. In undamped systems the waves are either purely propagating ($|\lambda| = 1$), decaying ($Im(\lambda) = 0$), or complex for all remaining λ . Though the mathematical solution is ambiguous with a periodicity of $2\pi/L_e$ for the real part of the wavenumber, a distinct identification, in this case in z -direction, is possible in contrast to most typical periodic systems. Assuring a high wavenumber periodicity length by selecting a very small periodic length L_e , the solution for lowest wavenumbers gives the physical results. For accurate results, the periodic length has to be much smaller than any occurring physical wavelength, $k_z L_e < 1$. This criterion is in accordance with standard FE-modelling guidelines where six elements per wavelength is a common rule of the thumb. As pointed out by Mead in [61] a selection of a small L_e increases the accuracy without increasing calculation time as the dimensions of the eigenproblem to solve are independent of this choice. This is illustrated also in the dispersion results of Fig. 5.29 and implies a significant advantage over standard FE-modeling techniques.⁴

The wave basis is constituted by the pairs of negative and positive travelling waves with eigenvalues λ_i and corresponding right eigenvectors as defined in Eq. (5.16), $\phi_i = [\xi_{f,i} \mathbf{F}_{f,i}]^T$, which define the wave shapes. These wave vectors can be assembled in an eigenvector matrix Φ .

5.4.2 Wave propagation in single subelement profiles

To gain insight in the principal wave propagation features of the generic light weight profiles the different subelements are investigated with free boundary conditions at left and right edge at first, forming profiles of single subelements in x -direction.

⁴The selection of a small L_e is bounded by numerical issues, resulting e.g. from round-off errors in the corresponding matrices for very small elements. [58]

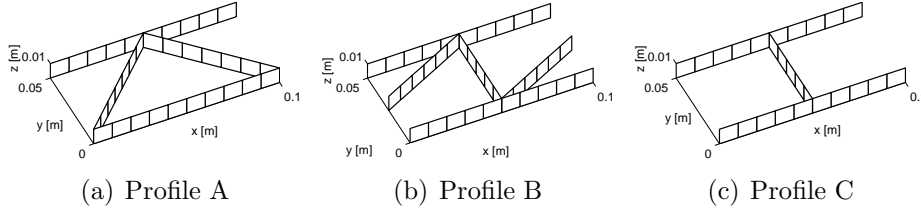


Figure 5.19: FE-models of subelements A-C, 10 mm element length

The dispersion characteristics of the three configurations are extracted from the FE-models shown in Fig. 5.19, using shell elements with an element length of 10 mm. Material parameters are listed in Tab. 5.1.

All six degrees of freedom at each node including the in-plane rotations are used in the extraction procedure.⁵

The propagating waves are identified by using a limit for λ , typically $0.99 < |\lambda| \leq 1$. The real part of these wavenumbers is plotted in Fig. 5.20 for subelements A-C.

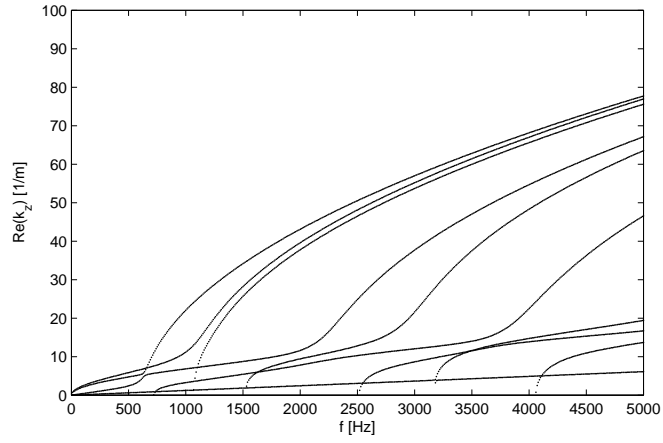
In the low frequency regime up to about 600 Hz for profile A global waves with wavenumber up to 8 m^{-1} are present. A typical wave shape is shown for profile A in Fig. 5.21(a) for 500 Hz. For higher frequencies wave propagation in the member plates cuts on and wave shapes with these local vibration patterns are shown for 2000 and 5000 Hz. The shading indicates the displacement in y -direction.

For profile B local wave propagation starts already at 300 Hz. This is related to the special layout of the subelement with three free plate edges on both lateral edges. The corresponding wave shapes are plotted in Fig. 5.22.

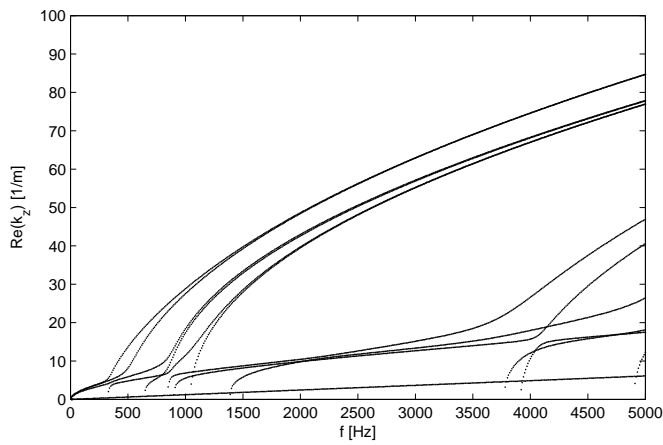
For profile C some characteristic waves are shown in Fig. 5.23. The wavenumber content comprises less branches which can be explained by four similar plate fields concentrating to the same bending wavenumbers.

All the profiles show a global bending branch exceeding the low frequency range and the non-dispersive longitudinal wave branch with low wavenumbers, reaching a wavenumber of about 7 m^{-1} at 5000 Hz.

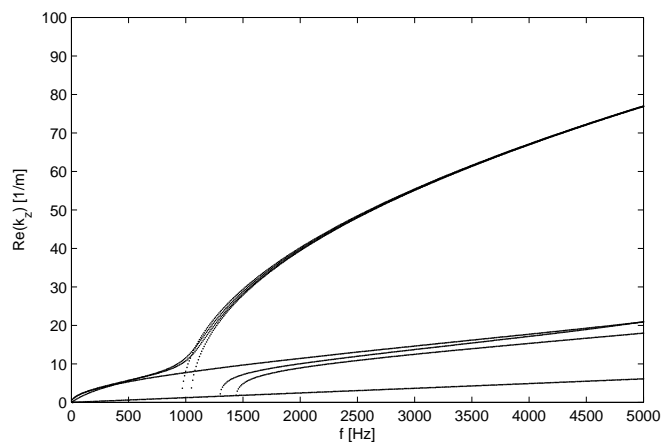
⁵CQUADR shell elements are used for a stable wavenumber extraction. In contrast to the CQUAD4 elements, these elements include the in-plane rotational DOF. This is important to get the waves in the diagonal stiffeners correctly, where a portion is in-plane also. [62]



(a) Profile A: wavenumber content



(b) Profile B: wavenumber content



(c) Profile C: wavenumber content

Figure 5.20: Wavenumbers of single subelement in z -direction (0.1 m width)

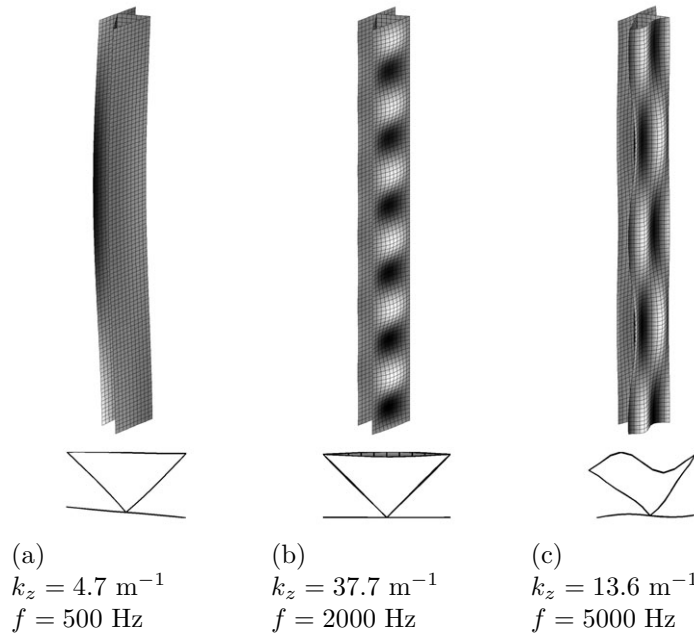


Figure 5.21: Selected wave shapes of single subelement profile A. Cross sectional plots (x - y) are included at the bottom for $z = 0$.

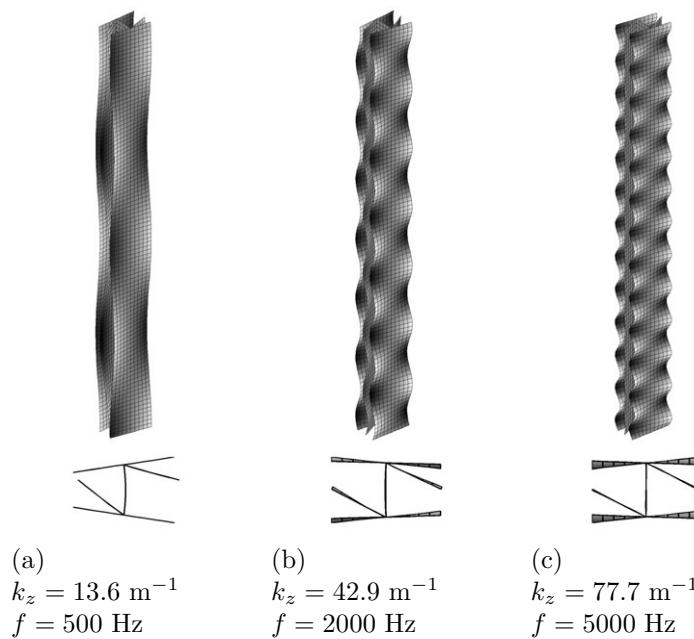


Figure 5.22: Selected wave shapes of single subelement profile B. Cross sectional plots (x - y) are included at the bottom for $z = 0$.

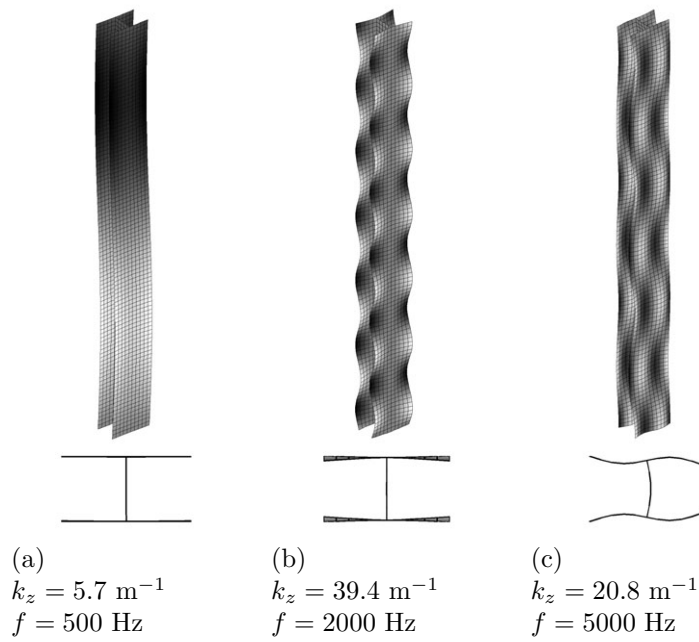


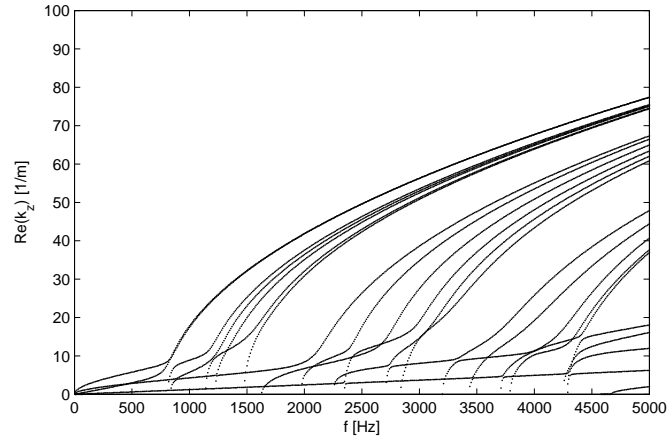
Figure 5.23: Selected wave shapes of single subelement profile C. Cross sectional plots (x - y) are included at the bottom for $z = 0$.

5.4.3 Wave propagation in multiple subelement profiles

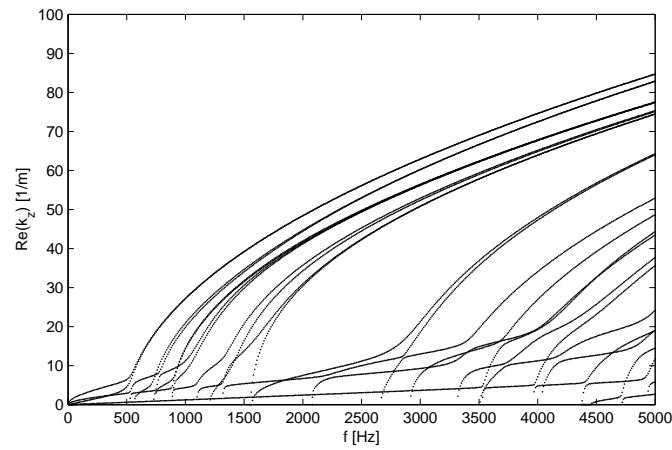
The dispersion investigation of a single free subelement profile is not representative for industrial applications where a full plate consists of several adjacent subelements. Hence, it is necessary to investigate the influence of building a complete profile of the subelements. In order to get an idea of the general trends, calculations with three and five subelements side by side are performed. The resulting dispersion characteristics for three and five subelements are shown in Figs. 5.24 and 5.25 respectively.

Comparing the dispersion plots for one, three and five subelements, it is obvious that the number of propagating waves increases with the plate width. Despite the diversity of waves it is possible to distinguish different local wave groups that can be found in the dispersion plots irrespective of plate width. Exemplified for profile A the following observations can be made:

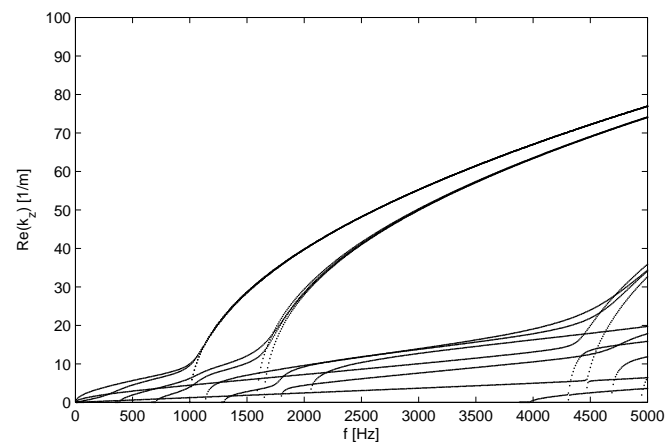
- The dispersion curve with the highest wavenumber is related to edge waves of the cantilevered sections. Because of the free edges these are the first local waves to cut on (see Fig. 5.26(a)).
- The second group is related to waves comprising first order mode shapes of the plate strip members. For the waves with the highest wavenumbers in this group, adjacent plate strips vibrate in anti-phase (simply supported mode shape, Fig. 5.26(b)), whereas for the lower wavenumbers they vibrate in-phase (clamped mode shape, Fig. 5.26(c)). This behaviour is similar to the characteristic wave shapes of a simply supported periodic beam [33, p. 186]. For a fixed wavenumber the region between these extremes can be regarded as a wave pass-band with the bounding frequencies of the plate strip with either simply supported or fixed edges.
- The third group ($k = 60 - 67 \text{ m}^{-1}$ for 5000 Hz) is dominated by vibrations of the intermediate inclined webs in the first cross mode (see Fig. 5.26(d)).
- The fourth group ($k = 35 - 48 \text{ m}^{-1}$ for 5000 Hz) is characterized by second order cross modes of the outer plate strips. Again the high wavenumber limit of this group corresponds to simply supported vibrations of the members (Fig. 5.26(e)) and the lower edge is related to clamped motion, not shown for the sake of brevity.



(a) Profile A: wavenumber content

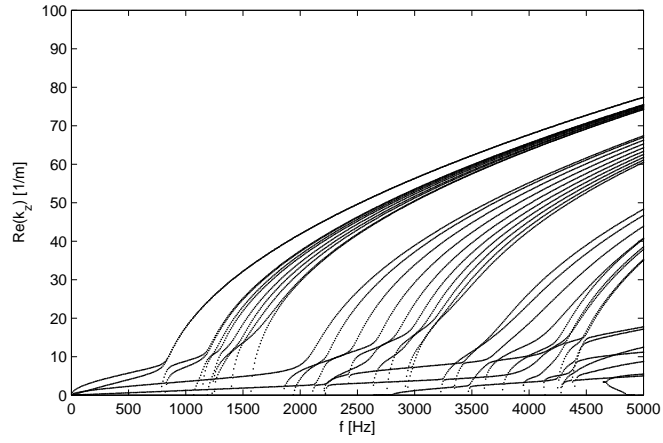


(b) Profile B: wavenumber content

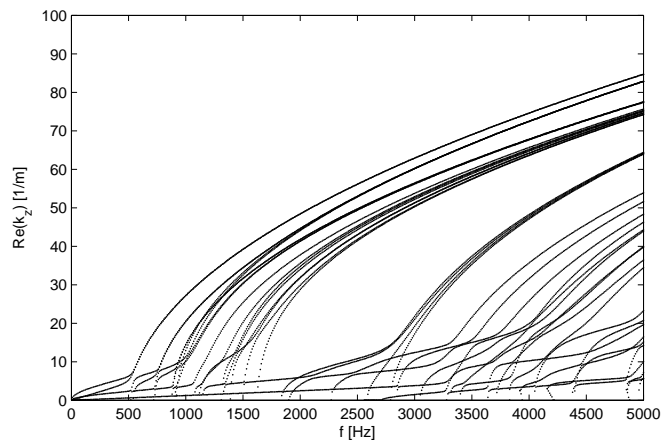


(c) Profile C: wavenumber content

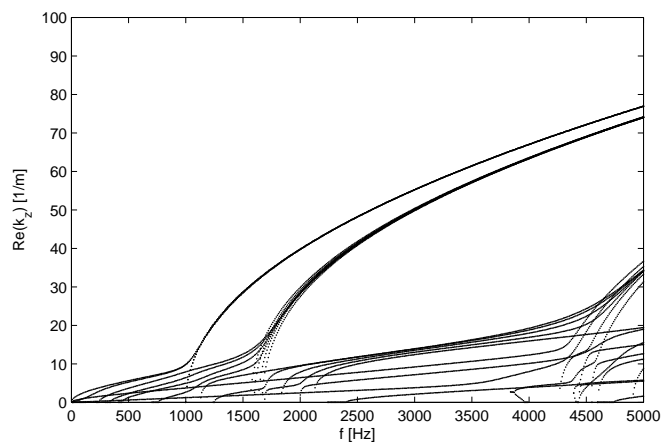
Figure 5.24: Wavenumbers in z -direction of three subelements (0.3 m width)



(a) Profile A: wavenumber content



(b) Profile B: wavenumber content



(c) Profile C: wavenumber content

Figure 5.25: Wavenumbers in z -direction of five subelements (0.5 m width)

- In the low wavenumber range ($k = 5 - 17 \text{ m}^{-1}$ for 5000 Hz) the waves comprise mainly rotational behaviour at the joints (Fig. 5.26(f)).
- Oblique directional wave propagation can be observed for the upper edges of the wave groups (Fig. 5.26(b) and (e)).

Similar observations for infinite periodically-stiffened plates are reported by Mace in [63], where the bounding frequencies of the propagation zones are shown to be linked to distinct propagation constants of $\mu = 0$ and $\mu = \pi$ in the lateral direction (in-phase and out-of phase motion of adjacent bays). Similar wave groups for extruded profile floor sections are also identified from spectral finite element investigations [64], but are not linked to the investigated strip width.

The general observation of wave groups holds also for profile B. An example of a low frequency global bending wave is shown in Fig. 5.27(a). Some selected mode shapes for higher frequencies are shown and support the general trends observed for profile A.

The wave groups for profile C are even clearer as the coupling between different wave types is more distinct than for profiles with inclined webs due to the right-angled web connections. Some typical wave shapes are plotted in Fig. 5.28. Global wave motion as shown in Fig. 5.28(a) in the lateral direction is characterized by significantly smaller wavelengths for a profile without inclined webs (see chapter 3). This is related to an increased number of global waves cutting on in the low frequency regime already for a plate width of 0.5 m. The local waves show similar trends as described previously for profile A.

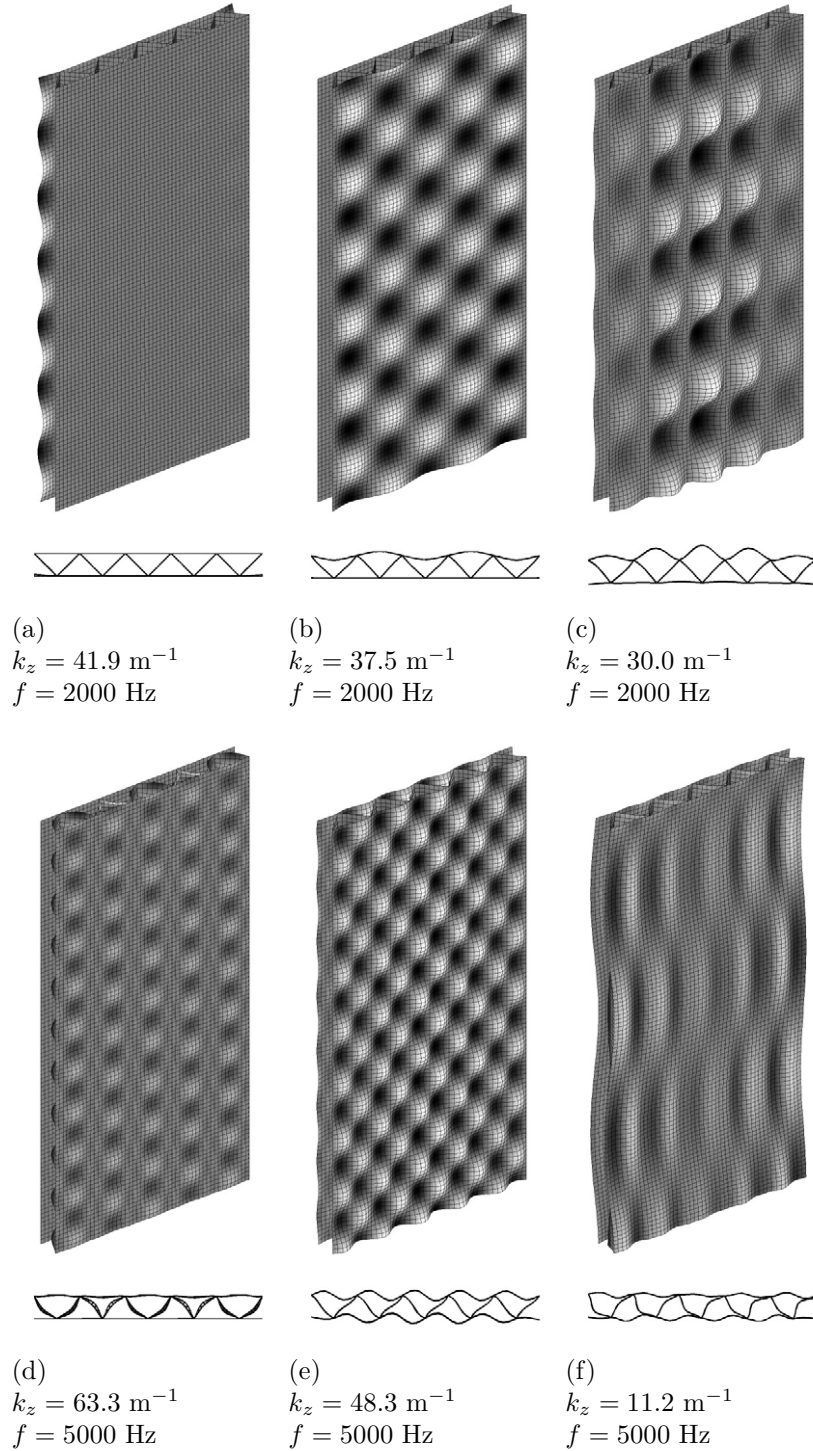


Figure 5.26: Selected wave shapes for profile A (0.5 m width). Cross sectional plots (x - y) are included at the bottom for $z = 0$.

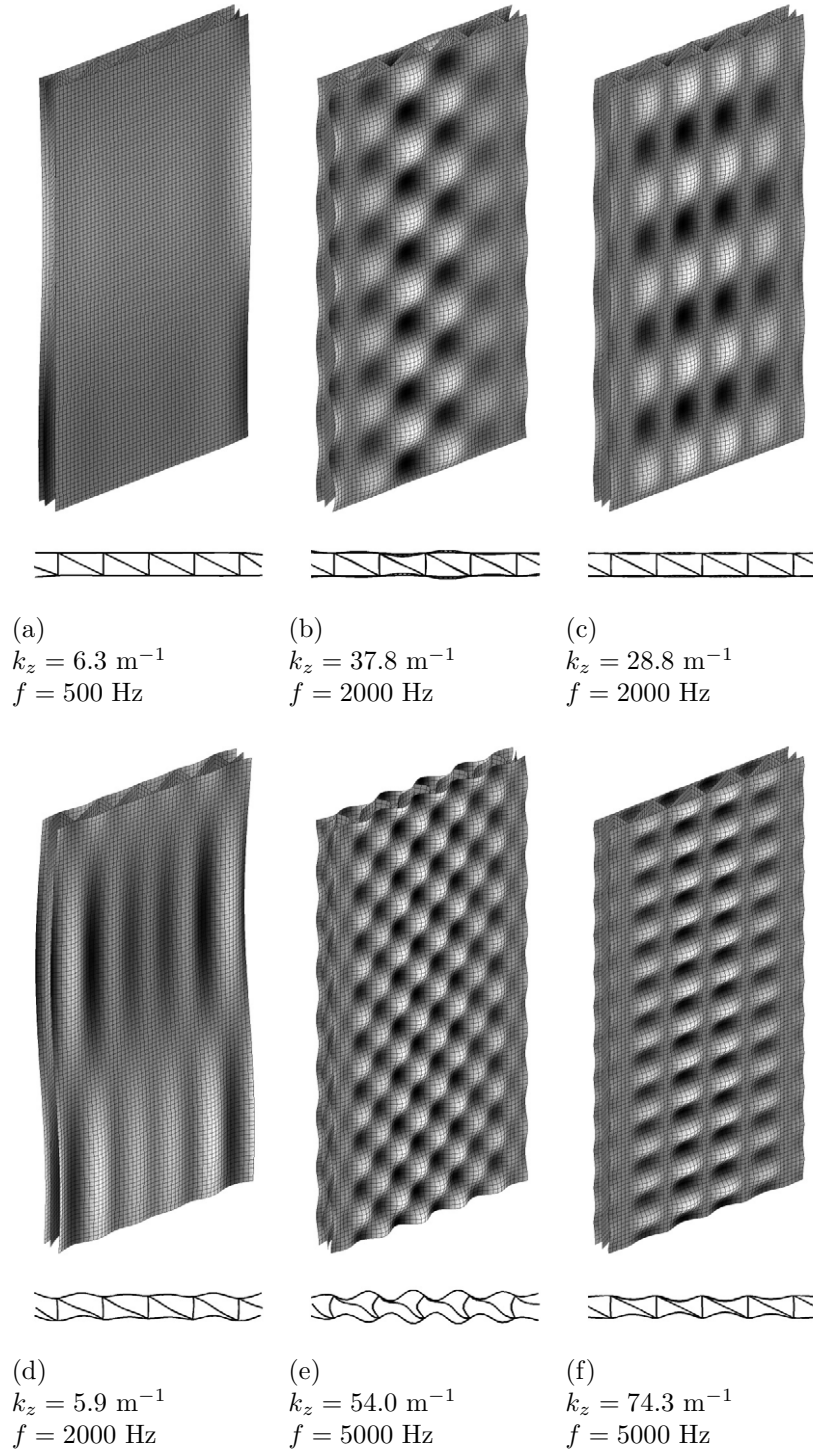


Figure 5.27: Selected wave shapes for profile B (0.5 m width). Cross sectional plots (x - y) are included at the bottom for $z = 0$.

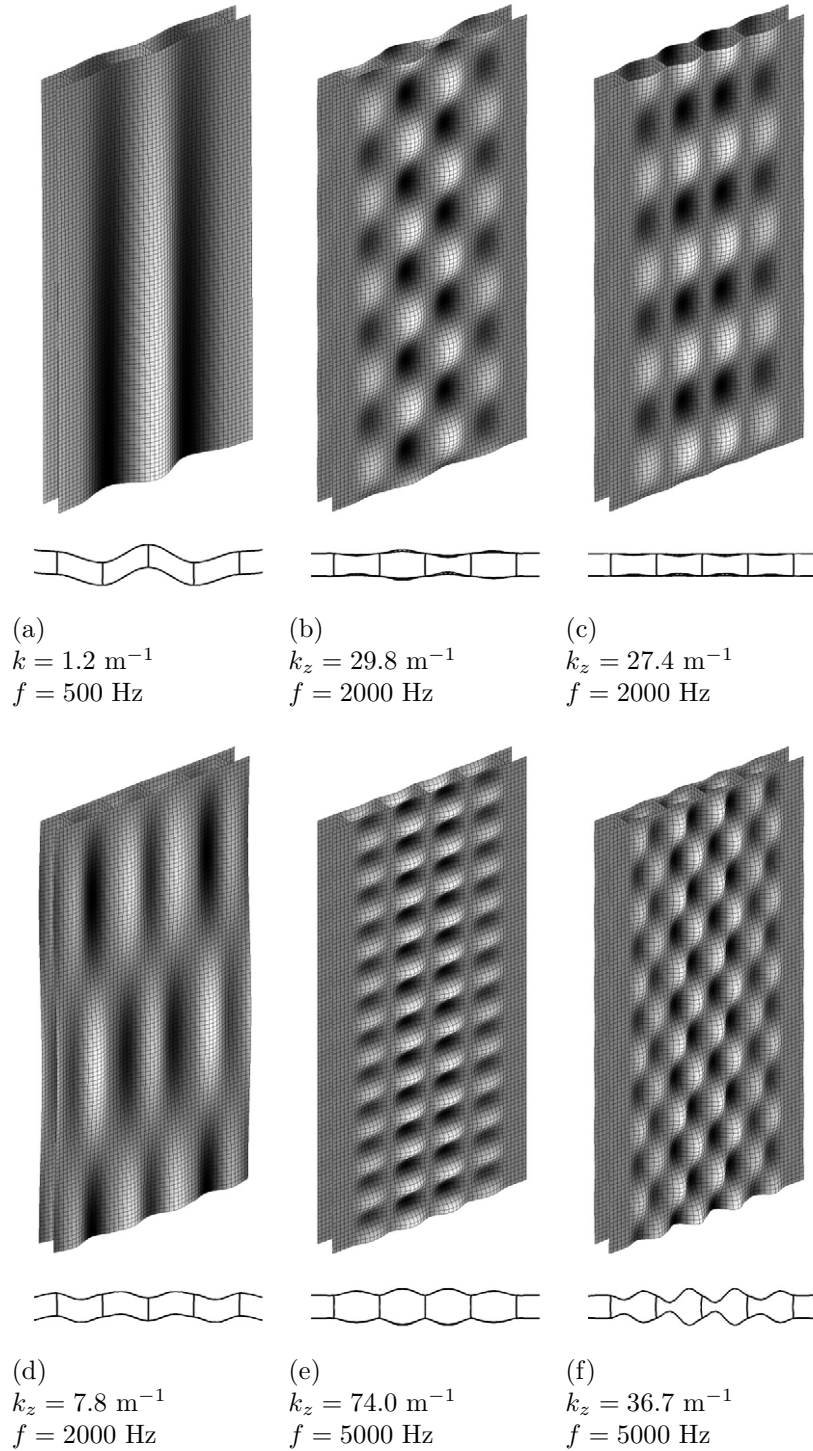


Figure 5.28: Selected wave shapes for profile C (0.5 m width). Cross sectional plots (x - y) are included at the bottom for $z = 0$.

5.4.4 Influence of dynamic reduction on dispersion characteristics

Calculation time and memory usage grows rapidly for increased number of elements in x -direction. This limits the application on standard personal computers currently, but no limitations are identified in principle for application to realistic plate width. Reduction techniques as described in section 6.5 or mesh coarsening are applied, but failed for the extraction of dispersion characteristics of high accuracy when compared to the full solution, especially in the high frequency regime. Dispersion results for a single subelement and different mesh sizes are shown in Fig. 5.29. The coarse mesh with 25 mm edge lengths of the quadratic shell elements cannot capture the wave propagation mechanisms for frequencies higher than 100 Hz. Significant reduction of the calculation effort without drastic reduction of accuracy can be achieved by keeping the coarse mesh length in the lateral direction of the cross section, but reducing the element length in z -direction to 5 mm. In this case deviations are acceptable up to about 3000 Hz without an increase in the calculation effort. This insight is of major importance for practical applications of the method and underlines the suggestions of Mead in [61] to use a small periodic length L_e .

The influence of Guyan reduction using all massless DOFs (see section 6.5) on dispersion characteristics is illustrated in Fig. 5.30. It is obvious that the static reduction technique in this case fails to represent the propagating waves with wavenumbers higher than 15 m^{-1} accurately. In the global regime up to 500 Hz the Guyan reduction is more reliable than mesh coarsening.

The comparison of fine and coarse mesh or full and reduced model dispersion curves can serve as a means to identify the frequency / wavenumber limit for the applied reduction to cover the salient physics.

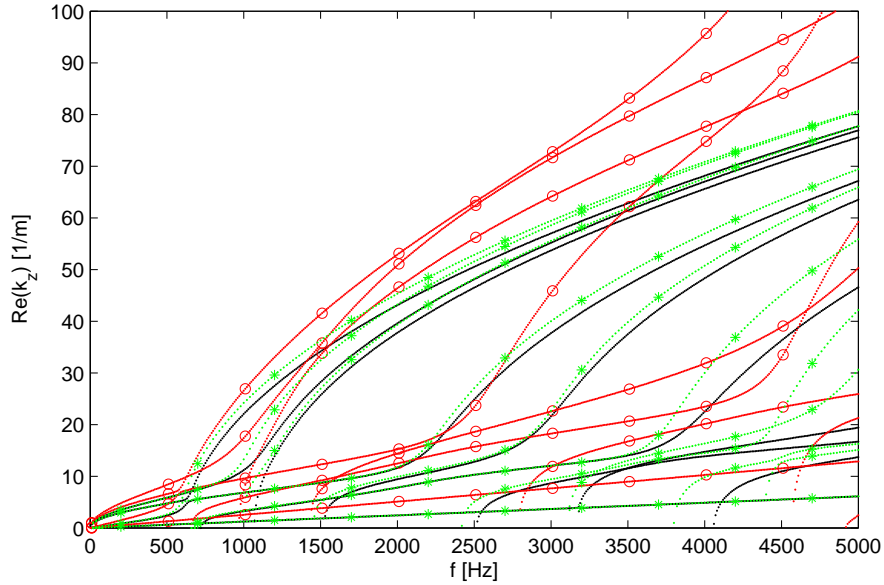


Figure 5.29: Influence of mesh size and periodic length L_e on evaluated dispersion characteristics of profile A, single subelement in x -direction. Black, no markers: $10\text{ mm} \times 10\text{ mm}$; Red, o: $25\text{ mm} \times 25\text{ mm}$; Green, *: $25\text{ mm} \times 5\text{ mm}$

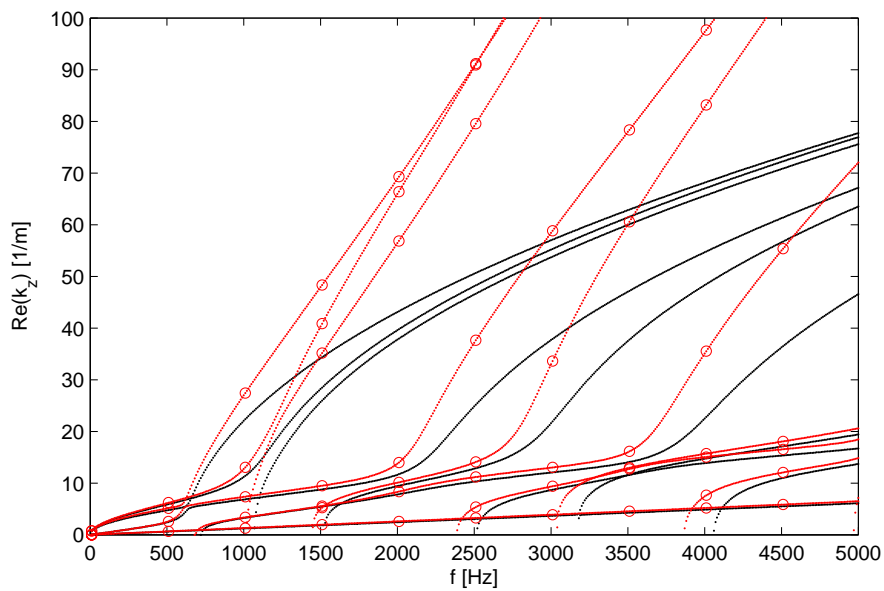


Figure 5.30: Influence of Guyan reduction with all massless DOFs on evaluated dispersion characteristics of profile A, single subelement in x -direction. Black, no markers: full calculation ($10\text{ mm} \times 10\text{ mm}$); Red, o: Guyan reduction ($10\text{ mm} \times 10\text{ mm}$)

5.5 Concluding remarks

The dispersion characteristics of light weight plates with truss-like core geometries demonstrates that wave beaming is not only limited to structures with periodicity in both directions, but also occurring for structures comprising periodicity only in one direction. The strong periodic effects identified from the two-dimensional investigation in the preceding chapters are retrieved in the three-dimensional plate investigation in the corresponding periodic direction. In contrast to the strip investigation, where power transmission and wave propagation is nearly completely abandoned in the stop-bands, the effect is reduced for the plates investigated. In the lateral stop-bands wave propagation in z -direction is still enabled and wave spreading in oblique directions depends on the geometric profile layout, which influences the coupling mechanisms and wave conversions at the joints. For profiles with inclined webs distinct wave beaming in oblique directions arises, whereas for a profile with straight webs lateral coupling and oblique propagation is reduced. In a way the frequency dependent stop-band behaviour for one-dimensional wave propagation is transformed in a frequency dependent and spatially varying attenuation for the two-dimensional propagation case, resulting in low vibration regions for point excited structures. The weakened stop-band effect makes general applications for noise control somewhat delicate. In special situations where low vibration is requested especially in certain regions, e.g. for installation of vibrational sensitive equipment, this strong wave beaming might be exploited. Moreover, design of damping treatments can be optimized, at least for point excited structures, by exploiting the wave beaming effects and aligning the damping treatments in the beaming directions from the point of excitation.

From a structural acoustic point of view it is vital to differentiate between subsonic and supersonic waves in the light weight plates. The dispersion characteristics presented in this chapter establish a basis for their discrimination. Only the supersonic waves can couple efficiently to the ambient fluid which is of major importance for radiation and transmission investigations. For proper acoustic design it could be valuable to investigate where major structural wave components become supersonic. In this respect the significant components of the space harmonic series have to be included as it seems to be possible that lower supersonic orders play a dominant role for radiation and transmission.

Chapter 6

Forced response of light weight profile plates

6.1 Introduction

The free wave propagation investigated in the preceding chapter forms the basis for forced response calculations in this chapter. The calculations are founded on the waveguide finite element (WFE) method. For structure-borne sound problems where the structure-borne input power from source to the receiving structure is imparted through contacts, which are smaller than the governing wavelengths, the connections can be treated as point contacts. This point force excitation is investigated in this chapter and a benchmark of the WFE forced response with standard FE results is performed with a section of a light weight plate. The calculation effort can be decreased by the application of reduction methods like the Guyan reduction. The influence of such reductions on input and transfer mobilities is investigated.

6.2 Theory

Forced response calculations for light weight plates of finite width can be performed using the wave basis extracted as outlined in chapter 5 for the WFE. For finite systems a global dynamic stiffness matrix containing the DOFs at the front and back ends can be defined and solved as shown in [40]. For infinite waveguide systems, which are treated in this work, the forced response can be calculated as outlined in [36]. For the systems investigated here it is favourable from a computational point of view to include only the most important (propagating) waves in the forced response calculations. The eigenvalue problem can then be solved only for propagating and slightly

decaying waves as discussed in [65].

The wave amplitude vector \mathbf{R} of the forward (positive z -direction) travelling waves can be calculated with the reduced wave basis for an infinite waveguide system by

$$\mathbf{R} = -\Psi_{\xi}^{+} \mathbf{F}_0 \quad (6.1)$$

\mathbf{F}_0 is the external force/moment excitation vector in the slice of excitation, Ψ_{ξ}^{+} is the matrix containing the displacement components for forward travelling waves ($|\lambda_i| < 1$) of the **left** eigenvector matrix Ψ . The individual left eigenvectors can be deduced from the right displacement eigenvectors by

$$\psi_i = \frac{1}{d_i} [\phi(1/\lambda_i)_{\xi,i}^T (\mathbf{K}_{bb} + \lambda_i \mathbf{K}_{fb}) \quad \phi(1/\lambda_i)_{\xi,i}^T] \quad (6.2)$$

The eigenvectors are normalized in Eq. (6.2) with d_i which is defined as $d_i = \psi_i \phi_i$.

Summing up the contributions of all characteristic waves gives the displacement results at the excitation slice. The response along the chain of elements can then be calculated from the wave amplitudes at the excitation position [40].

6.3 Numerical results

Forced response calculations are performed with the theory summarized in the preceding section. In order to benchmark the method and the implementation, a comparison with standard FE-calculated results is performed. The infinite extension in z -direction is approximated by a section of 2 m in the standard FE-calculation with increasing loss factor in z -direction at the edge ($\eta = 0.05 \dots 0.1$). This non-reflecting boundary is not assumed to be perfect, but will show the general trends. A real infinite extension in z -direction is not feasible in standard FE-calculations and a bigger extension in z -direction would increase calculation time prohibitively. Shell element edge length in the standard FE-calculation is 10 mm. In order to investigate the influence of mesh coarsening on forced response results, the calculation is performed additionally with an element size of 25 mm instead of 10 mm. The 10 mm WFE model and the full standard FE-model are plotted in Fig. 6.1.

Benchmark results for the comparison of standard FE-result and WFE-result are shown for the point of excitation and some selected points along the extension in z -direction in Figs. 6.2 to 6.7. Additional transfer mobility

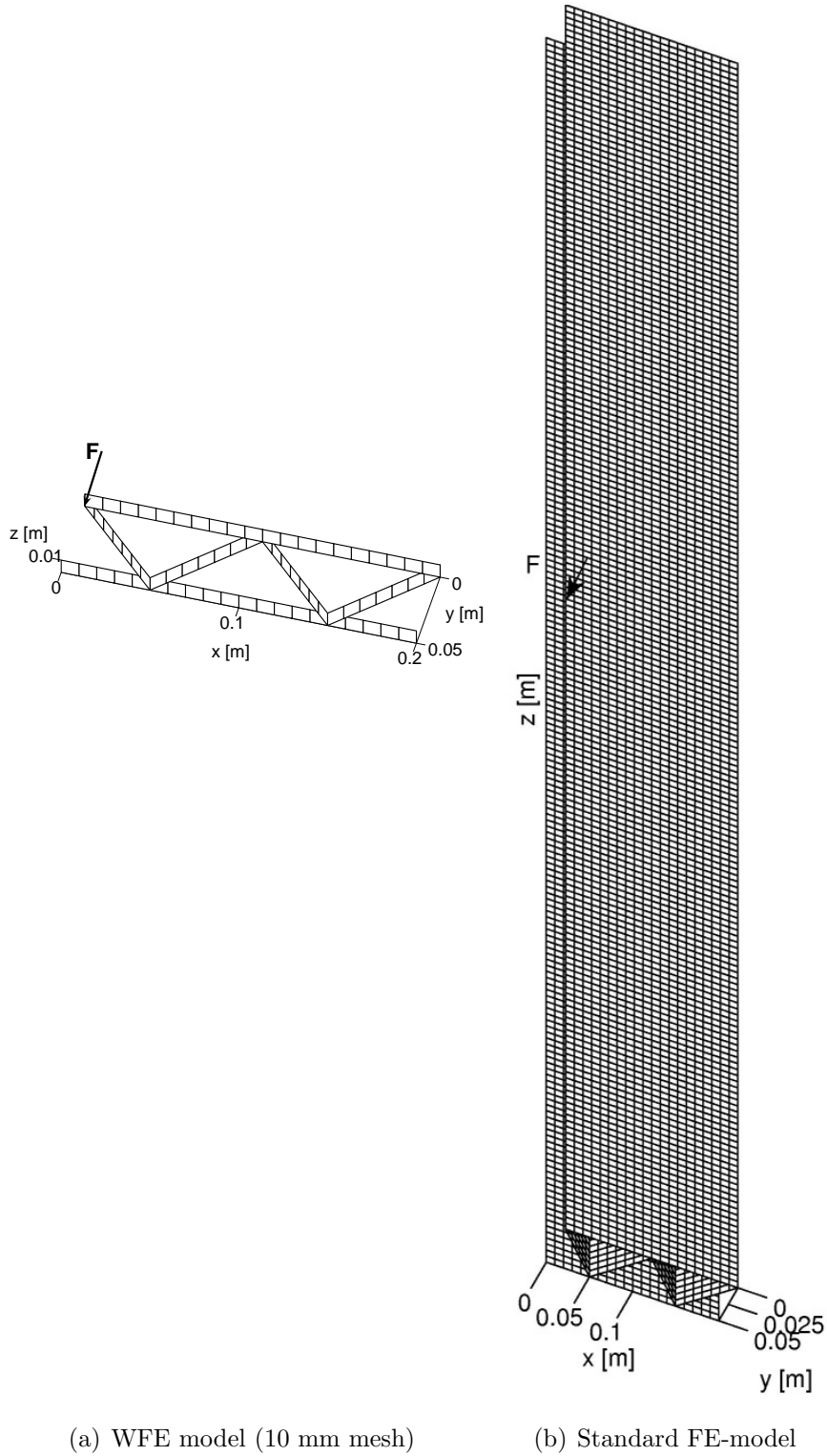


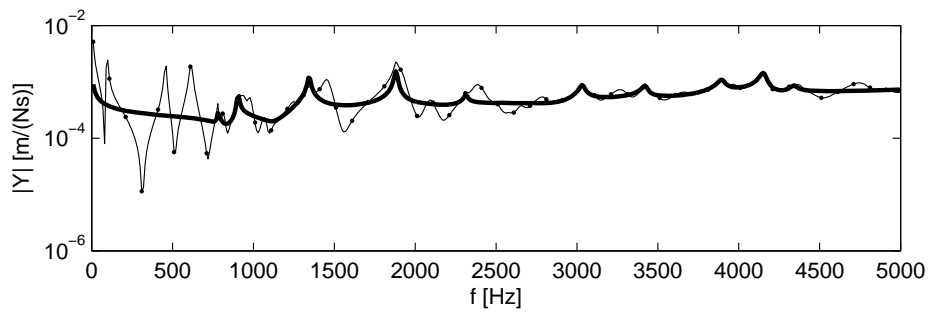
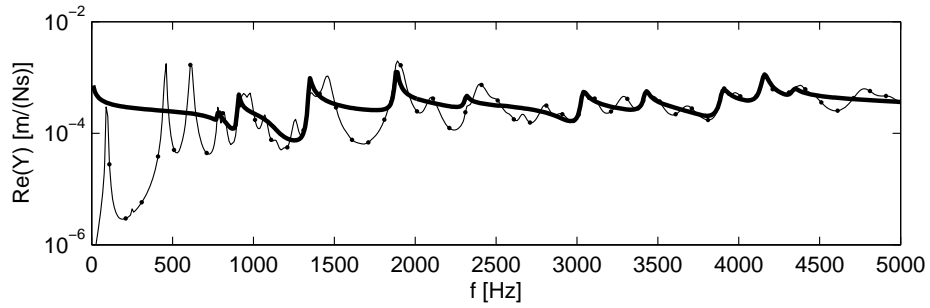
Figure 6.1: Models for forced response calculations

results are included in appendix D. The influence of mesh size is illustrated for the input mobility in Figs. 6.5 to 6.7.

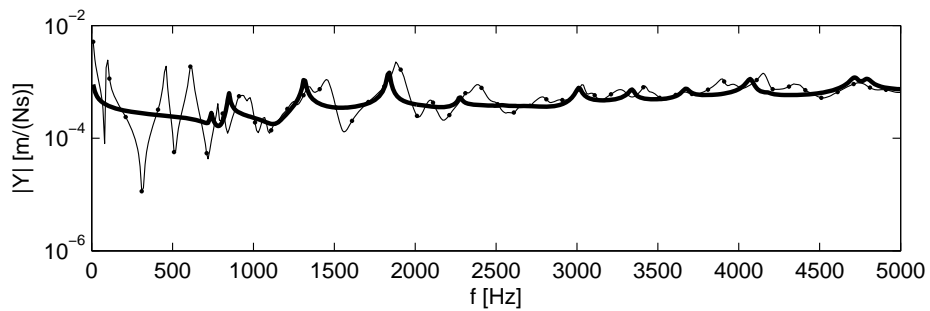
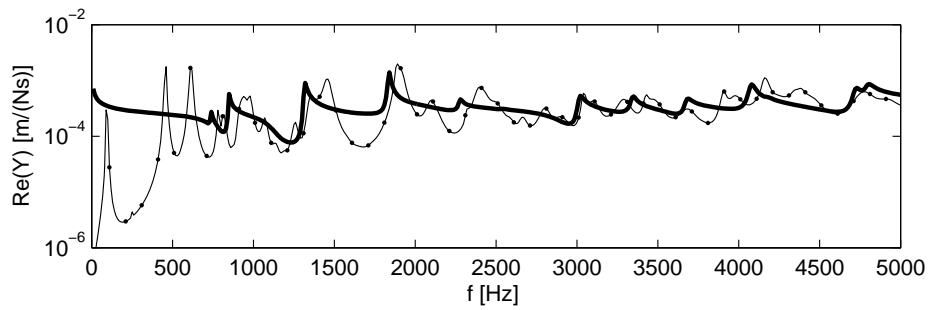
It is obvious that the course mesh does not give accurate results at frequencies higher than 2000 Hz. For lower frequencies, the differences are not very significant, but a slight frequency shift to lower frequencies can be observed for the coarse mesh.

The differences between standard FE-calculation and the WFE-calculation using the fine mesh reduce with increasing frequency. This is expected as the simulated non-reflective boundaries are not efficient at low frequencies where the damped section is far too small. Hence, reflections leading to additional resonances are expected.

The results demonstrate the applicability and reliability of the WFE-calculations for forced response. Tendencies for general structural-acoustic design of the profiles are emphasized in the mobility results, which are irrespective of the profile length. This is due to the fact that the mean, infinite behaviour is gained in z -direction, where probably misleading effects of resonances in this direction are suppressed.



(a) 10 mm mesh



(b) 25 mm mesh

Figure 6.2: Input mobility profile A, two subelements, free boundary: Standard FE-results -●- in comparison to WFE-results -(bold) for two mesh sizes

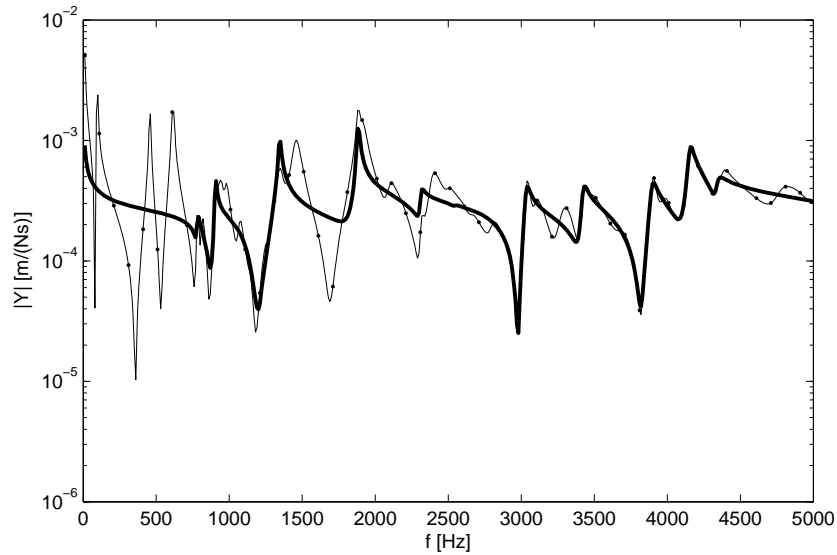


Figure 6.3: Transfer mobility profile A, two subelements, free boundary, 10 mm mesh: Standard FE-results -●- in comparison to WFE-results -(bold) (Resp. at $x=0, y=0, z=0.1$ m)

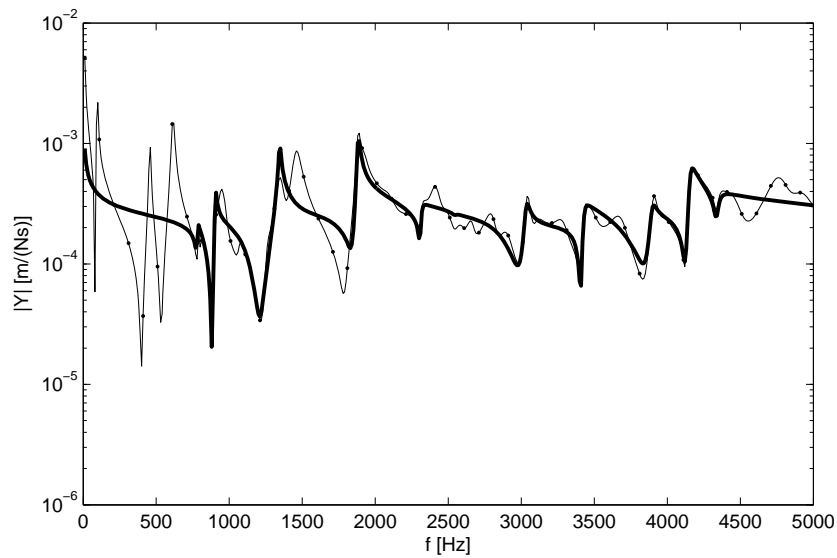
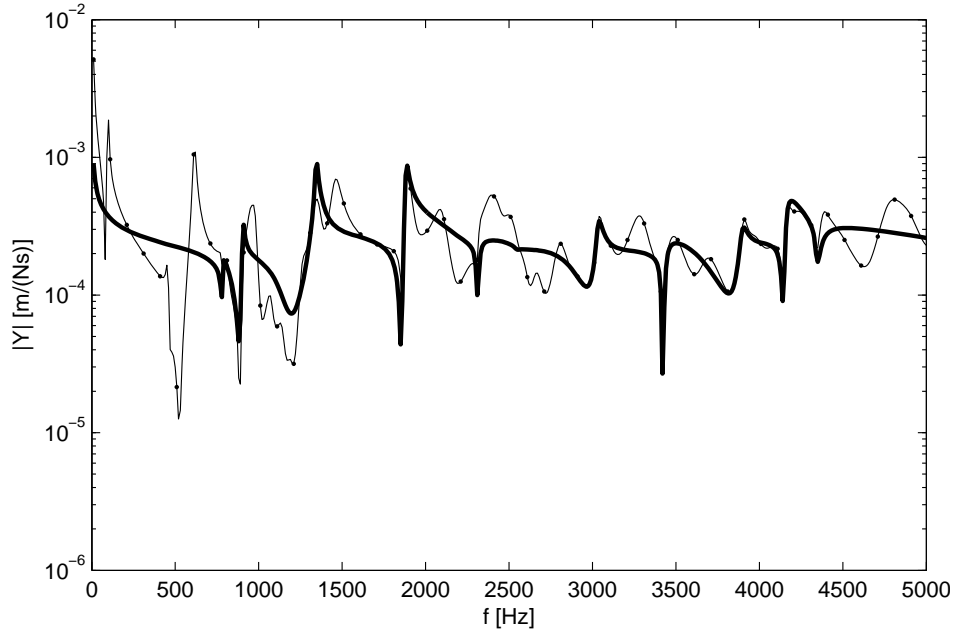
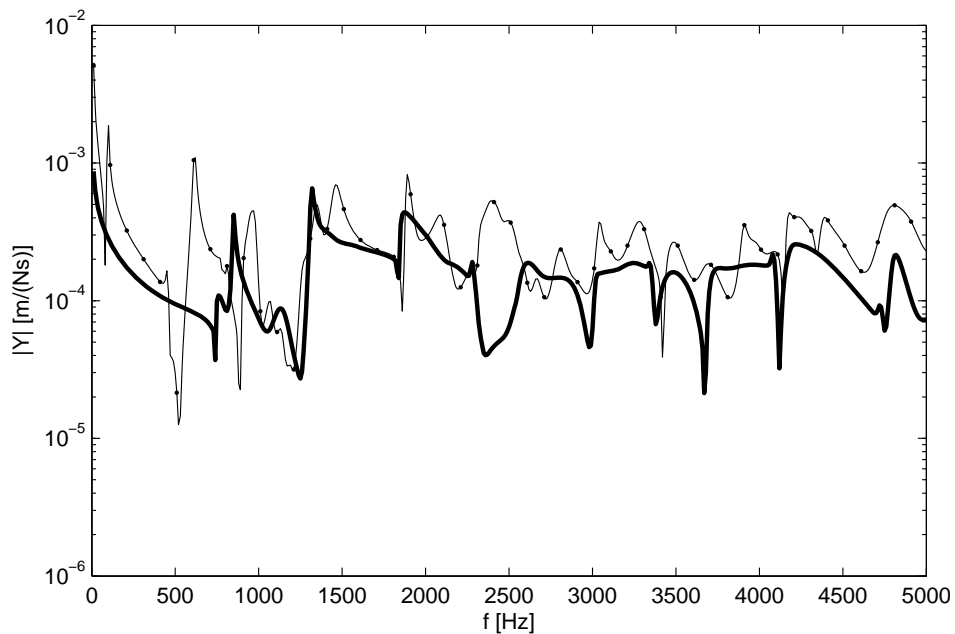


Figure 6.4: Transfer mobility profile A, two subelements, free boundary, 10 mm mesh: Standard FE-results -●- in comparison to WFE-results -(bold) (Resp. at $x=0, y=0, z=0.2$ m)

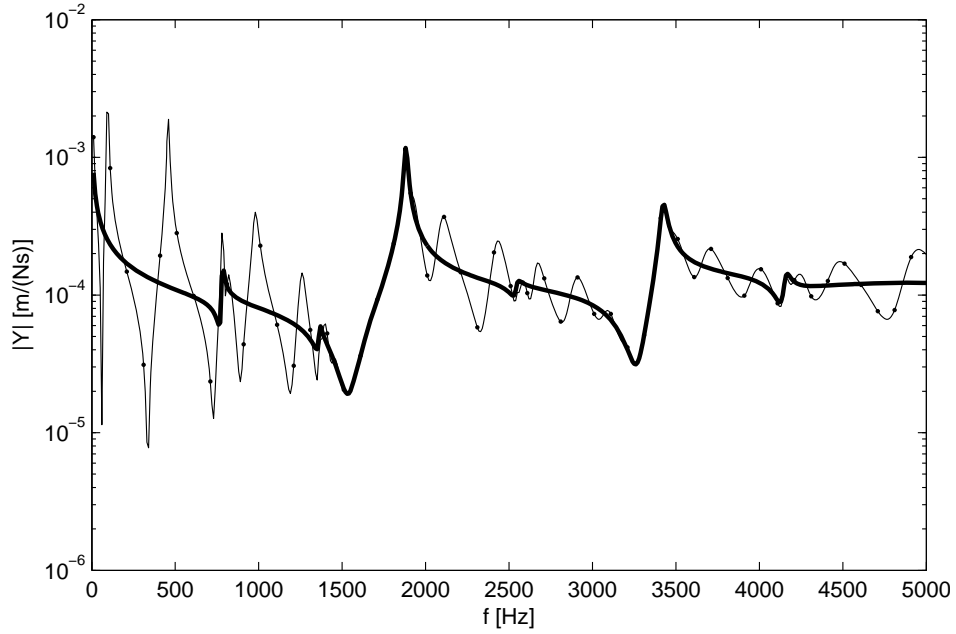


(a) 10 mm mesh

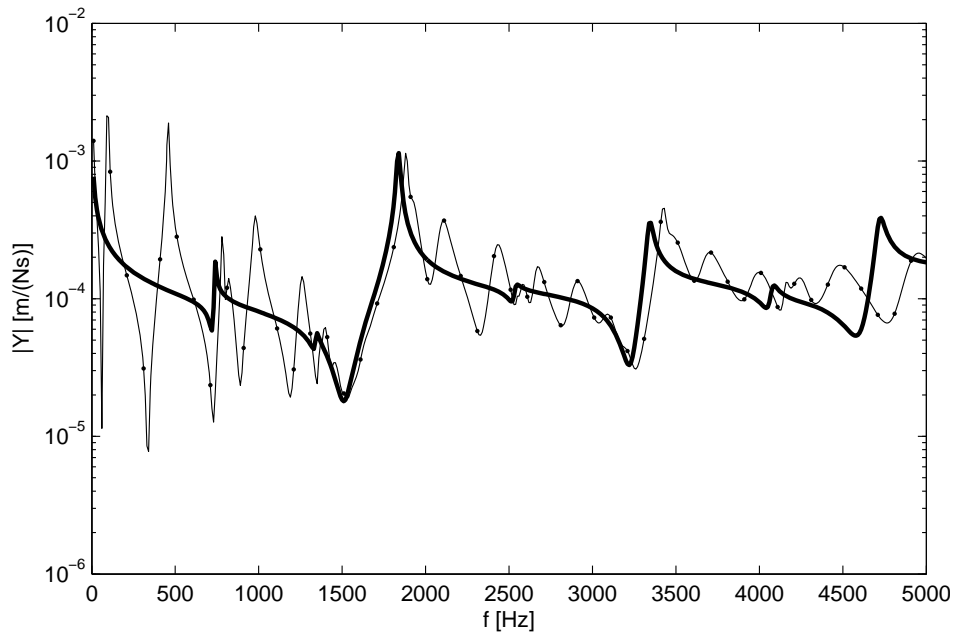


(b) 25 mm mesh

Figure 6.5: Transfer mobility profile A, two subelements, free boundary: Standard FE-results $-\bullet-$ in comparison to WFE-results $-(\text{bold})$ (Resp. at $x=0, y=0, z=0.3$ m) for two mesh sizes

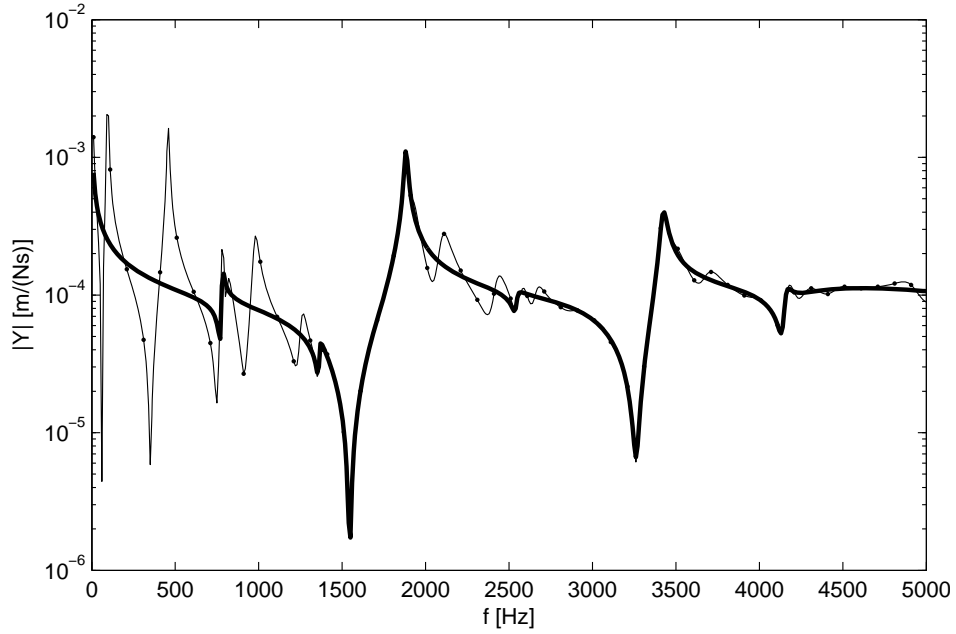


(a) 10 mm mesh

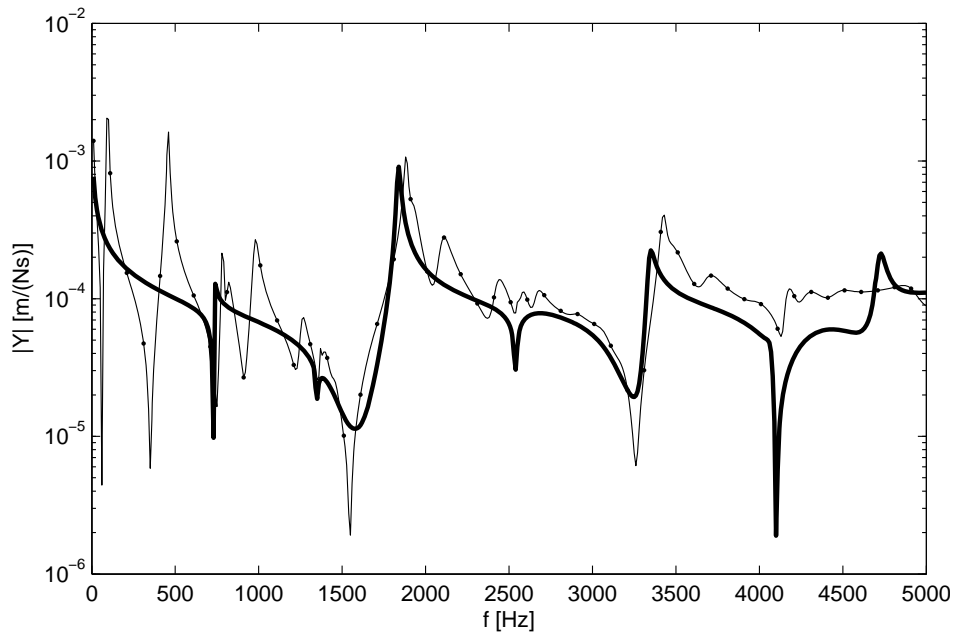


(b) 25 mm mesh

Figure 6.6: Transfer mobility profile A, two subelements, free boundary: Standard FE-results $-\bullet-$ in comparison to WFE-results $-(\text{bold})$ (Resp. at $x=0.1$ m, $y=0$, $z=0$) for two mesh sizes



(a) 10 mm mesh



(b) 25 mm mesh

Figure 6.7: Transfer mobility profile A, two subelements, free boundary: Standard FE-results $-\bullet-$ in comparison to WFE-results $-(\text{bold})$ (Resp. at $x=0.1$ m, $y=0$, $z=0.1$ m) for two mesh sizes

6.4 Forced response with reduced wave basis

As shown by Waki et.al. [65] the forced response can be calculated with a reduced wave basis by limiting the solution to the mainly propagating characteristic waves. Calculation time and memory usage can be significantly reduced by this approach as only a limited number of eigensolutions with $|\lambda| \approx 1$ have to be calculated and stored. This reduced wave basis can then be used for response calculations with arbitrary excitation and response points and directions. The loss of accuracy is demonstrated by calculating input and transfer mobilities for a different number of included waves in the forced response calculation and is shown in Figs. 6.8 to 6.12.

The reduction from 792 characteristic waves (full) to 150 mainly propagating waves ($|\lambda|$ closest to 1) gives satisfactory results in the complete frequency range investigated. As the nearfield in the vicinity of the excitation point is established by non-propagating waves which are not fully taken into account in the reduced basis, there is an observable underestimation for the magnitude of the input mobility (Fig. 6.8). A significant deviation can be observed also for the transfer mobilities to lateral points in x -direction (Figs. 6.9 and 6.11).

For remote positions the differences between full and moderately reduced wave basis are negligible which is expected as these positions are only influenced by propagating waves.

The reduction to only 50 propagating waves is related to stronger deviations, most pronounced in the vicinity of the excitation position, where nearfields, i.e. decaying and complex waves contribute significantly. The results get unreliable at some frequencies, where the strongly reduced wave basis is not an appropriate representation of the physics any more.

Overall, the reduced wave basis serves as an effective method to simplify forced response calculations with reliable results as long as the degree of reduction is moderate and nearfield effects are not of primary concern.

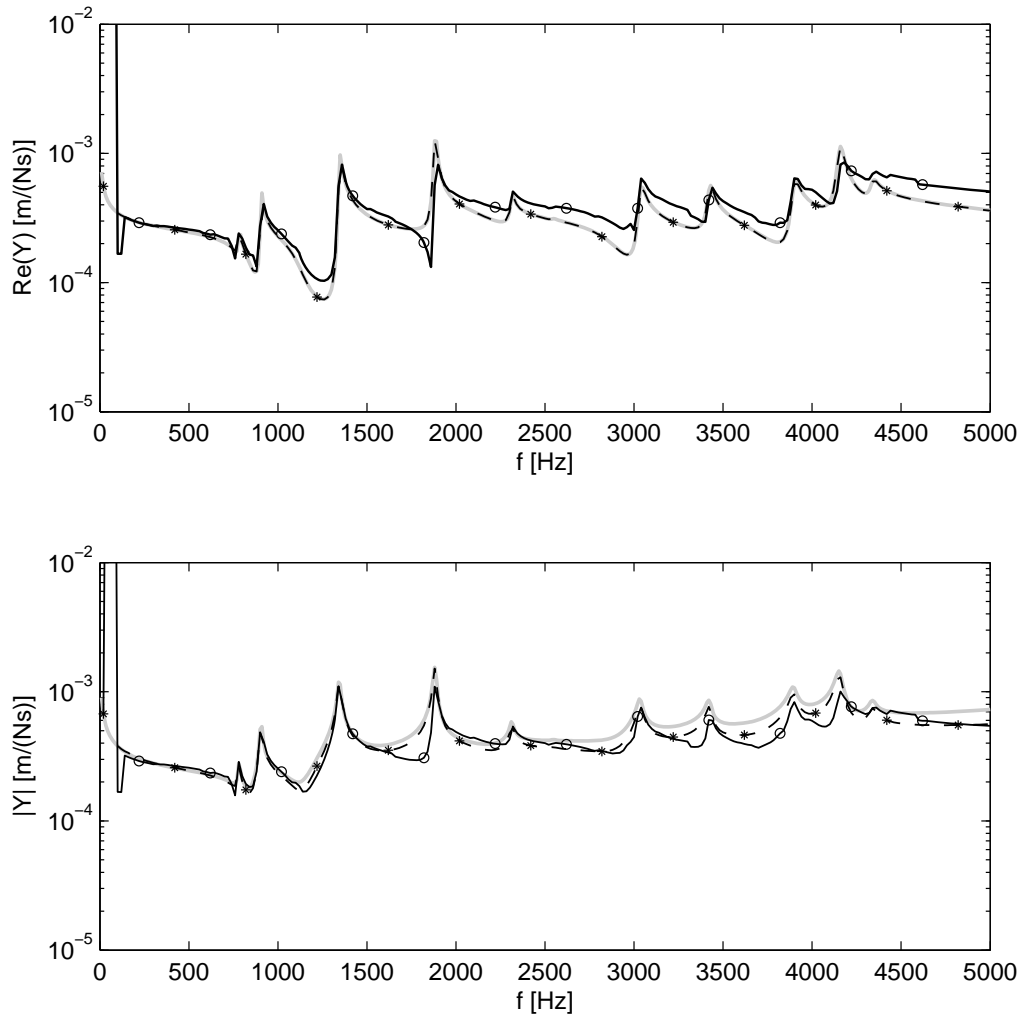


Figure 6.8: Input mobility of profile A, two subelements, free boundary, 10 mm mesh: Influence of wave basis reduction on forced response (full: —(grey), 150 waves: --*-- (black), 50 waves: -o- (black))

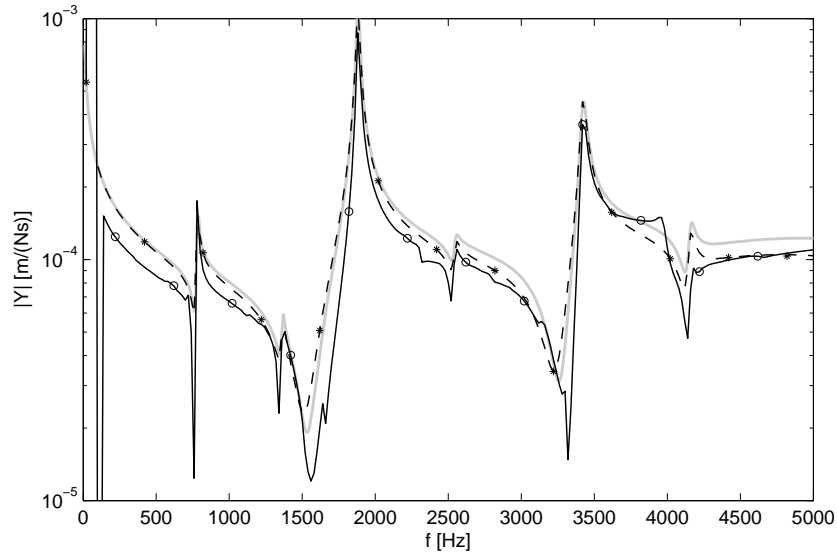


Figure 6.9: Transfer mobility of profile A, two subelements, free boundary, 10 mm mesh, (Response at $x=0.1$ m, $y=0$, $z=0$): Influence of wave basis reduction on forced response (full: —(grey), 150 waves: --*-- (black), 50 waves: -o- (black))

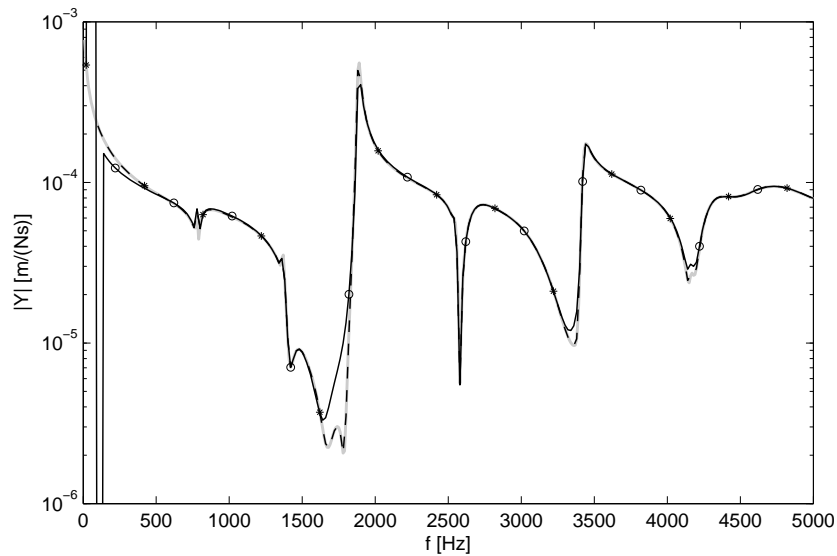


Figure 6.10: Transfer mobility of profile A, two subelements, free boundary, 10 mm mesh, (Response at $x=0.1$ m, $y=0$, $z=0.5$ m): Influence of wave basis reduction on forced response (full: —(grey), 150 waves: --*-- (black), 50 waves: -o- (black))

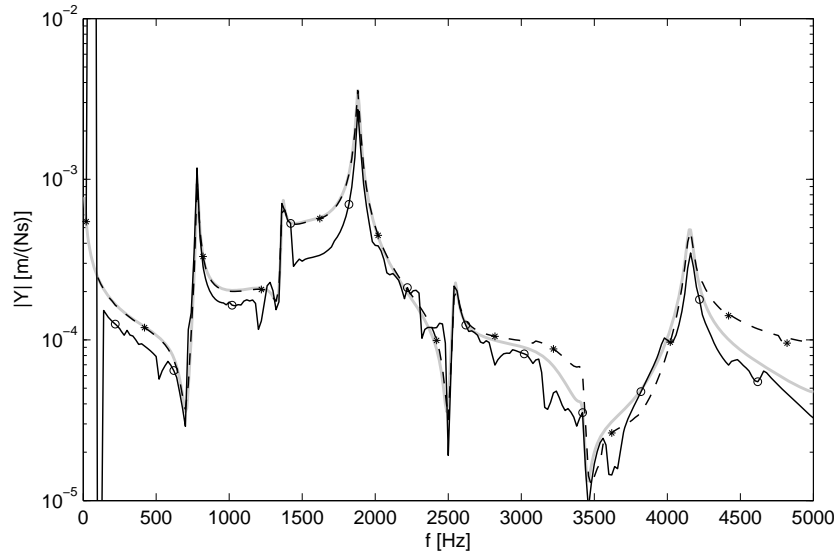


Figure 6.11: Transfer mobility of profile A, two subelements, free boundary, 10 mm mesh, (Response at $x=0.1$ m, $y=0.05$ m, $z=0$): Influence of wave basis reduction on forced response (full: —(grey), 150 waves: --*-- (black), 50 waves: -o- (black))

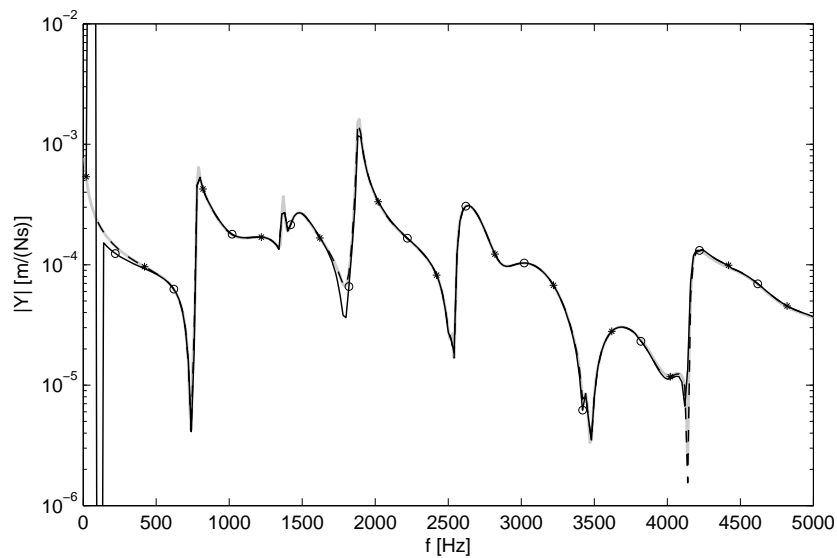


Figure 6.12: Transfer mobility of profile A, two subelements, free boundary, 10 mm mesh, (Response at $x=0.1$ m, $y=0.05$ m, $z=0.5$ m): Influence of wave basis reduction on forced response (full: —(grey), 150 waves: --*-- (black), 50 waves: -o- (black))

6.5 Forced response using dynamic reduction methods

The usage of a limited wave basis reduces the calculation effort considerably, but for large plate sections of many subelements it is desirable to further reduce the system matrices of the eigenvalue problem. The idea is to use standard dynamic finite element reduction methods commonly used in FE packages to reduce the calculation effort. Two methods are applied here, the Guyan or static reduction method [66] and the standard improved reduction system (IRS), [67]. In general, the IRS is more reliable, see. e.g. [68], but the widely used Guyan reduction shall be investigated also. After performing the reduction scheme, the reduced mass and stiffness matrices \mathbf{M}_{red} and \mathbf{S}_{red} respectively are applied for the WFE wave basis evaluation as outlined in section 5.4.1.

All the reduction methods eliminate some of the DOFs, the so called slave DOFs. The remaining DOFs are called master DOFs. For the reduction process the mass and stiffness matrices \mathbf{M} and \mathbf{S} are partitioned in the following way:

$$\mathbf{M} = \begin{bmatrix} \mathbf{M}_{\text{mm}} & \mathbf{M}_{\text{ms}} \\ \mathbf{M}_{\text{sm}} & \mathbf{M}_{\text{ss}} \end{bmatrix}, \quad \mathbf{S} = \begin{bmatrix} \mathbf{S}_{\text{mm}} & \mathbf{S}_{\text{ms}} \\ \mathbf{S}_{\text{sm}} & \mathbf{S}_{\text{ss}} \end{bmatrix} \quad (6.3)$$

Depending on the reduction method a reduction matrix \mathbf{W} is defined and the reduced mass and stiffness matrices are calculated by

$$\mathbf{M}_{\text{red}} = \mathbf{W}^T \mathbf{M} \mathbf{W} \quad \mathbf{S}_{\text{red}} = \mathbf{W}^T \mathbf{S} \mathbf{W}. \quad (6.4)$$

In the Guyan case the reduction matrix reads:

$$\mathbf{W}_{\text{Guyan}} = \begin{bmatrix} \mathbf{I} \\ -\mathbf{S}_{\text{ss}}^{-1} \mathbf{S}_{\text{sm}} \end{bmatrix} \quad (6.5)$$

This reduction neglects the inertia terms of the slave DOFs, which is a good approximation at low frequencies and is accurate in the static case, where inertia forces vanish.

The IRS method uses pseudo-static forces of the inertia terms at low frequencies and improves the Guyan reduction method in this way,¹

¹Due to the inherent inversion of the reduced mass matrix, it has to be assured that all massless DOFs are eliminated therein. Otherwise the matrix is rank deficient and the reduction process fails.

$$\mathbf{W}_{\text{IRS}} = \mathbf{W}_{\text{Guyan}} + \begin{bmatrix} \mathbf{0} & \mathbf{0} \\ \mathbf{0} & \mathbf{S}_{\text{SS}}^{-1} \end{bmatrix} \mathbf{M} \mathbf{W}_{\text{Guyan}} \mathbf{M}_{\text{red,Guyan}}^{-1} \mathbf{S}_{\text{red,Guyan}}. \quad (6.6)$$

For the Guyan reduction method all massless (rotational) degrees of freedom are selected as slave DOFs for the presented results. For the IRS half the nodes are retained and additionally the massless DOFs are reduced, which is roughly a reduction to a quarter of DOFs. The results are presented in Figs. 6.13 to 6.15.

Neither the Guyan reduced results nor the IRS results capture the mobilities of the full structure in an appropriate way. At very low frequencies below the first cross sectional resonances the static reduction is a good approximation. At higher frequencies the general trends are still appropriately represented by both methods, but there is a significant frequency shift to lower frequencies of about 10 – 20 %, illustrating a de-stiffening effect. The results for the input mobility are more satisfying and give an acceptable representation of the reference mobility.

6.6 Concluding remarks

The forced response results presented in this chapter demonstrate the strength of the WFE calculations by demonstrating the reliability in comparison with standard FE-calculations. The fact that an infinite plate in longitudinal direction can be investigated without enlarging the computational effort is especially valuable for general profile design where longitudinal resonances would obscure the trends for arbitrary lengths otherwise. It is demonstrated that the application of a reduced wave basis can serve as a promising way to limit the necessary calculation effort for WFE applications. Only if nearfield effects are of primary concern, the full wave basis has to be retained. The application of standard reduction methods like the Guyan or IRS is far less reliable and should be avoided.

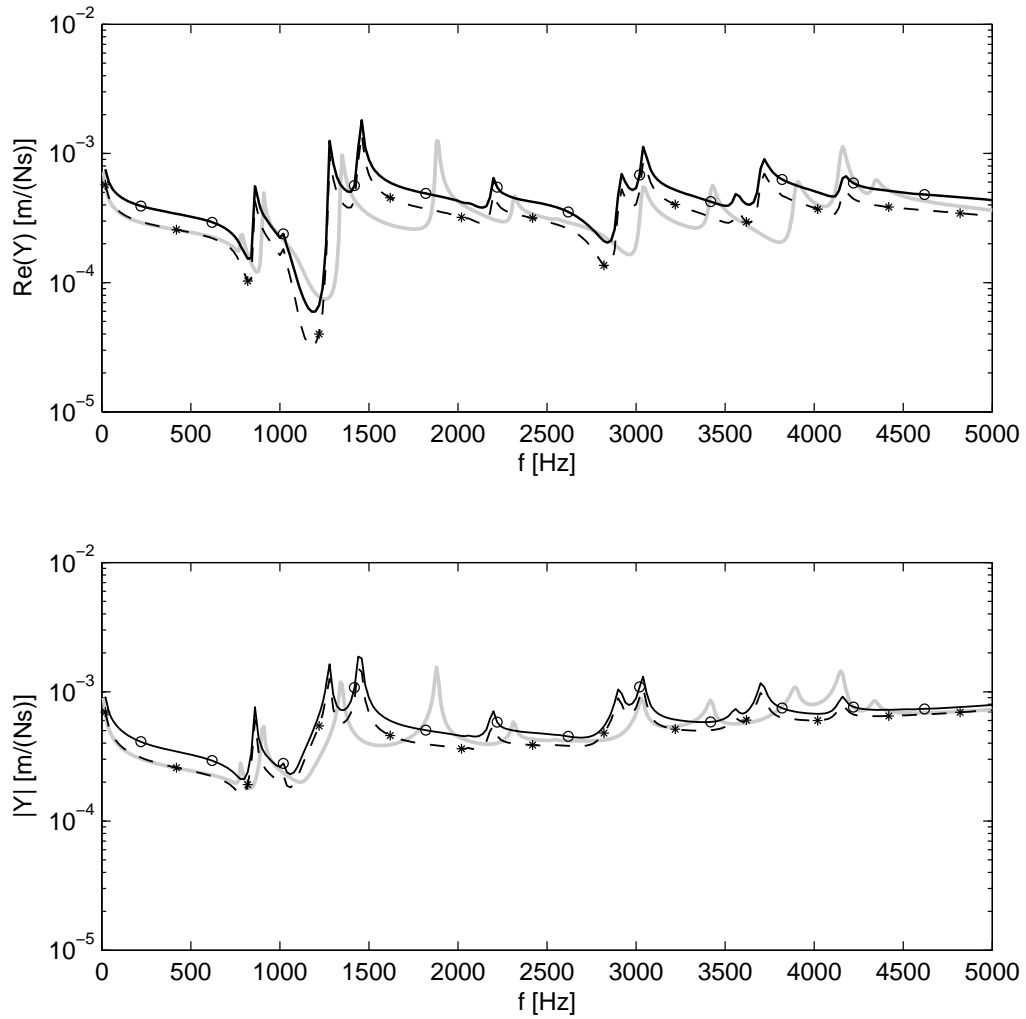


Figure 6.13: Input mobility of profile A, two subelements, free boundary, 10 mm mesh: Influence of Guyan reduction and IRS (full (396 DOFs): — (grey), Guyan (198 DOFs): --*-- (black), IRS (96 DOFs): -o- (black))

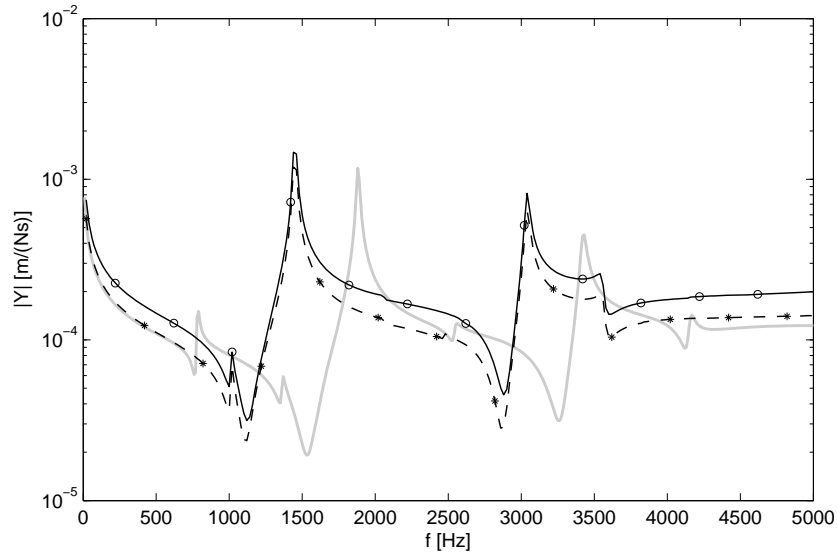


Figure 6.14: Transfer mobility of profile A, two subelements, free boundary, 10 mm mesh, (Response at $x=0.1$ m, $y=0$, $z=0$): Influence of Guyan reduction and IRS (full (396 DOFs): —(grey), Guyan (198 DOFs): --*-- (black), IRS (96 DOFs): -o- (black))

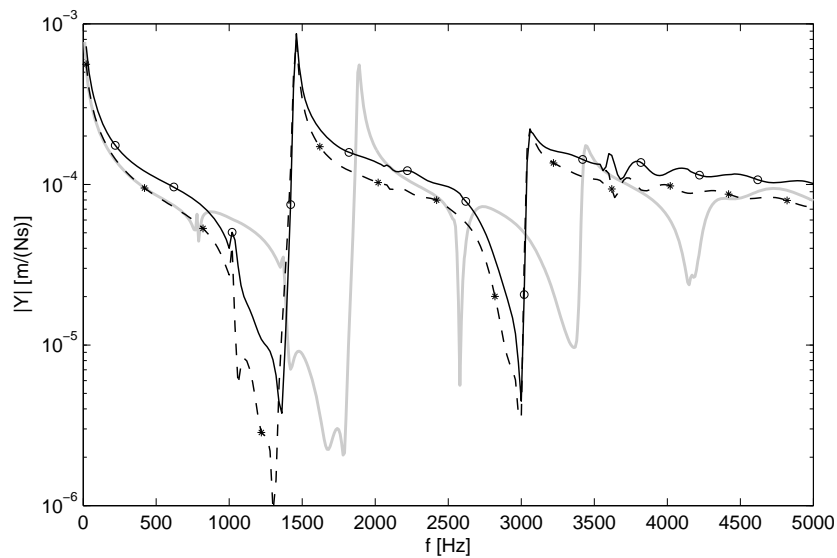


Figure 6.15: Transfer mobility of profile A, two subelements, free boundary, 10 mm mesh, (Response at $x=0.1$ m, $y=0$, $z=0.5$ m): Influence of Guyan reduction and IRS (full (396 DOFs): —(grey), Guyan (198 DOFs): --*-- (black), IRS (96 DOFs): -o- (black))

Chapter 7

Application example: Regional train floor section

In this chapter dispersion characteristics and forced response of a regional train floor section are investigated. Since the plate is not strictly periodic, the extraction of the dispersion characteristics using phase constant surfaces is not an option. Hence, WFE technique and spatial Fourier transform of standard FE results are applied. For experimental validation, dispersion characteristics are extracted using the Inhomogeneous Wave Correlation (IWC) technique.

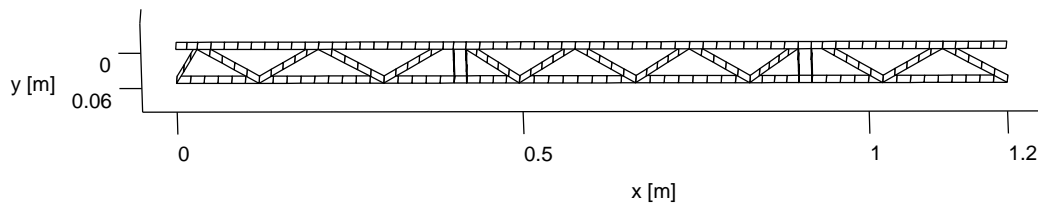
The light weight train floor section made of extruded aluminium sections which are line-welded in the longitudinal z -direction is shown in Fig. 7.1(a).

The detailed geometry is not given here for the sake of brevity, but the plate thicknesses are 2.5-3 mm, overall thickness is 60 mm and the main spacing between adjacent webs is about 180 mm. This structure is not strictly periodic and it has some outer ribs for inner floor and equipment fastening which are neglected in the simulations.

The FE-modelled half cross section is shown in Fig. 7.1(b). As the forced response for excitation in y -direction at the centre of the plate is investigated here, only the half cross section is modelled and symmetric boundary conditions are applied at the edge $x = 1.2$ m. The edge ($x = 0 - 0.4$ m) is highly damped with a loss factor of $\eta = 0.1$ to reduce edge reflections and simulate test conditions, where the edge is embedded in sand and partially filled with foam wedges and sand to establish a smooth transition to the damped regions, see [69] for details of the experimental set-up.



(a) Photo



(b) WFE model of half cross section, 20 mm element length in z -direction

Figure 7.1: Light weight train floor section (extruded aluminium) and WFE model

7.1 Free wave propagation

The dispersion characteristics extracted from the WFE eigenvalue problem for symmetric waves of the plate are shown in Fig. 7.2.¹

Because of the irregularity of the cross section, the wave dispersion is less distinct than for the ideal generic profiles investigated before. However, similar general trends can be observed. Solely global bending waves propagate at frequencies up to 300 Hz. At higher frequencies, again, different wave groups develop. For 4000 Hz, where most of the types have cut on, some wave shapes are plotted in Fig. 7.3 as examples of each wavegroup.

The group with highest wavenumbers in Fig. 7.2 at 4000 Hz is related to first order cross modes of the outer plate strips (see Fig. 7.3(a)). These local waves are the first to cut on in frequency because of the highest distance between adjacent web joints. The second dispersion group of Fig. 7.2 is dominated by first order cross modes of the interior diagonal plates (see Fig. 7.3(b)). The amplitudes of the outer plates for this group are significantly lower than for the inner webs.

For all the waves with high wavenumbers in z -direction, the vibrating

¹Only symmetric waves are included because of the symmetric boundary condition applied. This solution is sufficient to investigate the case of symmetric excitation in the centre position.

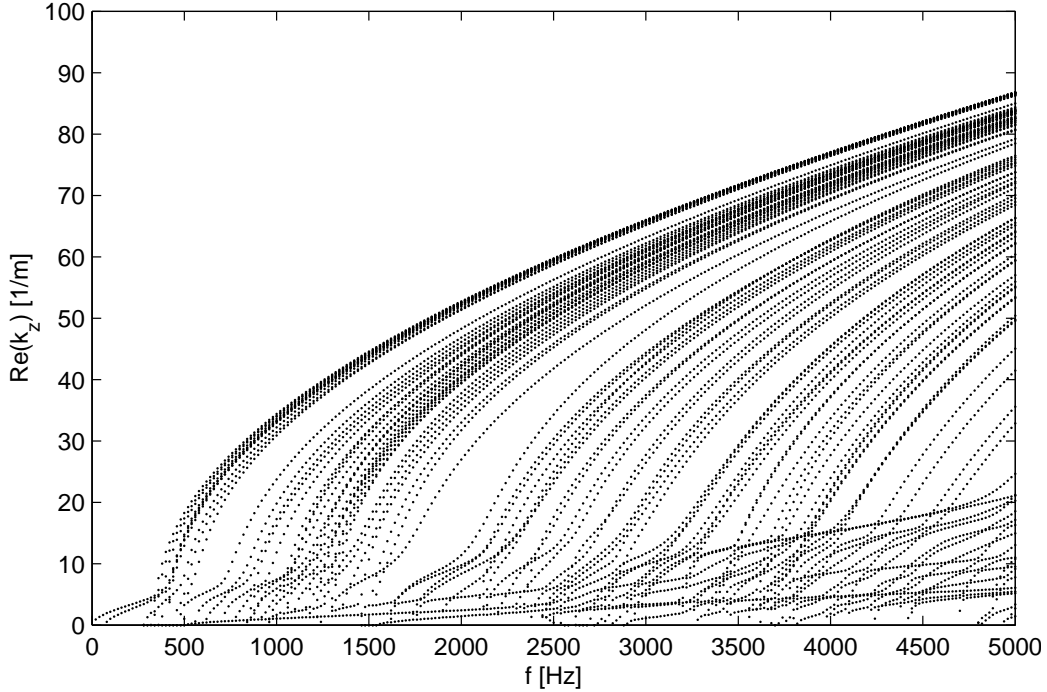


Figure 7.2: Dispersion characteristics of propagating waves in light weight train floor with symmetric boundary conditions and infinite extension in z -direction using WFE approach

region in x -direction is bounded and the different waves in each group belong to different vibrating regions in x -direction. The straight intermediate webs exhibit a strong barrier for the wave motion which is passed only by the waves with a low wavenumber in z -direction (Figs.7.3(h) and (i)).

The wavegroups with lower wavenumbers than 60 m^{-1} at 4000 Hz are not as distinct as the first order modes previously described since different wavegroups overlap.

Figs. 7.3(c) and (d) show examples of second and third order cross modes of the outer plate strips respectively. Fig. 7.3(e) is a combination of third order outer plate strip and second order diagonal plate strip modes, whereas Fig. 7.3(f) is a mixture of fourth order outer plate and first order straight inner web modes.

Some waves with global z -behaviour are shown in Figs. 7.3(g)-(i), where the last two waves comprise wave motion extended over the complete profile width.

From the nature of the characteristic wave shapes some important aspects of structure-borne sound propagation in the light weight profile at frequencies

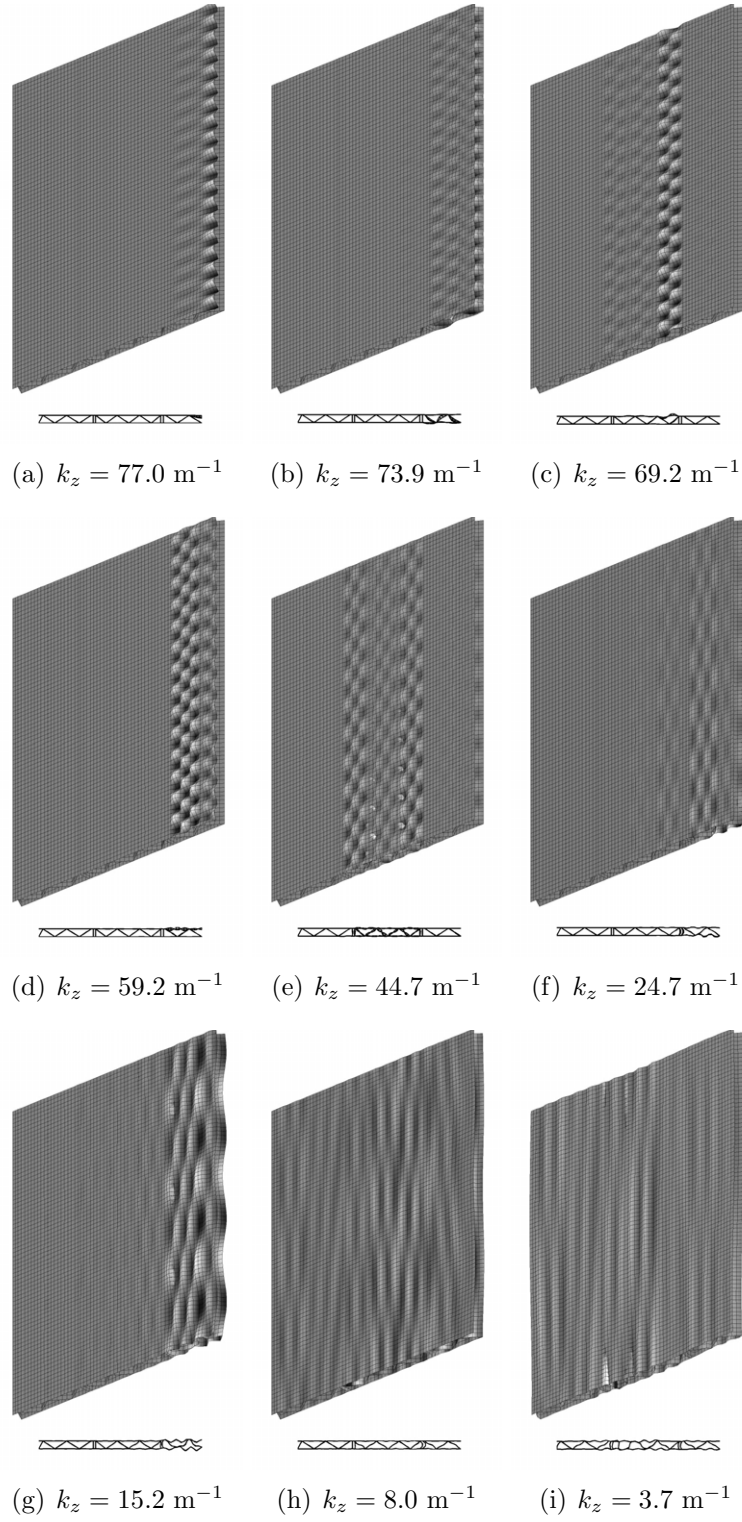


Figure 7.3: Selected wave shapes for half train floor plate with symmetric boundary conditions, $f = 4000 \text{ Hz}$

beyond the global wave region can be deduced:

- For local excitation of structures which are not strictly periodic, bounded wave motion is expected in the section of excitation with power flow mainly in the z -direction.
- Irregularities such as heavy straight webs behave as wave "blockers".
- Extended lateral vibration of the plate is likely to be connected to global wave motion in z -direction.
- Damping is acting locally in the region of the damped plate strips. The edge damping applied in the example has very little effect on the characteristic waves propagating in the central region of the plate.
- The cut-on frequencies for cross modes in the plate strips are somewhere between the lateral eigenfrequencies of simply supported and clamped plate strips. The low frequency edge of the wavegroup corresponds roughly to the simply supported case, whereas the high frequency edge belongs to the clamped case. This is in accordance with the observed wave shapes for the ideal periodic profiles investigated. The variety of boundary conditions is achieved by different combinations of displacement patterns of adjacent connected plate strips. For narrow light weight plates the amount of variations is limited which causes a reduced set of emerging boundary conditions and related characteristic waves. For wider plates the number of characteristic waves increases significantly as illustrated for the regional train floor example.

7.2 Forced Response - Calculation and experimental results

Depending on the excitation position and direction, it is expected that different characteristic waves are excited with different contributions to the overall response. For a local force excitation mainly the characteristic waves with significant vibration amplitudes at this point are excited. As an example, unit force excitation at the centre position of the train floor plate ($x = 1.2$ m, $z = 0$ m) in y -direction is applied. The wave amplitudes are calculated as described in chapter 6. The eigenvectors are normalized to unit length.

The WFE-calculated displacement field for 1000 Hz is shown in Fig. 7.4(b). For comparison the standard FE-calculated displacement field is plotted in

Fig. 7.4(a), where additionally edge damping in z -direction is applied to approximate the infinite extension. As expected wave propagation is confined to the region in the vicinity of the excitation point in x -direction and waves propagate mainly in z -direction. For validation purposes, test results from a fraction of the plate are shown in Fig. 7.4(c). Results for other frequencies are included in Appendix F.1. The tests are performed with strong edge damping applied to the light weight plate by means of foam wedges between the webs padded with sand and immersed in sand over the complete edges (0.5 m width). Electrodynamic point force excitation and contactless laser vibrometer response testing with manual surface scanning are applied. An irregular grid with increased grid point spacing for remote points of the excitation is used, see [69] for details. The general trend of local wave propagation can be recovered in the excited plate strip. Due to a stiffening effect of the fillets at the joints as reported in chapter 2 and [70], the experimental wavelength in z -direction is slightly larger and propagation in the adjacent strips is reduced. The latter observation can be influenced also by effects of the outer webs of the plate which are not included in the calculation models. Both aspects give rise to the discrepancies of measured and calculated displacement fields shown in Figs. F.1 to F.9.

The WFE displacement fields and standard FE results agree for all investigated frequencies. At high frequencies the additional edge damping in the standard FE-model, which simulates the non-reflective boundary at $z = 1.5$ m, gives rise to slight variations.

The corresponding wave amplitudes for the mainly propagating waves are shown in Fig. 7.5 and demonstrate the constitution of the displacement field from a small number of dominating waves. These waves are shown in Fig. 7.6 and corroborate the possibility to use a reduced wave basis for the calculations as described in chapter 6.

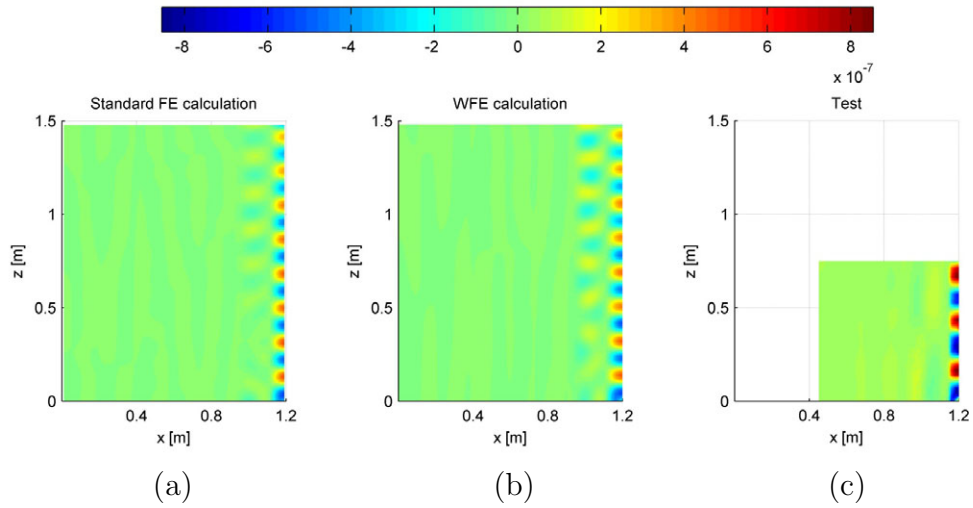


Figure 7.4: Displacement field of forced response (F_y at the centre of plate field, lower right corner of plots), $f = 1000$ Hz

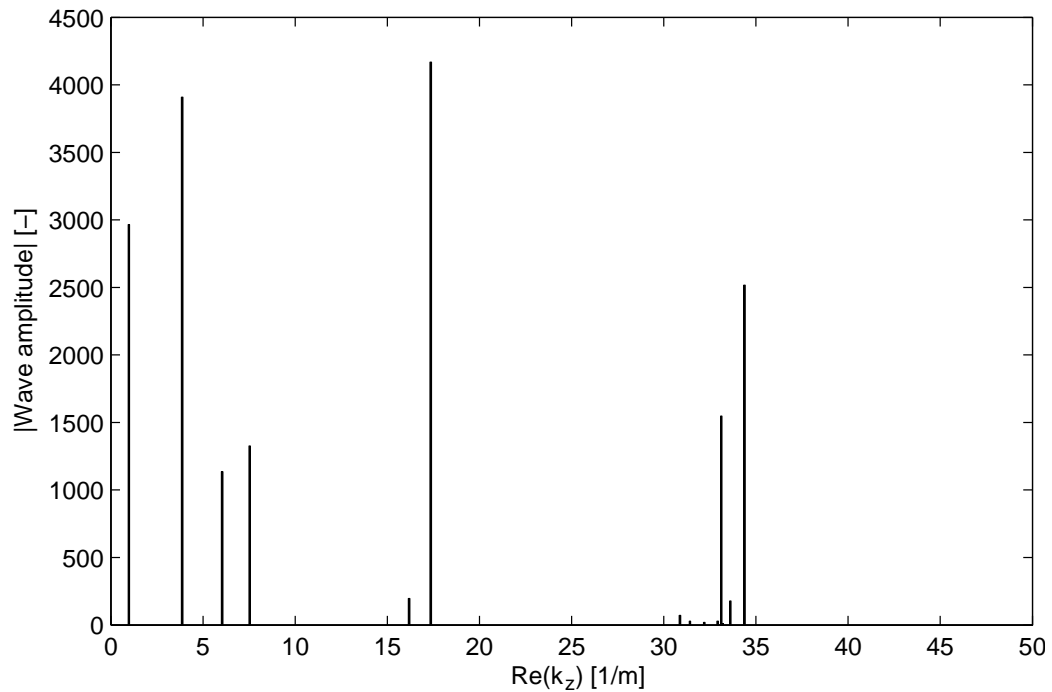


Figure 7.5: Propagating wave amplitudes for forced excitation (F_y at the centre of plate field, $f = 1000$ Hz)

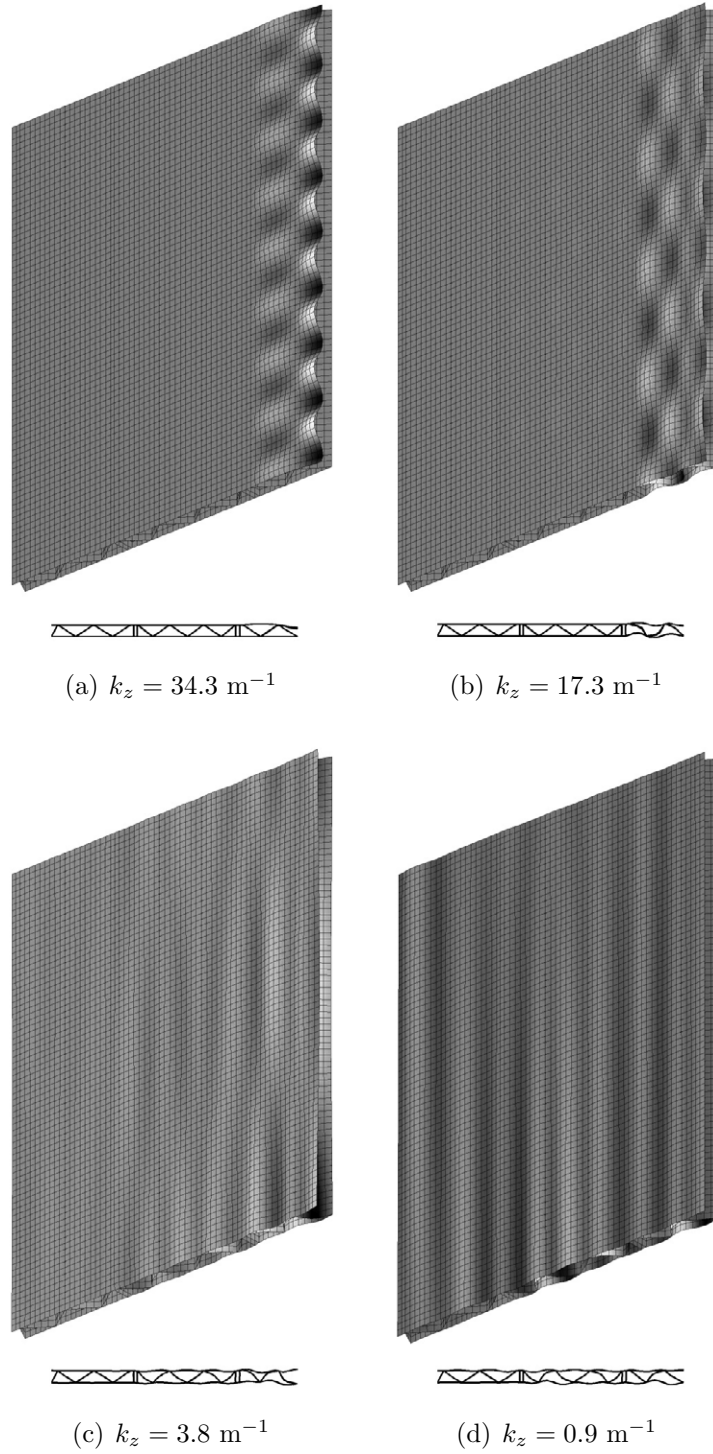


Figure 7.6: Dominating wave shapes for forced excitation of train floor plate with symmetric boundary conditions at right edge, (F_y at the centre of plate field, lower right corner of plots), $f = 1000 \text{ Hz}$

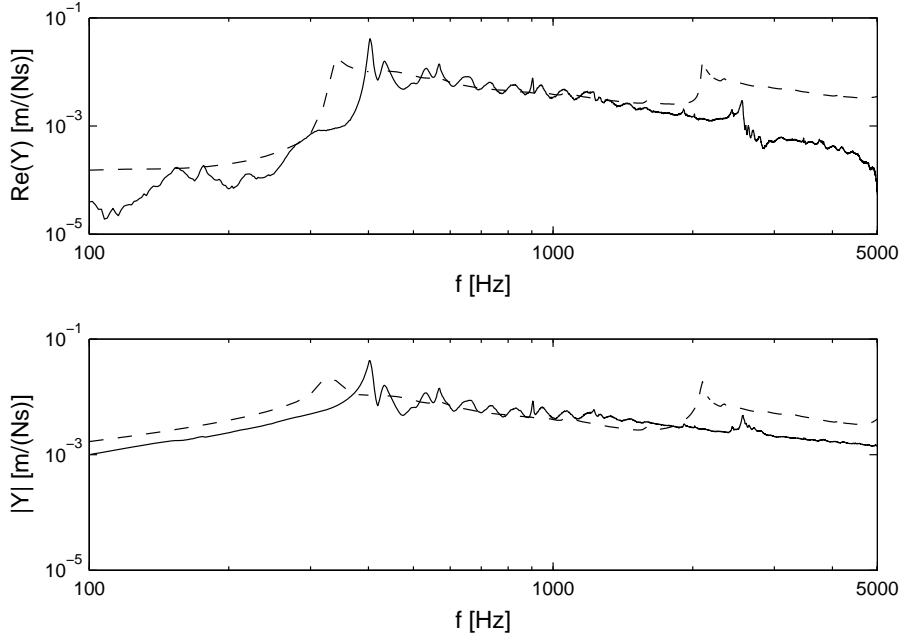


Figure 7.7: Measured (—) and WFE-calculated (---) input mobility of edge damped train floor section for normal force excitation at the centre position (plate field)

7.2.1 Calculated and measured mobility results

The input mobility for the damped test section in comparison with the WFE-calculated result is shown in Fig. 7.7.²

The general trends of calculated and measured input mobility for excitation at the centre of a plate strip are a stiffness-like behaviour at low frequencies below the first cut-on frequency of the strip, followed by a strong increase slightly below and a peak at the cut-on frequency of 340/400 Hz (calculated/measured). Up to the second cut-on frequency accompanied by a second mobility peak, the behaviour is essentially beam-like, since wave propagation is dominated by one-dimensional bending wave propagation along the plate strip in z -direction. The smaller peaks between the cut-on frequencies in the test data are caused by non-ideal anechoic terminations in the test set-up and are related to standing waves in z -direction. The frequency shift of the cut-on frequencies between calculated and measured data is related to the stiffening effect of the fillets at the joints of the extruded profile, reducing

²For practical reasons the acceleration could not be measured directly at the excitation point. The distance is about 1 cm. This and the fact that the measured mobility data is not phase calibrated results in a decreasing real part at frequencies greater than 3000 Hz.

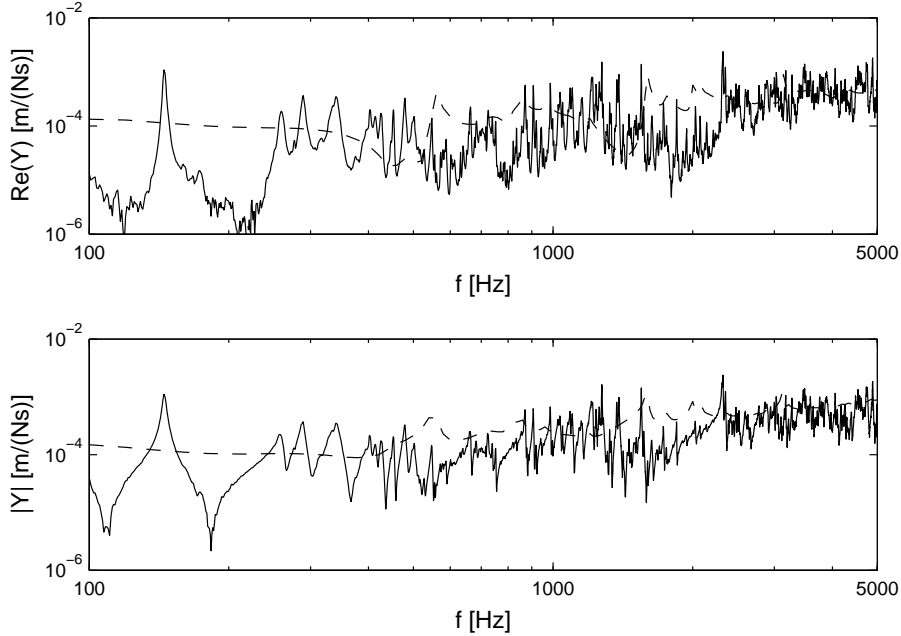


Figure 7.8: Measured, freely suspended (—) and infinite WFE-calculated, edge damped (— —) input mobility of train floor section for normal force excitation at stiffener position at the centre of plate

the free width of the plate strip and constraining the edges.

For the case of stiffener excitation test data of the damped test object is not available. Hence, the comparison is performed with test data of the freely suspended train floor section which reveals its strong, resonant behaviour in this case. Following the mean value approach of infinite systems [71], a comparison demonstrates the influence of the finite length, mainly in z -direction, but shows the general trends for this excitation case in Fig. 7.8. Details of the test set-up with free boundary conditions and additional test results are included in appendix F.4. Appendix F.5 shows a comparison of standard FE-calculated input and transfer mobilities with measured results for the case of free boundary conditions.

Though the similarity between calculation and measurement in this case is not obvious, general characteristics like alternating stop- and pass-band behaviour can be observed in both real parts. The frequency shift between calculation and measurement is stronger than in the plate field excitation case.

As expected, the mobility at a stiffener position is generally lower than in a plate field (see also Fig. F.30 in appendix F.4).

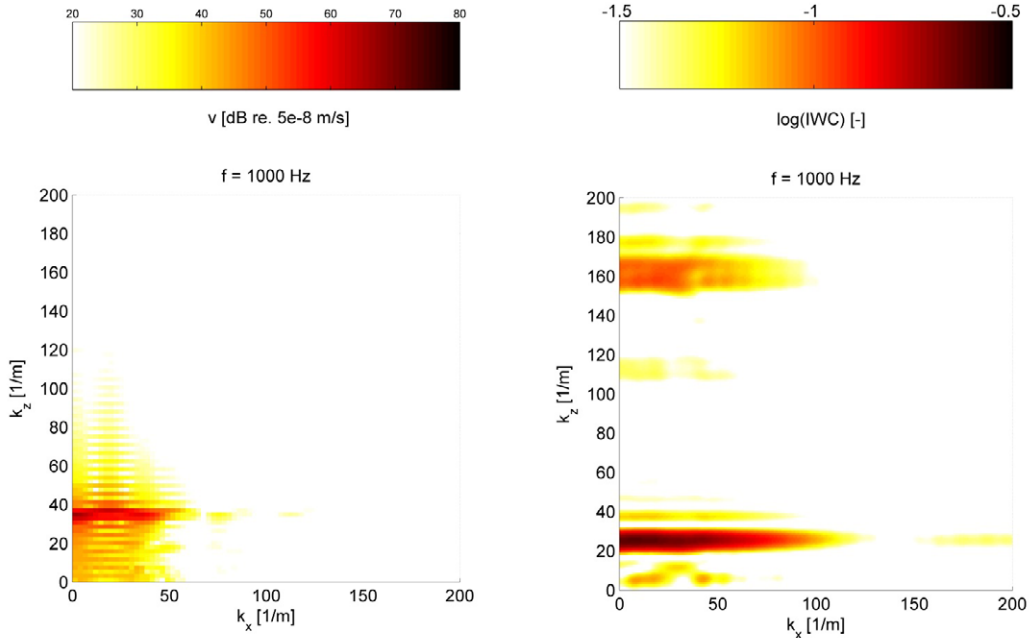


Figure 7.9: DFT-calculated (left) and IWC-measured (right) dispersion characteristics of regional train floor section, $f = 1000$ Hz, F_y at the centre of plate field

7.2.2 Dispersion characteristics

The measured velocity field of the face plate is used to extract its dispersion characteristics. The limited test area hampers the application of the spatial Fourier transform previously used for wavenumber extraction from calculated response fields. In order to improve the resolution and the applicability for arbitrary test positions the Inhomogeneous wave correlation method (IWC) is applied [45, 48] (see Appendix E for details of the IWC).

For each frequency, dispersion characteristics in the k_x - k_z domain can be extracted. As an example the results for 1000 Hz are shown in Fig. 7.9.³ Results for other frequencies can be found in appendix F.2. The strong wave guiding along the plate strip is obvious in the calculated and measured results of Fig. 7.9 with a dominant dispersion line parallel to the k_x -axis. The mentioned frequency shift is now manifested by a wavenumber shift for k_z . The stiffening effect speeds up the bending wave and reduces the wavenumbers.

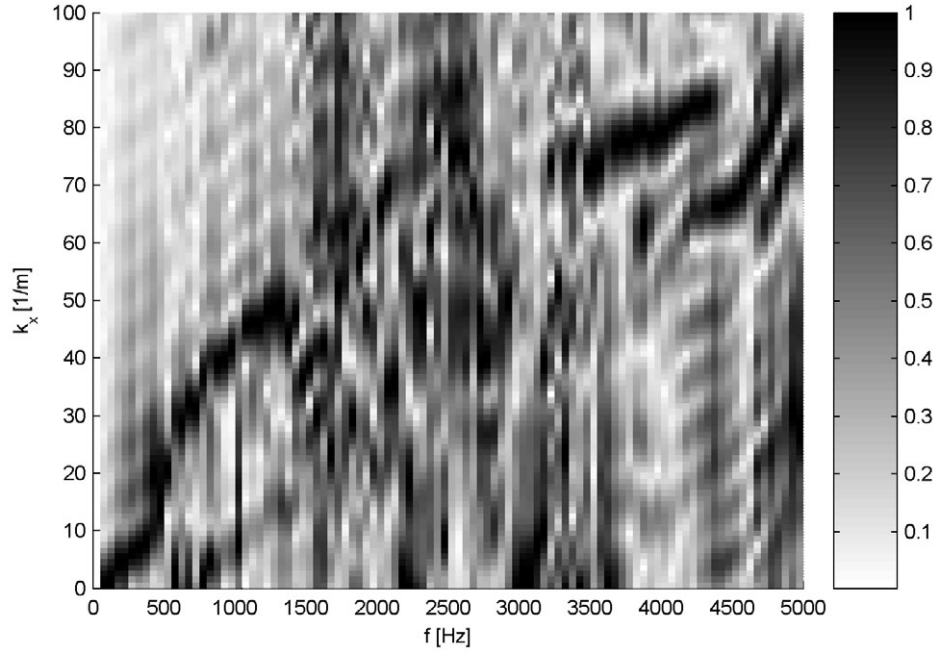
Evaluated frequency dependent measured dispersion characteristics in the

³Due to different evaluation techniques (DFT and IWC) a direct quantitative comparison of the results is not possible. Interpretation should be based on pattern recognition.

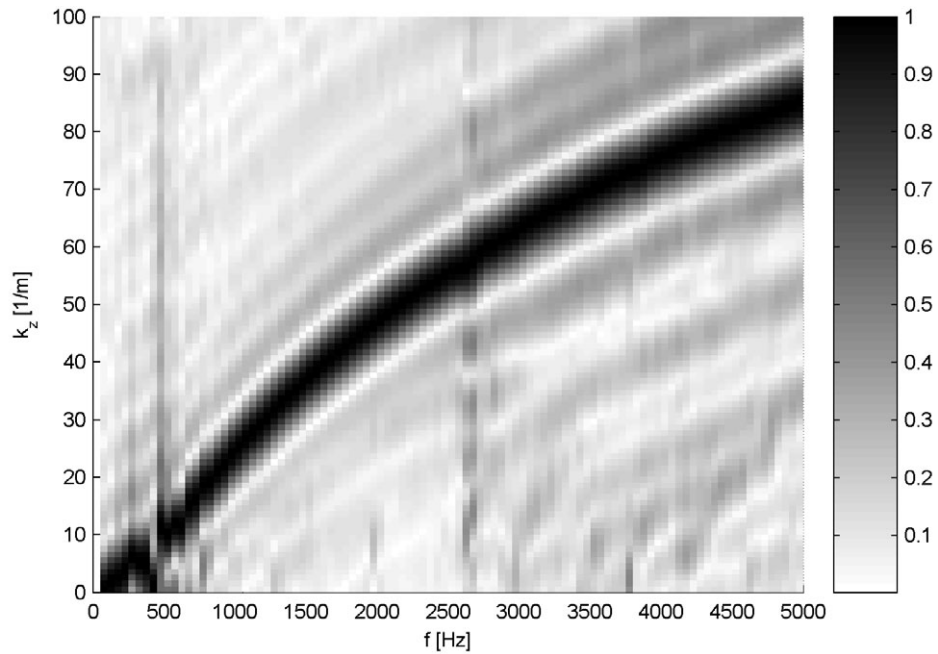
x - and z -direction are shown in Fig. 7.10. In order to increase legibility the correlation values are normalized by the maximum value at each frequency. Dispersion characteristics extracted using the spatial Fourier transform approach of the force excited plate are shown in Fig. 7.11 for comparison.

In general, wave propagation in x -direction is not so distinct as in z -direction. In the low frequency range, global wave propagation with similar wavenumbers in both directions exists. For higher frequencies waves with first order cross modes dominate the propagation along the plate strips corroborating the insights gained from the WFE investigations. A slight periodicity of the wavenumbers in x -direction can be observed as expected for nearly periodic systems. Faint decreasing dispersion lines related to reflected waves are also detectable for calculated and measured results.

Dispersion in z -direction can be compared also with WFE-results of Fig. 7.2 and show a high degree of similarity for both calculation results. The measured dispersion follows the WFE-dispersion characteristics with highest wavenumbers. All other WFE dispersion branches with lower wavenumbers are not excited in the measurement set-up with normal force excitation at the centre of a plate field.

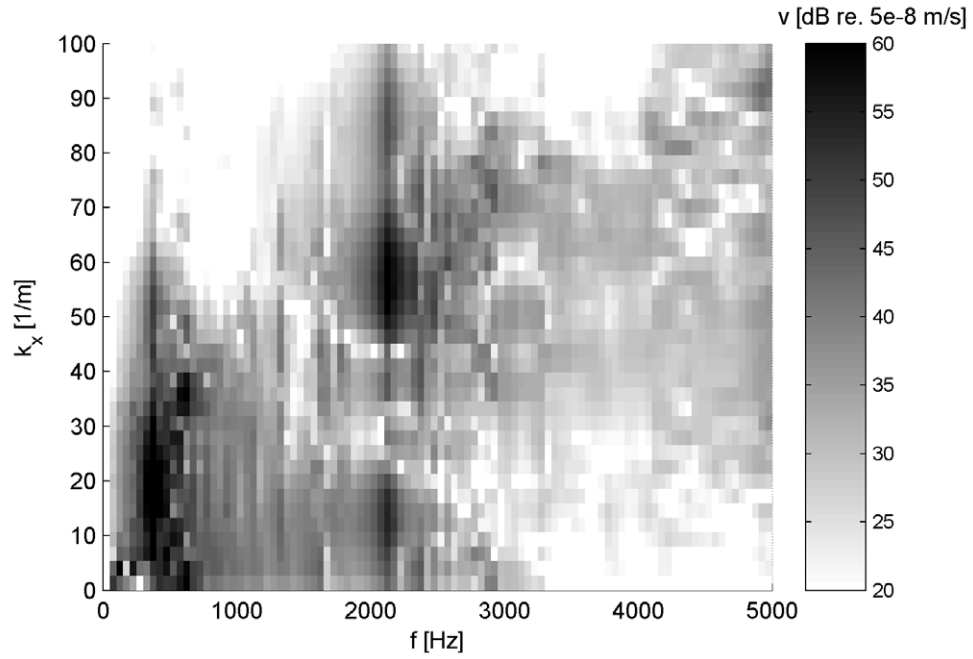


(a) k_x

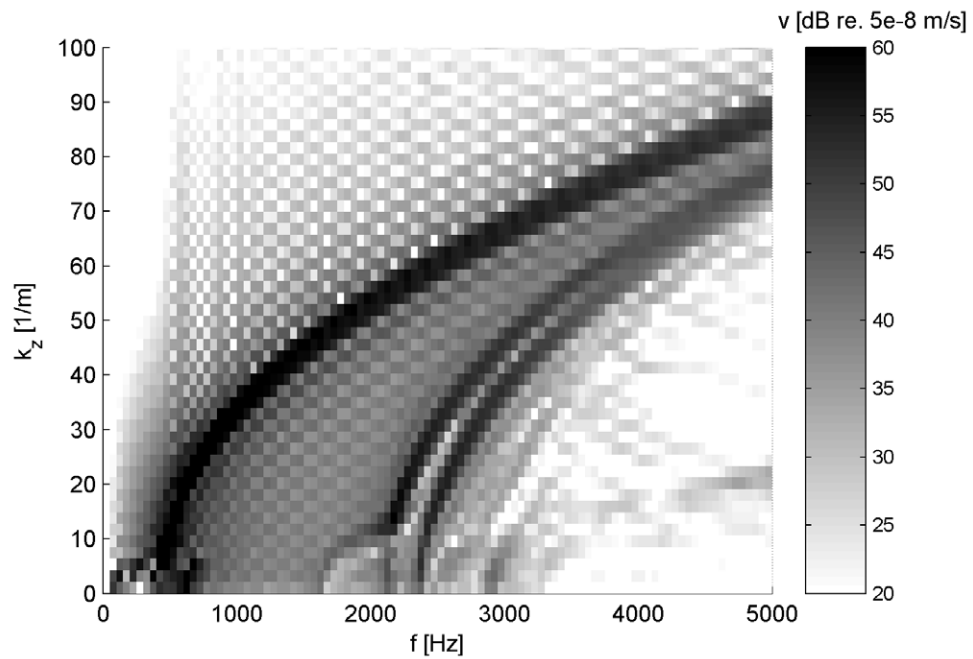


(b) k_z

Figure 7.10: Measured dispersion characteristics using IWC method in (a) x - and (b) z -direction, normalized by maximum of each frequency, F_y at the centre of plate field



(a) k_x



(b) k_z

Figure 7.11: Calculated dispersion of train floor section in (a) x - and (b) z -direction using spatial Fourier transform of standard FE-results, F_y at the centre of plate field

7.2.3 Impulse propagation

The dispersion characteristics of structures can be exploited not only using the wavenumber identification techniques previously described, but also from the measured or calculated impulse response of the structure. The advantage of this method for experimental application is the simple test set-up and the small measurement time. The structure is excited with an impulse hammer at a certain position and at some remote distances the response is recorded as a time signal. For non-dispersive wave propagation the time of flight can be directly extracted from the measured response signal or the cross correlation peak of excitation and response. For dispersive waves, the pulse broadens with travel time. For typical bending wave dispersion, the low frequency components are slower than the high frequency components. The frequency dependent propagation time $\Delta t(f)$ in connection with the distance between excitation and response Δx results in an estimate for the group speed $c_g(f) = \Delta x / \Delta t(f)$. Hence, it is necessary to perform a joint time-frequency analysis of the response signal with proper resolution in time and frequency domain, which can be achieved e.g. by a short-time Fourier transform, Wavelet transform or the (Pseudo-)Wigner-Ville distribution [72]. Wavelet transform seems to be best suited for this application [73], but a higher resolution can be achieved by the Wigner-Ville distribution [74]. The limitations of the latter are that it creates unphysical interferences and negative energy contributions in the regions between physical signal components which makes the interpretation difficult for complex multi-wave signals.

The time-frequency representation of the signals is performed with the algorithm and script written by Büsow [75] for the wavelet part and with a Matlab time frequency toolbox for the Pseudo-Wigner-Ville distribution [76].

When exciting the regional train floor plate at the centre of a plate field and recording the signal at a distance of 0.5 m in z -direction in the same plate field, bending wave dispersion is expected according to plate strip behaviour. For a simply supported plate strip sketched in Fig. 7.13(a) the bending wavenumbers in z -direction $k_{z,n}$ read, where k_b is the free plate bending wavenumber, [77].

$$k_{z,n}^2 = k_b^2 - (n \pi / l_x)^2 \quad n = 1, 2, 3 \dots \quad (7.1)$$

The wavenumbers, phase and group velocities of the ideal simply supported plate strip (aluminium, plate thickness 3 mm, plate width 0.18 m) are plotted in Fig. 7.12. For comparison, the ordinary infinite bending plate behaviour is also included in the plots. Free wave propagation is not possible below the frequency where the first cross-mode cuts on at about 300 Hz.

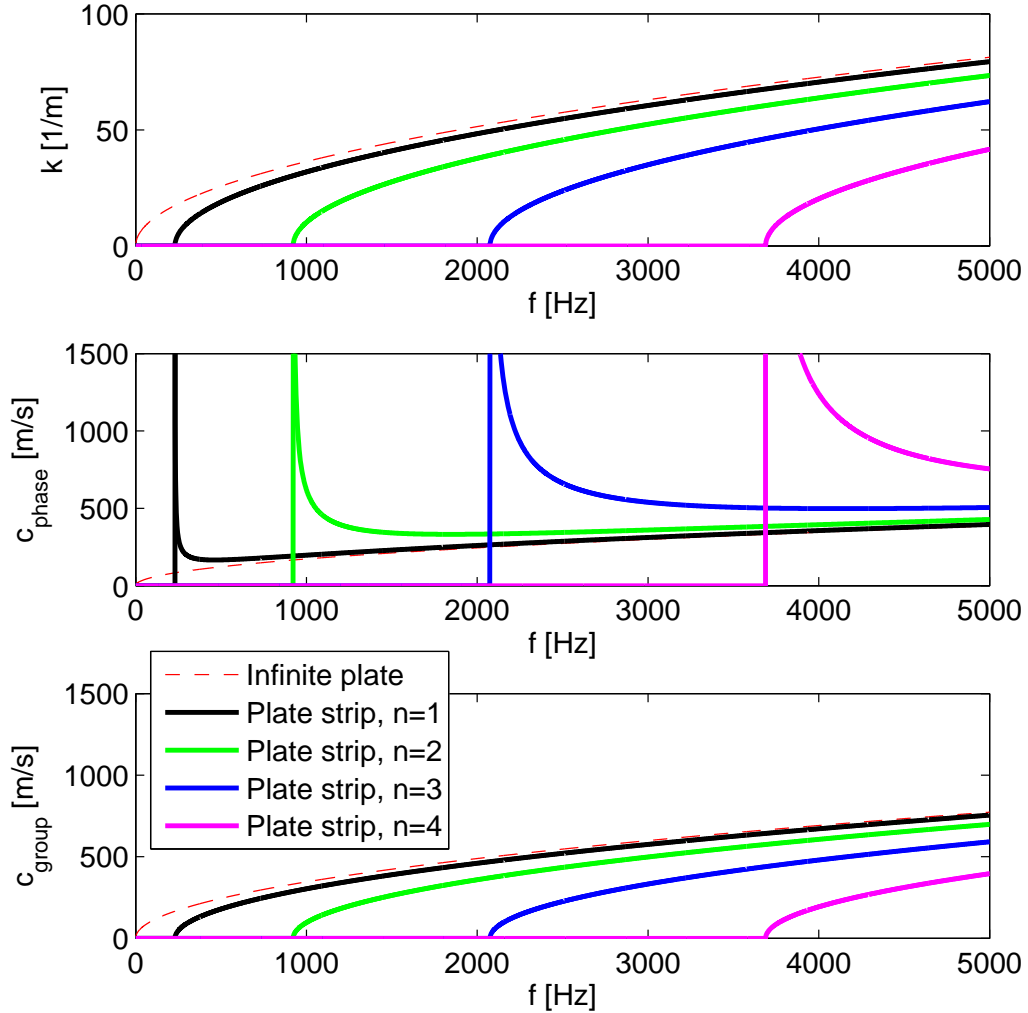
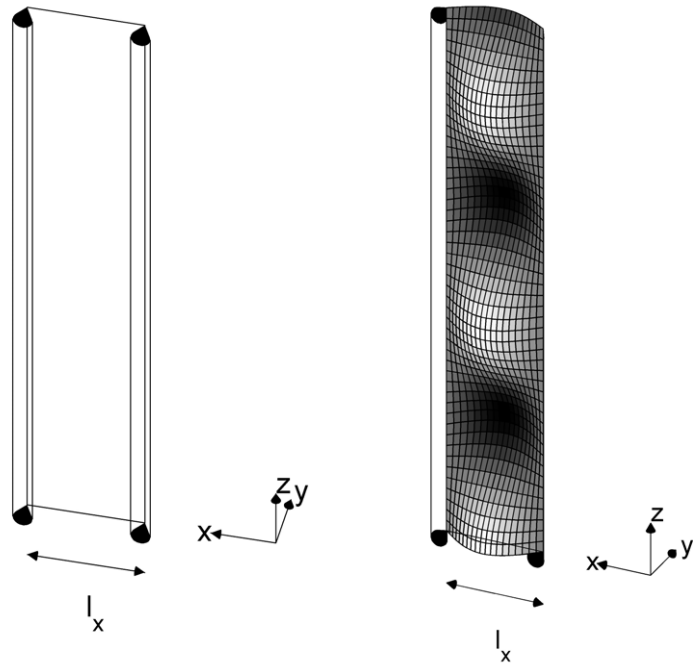


Figure 7.12: Dispersion characteristics of a simply supported plate strip for bending waves, (aluminium, plate thickness 3 mm, plate width 0.18 m) and infinite plate bending wave behaviour

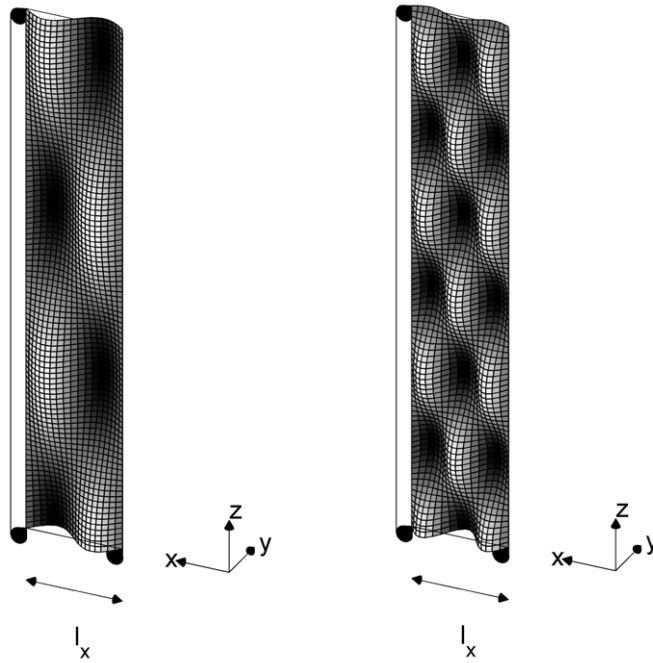
Upon going higher in frequency, the high order cross modes cut on and start to propagate. The related wave shapes are illustrated for the lowest cross modes in Fig. 7.13(b)-(d).

From the wavenumbers the expected travel time for the propagating cross modes can be deduced using the group velocity c_g , defined as $c_g = \frac{\partial \omega}{\partial k}$ and the propagation distance. The results for the investigated plate strip are illustrated in Fig. 7.14.



(a) Sketch

(b) First cross mode, $n=1$



(c) Second cross mode, $n=2$

(d) Third cross mode, $n=3$

Figure 7.13: Bending wave shapes in simply supported infinite plate strip

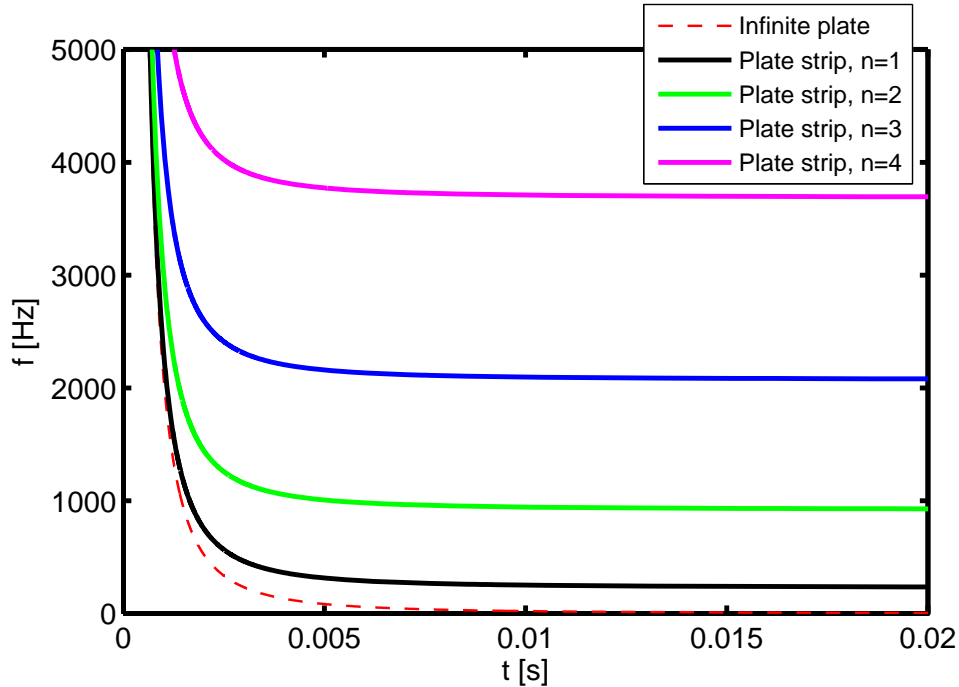


Figure 7.14: Simply supported plate strip arrival times of bending waves for a propagation distance of 0.5 m, (aluminium, plate thickness 3 mm, plate width 0.18 m) and infinite plate bending wave behaviour

For the investigated train floor section the results of a joint time-frequency analysis of FE-calculated (time-domain) and measured impulse response data at a distance of 0.5 m are shown in Figs. 7.15 and 7.16 respectively. The plot at the top shows the acceleration signal in time domain, the central plot is the time-frequency content extracted using the wavelet method and the bottom plot corresponds to the time-frequency content of the Pseudo-Wigner-Ville distribution. The time-frequency plots are scaled for each frequency with the maximum amplitude in order to enhance visibility of dispersion characteristics for all frequencies. As expected the arrival times follow plate strip behaviour which is included in the plots for ideal simply-supported boundaries for the first cross mode with a green dashed line. Below this line, no free wave propagation in the strip is possible. The calculated and measured behaviour is somewhat shifted. This is due to the fact that the boundaries are not simply supported, but connected to the adjacent plate fields. Moreover, the fillets at the joints increase the rotational stiffness at these edges. Marked by the blue line, the dispersion in the plate field matches the result of a simply supported plate strip of reduced width (0.13 m for the blue

line). The green line shows the result for 0.18 m plate strip width which represents the overall distance between the joints to the diagonal webs. The Pseudo-Wigner-Ville result gives a clearer picture of the wave dispersion but introduces interferences which have no physical meaning. In the measured results, edge reflections arise from the free plate field edges in the test set-up.

For propagation in lateral direction of the plate crossing the webs of the plate it is difficult to interpret the corresponding time-frequency results and extraction of group velocities becomes cumbersome and ambiguous [69]. As an example, the results for lateral propagation in a distance of 0.5 m from the plate centre are shown in Figs. 7.17 and 7.18 for calculated and measured cases respectively. Because of overestimated damping in the calculation, the response diminishes more rapidly in this case. Because of the multiple reflections induced within the structure and at the plate edges, no distinct arrival times can be identified in most of the frequency range. The interferences in the Pseudo-Wigner-Ville distribution are amplified and hamper physical interpretations. Results for the case of stiffener excitation in the plate centre are included in Appendix F.3.

Because of the difficult group velocity identification in the reflective and multi-wave structure, the joint time-frequency analysis is not suitable for experimental extraction of dispersion characteristics except for the plate field dispersion. From the evaluated group velocities it is not possible to differentiate the components of possible inherent space harmonics. This is leading to all components as they all have the same group velocities. Only their phase velocities and corresponding wavenumbers are different. If fluid coupling is of interest phase velocities and corresponding wavenumbers are vital to separate radiating and non-radiating components of the space harmonic series. Surface scanning techniques in combination with IWC seem to be unavoidable to extract the dispersion characteristics of such complex periodic structures.

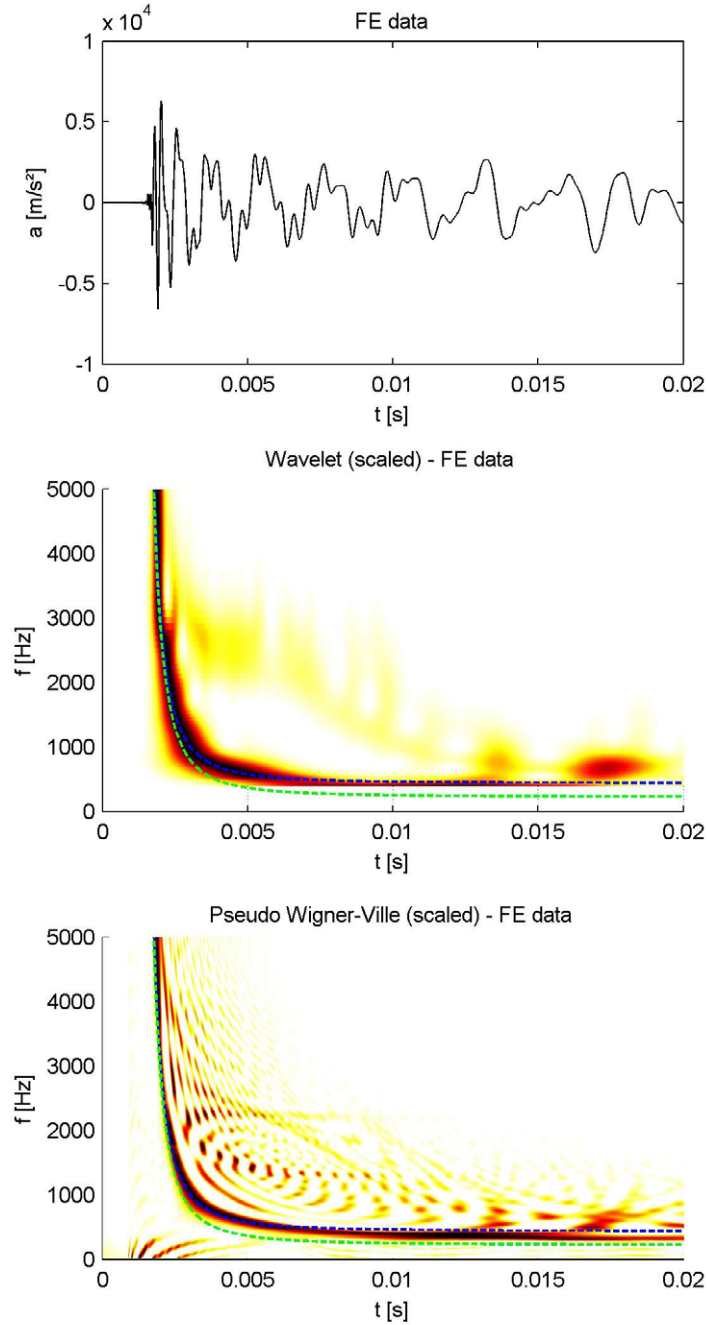


Figure 7.15: FE-calculated impulse response along plate field of train floor section (response at 0.5 m distance in z -direction) and time-frequency content of train floor section. Arrival times of first order bending waves in simply-supported plate strip included by green line (0.18 m width) and blue line (0.13 m width)

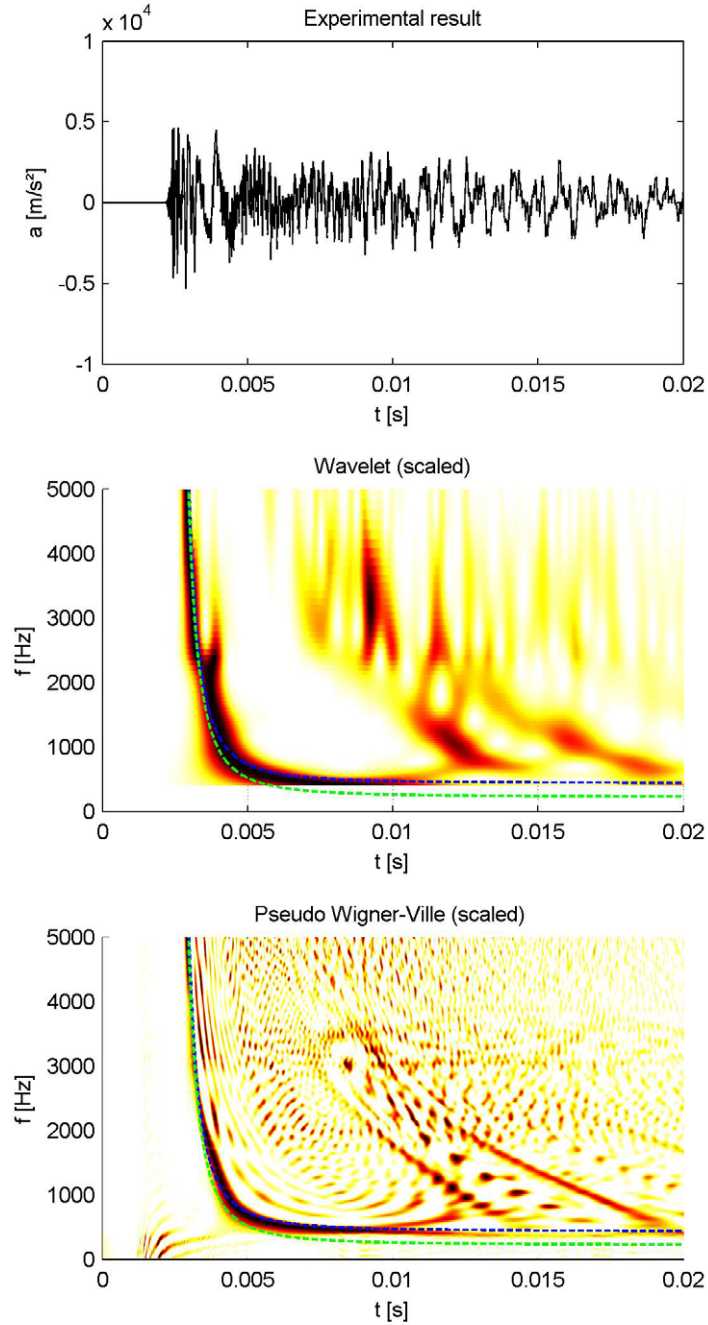


Figure 7.16: Measured impulse response along plate field of train floor section (response at 0.5 m distance in z -direction) and time-frequency content of train floor section. Arrival times of first order bending waves in simply-supported plate strip included by green line (0.18 m width) and blue line (0.13 m width)

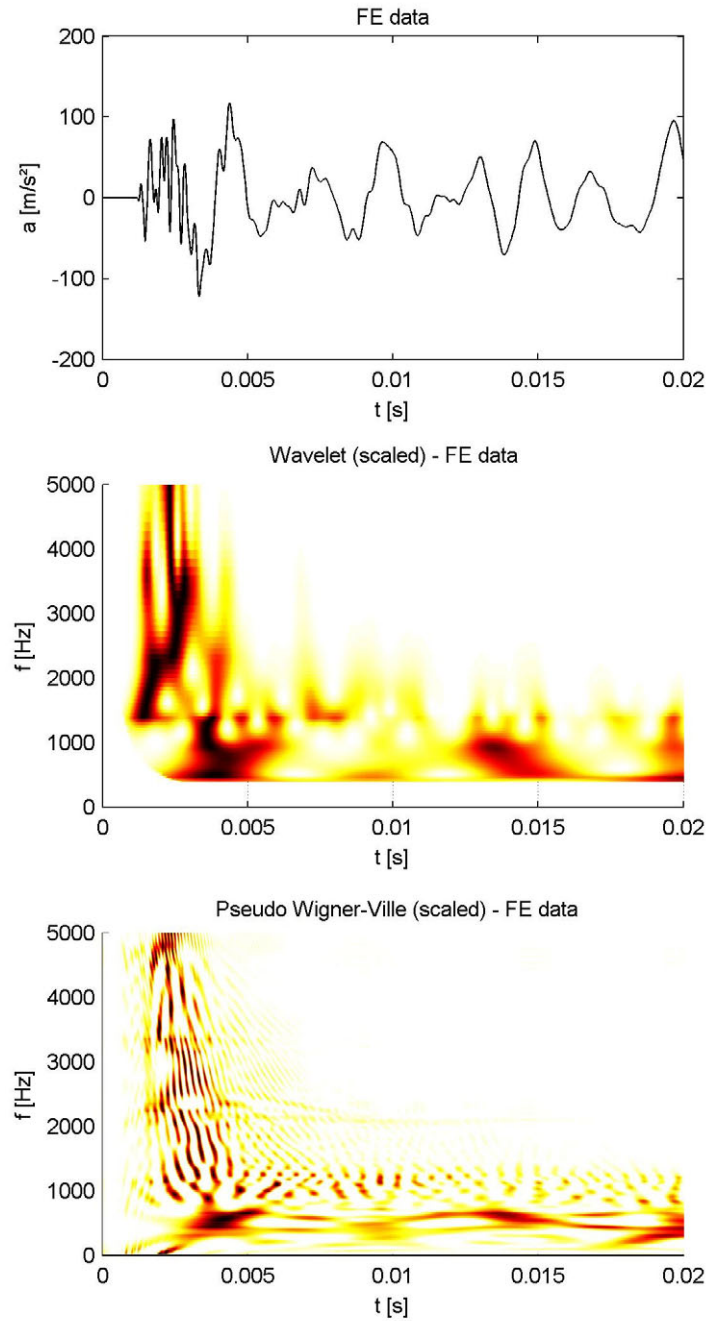


Figure 7.17: FE-calculated impulse response at 0.5 m in x -direction and time-frequency content of train floor section, plate field excitation

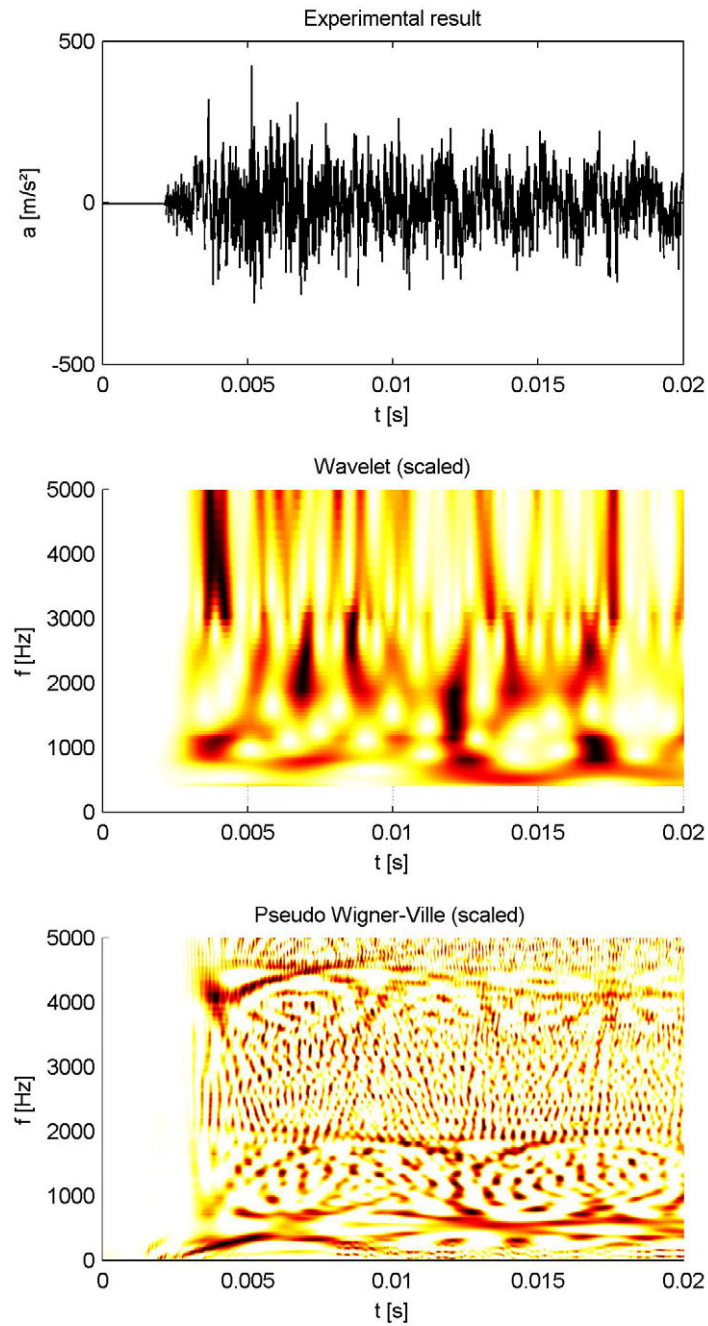


Figure 7.18: Measured impulse response at 0.5 m in x -direction and time-frequency content of train floor section, plate field excitation

7.3 Concluding remarks

The regional train floor example demonstrates the applicability of the WFE-method for free and forced wave propagation on real extruded profile plates. It is demonstrated by validation measurements on dispersion and mobility that the salient physical behaviour is adequately described by the calculation model. An improved model could be established if the outer webs of the real floor would be included, which is possible in principle by extending the WFE cross section model in this respect. Moreover, the stiffening effect of the fillets at the joints should be included to improve accuracy of the models, e.g. by increasing the shell element thickness at the joints.

The WFE investigation of wave propagation reveals some interesting aspects for profile design. For structures which show a significant aperiodicity, bounded wave motion is expected in the section of local excitation with power flow mainly in the direction parallel to the webs. Strong irregularities e.g. a pair of straight webs, mainly arising at weld junctions can behave as wave blockers in lateral direction. Damping is expected to act locally in the region of the damped plate strip. This observation can be used for efficient damping layer layout, if local structure-borne excitation is of concern.

For measurements of dispersion characteristics surface scanning in combination with IWC is recommended. Impulse response and joint time-frequency evaluation is difficult if multiple reflections appear. For the light weight plate all the reflections induced by the multiple webs prevent the reasonable extraction and interpretation of dispersion characteristics for propagation in lateral direction.

Chapter 8

Summary and Outlook

The thesis deals with structure-borne sound propagation in light weight profiles with truss like core geometries. The focus is on the theoretical and experimental investigation of wave propagation and dispersion characteristics for plates with structural periodicity in lateral direction. Periodic structure theory can be exploited to extract the one- and two-dimensional dispersion characteristics for strips and full plates respectively.

For the first case, a calculation model for cross sections of typical light weight profiles based on beam vibrations is established and experimentally validated for a profile strip with vertical webs. Parameter studies on generic profile strips reveal the significance of periodic system effects. Distinct pass- and stop-band behaviour is prominent, especially in the case of solely vertical webs. The periodic effects are also clearly visible in the experimental results. The influence of welds and thicker ends of the webs at the joints are mainly characterized by a stiffening effect, manifested by an eigenfrequency shift towards higher frequencies. The additional mass seems to be of minor importance.

A brief study on irregularity effects in the strip investigation shows that the influence is limited. The general dynamic behaviour of the periodic profile strips are conserved even for high random length variations of up to 5%. It is expected that the same is true for full profile plates.

The wave propagation at low frequencies (global vibrations) can be approximated for profiles with inclined members by equivalent bending beams or plates. Despite the obvious geometric orthotropicity of the layout, the global behaviour for plates with inclined webs can be described by equivalent isotropic bending behaviour. Only in the case of solely vertical webs, strong orthotropicity can be identified represented by significantly higher wavenumbers in the lateral direction, normal to the webs. At high frequencies the detailed description of the dynamics for both configurations is inevitable.

The complete picture of propagating, decaying and complex waves can be gained for a profile strip by solving the transfer-matrix eigenvalue problem. For the profiles considered, up to six characteristic waves can be identified, travelling in each direction. The wavenumber content in each characteristic wave is formed of several "space harmonics", realising a periodic wavenumber spectrum. The relative contributions in the wavenumber series are fixed for each characteristic wave and can be identified from the complete characteristic wave forms. For the investigation of the two-dimensional dispersion characteristics, evaluation of the phase constant surfaces of a 2D-periodic subelement is the easiest way to gain the wavenumber content. The drawback in this case is that the significance of the space harmonic components in the periodic lateral direction are not directly extractable. In principle it should be possible to identify the relative contributions for each characteristic wave in analogy with the procedure described in chapter 3 for the strip. This and an extension to forced response could be a valuable area of future research. The major challenge is the stable and applicable extension to include decaying and complex waves, which is possible but computationally demanding.

By concentrating on the propagating waves, forced response investigations can be simplified and especially for calculations of the full profile plate, calculation effort and memory usage can be reduced significantly. Only when nearfield effects are of primary concern, the full wave basis should be retained.

The waveguide finite element method (WFE) is favourable for plate investigations, where the lateral direction is finite. Standard FE-packages can be used to gain the mass and stiffness matrices of a small slice of the plate. Dispersion characteristics for wave propagation in the longitudinal direction can be extracted in combination with cross mode shapes for the lateral direction. Results of forced response calculations for infinite extension in longitudinal direction are valuable for generic profile design, where the length in the extruded direction is unknown or very large so that edge reflections are suppressed.

The dispersion characteristics of light weight plates with truss-like core geometries demonstrate that wave beaming is not only emerging for structures with periodicity in both directions, but also for structures being periodic only in one direction. The strong periodic effects identified from the two-dimensional investigation remain in the three-dimensional plate investigation in the corresponding periodic direction. In contrast to the strip investigation, where power transmission and wave propagation is nearly completely suppressed in the stop-bands, the effect is weakened for the plates investigated. In the lateral stop-bands wave propagation in longitudinal direction is still possible and wave spreading in oblique directions depends on the de-

tailed coupling mechanisms involved. For profiles with inclined webs, distinct wave beaming in oblique directions arises, whereas for a profile with straight webs lateral coupling and oblique propagation is reduced. In a way the frequency dependent stop-band behaviour for one-dimensional wave propagation is transformed in a frequency dependent and spatially varying attenuation in the two-dimensional propagation case, resulting in low vibration regions for point excited structures. The weakened stop-band effect makes general applications for noise control somewhat delicate. In special situations where low vibration is requested especially in certain regions, e.g. for installation of vibrational sensitive equipment, this strong wave beaming might be exploited. Moreover, design of damping treatments can be optimized, at least for point excited structures, by exploiting the wave beaming effects and aligning the damping treatments in the beaming directions from the point of excitation.

From a structural acoustic point of view it is vital to differentiate between subsonic and supersonic waves in the light weight plates. Only the supersonic waves can couple efficiently to the ambient fluid which is of major importance for radiation and transmission investigations. For proper acoustic design it could be valuable to investigate where major structural wave components become supersonic. In this respect the significant components of the space harmonic series have to be included as it seems possible that lower supersonic orders play a dominant role for radiation and transmission.

The forced response results presented for the light weight plates illustrate the strength of the WFE calculations by demonstrating the reliability in comparison with standard FE-calculations. The fact that an infinite plate in longitudinal direction can be investigated without enlarging the computational effort is especially valuable for general profile design where longitudinal resonances would obscure the trends for arbitrary lengths otherwise. It is demonstrated that the application of a reduced wave basis can serve as a promising way to limit the necessary calculation effort for WFE applications. Only if nearfield effects are of primary concern, the full wave basis has to be retained. The application of standard reduction methods like the Guyan or IRS is far less reliable and should be avoided.

The regional train floor example demonstrates the applicability of the WFE-method for free and forced wave propagation on real extruded profile plates. It is demonstrated by validation measurements of dispersion and mobility that the salient physical behaviour is adequately described by the calculation model. An improved model could be gained if the outer webs of the real floor would be included, which is possible in principle by extending the WFE cross section model in this respect. Moreover, the stiffening effect of the fillets at the joints should be included to improve accuracy of the

models, e.g. by increasing the shell element thickness at the joints.

The WFE investigation of wave propagation reveals some interesting aspects for mid to high frequency profile design. For structures which show a significant aperiodicity, bounded wave motion is expected in the section of local excitation with power flow mainly in the direction parallel to the webs. Strong irregularities e.g. a pair of straight webs, mainly occurring at weld junctions can behave as wave blockers in lateral direction. Damping is expected to act locally in the region of the damped plate strip.

For measurements of dispersion characteristics surface scanning in combination with the "Inhomogeneous Wave Correlation" method is recommended. Impulse response and joint time-frequency evaluation is difficult if multiple reflections appear. In this light weight plate case all the reflections induced by the multiple webs prevent the proper extraction and interpretation of dispersion characteristics for propagation in lateral direction.

Provided computing resources continue to grow in capacity, it seems to be possible to extend the WFE application on standard computers for investigations on full cross sections of extruded aluminium carriages or aircraft fuselages resulting in detailed understanding of the wave propagation along the vehicles.

References

- [1] T. S. Lok and Q. H. Cheng. Free and forced vibration of simply supported, orthotropic sandwich panel. *Computers and Structures*, 79:301–312, 2001.
- [2] T. Kohrs. Structural-acoustic investigation of orthotropic plates. Master's thesis, Technische Universität Berlin, Institut für Technische Akustik, 2002.
- [3] B. A. T. Petersson and B. M. Gibbs. Towards a structure-borne sound source characterization. *Applied Acoustics*, 61:325–343, 2000.
- [4] Torsten Kohrs and B. A. T. Petersson. Körperschallinduzierte Luftschallabstrahlung von Schienenfahrzeugen (Leiser Verkehr - Akustisches Qualitätsmanagement). Technical report, Technische Universität Berlin - Institut für Technische Akustik, Juli 2003.
- [5] T. Kohrs and B. A. T. Petersson. Structure-borne sound radiation from train carriages using a cylinder model. *Acta Acustica united with Acustica*, 92:35–44, 2006.
- [6] M. Goede. Contribution of light weight car body design to CO2 reduction. In *16. Aachener Kolloquium Fahrzeug- und Motorentechnik 2007*, 2007.
- [7] D.C. Sandeman, J. Tautz, and M. Lindauer. Transmission of vibration across honeycombs and its detection by bee leg receptors. *The Journal of Experimental Biology*, 199:2585–2594, 1996.
- [8] L. Brillouin. *Wave propagation in periodic structures*. McGraw-Hill, New York, 1946.
- [9] D. J. Mead. Wave propagation and natural modes in periodic systems: I. Mono-coupled systems. *Journal of Sound and Vibration*, 40(1):1–18, 1975.

REFERENCES

- [10] D. J. Mead. Wave propagation and natural modes in periodic systems: II. Multi-coupled systems with and without damping. *Journal of Sound and Vibration*, 40(1):19–39, 1975.
- [11] D. J. Mead. Wave propagation in continuous periodic structures: Research contributions from Southampton, 1964-1995. *Journal of Sound and Vibration*, 190(3):495–524, 1996.
- [12] P. W. Anderson. Absence of diffusion in certain random lattices. *Physical Review: Journal of Experimental and Theoretical Physics*, 109:1492–1505, 1958.
- [13] Y. Lin. Dynamics of disordered periodic structures. *Applied Mechanics Reviews*, 49(2):57–64, February 1996.
- [14] C. Pierre, M. P. Castanier, and W. J. Chen. Wave localization in multi-coupled periodic structures: Application to truss beams. *Applied Mechanics Reviews*, 49(2):65–86, February 1996.
- [15] C. H. Hodges and J. Woodhouse. Vibration isolation from irregularity in a nearly periodic structure: Theory and measurements. *J. Acoust. Soc. Am.*, 74(3):894–905, 1983.
- [16] D. J. Mead. Free wave propagation in periodically supported infinite beams. *Journal of Sound and Vibration*, 11(2):181–197, 1970.
- [17] B. A. T. Petersson. Influence of structural periodicity perturbations on transfer and cross transfer mobilities. TNO-report TPD-HAG-RPT-950093, TNO Institute of Applied Physics, Delft, The Netherlands, May 1995.
- [18] T. S. Lok and Q. H. Cheng. Bending and forced vibration response of a clamped orthotropic thick plate and sandwich panel. *Journal of Sound and Vibration*, 245(1):63–78, 2001.
- [19] P. Geissler and D. Neumann. Modeling extruded profiles for railway coaches using SEA. In *Proceedings of the 1999 ASME Design Engineering Technical Conferences, September 12-15, Las Vegas, Nevada*, 1999.
- [20] G. Xie, D. J. Thompson, and C. J. C. Jones. A modelling approach for extruded plates. In *Tenth International Congress on Sound and Vibration, 7-10 July 2003, Stockholm, Sweden*, number 882, July 2003.

REFERENCES

- [21] G. Xie, D. J. Thompson, and C. J. C. Jones. A modelling approach for the vibroacoustic behaviour of aluminium extrusions used in railway vehicles. *Journal of Sound and Vibration*, 293:921–932, 2006.
- [22] G. Xie, D. J. Thompson, and C. J. C. Jones. Mode count and modal density of structural systems: relationships with boundary conditions. *Journal of Sound and Vibration*, 274:621–651, 2004.
- [23] C. Pezerat and J. L. Guyader. Analytical modelling of extruded plates. In *Proceedings of Euronoise, Naples 2003*, pages 1–6, 2003.
- [24] M. El-Raheb. Frequency response of a two-dimensional trusslike periodic panel. *J. Acoust. Soc. Am.*, 101(6):3457–3465, June 1997.
- [25] Y. Y. Pang. Modelling sound transmission through floor structures in trains based on extruded profiles. In *Nordic Vibration Research 2004, KTH Stockholm, June 3-4*, 2004.
- [26] C. M. Nilsson and C. Jones. A coupled waveguide finite and boundary element method for calculating the sound transmission through complex panel structures. In Michael J. Brennan, editor, *IX International Conference on Recent Advances in Structural Dynamics*. Institute of Sound and Vibration Research, University of Southampton, UK, 2006.
- [27] J. Signorelli and A. H. Von Flotow. Wave propagation, power flow, and resonance in a truss beam. *Journal of Sound and Vibration*, 126(1):127–144, 1988.
- [28] E. Emaci, M. A. F. Azeez, and A. F. Vakakis. Dynamics of trusses: numerical and experimental results. *Journal of Sound and Vibration*, 214(5):953–964, 1998.
- [29] M. Ruzzene. Vibration and sound radiation of sandwich beams with honeycomb truss core. *Journal of Sound and Vibration*, 277:741–763, 2004.
- [30] Vladimir Kolousek. *Dynamics in engineering structures*. ACADEMIA - Czechoslovak academy of sciences (also published by Butterworth & Co. Ltd), 1 edition, 1973.
- [31] R. E. D. Bishop and D. C. Johnson. *The mechanics of vibration*. Cambridge University Press, 1979.
- [32] L. Cremer, M. Heckl, and B. A. T. Petersson. *Structure-Borne Sound*. Springer, 3rd edition, 2005.

REFERENCES

- [33] D. J. Mead. *Passive Vibration Control*. John Wiley & Sons, Chichester, 1998.
- [34] K. Tamm and O. Weis. Untersuchungen über periodische Wellen, exponentielle und komplexe Nahfelder im begrenzten Festkörper. *ACUSTICA*, 9:275–288, 1959.
- [35] R. C. Engels. Response of infinite periodic structures. *Journal of Sound and Vibration*, 69(2), 1980.
- [36] D. J. Thompson. Wheel-rail noise generation, III: Rail vibration. *Journal of Sound and Vibration*, 161(3):421–446, 1993.
- [37] G. P. Brown. Determining the response of infinite, one-dimensional, non-uniform periodic structures by substructuring using waveshape coordinates. *Journal of Sound and Vibration*, 287:505–523, 2005.
- [38] R. S. Langley and N. S. Bardell. The response of two-dimensional periodic structures to harmonic point loading: A theoretical and experimental study of a beam grillage. *Journal of Sound and Vibration*, 207(4):521–535, 1997.
- [39] M. Ruzzene and P. Tsopelas. Control of wave propagation in sandwich plate rows with periodic honeycomb core. *Journal of Engineering Mechanics*, 129(9):975–986, 2003.
- [40] D. Duhamel, B. R. Mace, and M. J. Brennan. Finite element analysis of the vibrations of waveguides and periodic structures. *Journal of Sound and Vibration*, 294(1-2):205–220, 2006.
- [41] B. R. Mace, D. Duhamel, M. J. Brennan, and L. Hinke. Finite element prediction of wave motion in structural waveguides. *J. Acoust. Soc. Am.*, 117(5):2835–2843, May 2005.
- [42] K. Grosh and E. G. Williams. Complex wave-number decomposition of structural vibrations. *J. Acoust. Soc. Am.*, 93(2):836–848, 1993.
- [43] J. G. McDaniel and W. S. Shepard Jr. Estimation of structural wave numbers from spatially sparse response measurements. *J. Acoust. Soc. Am.*, 108(4):1674–1682, 2000.
- [44] P. J. Halliday and K. Grosh. Maximum likelihood estimation of structural wave components from noisy data. *J. Acoust. Soc. Am.*, 111(4):1709–1717, 2002.

REFERENCES

- [45] J. Berthaut, M. N. Ichchou, and L. Jezequel. K-space identification of apparent structural behaviour. *Journal of Sound and Vibration*, 280:1125–1131, 2005.
- [46] N. S. Ferguson, C. R. Halkyard, B. R. Mace, and K. H. Heron. The estimation of wavenumbers in two-dimensional structures. In *Proc. of ISMA 2002, Leuven*, 2002.
- [47] C. R. Halkyard. Maximum likelihood estimation of flexural wavenumbers in lightly damped plates. *Journal of Sound and Vibration*, 300:217–240, 2007.
- [48] O. Bareille, M. Ichchou, J. Berthaut, and L. Jezequel. Numerical extraction of dispersion curves from experimental data. In *NOVEM 2005, St. Raphael, France*, 2005.
- [49] T. Kohrs and B. A. T. Petersson. Wave guiding effects in light weight plates with truss-like core geometries. In *19th INTERNATIONAL CONGRESS ON ACOUSTICS MADRID, 2-7 SEPTEMBER 2007*, 2007.
- [50] R. S. Langley. The response of two-dimensional periodic structures to point harmonic forcing. *Journal of Sound and Vibration*, 197(4):447–469, 1996.
- [51] D. J. Mead, D. C. Zhu, and N. S. Bardell. Free vibration of an orthogonally stiffened flat plate. *Journal of Sound and Vibration*, 127(1):19–48, 1988.
- [52] S. M. Jeong and M. Ruzzene. Analysis of vibration and wave propagation in cylindrical grid-like structures. *Shock and Vibration*, 11:311–331, 2004.
- [53] S. Finnveden. Exact spectral finite element analysis of stationary vibrations in a railway car structure. *Acta Acustica*, 2:461–482, December 1994.
- [54] J. Gomez, E. G. Vadillo, and J. Santamaria. A comprehensive track model for the improvement of corrugation models. *Journal of Sound and Vibration*, 293:522–534, 2006.
- [55] I. Bartoli, A. Marzani, L. Lanza di Scalea, and E. Viola. Modeling wave propagation in damped waveguides of arbitrary cross-section. *Journal of Sound and Vibration*, 295:586–707, 2006.

REFERENCES

- [56] W. X. Zhong and F. W. Williams. On the direct solution of wave propagation for repetitive structures. *Journal of Sound and Vibration*, 181(3):485–501, 1995.
- [57] L. Houillon, M. N. Ichchou, and L. Jezequel. Wave motion in thin-walled structures. *Journal of Sound and Vibration*, 281:483–507, 2005.
- [58] Y. Waki, B. R. Mace, and M. J. Brennan. On numerical issues for the wave/finite element method. Technical Memorandum No. 964, Institute of Sound and Vibration Research, University of Southampton, December 2006.
- [59] T. Hayashi, W.-J. Song, and J. L. Rose. Guided wave dispersion curves for a bar with an arbitrary cross-section, a rod and a rail example. *Ultrasonics*, 41:175–183, 2003.
- [60] T. Hayashi, C. Tamayama, and M. Murase. Wave structure analysis of guided waves in a bar with an arbitrary cross-section. *Ultrasonics*, 44:17–24, 2006.
- [61] D. J. Mead. An introduction to FE-PST the combined use of finite element analysis and periodic structure theory. Technical Memorandum No. 959, Institute of Sound and Vibration Research, University of Southampton, March 2006.
- [62] D. Weinberg. Development and comparison of the CQUADR element in NEiNASTRAN. online.
- [63] B. R. Mace. Periodically stiffened fluid-loaded plates, II: Response to line and point forces. *Journal of Sound and Vibration*, 73(4):487–504, 1980.
- [64] Y. Y. Pang. Modelling acoustic properties of trusslike periodic panels: Application to extruded aluminium profiles for rail vehicles. Master’s thesis, KTH Stockholm, Sweden, 2004.
- [65] Y. Waki, B. R. Mace, and M. J. Brennan. Vibration analysis of a tyre mode using the wave finite element method. In *19th International Congress on Acoustics, Madrid, 2-7 September 2007*, 2007.
- [66] R. J. Guyan. Reduction of stiffness and mass matrices. *AIAA J.*, 3:380, 1965.

REFERENCES

- [67] J. O’Callahan. A new procedure for an improved reduced system (IRS). In *Seventh International Modal Analysis Conference, Las Vegas, Nevada*, February 1989.
- [68] P. E. McGowan, A. F. Angelucci, and M. Javeed. Dynamic test/analysis correlation using reduced analytical models. NASA Technical Memorandum 107671, Langley Research Center, Hampton, Virginia, September 1992.
- [69] C. Hoever. Experimental evaluation of dispersion characteristics. Project report, Institute of Fluid Mechanics and Engineering Acoustics, Technische Universität Berlin, Germany, December 2007.
- [70] T. Kohrs and B. A. T. Petersson. Investigation of the two-dimensional wave propagation in typical light-weight profiles. In Michael J. Brennan, editor, *IX International Conference on Recent Advances in Structural Dynamics*. Institute of Sound and Vibration Research, University of Southampton, Southampton, UK, 2006.
- [71] Eugen Skudrzyk. The mean-value method of predicting the dynamic response of complex vibrators. *J. Acoust. Soc. Am.*, 67(4):1105–1135, 1980.
- [72] L. Cohen. *Time-Frequency Analysis*. Prentice-Hall, Englewood Cliffs, NJ, 1995.
- [73] Y. Y. Kim and E.-H. Kim. Effectiveness of the continuous wavelet transform in the analysis of some dispersive elastic waves. *J. Acoust. Soc. Am.*, 110(1):86–94, 2001.
- [74] W. H. Prosser, D. Seale, and B. T. Smith. Time-frequency analysis of the dispersion of Lamb modes. *J. Acoust. Soc. Am.*, 105(5):2669–2676, 1999.
- [75] R. Büssow. An algorithm for the continuous morlet wavelet transform. *Mechanical Systems and Signal Processing*, 21(8):2970–2979, 2007.
- [76] F. Auger, P. Flandrin, P. Goncalves, and O. Lemoine. Matlab time-frequency toolbox tutorial, 1996.
- [77] F. Fahy and P. Gardonio. *Sound and structural vibration: Radiation, transmission and response*. Elsevier, Amsterdam, 2 edition, 2007.
- [78] D. J. Ewins. *Modal Testing: Theory, Practice and Application*. Research Studies Press, Baldock, second edition, 2003.

Appendix A

Slope deflection method and subsystem dynamic stiffness matrix

Betti's reciprocal theorem, extended by Maxwell for dynamics, states that if there is a mechanical system under two different load situations \mathbf{F}_1 and \mathbf{F}_2 , which are equilibrium states with displacements $\boldsymbol{\xi}_1$ and $\boldsymbol{\xi}_2$, the work of forces \mathbf{F}_1 acting through displacements $\boldsymbol{\xi}_2$ is equal to the work of forces \mathbf{F}_2 acting through displacements $\boldsymbol{\xi}_1$. In vector notation it can be expressed by the following equation

$$\mathbf{F}_1 \cdot \boldsymbol{\xi}_2 = \mathbf{F}_2 \cdot \boldsymbol{\xi}_1 \quad (\text{A.1})$$

The equations of motion can be developed by applying the reciprocal theorem n times (for n degrees of freedom) in succession to two states of the system. One is always the actual state of motion and the others are auxiliary states, in the slope deflection case unit displacements (rotations) for the considered degree of freedom with all other displacements and rotations set to zero (blocked boundary conditions). This method results in a system of equations, in which the left side consists only of the force (moment) loadings multiplied by the corresponding unit displacements (rotations). The right side consist of the forces and moments in the case of unit displacement (with all other degrees of freedom blocked) multiplied by the unknown displacements and rotations.

Considering external harmonic excitation at joint g with an external moment M_g , an external horizontal force X_g and a vertical force Y_g there will be a harmonic response at the joint with rotational angle φ_g , horizontal displacement u_g and vertical displacement v_g . Applying successively auxiliary states using unit rotation and unit displacements, illustrated in figure A.1

APPENDIX A. SLOPE DEFLECTION METHOD AND SUBS. DYN.
STIFFNESS MATRIX

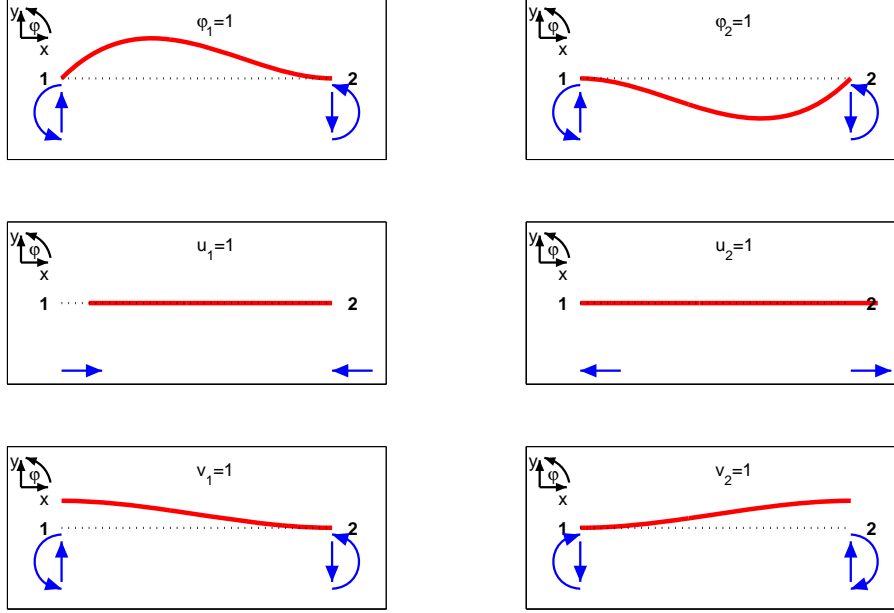


Figure A.1: Auxiliary unit displacement states of a single beam element (longitudinal and bending vibrations included)

for a single beam, the reciprocal theorem delivers the following system of equations.

$$\begin{aligned}
 M_g \cdot 1 \text{ rad} &= \varphi_g \sum_h M_{gh}^{\varphi_g} + \sum_h M_{hg}^{\varphi_h} \varphi_h + u_g \sum_h X_{gh}^{\varphi_g} + \sum_h X_{hg}^{\varphi_h} u_h + v_g \sum_h Y_{gh}^{\varphi_g} + \sum_h Y_{hg}^{\varphi_h} v_h \\
 X_g \cdot 1 \text{ m} &= \varphi_g \sum_h M_{gh}^{u_g} + \sum_h M_{hg}^{u_h} \varphi_h + u_g \sum_h X_{gh}^{u_g} + \sum_h X_{hg}^{u_h} u_h + v_g \sum_h Y_{gh}^{u_g} + \sum_h Y_{hg}^{u_h} v_h \\
 Y_g \cdot 1 \text{ m} &= \varphi_g \sum_h M_{gh}^{v_g} + \sum_h M_{hg}^{v_h} \varphi_h + u_g \sum_h X_{gh}^{v_g} + \sum_h X_{hg}^{v_h} u_h + v_g \sum_h Y_{gh}^{v_g} + \sum_h Y_{hg}^{v_h} v_h
 \end{aligned} \tag{A.2}$$

Here $M_{gh}^{\varphi_g}$ is the moment at end g of bar gh at $\varphi_g = 1$ rad. $X_{hg}^{\varphi_h}$ is the horizontal force at end h of bar gh at $\varphi_h = 1$ rad etc. Accordingly $M_{gh}^{u_g}$ is the moment at point g of bar gh resulting from $u_g = 1$ m.

The resulting system of equations can be written in a condensed matrix form using the dynamic stiffness matrix \mathbf{K} :

$$\mathbf{K}\boldsymbol{\xi} = \mathbf{F} \tag{A.3}$$

The end forces and moments for unit displacement or rotation, necessary

APPENDIX A. SLOPE DEFLECTION METHOD AND SUBS. DYN.
STIFFNESS MATRIX

to establish the elements of the matrix \mathbf{K} are tabulated in standard dynamics text books, e.g. [30, 31].

For the subsystem sketched in Fig. 2.1 the elements of the dynamic stiffness matrix are given by:

$$\begin{aligned}
 k_{1,1} &= M_{13}^{\varphi_1}, & k_{1,3} &= Y_{13}^{\varphi_1}, & k_{1,7} &= M_{31}^{\varphi_1}, & k_{1,9} &= Y_{31}^{\varphi_1} \\
 k_{2,2} &= X_{13}^{u_1}, & k_{2,8} &= X_{31}^{u_1} \\
 k_{3,3} &= Y_{13}^{v_1}, & k_{3,7} &= M_{31}^{v_1}, & k_{3,9} &= Y_{31}^{v_1} \\
 k_{4,4} &= M_{23}^{\varphi_2} + M_{24}^{\varphi_2}, & k_{4,5} &= X_{23}^{\varphi_2}, & k_{4,6} &= Y_{23}^{\varphi_2} + Y_{24}^{\varphi_2}, & k_{4,7} &= M_{32}^{\varphi_2}, \\
 & & k_{4,8} &= X_{32}^{\varphi_2}, & k_{4,9} &= Y_{32}^{\varphi_2}, & k_{4,10} &= M_{42}^{\varphi_2}, & k_{4,12} &= Y_{42}^{\varphi_2} \\
 k_{5,5} &= X_{23}^{u_2} + X_{24}^{u_2}, & k_{5,6} &= Y_{23}^{u_2}, & k_{5,7} &= M_{32}^{u_2}, & k_{5,8} &= X_{32}^{u_2}, \\
 & & k_{5,9} &= Y_{32}^{u_2}, & k_{5,11} &= X_{42}^{u_2} \\
 k_{6,6} &= Y_{23}^{v_2} + Y_{24}^{v_2}, & k_{6,7} &= M_{32}^{v_2}, & k_{6,8} &= X_{32}^{v_2}, & k_{6,9} &= Y_{32}^{v_2}, \\
 & & k_{6,10} &= M_{42}^{v_2}, & k_{6,12} &= Y_{42}^{v_2} \\
 k_{7,7} &= M_{31}^{\varphi_3} + M_{32}^{\varphi_3}, & k_{7,8} &= X_{32}^{\varphi_3}, & k_{7,9} &= Y_{31}^{\varphi_3} + Y_{32}^{\varphi_3} \\
 k_{8,8} &= X_{31}^{u_3} + X_{32}^{u_3}, & k_{8,9} &= Y_{32}^{u_3} \\
 k_{9,9} &= Y_{31}^{v_3} + Y_{32}^{v_3} \\
 k_{10,10} &= M_{42}^{\varphi_4}, & k_{10,12} &= Y_{24}^{\varphi_4} \\
 k_{11,11} &= X_{42}^{u_4} \\
 k_{12,12} &= Y_{24}^{v_4}
 \end{aligned} \tag{A.4}$$

As an example the forces and moments for the auxiliary states using Kolousek's beam functions F_i for bending vibration are shown for beam I between points 1 and 3 (see Fig. 2.1 and Eq. (A.5)). The beam functions are listed in Eq. (A.6). E_{13} is Young's modulus, I_{13} the cross sectional moment of inertia, S_{13} the cross sectional area, L_{13} the length of the beam, $\Lambda_{13} = L_{13}k_B = L_{13} \left(\frac{m'_{13}\omega^2}{E_{13}I_{13}} \right)^{1/4}$ the Helmholtz number for bending waves, m'_{13} the mass per unit length and $\Psi_{13} = L_{13} \left(\frac{m'_{13}\omega^2}{E_{13}S_{13}} \right)^{1/2}$ the Helmholtz number for longitudinal waves, ω denoting the angular frequency.

APPENDIX A. SLOPE DEFLECTION METHOD AND SUBS. DYN.
STIFFNESS MATRIX

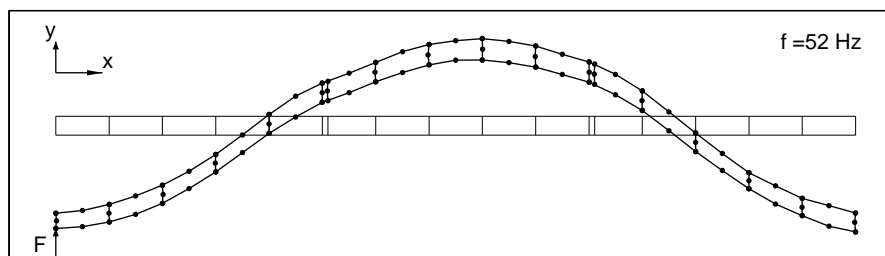
$$\begin{aligned}
M_{13}^{\varphi_1} &= \frac{E_{13}I_{13}}{L_{13}} F_2(\Lambda_{13}) \\
Y_{13}^{\varphi_1} &= -\left(\frac{E_{13}I_{13}}{L_{13}}\right)^2 F_4(\Lambda_{13}) \cos \alpha \\
M_{31}^{\varphi_1} &= \frac{E_{13}I_{13}}{L_{13}} F_1(\Lambda_{13}) \\
Y_{31}^{\varphi_1} &= -\left(\frac{E_{13}I_{13}}{L_{13}}\right)^2 F_3(\Lambda_{13}) \cos \alpha \\
X_{13}^{u_1} &= \frac{E_{13}S_{13}}{L_{13}} \Psi_{13} \cot \Psi_{13} (\cos \alpha)^2 + \left(\frac{E_{13}I_{13}}{L_{13}}\right)^3 F_6(\Lambda_{13}) (\sin \alpha)^2 \quad (\text{A.5}) \\
X_{31}^{u_1} &= -\frac{E_{13}S_{13}}{L_{13}} \Psi_{13} \csc \Psi_{13} (\cos \alpha)^2 + \left(\frac{E_{13}I_{13}}{L_{13}}\right)^3 F_5(\Lambda_{13}) (\sin \alpha)^2 \\
Y_{13}^{v_1} &= \frac{E_{13}S_{13}}{L_{13}} \Psi_{13} \cot \Psi_{13} (\sin \alpha)^2 + \left(\frac{E_{13}I_{13}}{L_{13}}\right)^3 F_6(\Lambda_{13}) (\cos \alpha)^2 \\
M_{31}^{v_1} &= \left(\frac{E_{13}I_{13}}{L_{13}}\right)^2 F_3(\Lambda_{13}) \cos \alpha \\
Y_{31}^{v_1} &= -\frac{E_{13}S_{13}}{L_{13}} \Psi_{13} \csc \Psi_{13} (\sin \alpha)^2 + \left(\frac{E_{13}I_{13}}{L_{13}}\right)^3 F_5(\Lambda_{13}) (\cos \alpha)^2
\end{aligned}$$

$$\begin{aligned}
F_1 &= -\Lambda \frac{\sinh \Lambda - \sin \Lambda}{\cosh \Lambda \cos \Lambda - 1} \\
F_2 &= -\Lambda \frac{\cosh \Lambda \sin \Lambda - \sinh \Lambda \cos \Lambda}{\cosh \Lambda \cos \Lambda - 1} \\
F_3 &= -\Lambda^2 \frac{\cosh \Lambda - \cos \Lambda}{\cosh \Lambda \cos \Lambda - 1} \\
F_4 &= \Lambda^2 \frac{\sinh \Lambda \sin \Lambda}{\cosh \Lambda \cos \Lambda - 1} \\
F_5 &= \Lambda^3 \frac{\sinh \Lambda + \sin \Lambda}{\cosh \Lambda \cos \Lambda - 1} \\
F_6 &= -\Lambda^3 \frac{\cosh \Lambda \sin \Lambda + \sinh \Lambda \cos \Lambda}{\cosh \Lambda \cos \Lambda - 1}
\end{aligned} \tag{A.6}$$

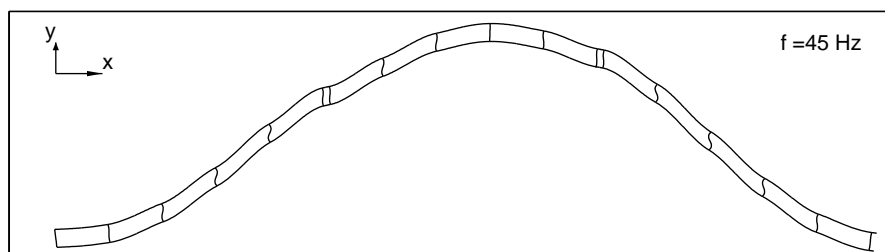
Appendix B

Comparison of measured and calculated deflection shapes of profile strip

In the comparison the identified frequency shift between measurement and calculation is included. The measured deflection shapes are constructed only from measured translational y -components at the positions indicated by small circles with linear interpolation in between.



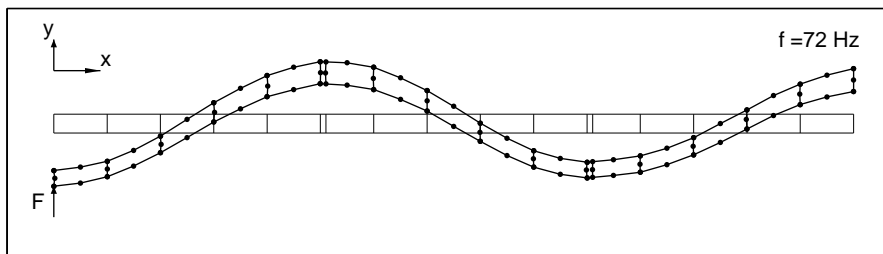
(a) Measured



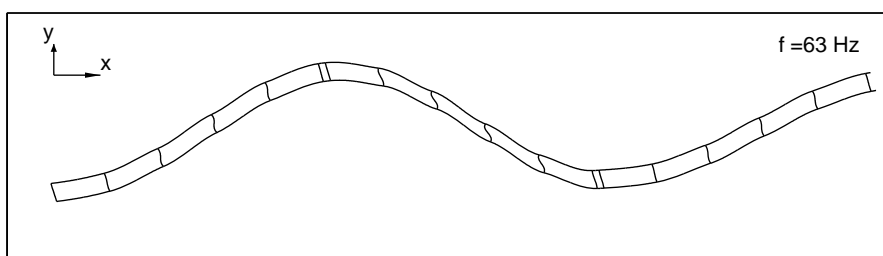
(b) Calculated, compatible frequency

Figure B.1: Comparison of deflection shapes

APPENDIX B. MEASURED AND CALCULATED DEFLECTION SHAPES OF PROFILE STRIP

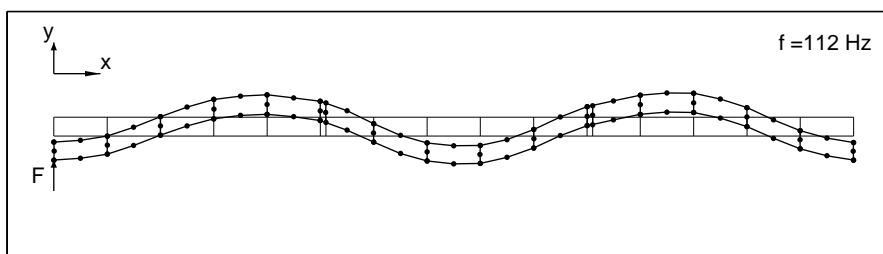


(a) Measured

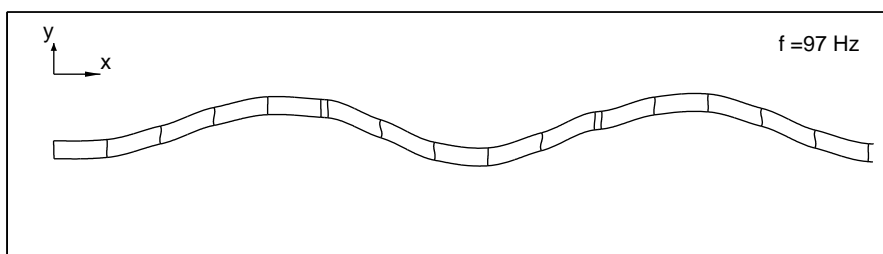


(b) Calculated, compatible frequency

Figure B.2: Comparison of deflection shapes



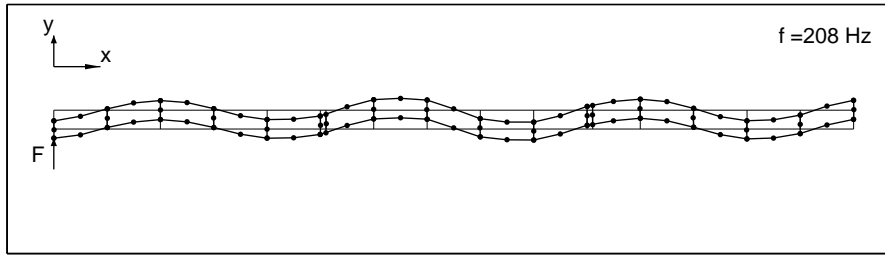
(a) Measured



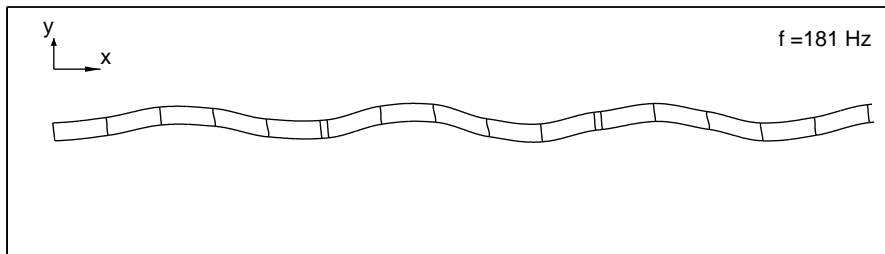
(b) Calculated, compatible frequency

Figure B.3: Comparison of deflection shapes

APPENDIX B. MEASURED AND CALCULATED DEFLECTION SHAPES OF PROFILE STRIP

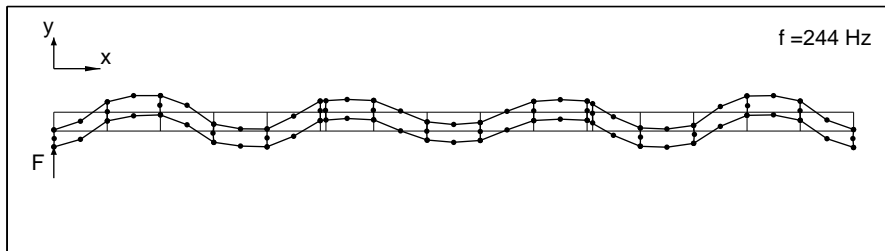


(a) Measured

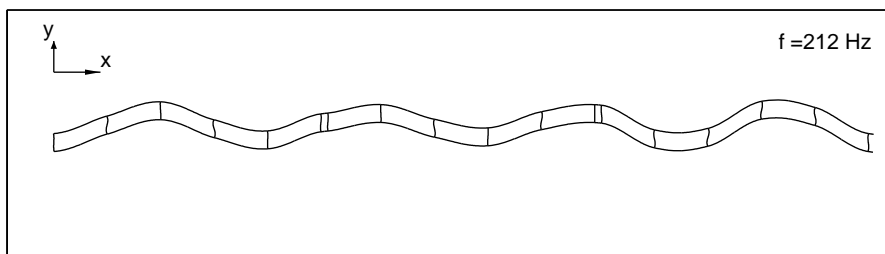


(b) Calculated, compatible frequency

Figure B.4: Comparison of deflection shapes



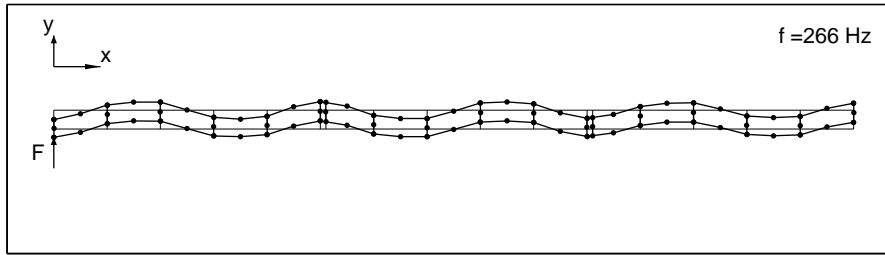
(a) Measured



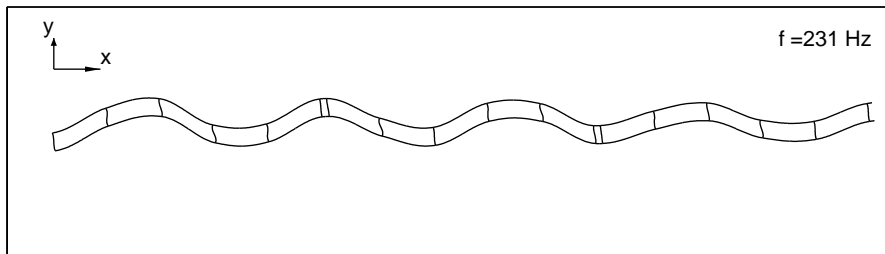
(b) Calculated, compatible frequency

Figure B.5: Comparison of deflection shapes

APPENDIX B. MEASURED AND CALCULATED DEFLECTION SHAPES OF PROFILE STRIP

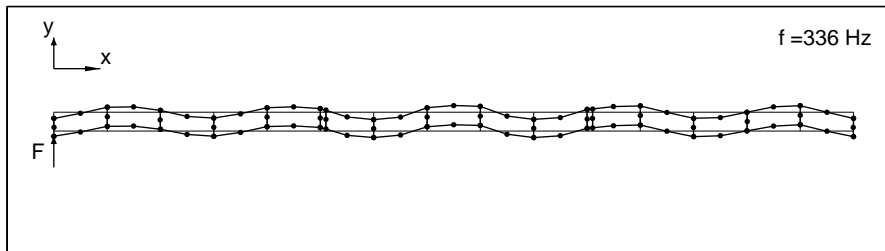


(a) Measured

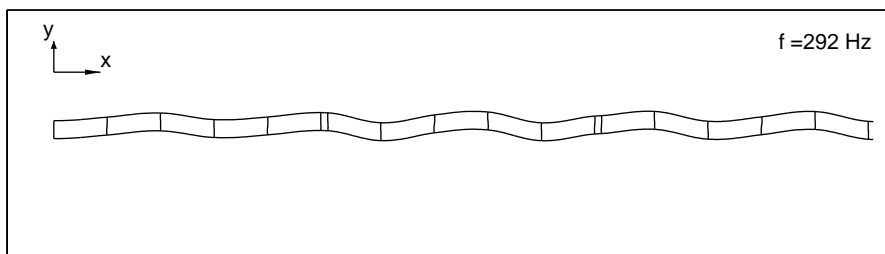


(b) Calculated, compatible frequency

Figure B.6: Comparison of deflection shapes



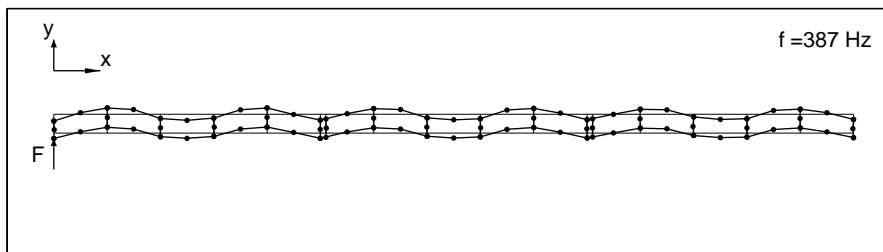
(a) Measured



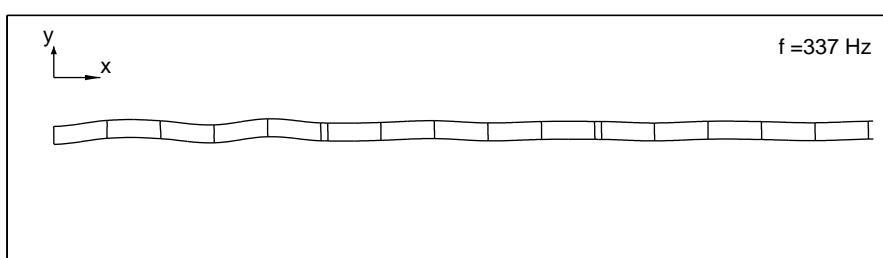
(b) Calculated, compatible frequency

Figure B.7: Comparison of deflection shapes

APPENDIX B. MEASURED AND CALCULATED DEFLECTION SHAPES OF PROFILE STRIP

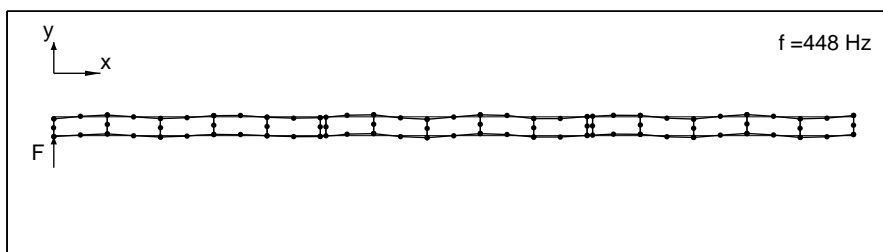


(a) Measured

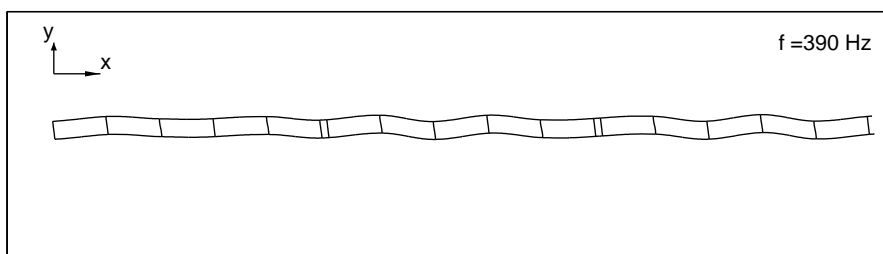


(b) Calculated, compatible frequency

Figure B.8: Comparison of deflection shapes. The higher damping results from a higher loss factor used in the calculations compared to the real, measured loss factor.



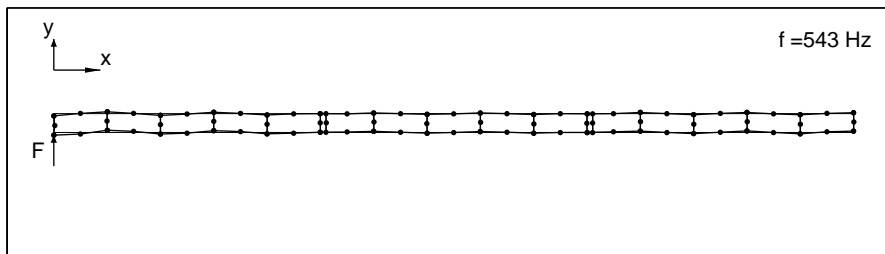
(a) Measured



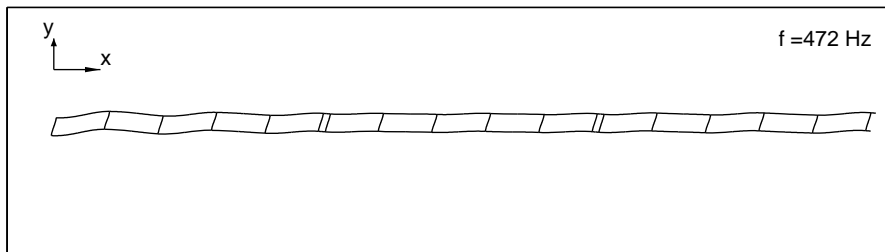
(b) Calculated, compatible frequency

Figure B.9: Comparison of deflection shapes

APPENDIX B. MEASURED AND CALCULATED DEFLECTION SHAPES OF PROFILE STRIP



(a) Measured



(b) Calculated, compatible frequency

Figure B.10: Comparison of deflection shapes. The rotational character of the calculated deflection shape is not included in the measured results as only the y -component is measured at the locations indicated by the small circles.

Appendix C

Profile strip spatial Fourier transform results

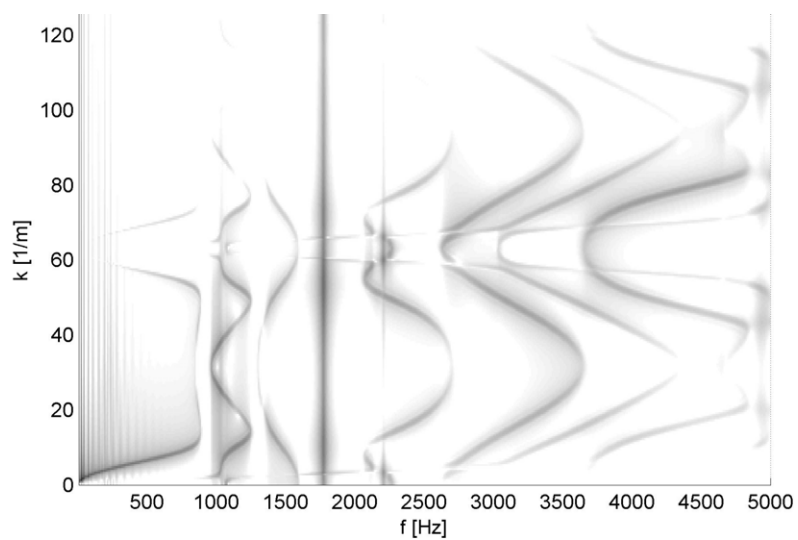


Figure C.1: DFT plot of lower flange of profile strip B, unit y -force excitation at left lower side, shading limits $L_{v,DFT}$: 10 (white) ... 90 (black) dB re. 5×10^{-8} m/s

APPENDIX C. PROFILE STRIP SPATIAL FOURIER TRANSFORM RESULTS

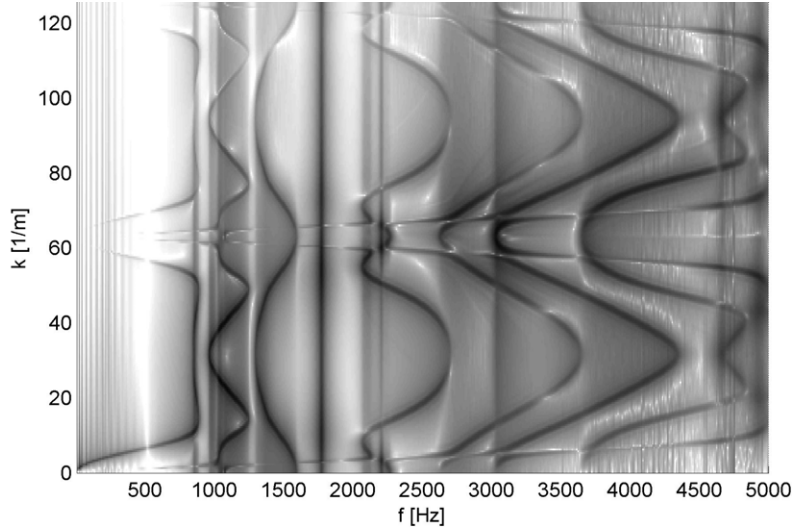


Figure C.2: DFT plot of lower flange of profile strip B, unit moment excitation at left lower side, shading limits $L_{v,DFT}$: 10 (white) ... 90 (black) dB re. 5×10^{-8} m/s

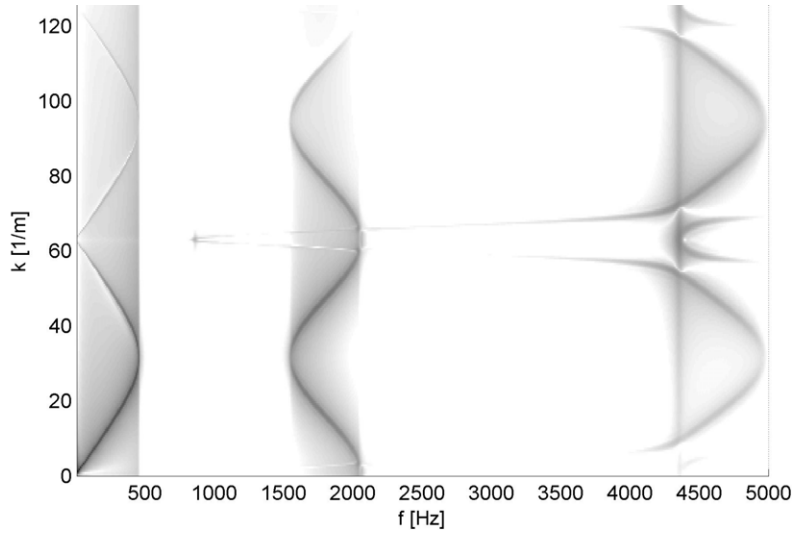


Figure C.3: DFT plot of lower flange of profile strip C, unit y -force excitation at left lower side, shading limits $L_{v,DFT}$: 10 (white) ... 90 (black) dB re. 5×10^{-8} m/s

APPENDIX C. PROFILE STRIP SPATIAL FOURIER TRANSFORM RESULTS

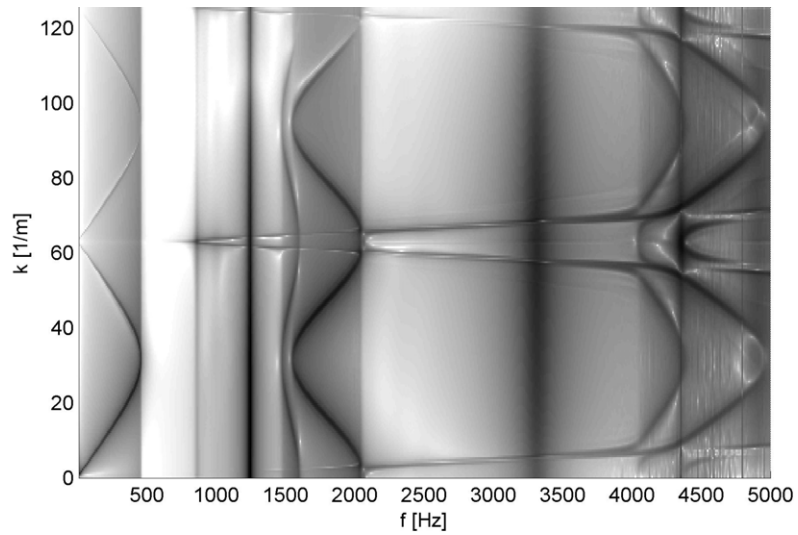
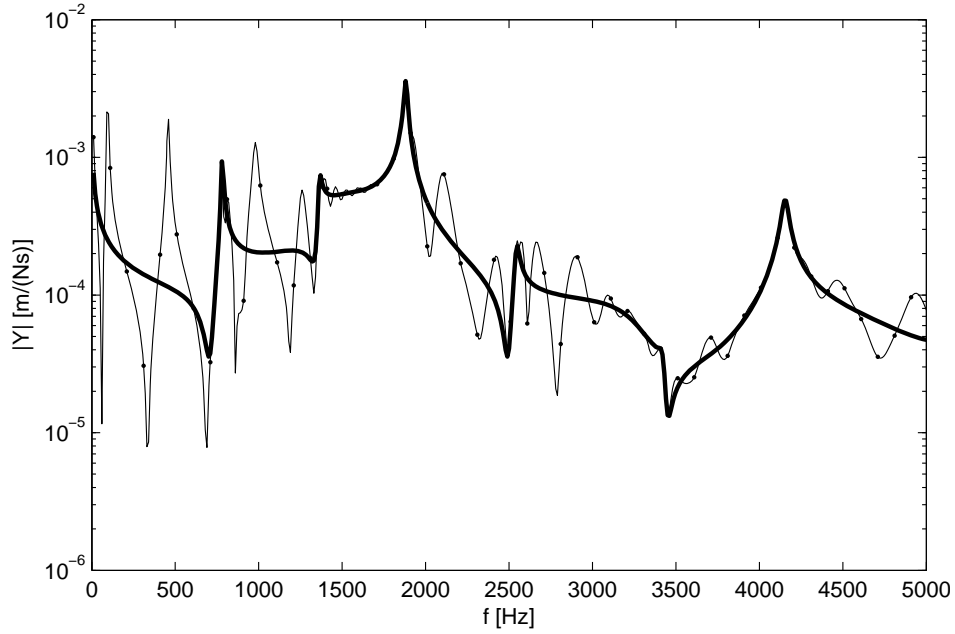


Figure C.4: DFT plot of lower flange of profile strip C, unit moment excitation at left lower side, shading limits $L_{v,DFT} : 10$ (white) \dots 90 (black) dB re. 5×10^{-8} m/s

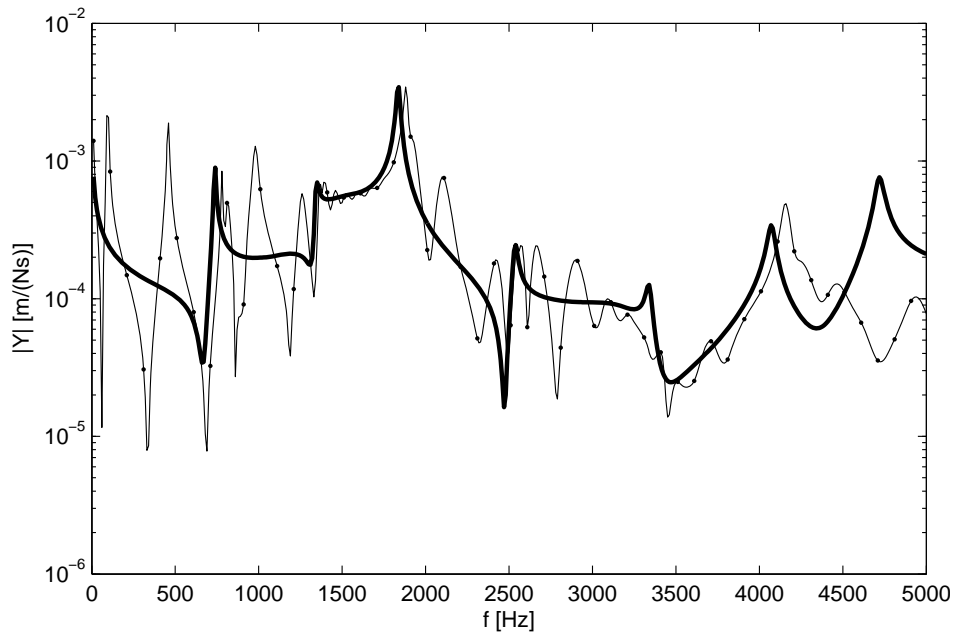
Appendix D

WFE forced response benchmark results

APPENDIX D. WFE FORCED RESPONSE BENCHMARK RESULTS



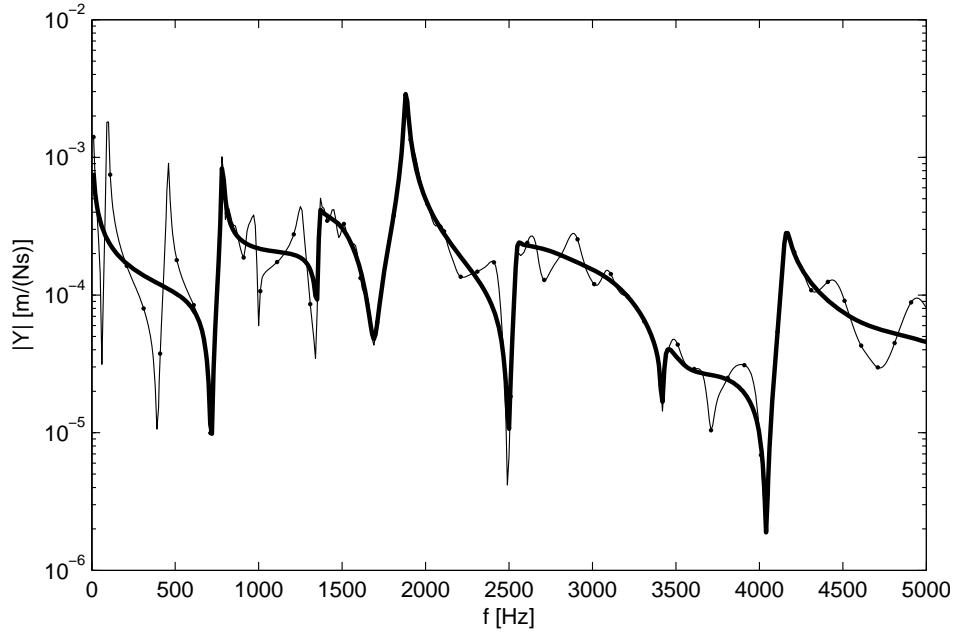
(a) 10 mm mesh



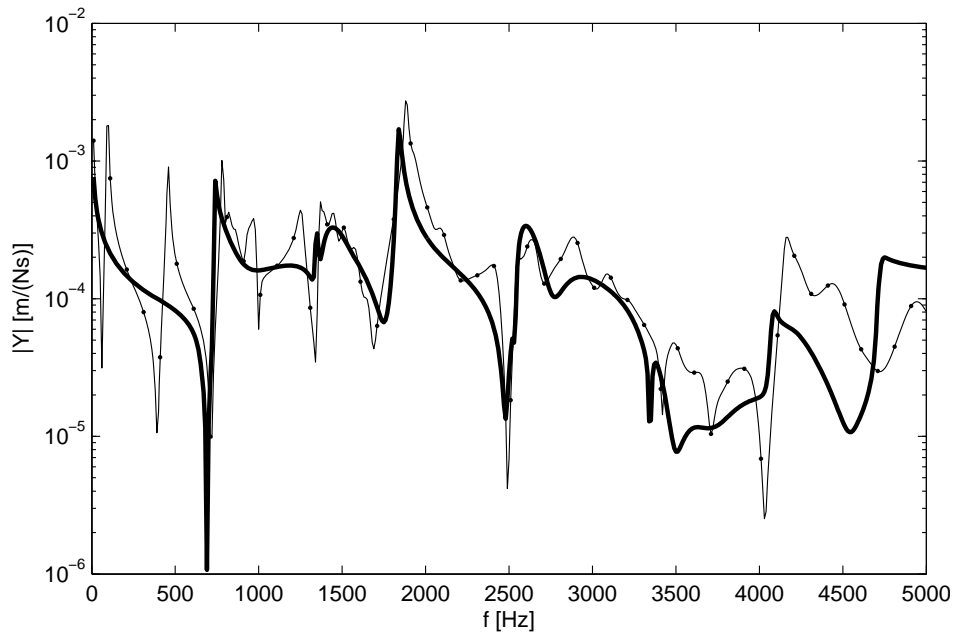
(b) 25 mm mesh

Figure D.1: Transfer mobility of profile A, two subelements, free boundary: Standard FE-results $-●-$ in comparison to WFE-results $-$ (bold) (Response at $x=0.1$ m, $y=0.05$ m, $z=0$) for two mesh sizes

APPENDIX D. WFE FORCED RESPONSE BENCHMARK RESULTS



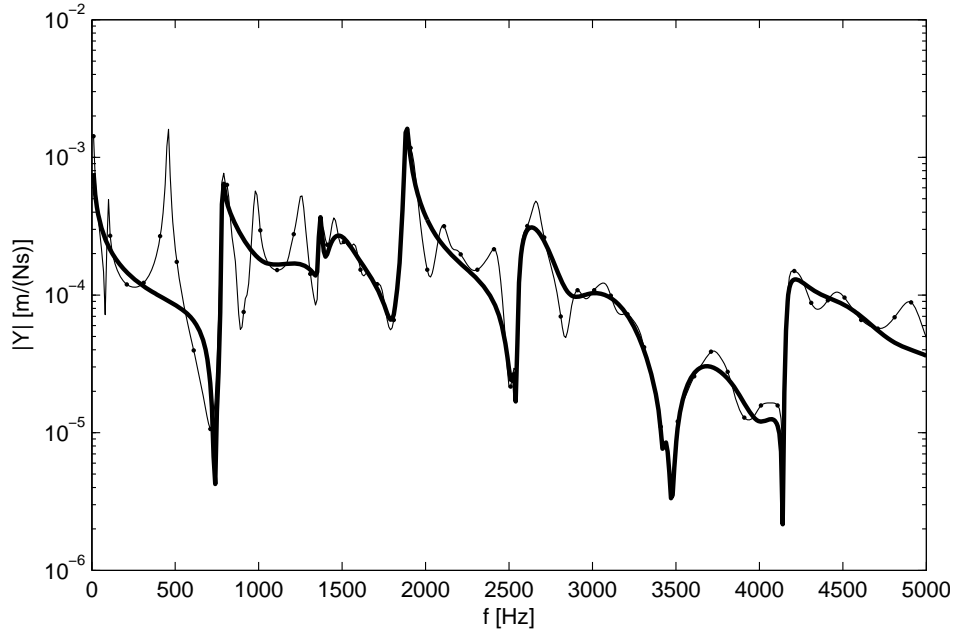
(a) 10 mm mesh



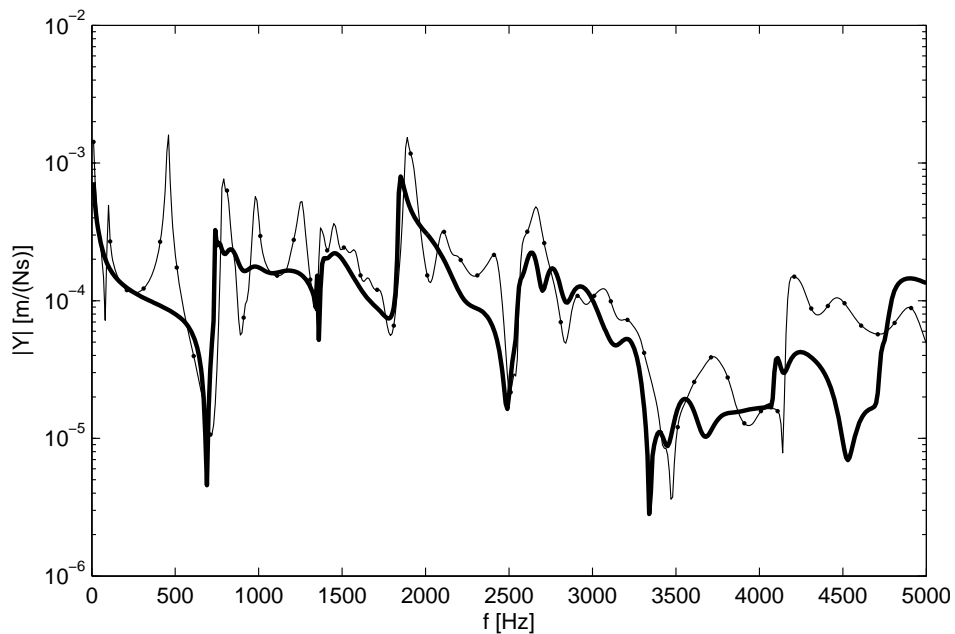
(b) 25 mm mesh

Figure D.2: Transfer mobility of profile A, two subelements, free boundary: Standard FE-results $-\bullet-$ in comparison to WFE-results $-(\text{bold})$ (Response at $x=0.1$ m, $y=0.05$ m, $z=0.2$ m) for two mesh sizes

APPENDIX D. WFE FORCED RESPONSE BENCHMARK RESULTS



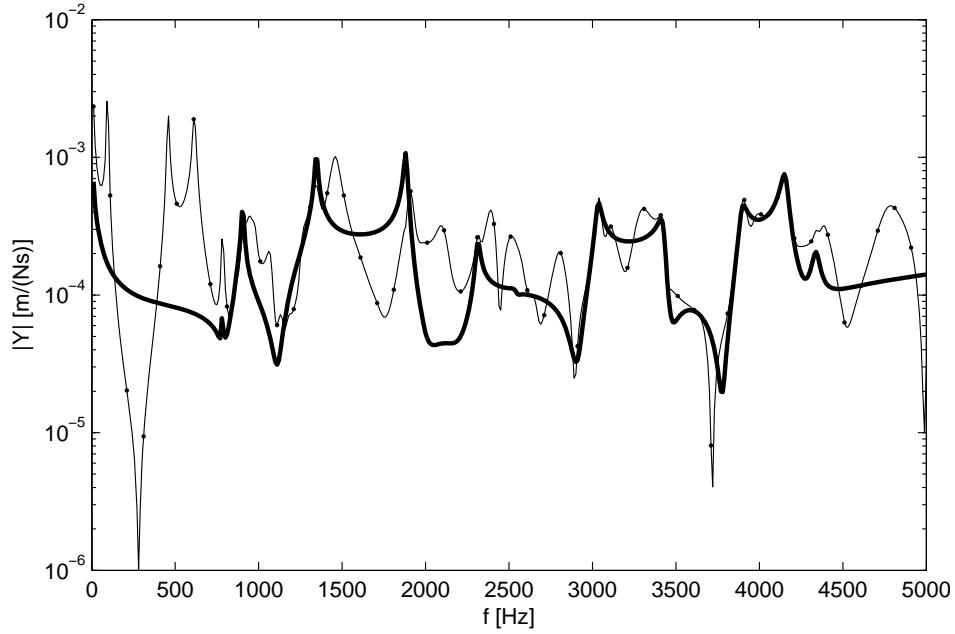
(a) 10 mm mesh



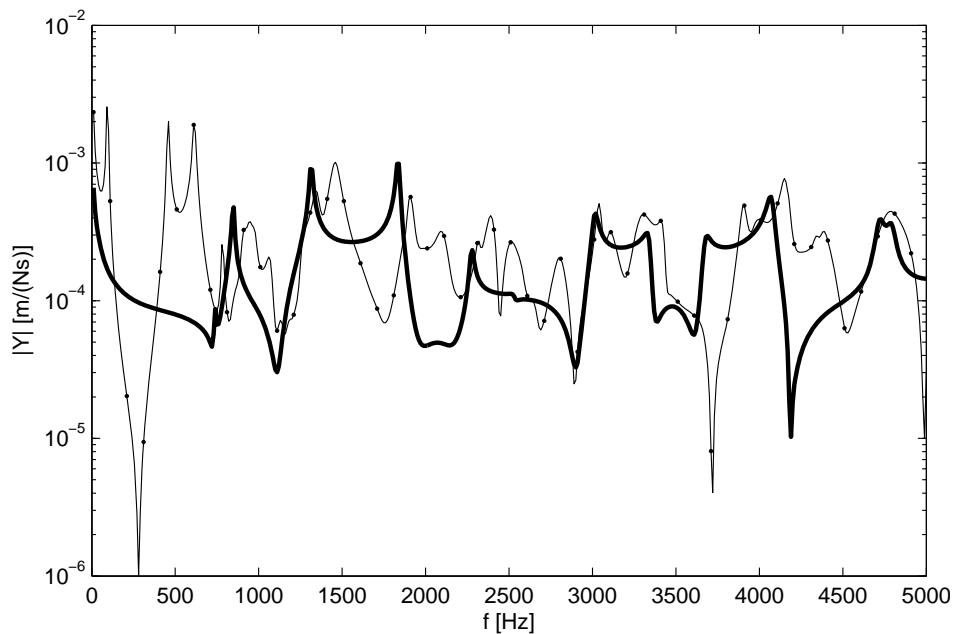
(b) 25 mm mesh

Figure D.3: Transfer mobility of profile A, two subelements, free boundary: Standard FE-results -●- in comparison to WFE-results -(bold) (Response at $x=0.1$ m, $y=0.05$ m, $z=0.5$ m) for two mesh sizes

APPENDIX D. WFE FORCED RESPONSE BENCHMARK RESULTS



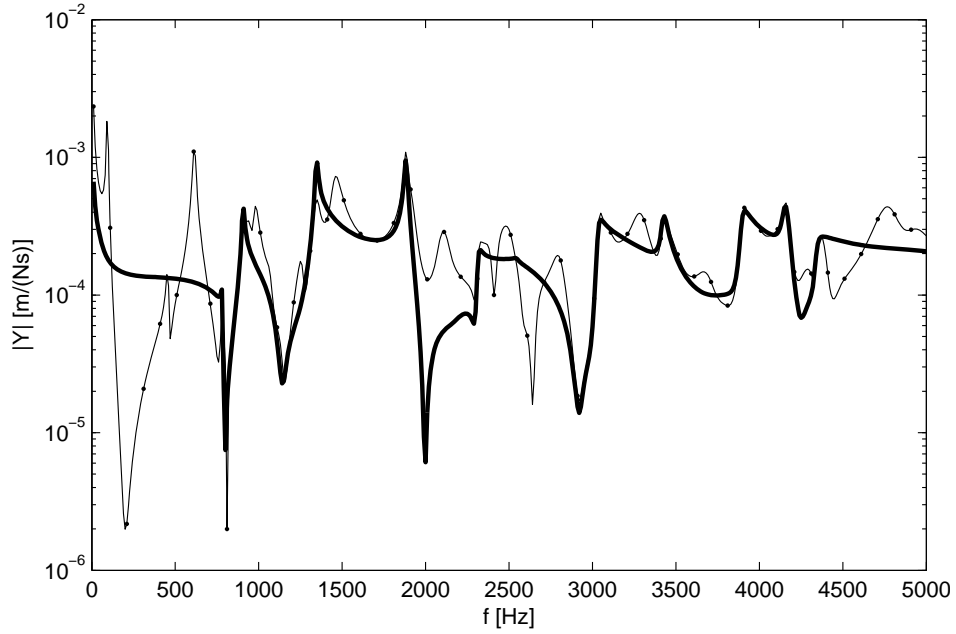
(a) 10 mm mesh



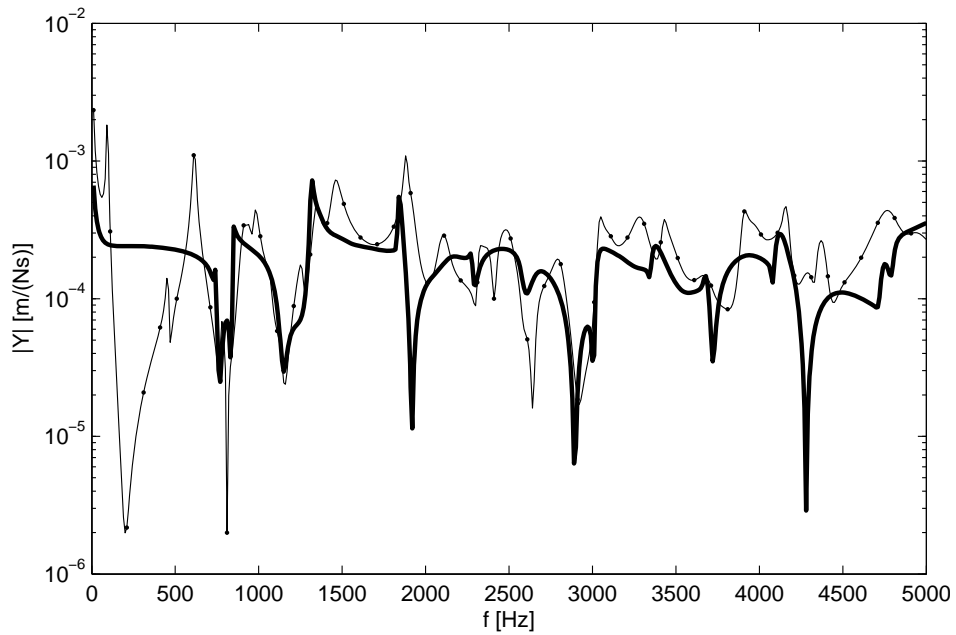
(b) 25 mm mesh

Figure D.4: Transfer mobility of profile A, two subelements, free boundary: Standard FE-results -•- in comparison to WFE-results -(bold) (Response at $x=0.2$ m, $y=0$, $z=0$) for two mesh sizes

APPENDIX D. WFE FORCED RESPONSE BENCHMARK RESULTS



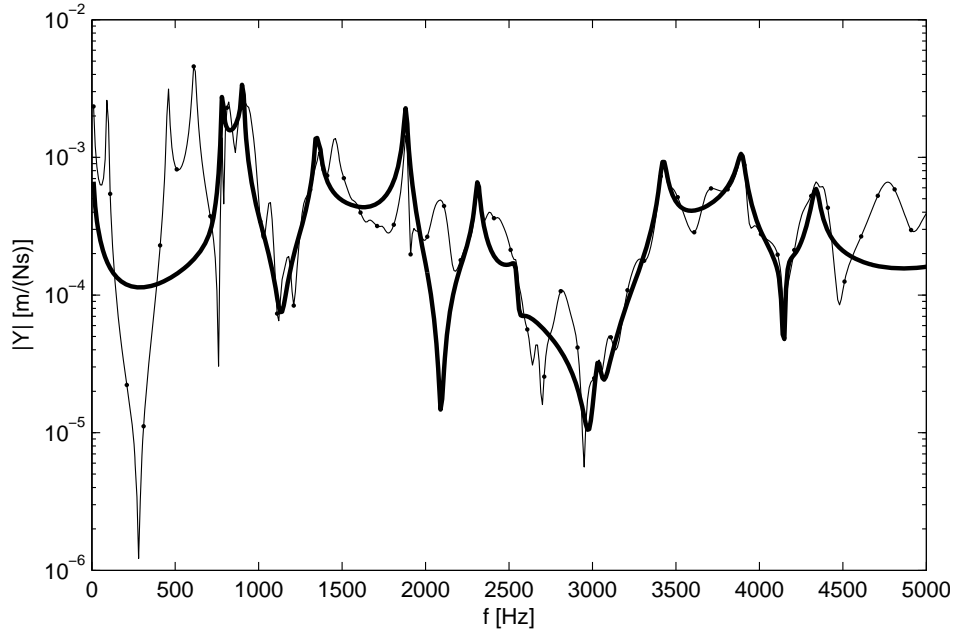
(a) 10 mm mesh



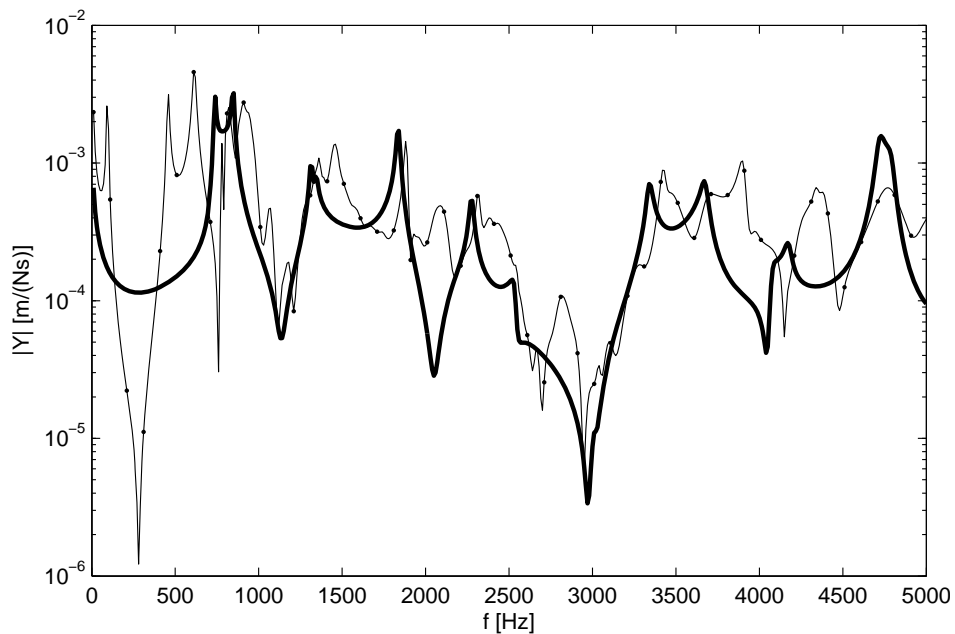
(b) 25 mm mesh

Figure D.5: Transfer mobility of profile A, two subelements, free boundary: Standard FE-results -•- in comparison to WFE-results -(bold) (Response at $x=0.2$ m, $y=0$, $z=0.3$ m) for two mesh sizes

APPENDIX D. WFE FORCED RESPONSE BENCHMARK RESULTS



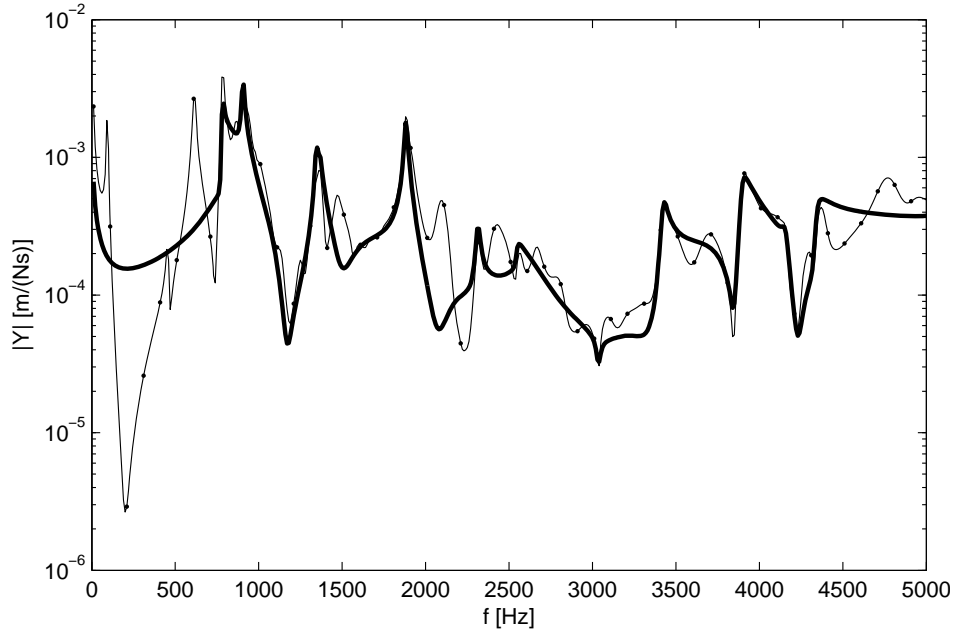
(a) 10 mm mesh



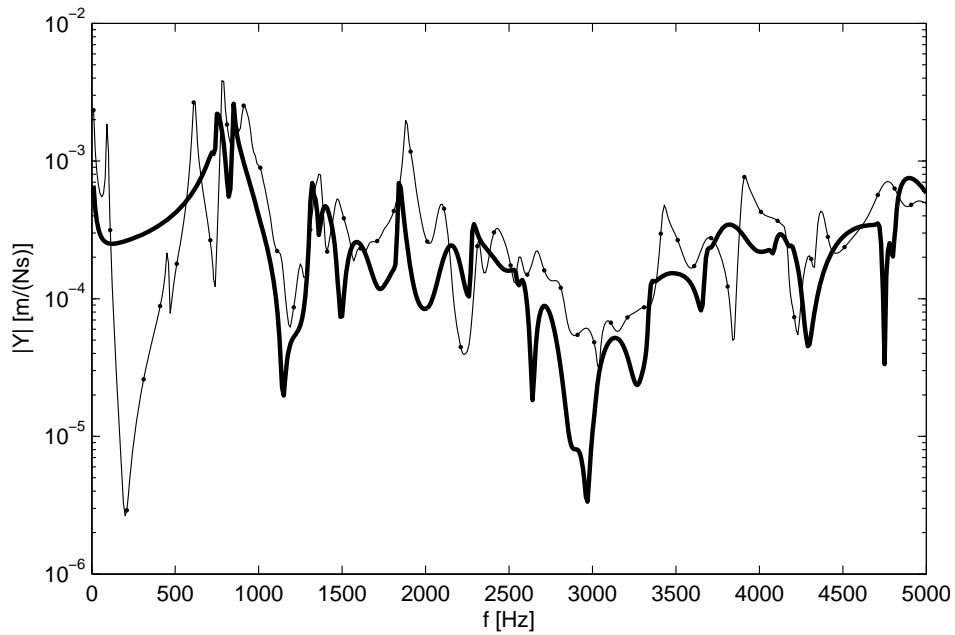
(b) 25 mm mesh

Figure D.6: Transfer mobility of profile A, two subelements, free boundary: Standard FE-results \bullet in comparison to WFE-results -- (bold) (Response at $x=0.2$ m, $y=0.05$ m, $z=0$) for two mesh sizes

APPENDIX D. WFE FORCED RESPONSE BENCHMARK RESULTS



(a) 10 mm mesh



(b) 25 mm mesh

Figure D.7: Transfer mobility of profile A, two subelements, free boundary: Standard FE-results $-\bullet-$ in comparison to WFE-results $-(\text{bold})$ (Response at $x=0.2$ m, $y=0.05$ m, $z=0.3$ m) for two mesh sizes

Appendix E

Inhomogeneous wave correlation method

The inhomogeneous wave correlation method (IWC) published by Berthaut and Bareille [48] is a method to determine two-dimensional dispersion characteristics from experimental (or numerical) data. The idea is to correlate a synthetic wave field resulting from a damped or undamped plane wave propagating in a certain direction with the measured or calculated field. In analogy with the Modal Assurance Criterion (MAC), [78], which is used to compare measured and calculated mode shapes of structures, an inhomogeneous wave correlation criterion is defined.

An estimated wave field \hat{W} , representing a plane propagating damped wave in direction θ is introduced,

$$\hat{W}_{k,\theta}(x, y) = e^{ik(\theta)(x \cos(\theta) + y \sin(\theta))} \quad \text{with} \quad k = k_{prop} + ik_{decay}. \quad (\text{E.1})$$

The correlation between the estimated wave field \hat{W} and the measured (or calculated) field W is quantified by introducing a correlation criterion:

$$IWC(k, \theta) = \frac{|\int \int_S W(x, y) \hat{W}_{k,\theta}(x, y)^* dx dy|}{\sqrt{\int \int_S |W(x, y)|^2 dx dy \int \int_S |\hat{W}_{k,\theta}(x, y)|^2 dx dy}} \quad (\text{E.2})$$

The criterion detects, how similar (in shape) this distribution is with the real measured distribution. The identification of the complex wavenumber k for a given direction θ can then be achieved by maximizing $IWC(k, \theta)$ for a fixed θ . Note that it is only possible to identify single wavenumbers in this way. When multiple wavenumbers are expected it is possible to use the

APPENDIX E. INHOMOGENEOUS WAVE CORRELATION METHOD

method in such a way that the magnitude of the IWC is plotted, where high correlation is expected for inherent waves.

For all practical applications, indeed, the integral will be reduced to sums over the sampled grid points.

The IWC can easily be modified from an angle-dependance handling to a handling of two-dimensional wavenumbers k_x and k_z . In fact this is only a question of representing the wavenumber in polar or cartesian space.

$$\hat{W}_{k_x, k_z}(x, z) = e^{i(k_x x + k_z z)} \quad (\text{E.3})$$

In this case k_x and k_z can be both complex including an imaginary damping fraction.

The advantage of the method for experimental wavenumber extraction is that the achievable resolution from a limited test area is higher than for the spatial Fourier transform. Moreover, the discrete, uniform sampling necessary for Fourier transform can be circumvented and less test positions are necessary which greatly simplifies the measurement procedure. In this thesis only purely propagating waves are extracted from the IWC.

Appendix F

Regional train floor section results

F.1 Measured and calculated displacement fields

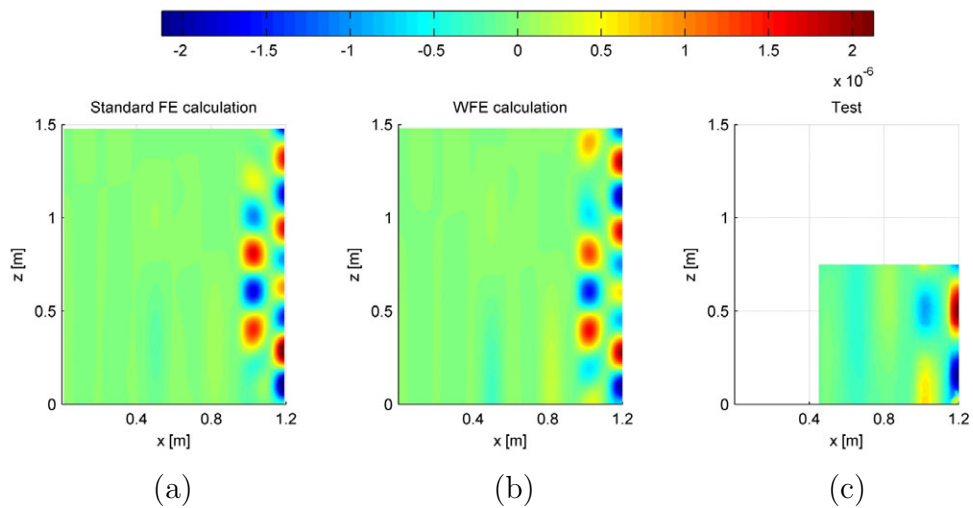


Figure F.1: Displacement field of forced response (F_y at the centre of plate field, lower right corner of plots), $f = 500$ Hz

APPENDIX F. REGIONAL TRAIN FLOOR SECTION RESULTS

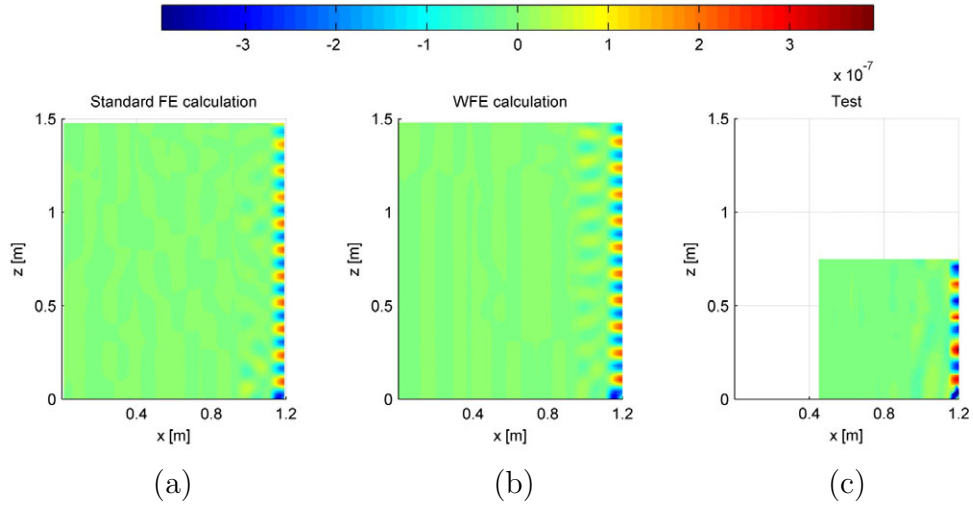


Figure F.2: Displacement field of forced response (F_y at the centre of plate field, lower right corner of plots), $f = 1500$ Hz

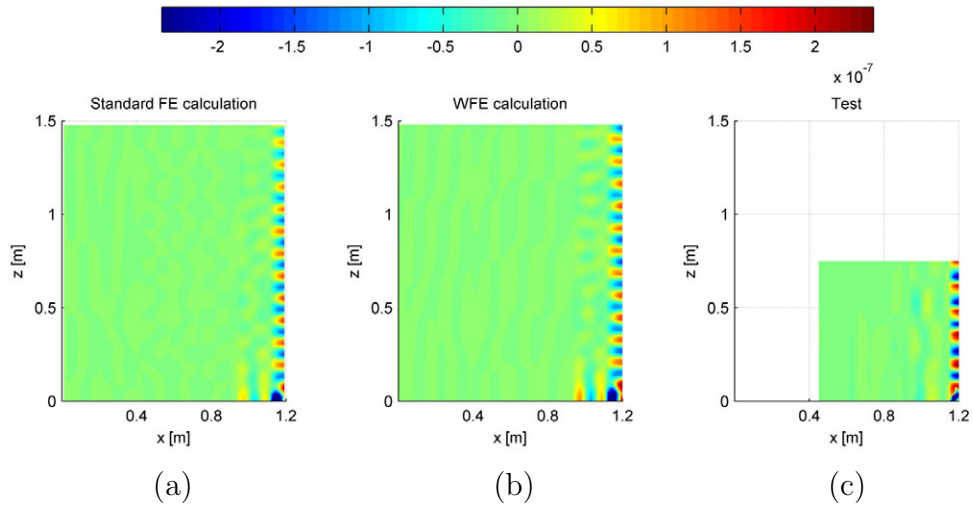


Figure F.3: Displacement field of forced response (F_y at the centre of plate field, lower right corner of plots), $f = 2000$ Hz

APPENDIX F. REGIONAL TRAIN FLOOR SECTION RESULTS

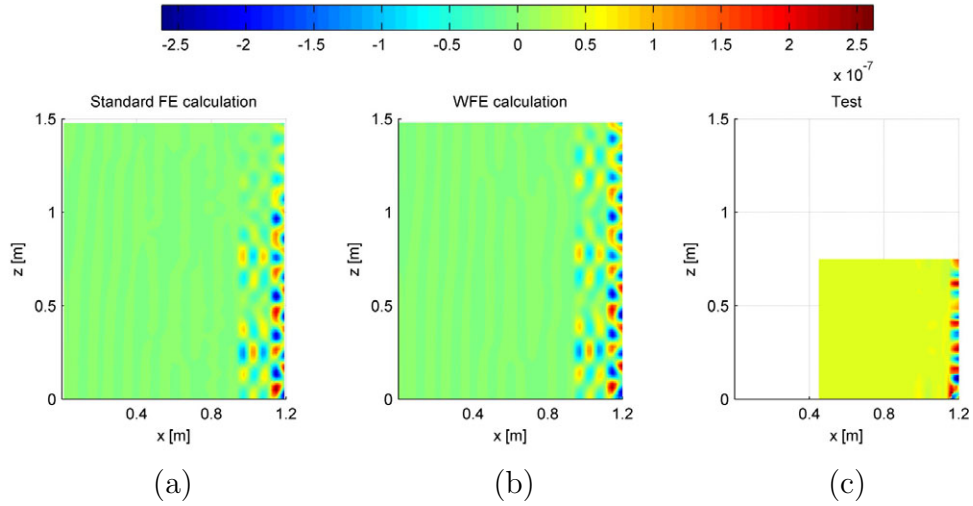


Figure F.4: Displacement field of forced response (F_y at the centre of plate field, lower right corner of plots), $f = 2500$ Hz

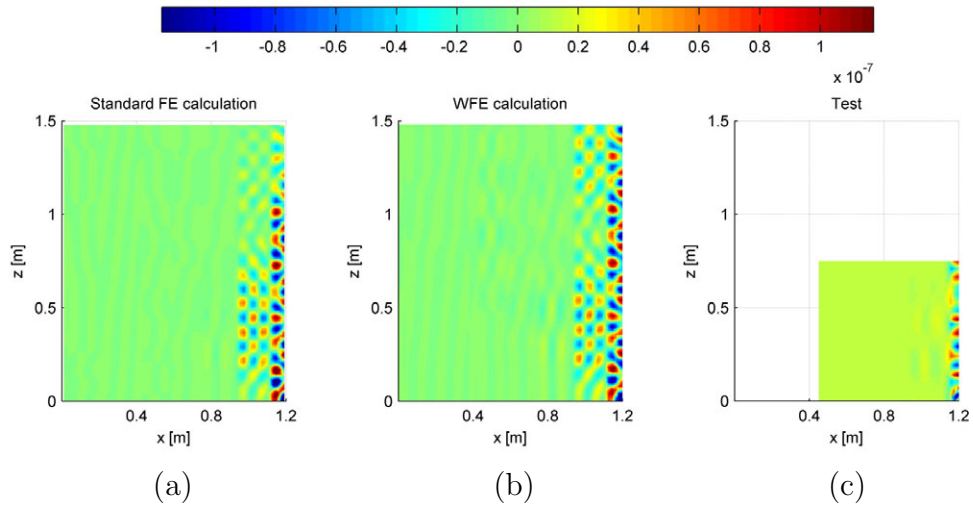


Figure F.5: Displacement field of forced response (F_y at the centre of plate field, lower right corner of plots), $f = 3000$ Hz

APPENDIX F. REGIONAL TRAIN FLOOR SECTION RESULTS

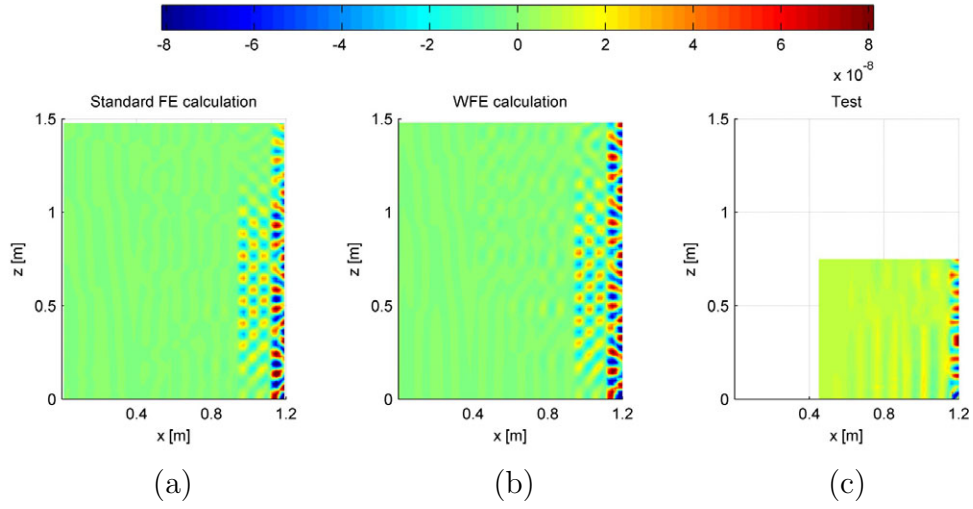


Figure F.6: Displacement field of forced response (F_y at the centre of plate field, lower right corner of plots), $f = 3500$ Hz

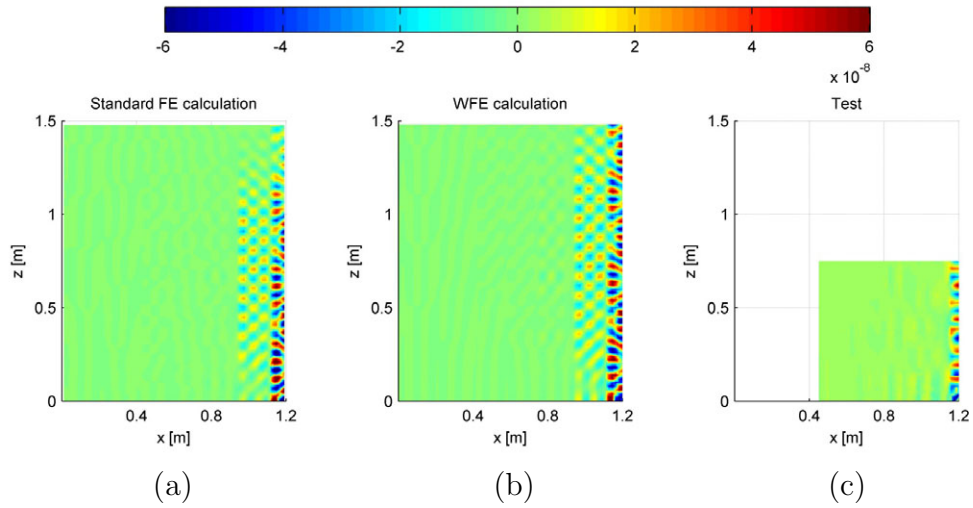


Figure F.7: Displacement field of forced response (F_y at the centre of plate field, lower right corner of plots), $f = 4000$ Hz

APPENDIX F. REGIONAL TRAIN FLOOR SECTION RESULTS

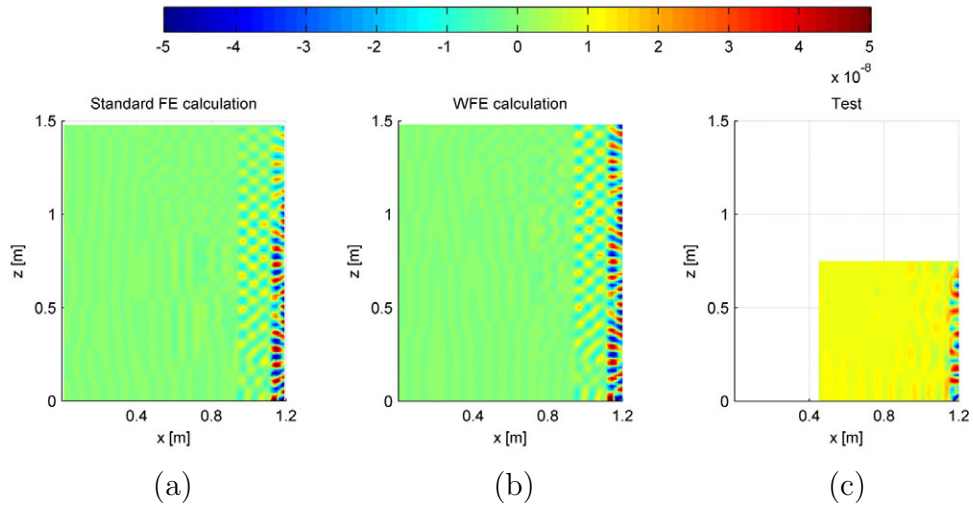


Figure F.8: Displacement field of forced response (F_y at the centre of plate field, lower right corner of plots), $f = 4500$ Hz

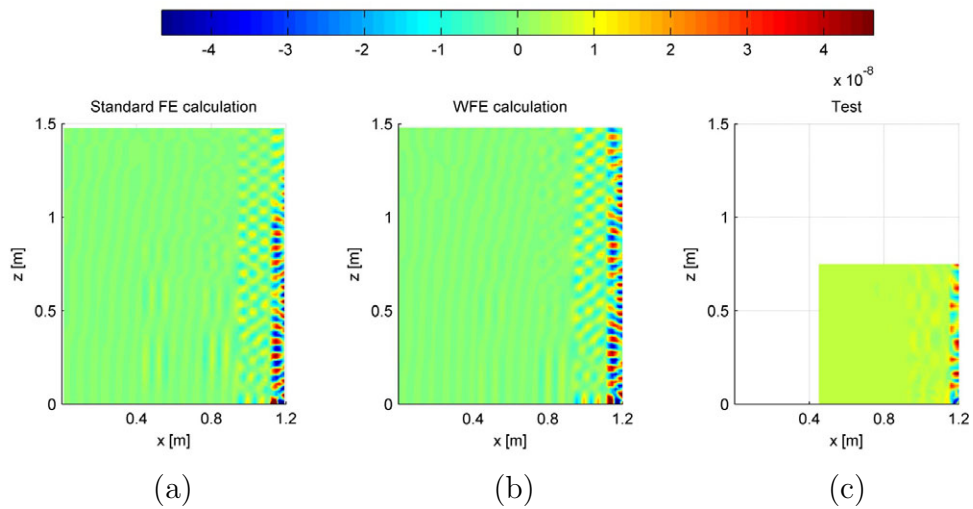


Figure F.9: Displacement field of forced response (F_y at the centre of plate field, lower right corner of plots), $f = 5000$ Hz

F.2 Measured and calculated dispersion characteristics

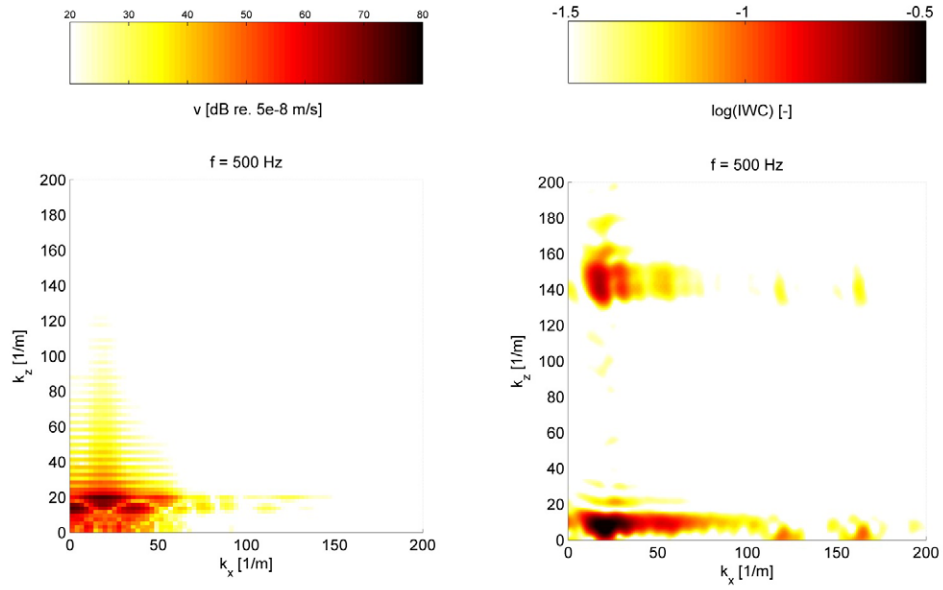


Figure F.10: DFT-calculated (left) and measured (right) dispersion characteristics of regional train floor section, $f = 500$ Hz, F_y at the centre of plate field

APPENDIX F. REGIONAL TRAIN FLOOR SECTION RESULTS

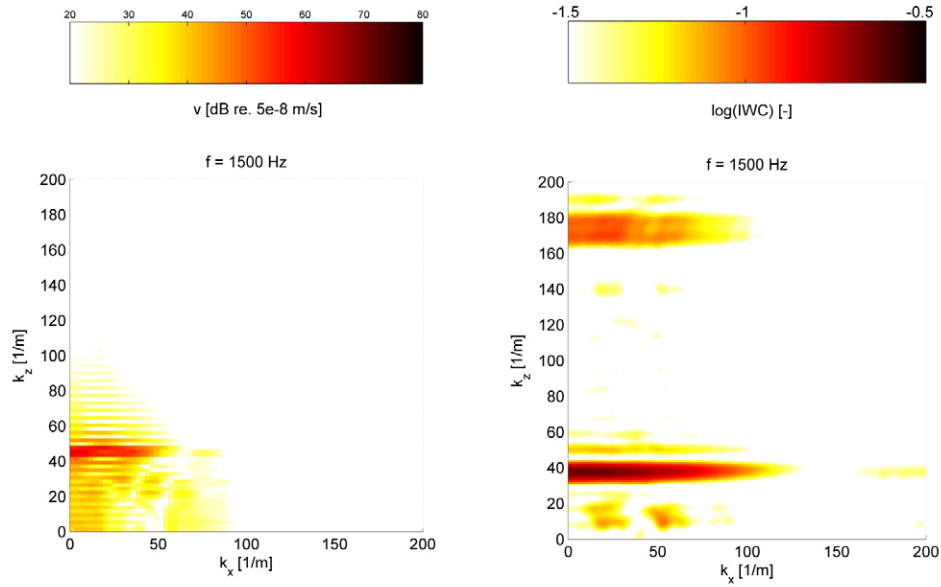


Figure F.11: DFT-calculated (left) and measured (right) dispersion characteristics of regional train floor section, $f = 1500$ Hz, F_y at the centre of plate field

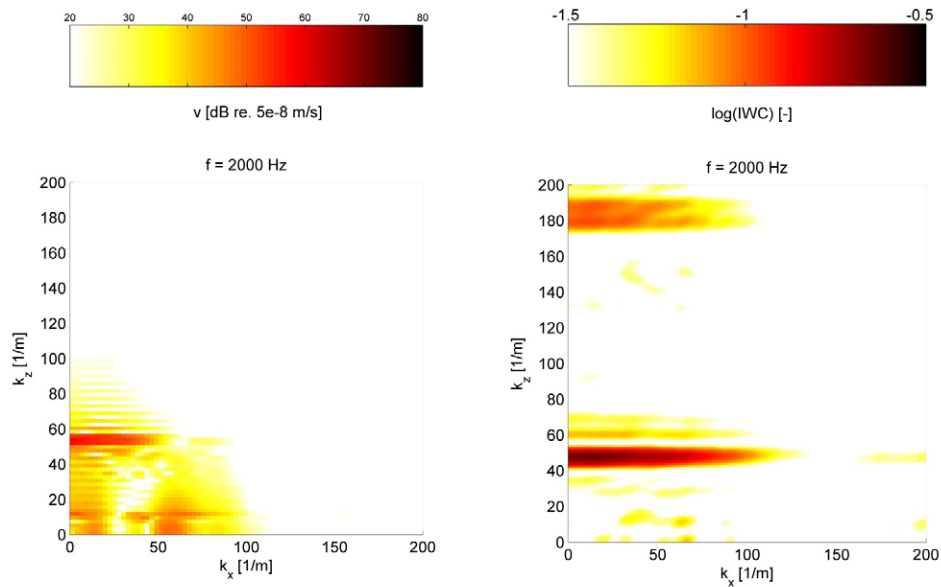


Figure F.12: DFT-calculated (left) and measured (right) dispersion characteristics of regional train floor section, $f = 2000$ Hz, F_y at the centre of plate field

APPENDIX F. REGIONAL TRAIN FLOOR SECTION RESULTS

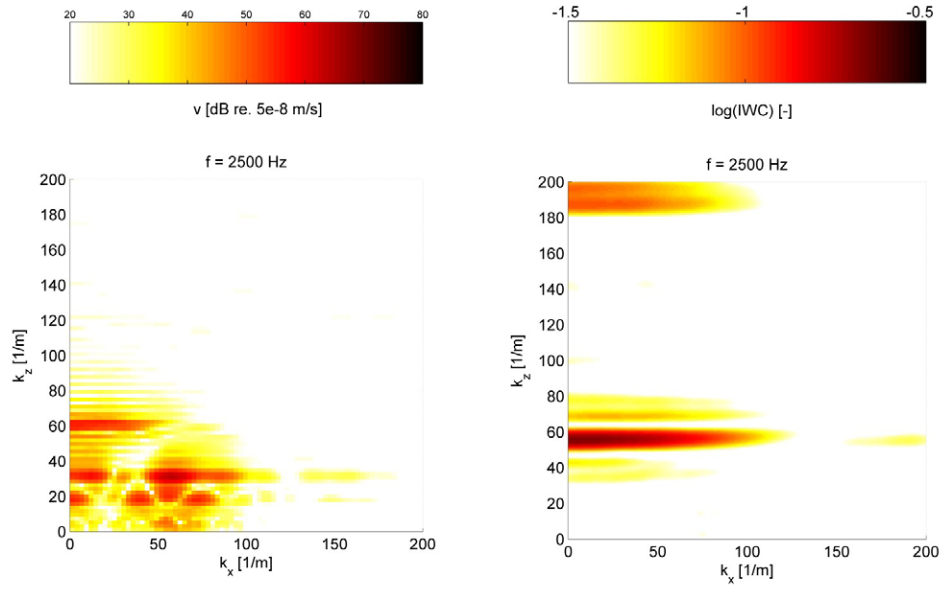


Figure F.13: DFT-calculated (left) and measured (right) dispersion characteristics of regional train floor section, $f = 2500$ Hz, F_y at the centre of plate field

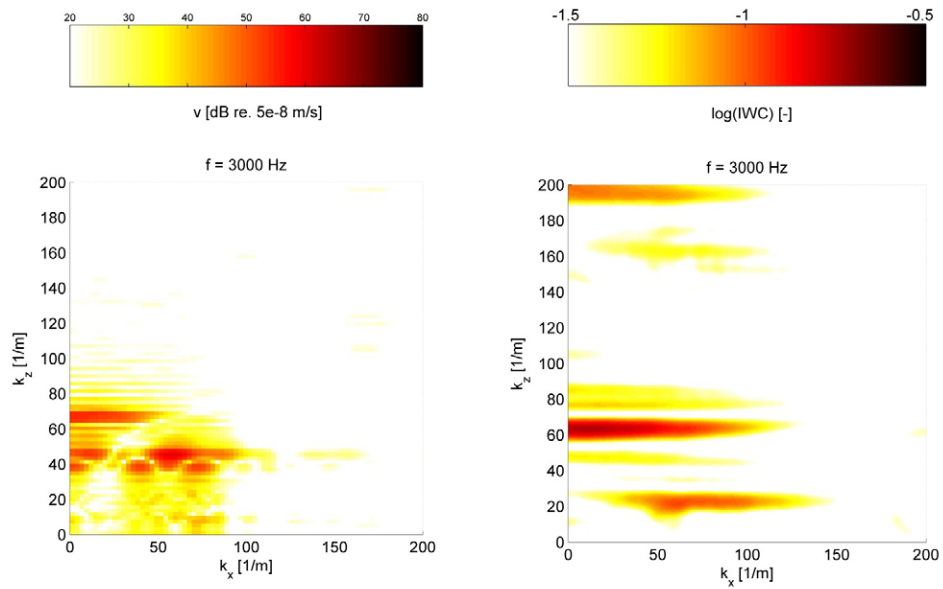


Figure F.14: DFT-calculated (left) and measured (right) dispersion characteristics of regional train floor section, $f = 3000$ Hz, F_y at the centre of plate field

APPENDIX F. REGIONAL TRAIN FLOOR SECTION RESULTS

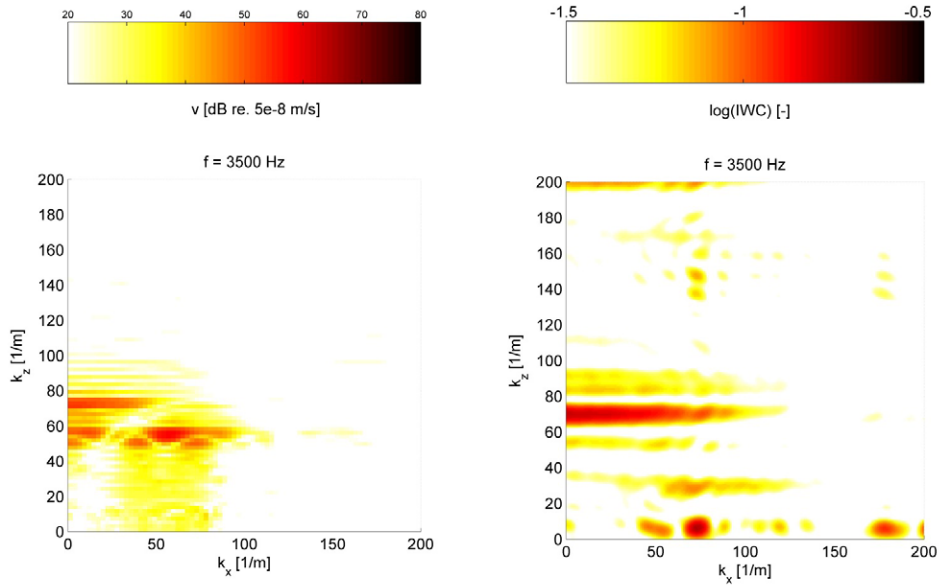


Figure F.15: DFT-calculated (left) and measured (right) dispersion characteristics of regional train floor section, $f = 3500$ Hz, F_y at the centre of plate field

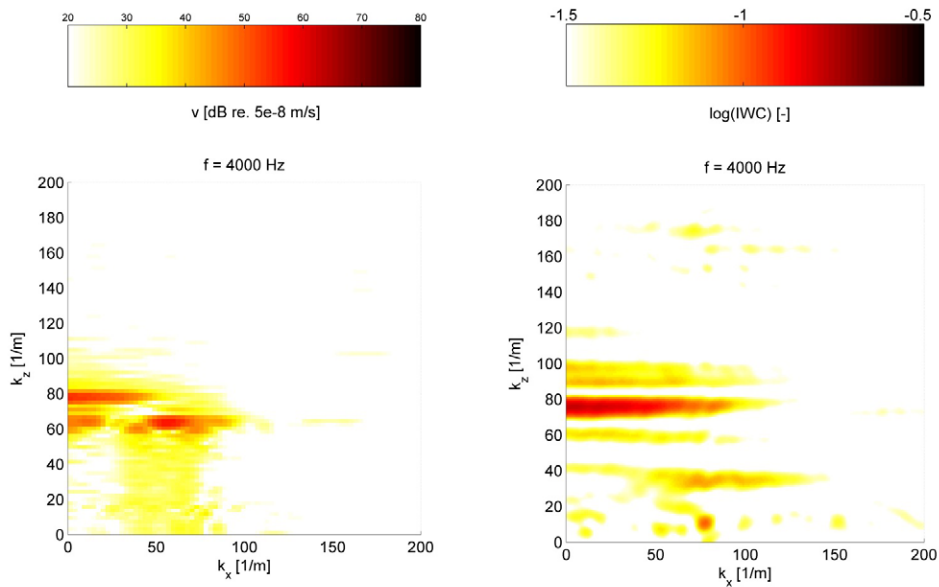


Figure F.16: DFT-calculated (left) and measured (right) dispersion characteristics of regional train floor section, $f = 4000$ Hz, F_y at the centre of plate field

APPENDIX F. REGIONAL TRAIN FLOOR SECTION RESULTS

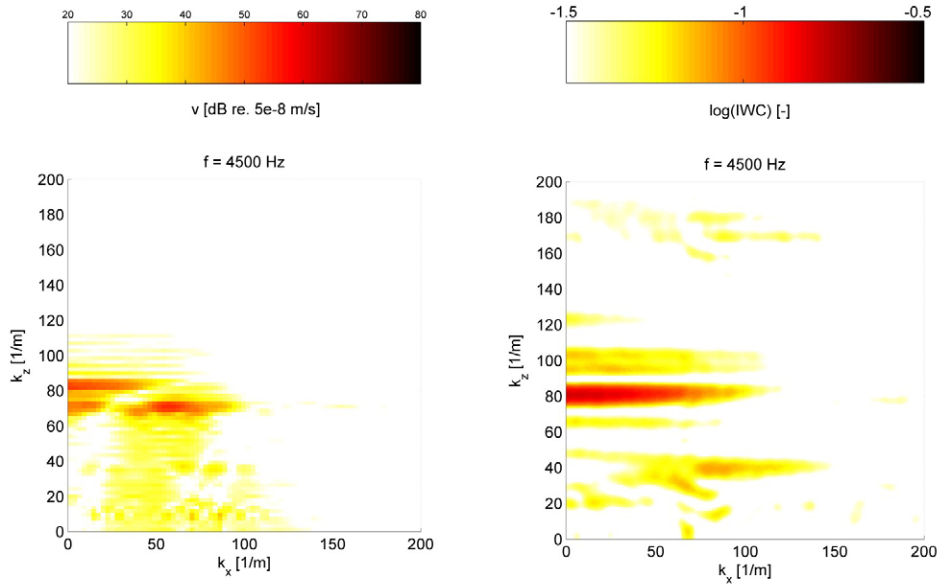


Figure F.17: DFT-calculated (left) and measured (right) dispersion characteristics of regional train floor section, $f = 4500$ Hz, F_y at the centre of plate field

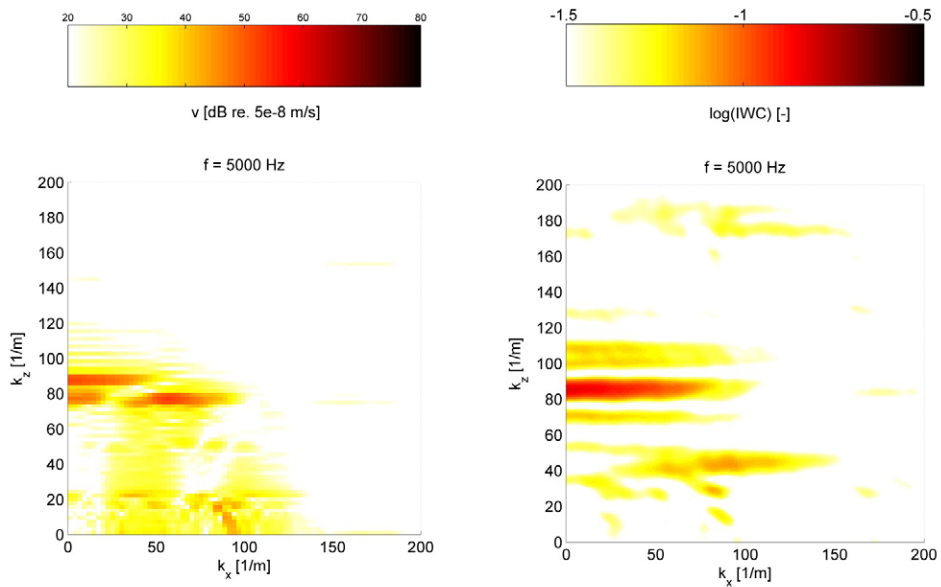


Figure F.18: DFT-calculated (left) and measured (right) dispersion characteristics of regional train floor section, $f = 5000$ Hz, F_y at the centre of plate field

F.3 Time-frequency content

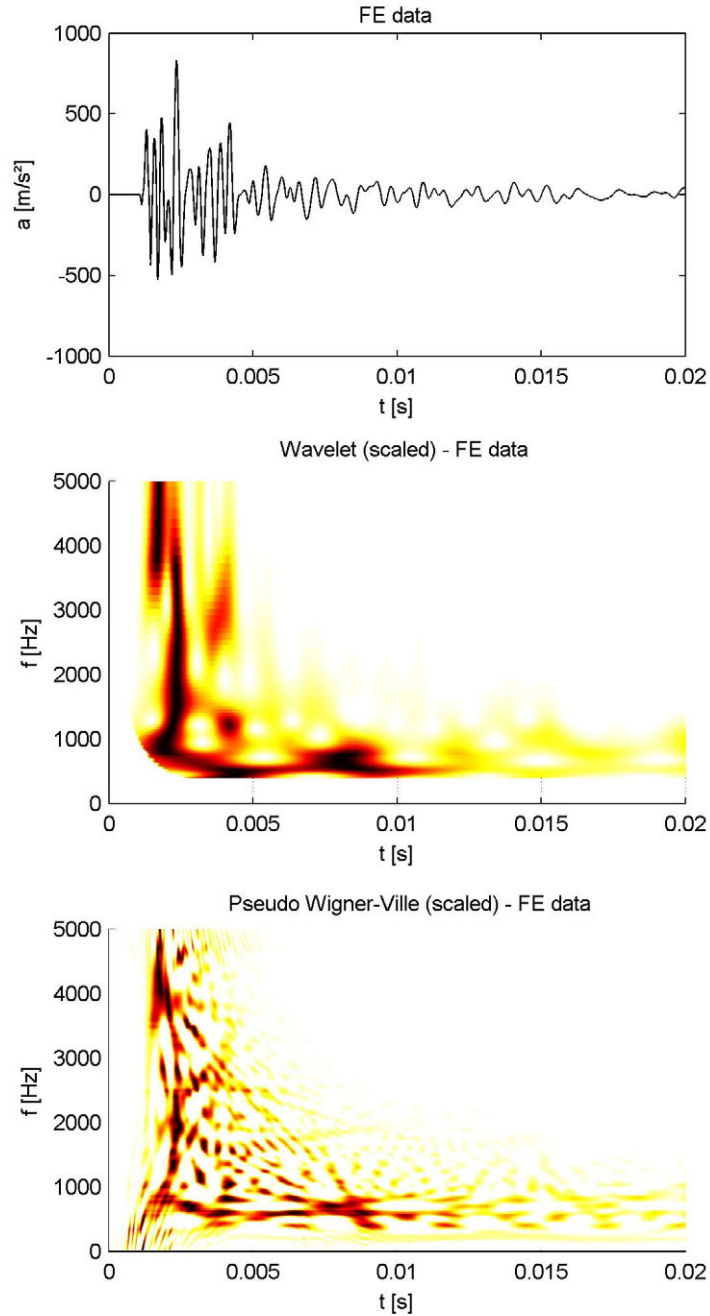


Figure F.19: FE-calculated impulse response at 0.5 m in z -direction and time-frequency content of train floor section, stiffener excitation

APPENDIX F. REGIONAL TRAIN FLOOR SECTION RESULTS

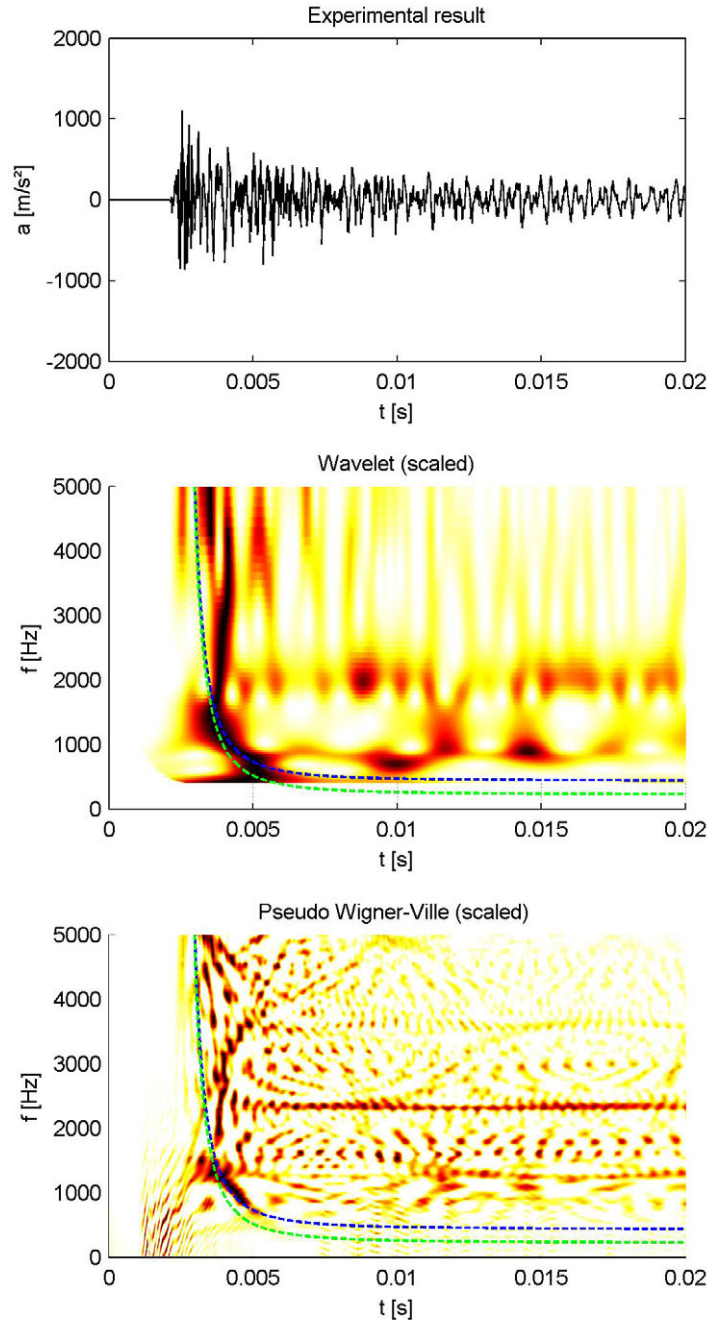


Figure F.20: Measured impulse response at 0.5 m in z -direction and time-frequency content of train floor section, stiffener excitation. Arrival times of first order bending waves in simply-supported plate strip included by green line (0.18 m width) and blue line (0.13 m width).

APPENDIX F. REGIONAL TRAIN FLOOR SECTION RESULTS

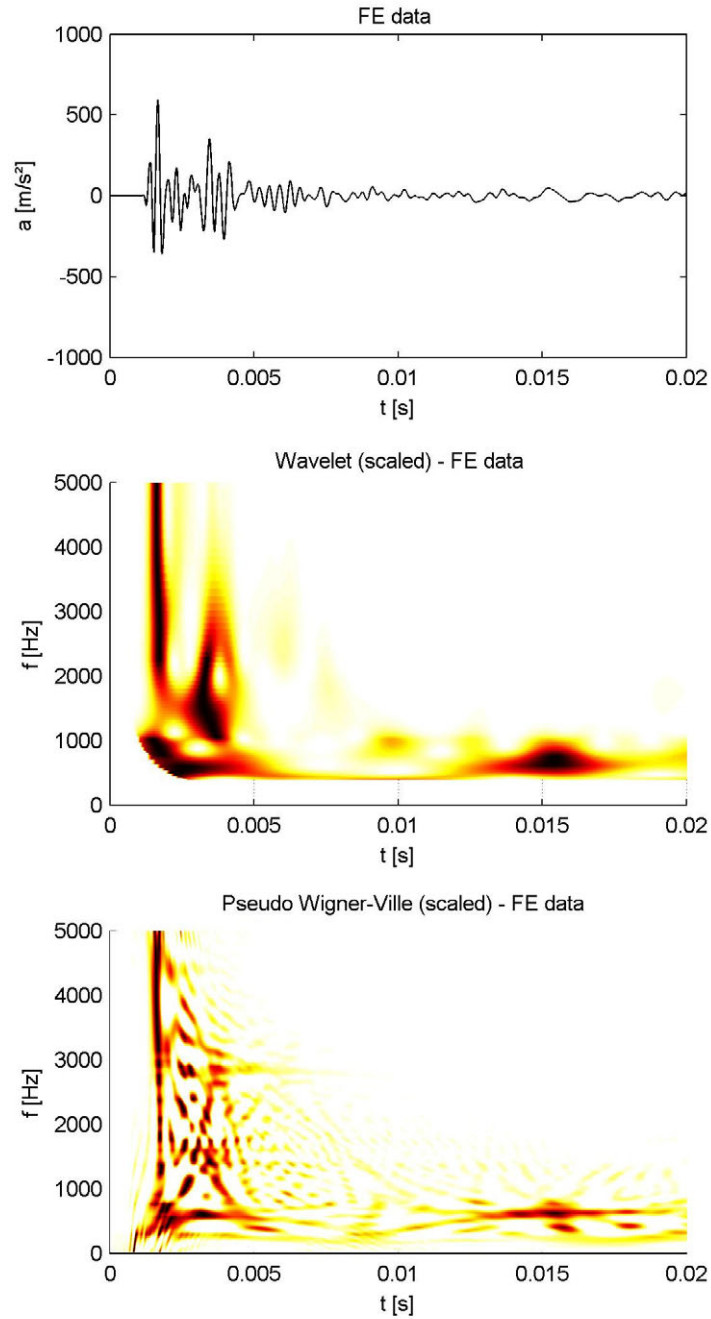


Figure F.21: FE-calculated impulse response at 0.5 m in x -direction and time-frequency content of train floor section, stiffener excitation

APPENDIX F. REGIONAL TRAIN FLOOR SECTION RESULTS

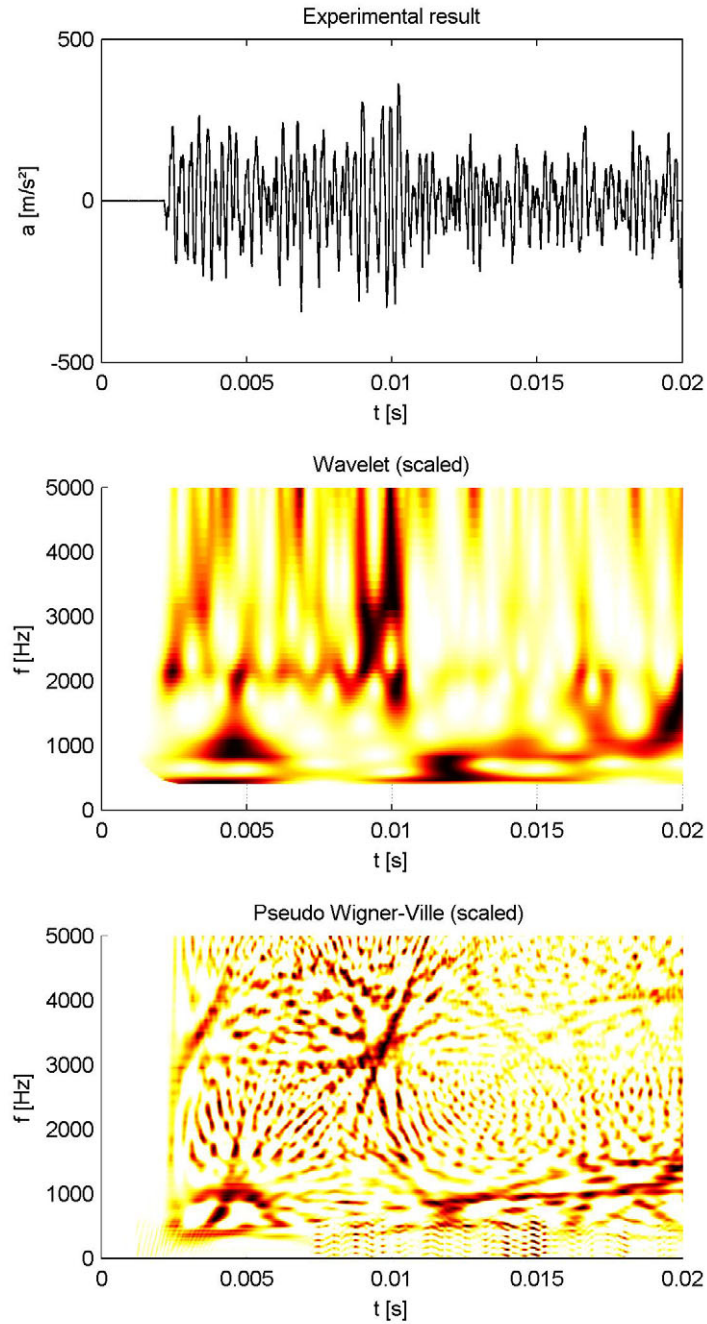


Figure F.22: Measured impulse response at 0.5 m in x -direction and time-frequency content of train floor section, stiffener excitation

F.4 Mobility Tests on regional train floor plate

F.4.1 Test setup

Mobility testing is performed on a freely suspended regional floor section with dimensions 3 m x 2.4 m. The dynamic free boundary condition is achieved by placing the plate on four air-filled rubber balls at the corners, resulting in an eigenfrequency of about 4 Hz in y-direction. This low resonance frequency assures dynamic free boundary conditions in the investigated frequency range. A B&K miniature shaker is used for force excitation by placing the shaker directly on top of the plate and measuring the excitation force with a force transducer. A photo of the test set-up is included in Fig. F.23. The positions of the investigated sensor points are indicated in Fig. F.24.



Figure F.23: Photo of test set-up, suspension by air-filled balls in red

F.4.2 Mass calibration

A mass calibration is performed to assure magnitude and phase correct measurements. Therefore a calibration mass of 50 g is placed on top of the force transducer, that is positioned on a white-noise excited shaker. The acceleration is measured with each accelerometer on top of the calibration mass and the mobility is evaluated.

A correction factor for each accelerometer - force transducer combination i is calculated from the measured results by:

$$Corr_i = Y_{m,50g,theoretical} / Y_{meas,i}$$

The resulting corrections are plotted as magnitude and phase in Fig. F.25. It is obvious that the corrections in the investigated frequency range up to 5000 Hz are quite small.

F.4.3 Support influence

In order to investigate the influence of the support on input and transfer mobilities in the centre of the plate tests with the plate on four steel supports

APPENDIX F. REGIONAL TRAIN FLOOR SECTION RESULTS

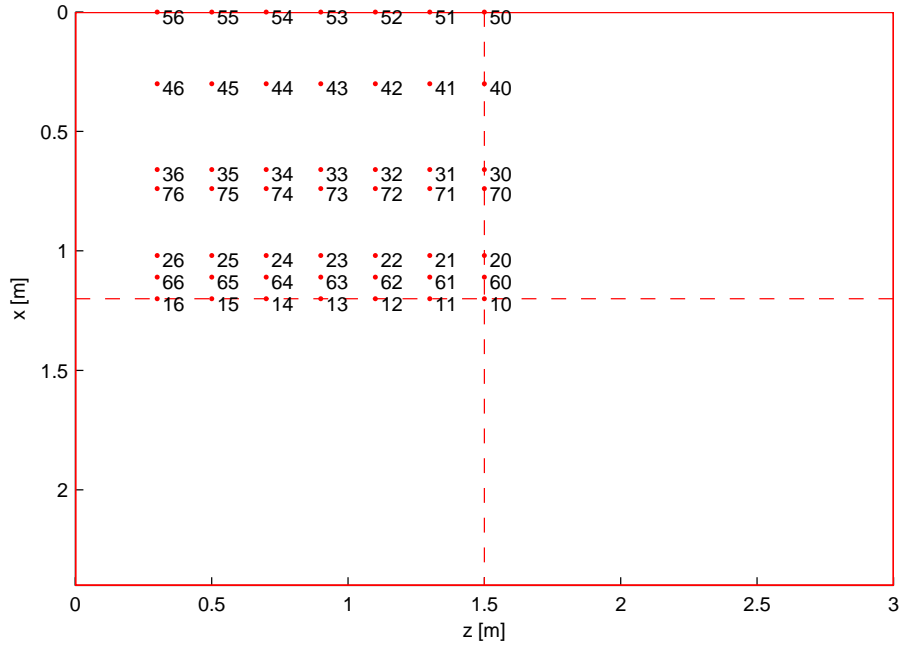


Figure F.24: Sketch of measurement point locations, MP 10 (stiffener) and MP 60 (plate field) are used for force excitation. Stiffener locations: MP 10-56, plate field locations MP 60-66 & 70-76

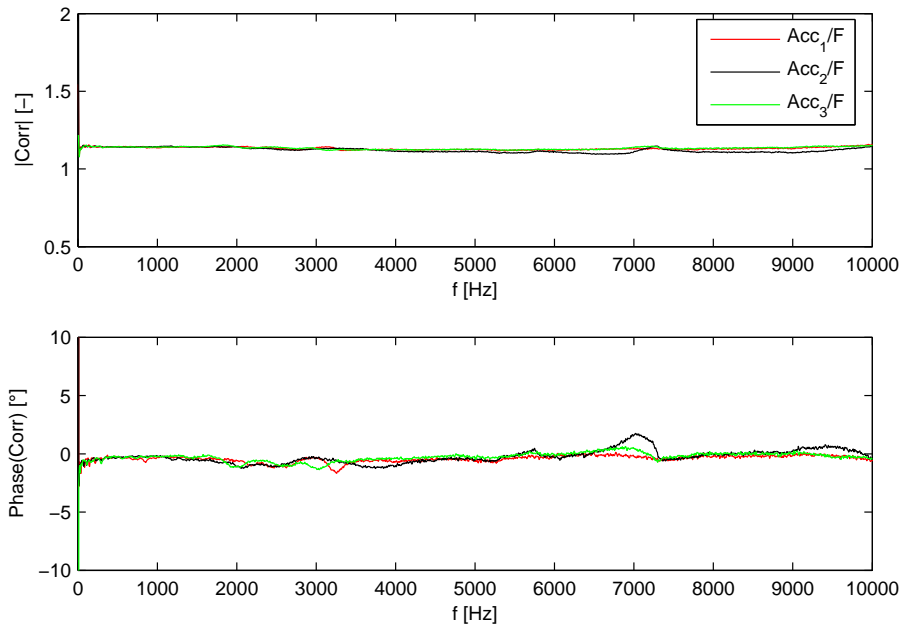


Figure F.25: Complex correction factors for mobility tests



Figure F.26: Test set-up for boundary conditions with steel support

were also conducted (see Fig. F.26).

Some results for measured input and transfer mobilities are shown in Fig. F.27. It is obvious that the support at the corners has only negligible influence on the high frequency characteristics in the centre of the plate, above 500 Hz. As expected, the influence is significant at low frequencies.

F.4.4 Input mobility for stiffener excitation

Measurement point (MP) 10 is located directly at a stiffener in the centre axis of the plate. Force excitation is applied at this point and the acceleration is measured in the vicinity of the excitation point to get the input mobility.

The resulting input mobility with magnitude and phase is plotted in Fig. F.28.

F.4.5 Input mobility for plate field excitation

MP 60 is located in the centre of a plate field (0.18 cm width). Force excitation is applied at this point and the acceleration is measured in the vicinity of the excitation point to get the input mobility.

The resulting input mobility with magnitude and phase is plotted in Fig. F.29.

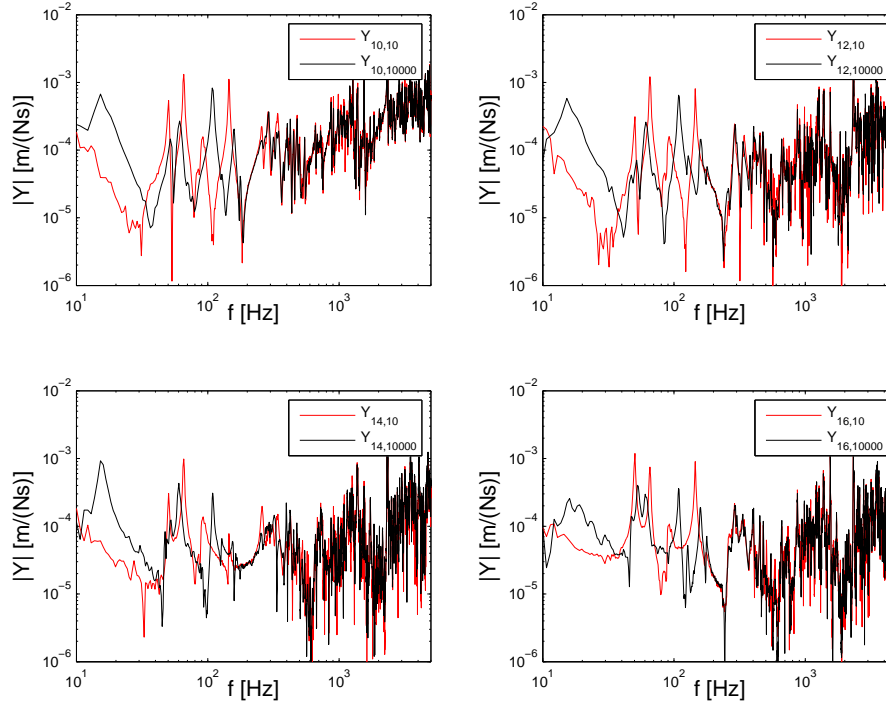


Figure F.27: Comparison of selected input and transfer mobilities on centre of plate for free and steel column support at the four corners, (10000 indicates steel support case)

F.4.6 Comparison of input mobilities

A direct comparison of input mobilities for stiffener and plate field excitation is shown in Fig. F.30 and reveals the significantly higher mobility on the plate field. Only at very low frequencies, the real part of both excitation points is similar.

F.4.7 Transfer mobilities

Transfer mobilities for excitation at MP10 (stiffener) and MP60 (plate field) are plotted in this section.

The transfer mobilities along a stiffener are quite similar in the local vibration region (Fig. F.31). Only in the global frequency region below 300 Hz there are significant differences. Despite the short distance there is a significant stop-band behaviour in the frequency range 1600-2300 Hz which does not appear to this extent for the plate field excitation case (Figs. F.32 and F.40). The transfer mobilities in lateral direction are shown in Figs. F.33 to

APPENDIX F. REGIONAL TRAIN FLOOR SECTION RESULTS

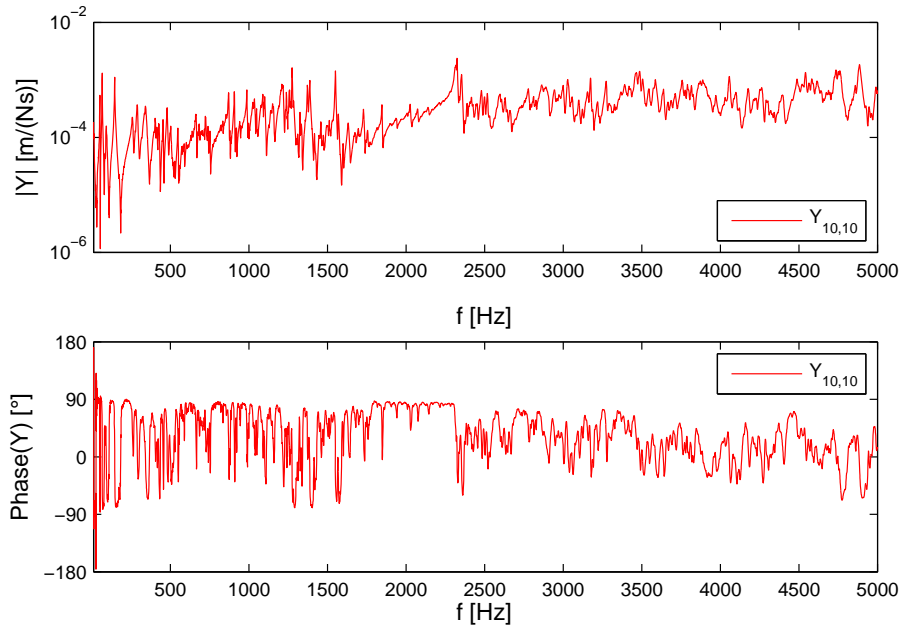


Figure F.28: Input mobility at stiffener excitation point MP10

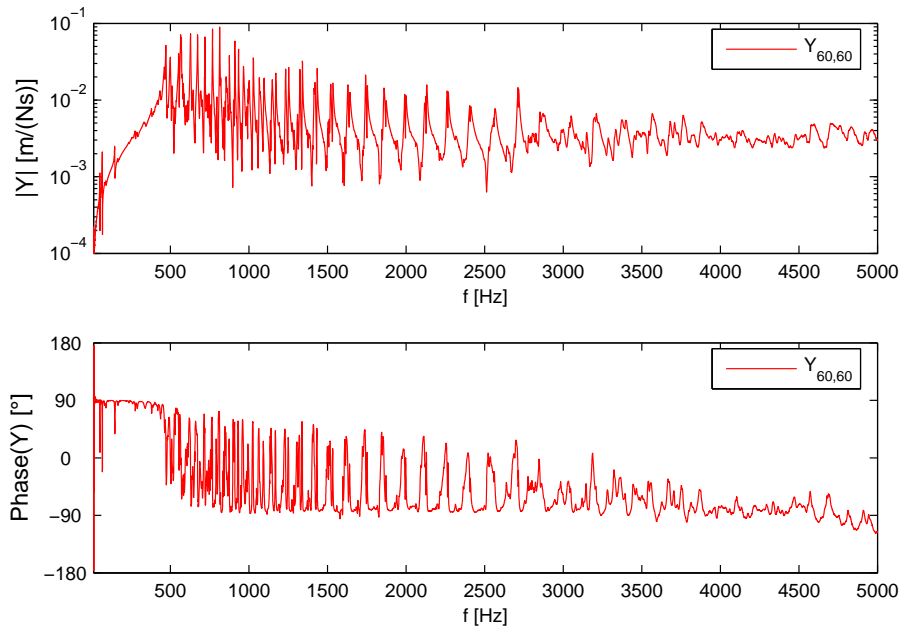


Figure F.29: Input mobility at plate field excitation point MP60

APPENDIX F. REGIONAL TRAIN FLOOR SECTION RESULTS

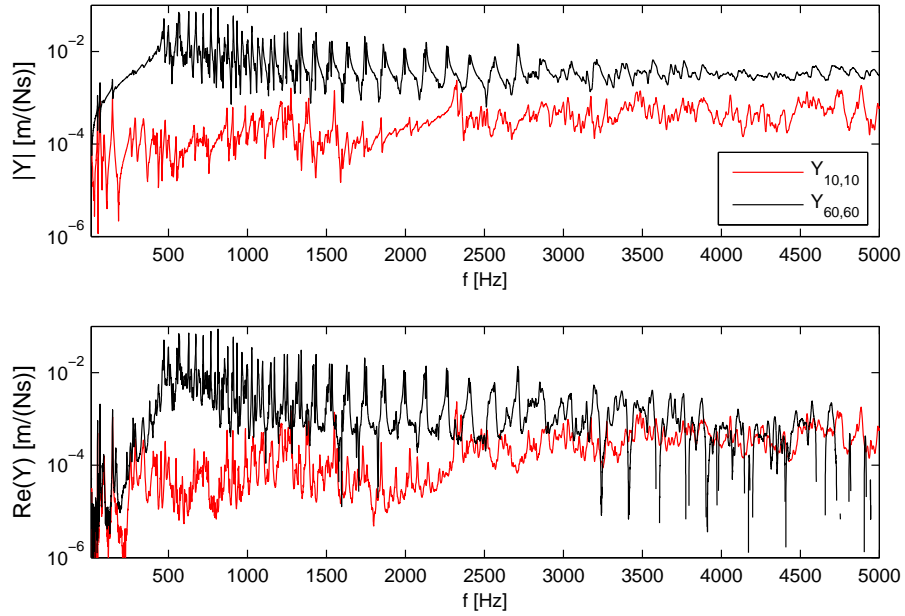


Figure F.30: Comparison of input mobilities at stiffener excitation point MP10 and plate field excitation point MP60

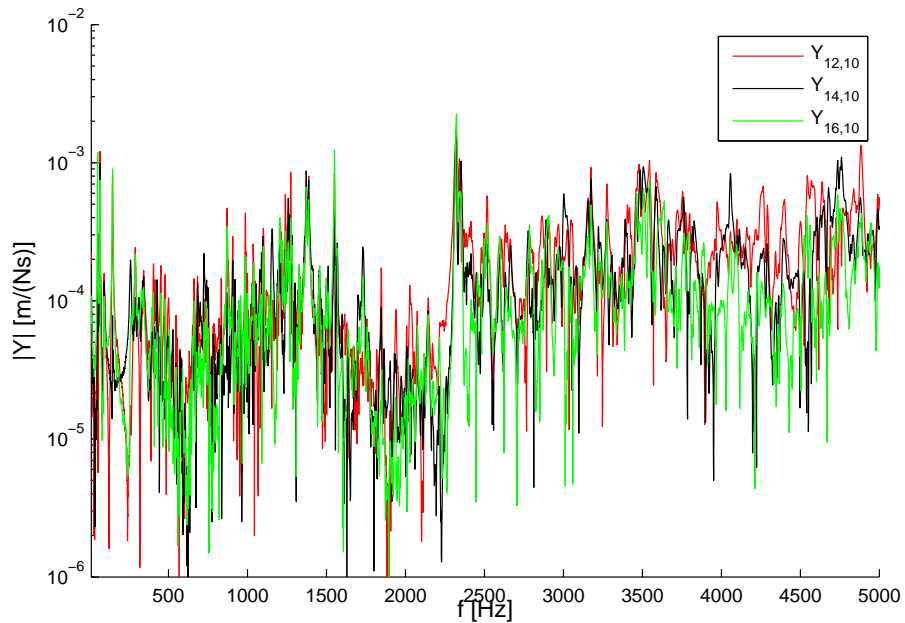


Figure F.31: Transfer mobilities along stiffener, excitation at MP10, response at MP12, MP14 and MP16

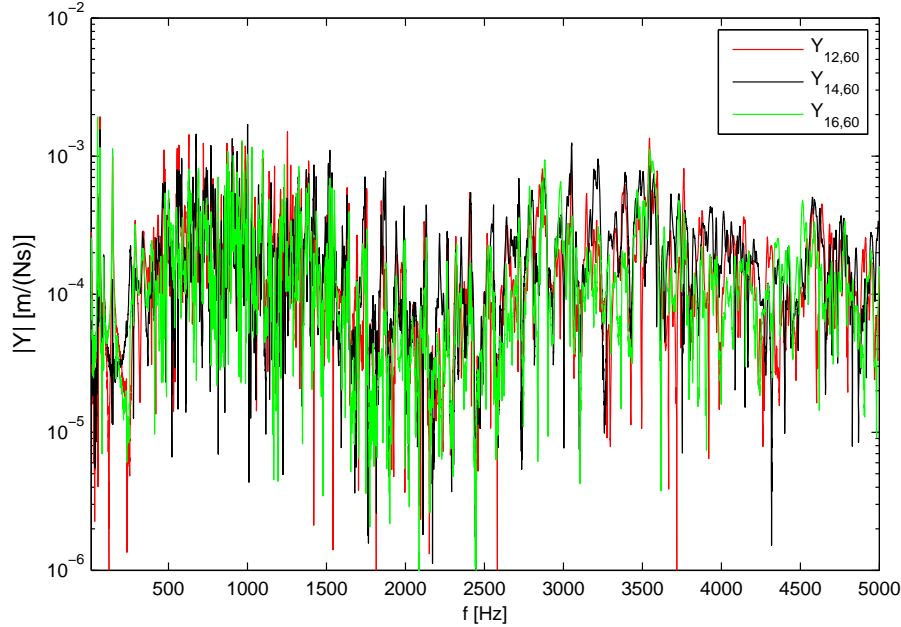


Figure F.32: Transfer mobilities, excitation at MP60, response at MP12, MP14 and MP16

F.38, where the filtered wave propagation in lateral direction is obvious: a strong stop-band is visible between 1300 and 2400 Hz, most pronounced for the stiffener excitation case.

As shown in Fig. F.39 the transfer mobilities to the adjacent plate field are nearly identical, independent of the distance to the excitation point. Fig. F.40 illustrates the waveguide behaviour of the excited plate strip. At low frequencies below 500 Hz wave propagation in the strip is not possible and the transfer mobility is dominated by global effects. With a strong rise of the transfer mobility at 500 Hz, the first propagating waves in the strip cut on.

The transfer mobilities to oblique and lateral response positions illustrate the strong directivity and stop-band behaviour of the wave propagation in Figs. F.41 to F.48 irrespective of the excitation position. The results demonstrate that the detailed response location in z -direction is of minor importance for oblique and lateral wave propagation.

APPENDIX F. REGIONAL TRAIN FLOOR SECTION RESULTS

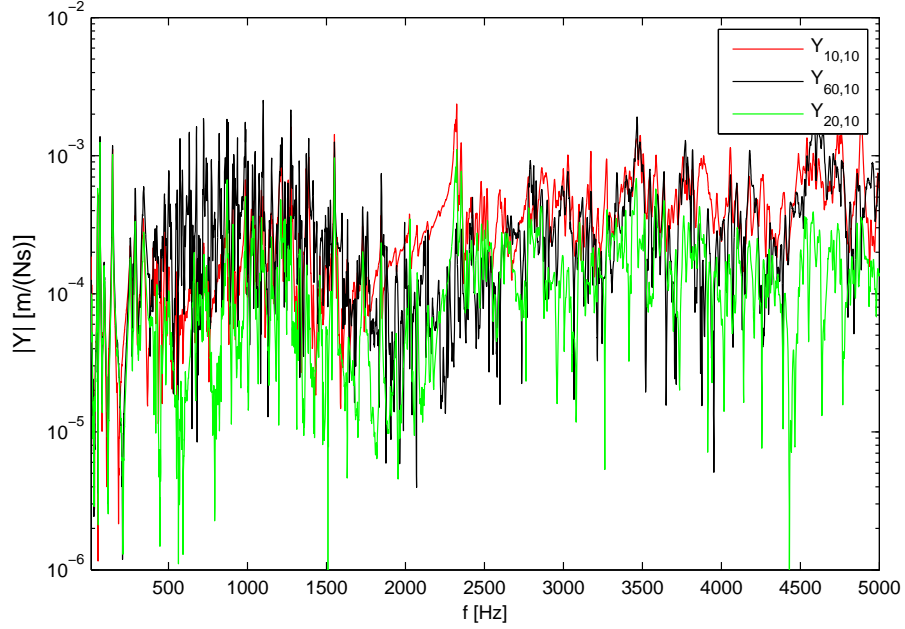


Figure F.33: Transfer mobilities across stiffeners (lateral), excitation at MP10, response at MP10, MP60 and MP20

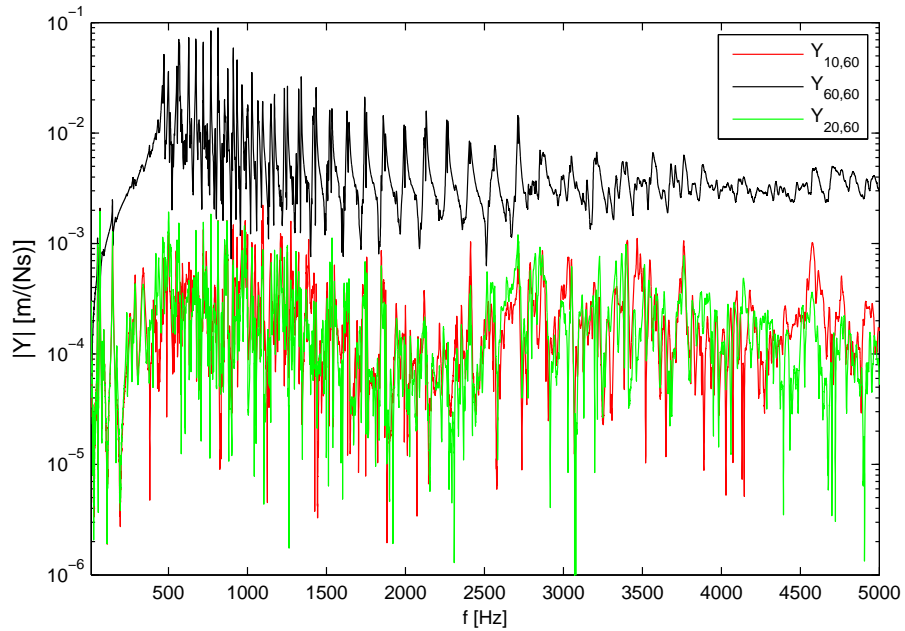


Figure F.34: Transfer mobilities across stiffeners (lateral), excitation at MP60, response at MP10, MP60 and MP20

APPENDIX F. REGIONAL TRAIN FLOOR SECTION RESULTS

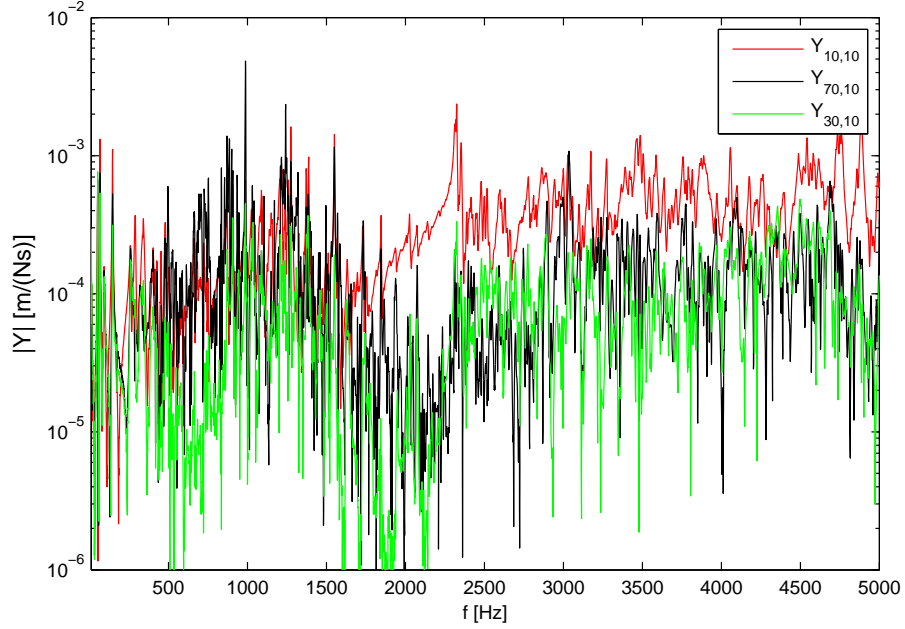


Figure F.35: Transfer mobilities across stiffeners (lateral), excitation at MP10, response at MP10, MP70 and MP30

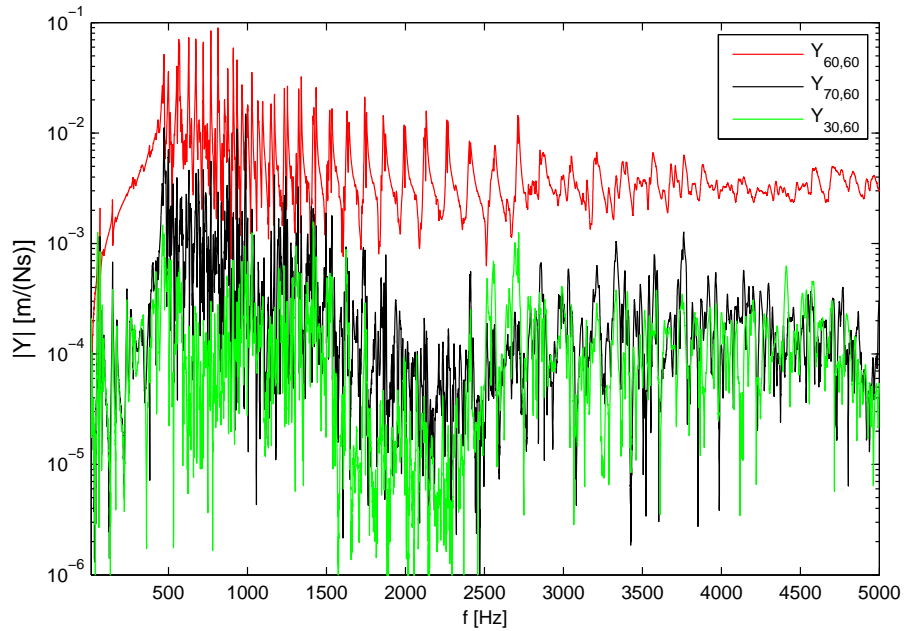


Figure F.36: Transfer mobilities across stiffeners (lateral), excitation at MP60, response at MP60, MP70 and MP30

APPENDIX F. REGIONAL TRAIN FLOOR SECTION RESULTS

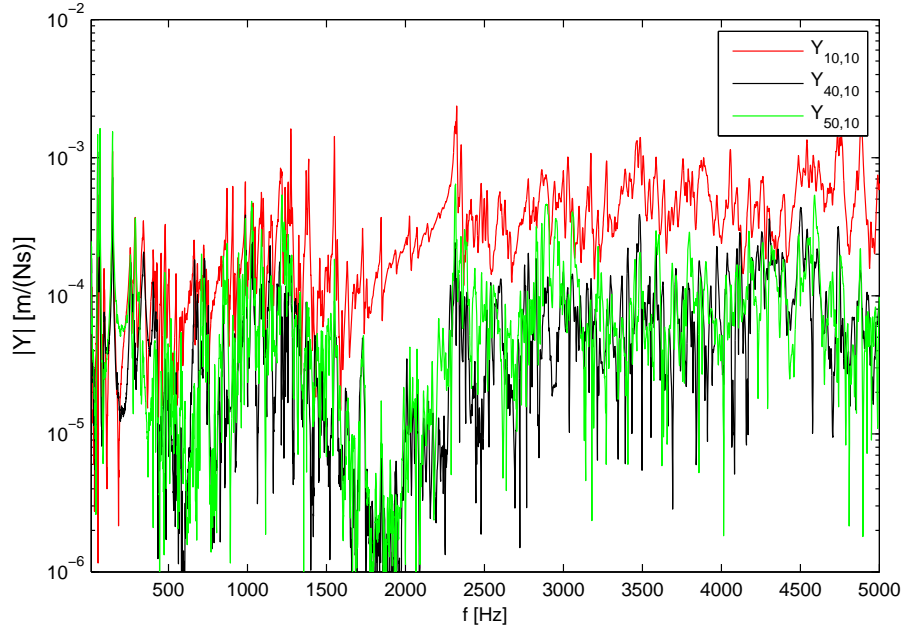


Figure F.37: Transfer mobilities across stiffeners (lateral), excitation at MP10, response at MP10, MP40 and MP50

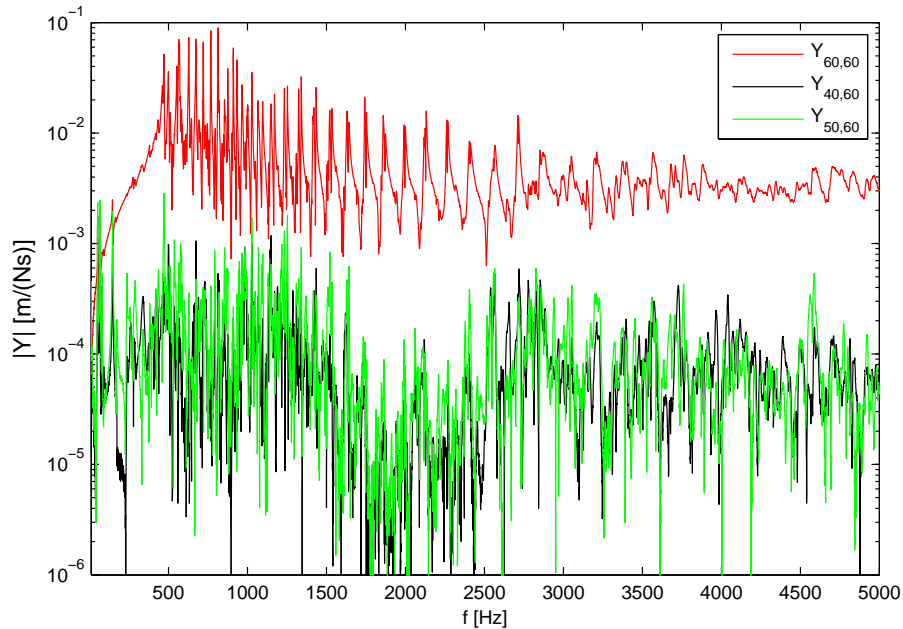


Figure F.38: Transfer mobilities across stiffeners (lateral), excitation at MP60, response at MP60, MP40 and MP50

APPENDIX F. REGIONAL TRAIN FLOOR SECTION RESULTS

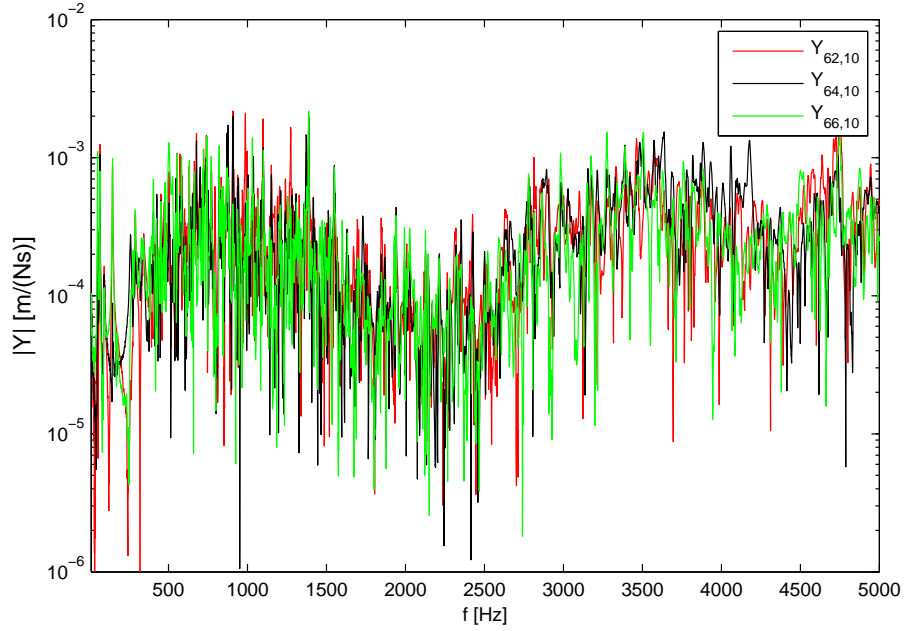


Figure F.39: Transfer mobilities (response in adjacent plate field), excitation at MP10, response at MP62, MP64 and MP66

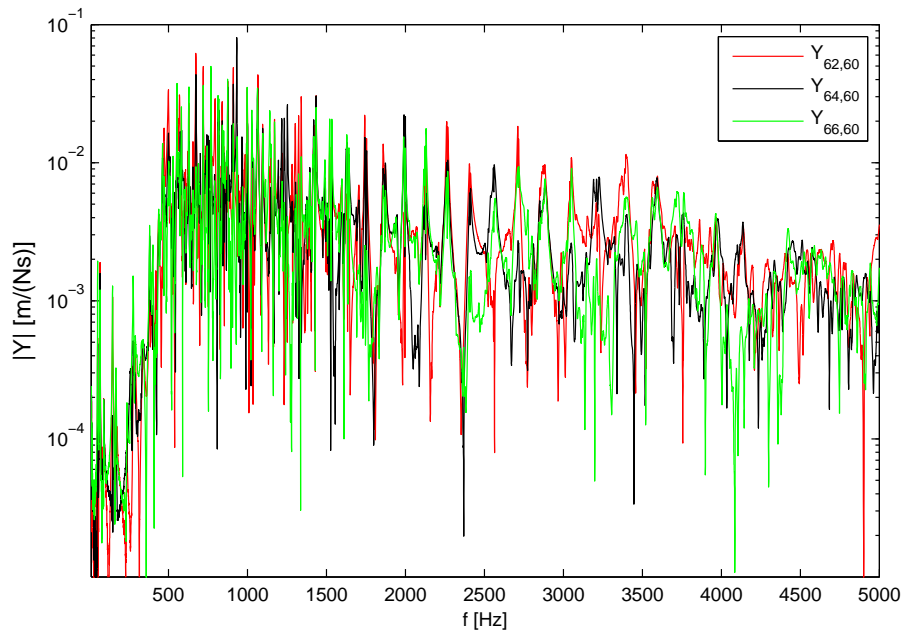


Figure F.40: Transfer mobilities (response in the same plate field), excitation at MP60, response at MP62, MP64 and MP66

APPENDIX F. REGIONAL TRAIN FLOOR SECTION RESULTS

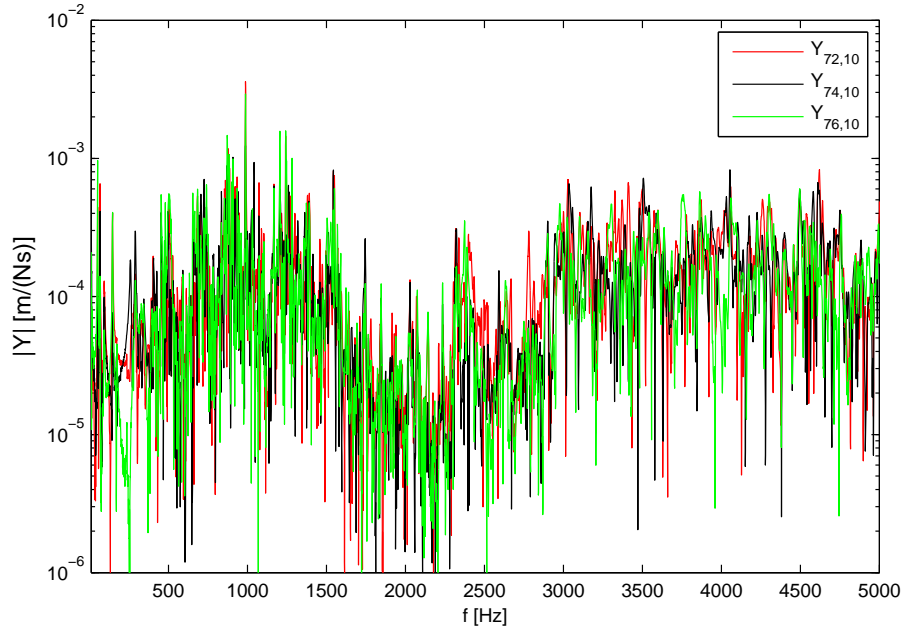


Figure F.41: Transfer mobilities, excitation at MP10, response at MP72, MP74 and MP76

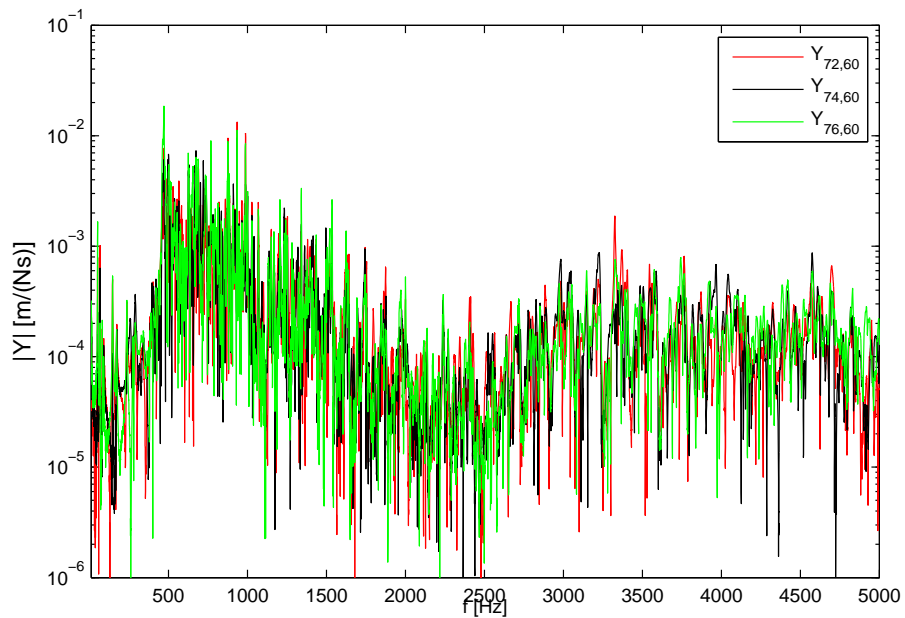


Figure F.42: Transfer mobilities, excitation at MP60, response at MP72, MP74 and MP76

APPENDIX F. REGIONAL TRAIN FLOOR SECTION RESULTS

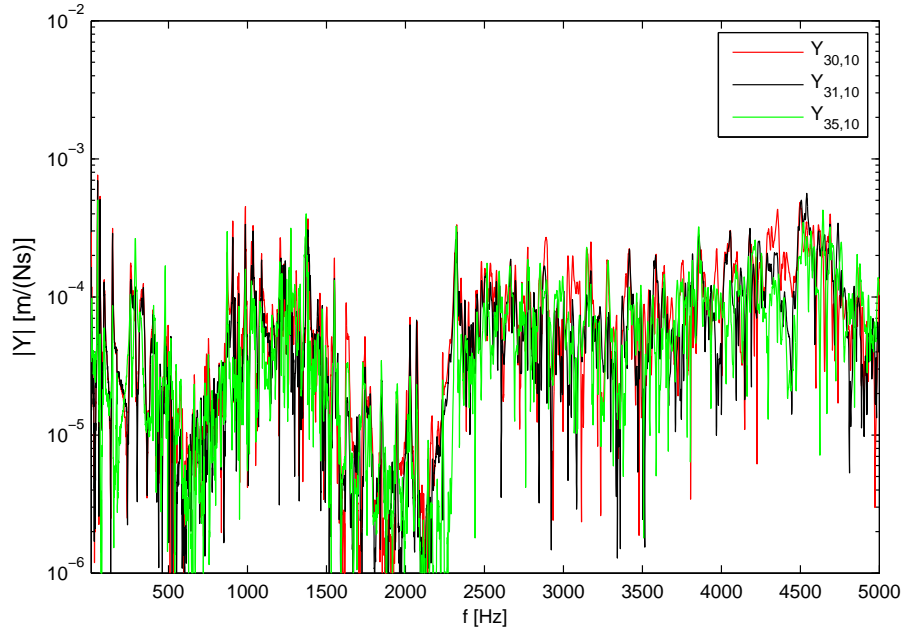


Figure F.43: Transfer mobilities, excitation at MP10, response at MP30, MP31 and MP35

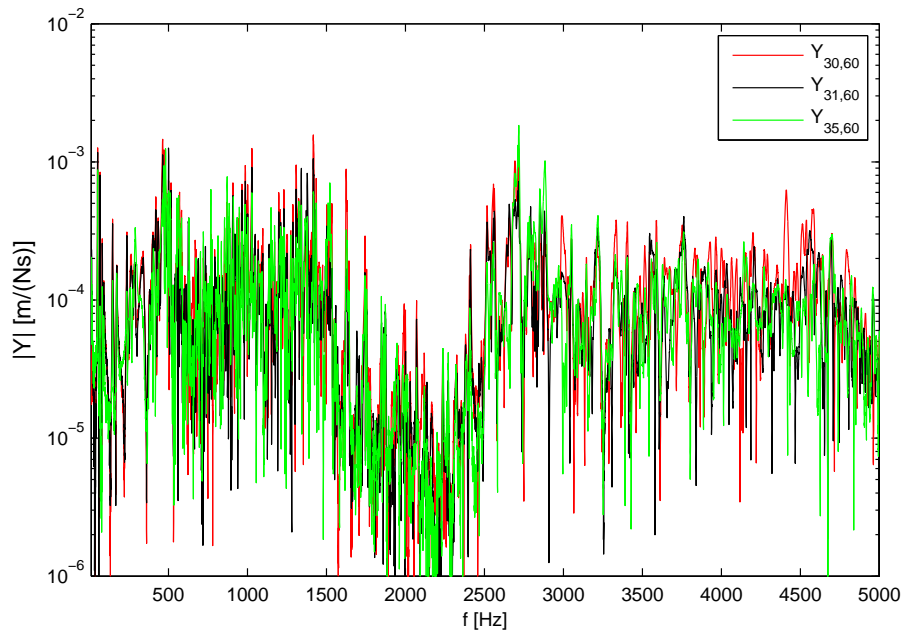


Figure F.44: Transfer mobilities, excitation at MP60, response at MP30, MP31 and MP35

APPENDIX F. REGIONAL TRAIN FLOOR SECTION RESULTS

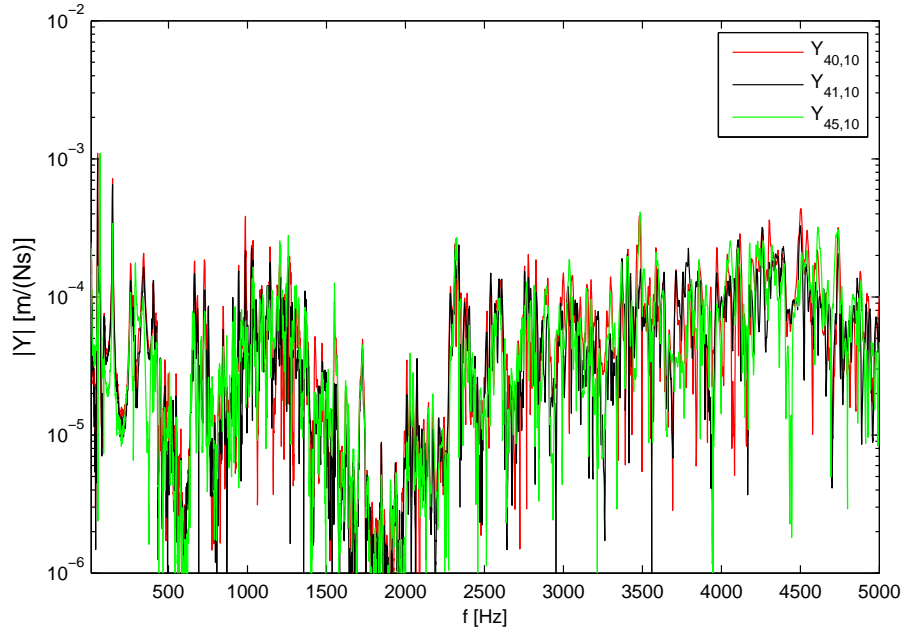


Figure F.45: Transfer mobilities, excitation at MP10, response at MP40, MP41 and MP45

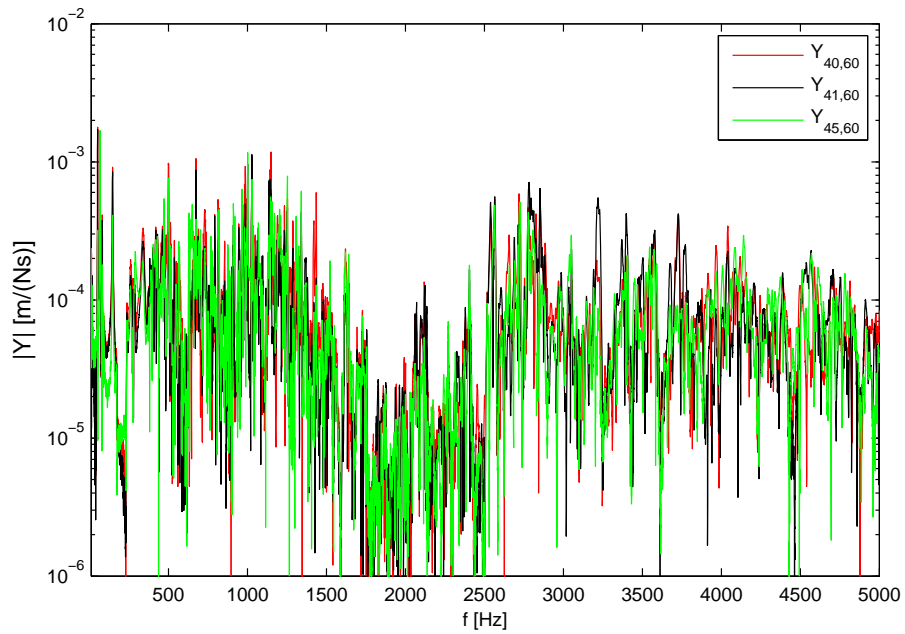


Figure F.46: Transfer mobilities, excitation at MP60, response at MP40, MP41 and MP45

APPENDIX F. REGIONAL TRAIN FLOOR SECTION RESULTS

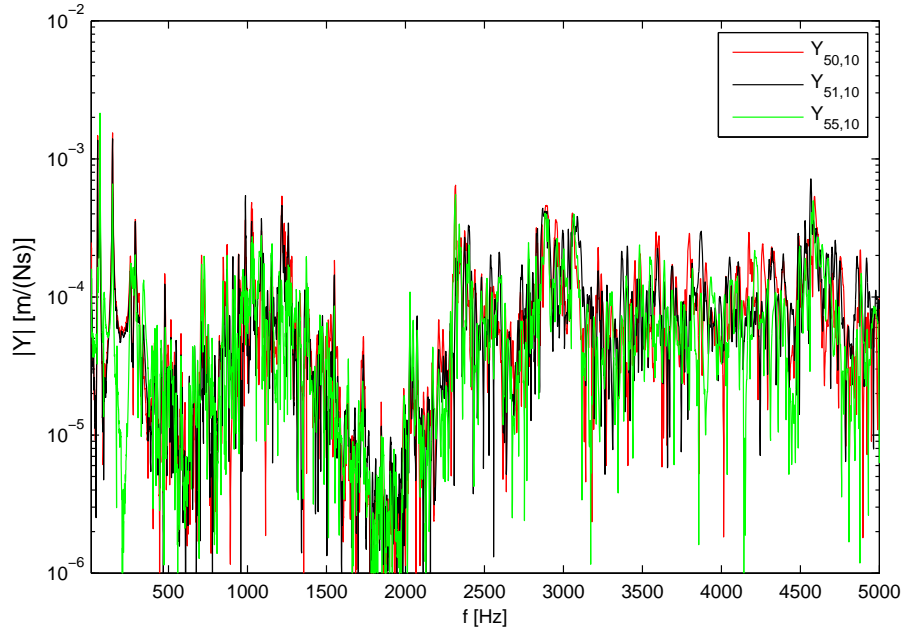


Figure F.47: Transfer mobilities, excitation at MP10, response at MP50, MP51 and MP55

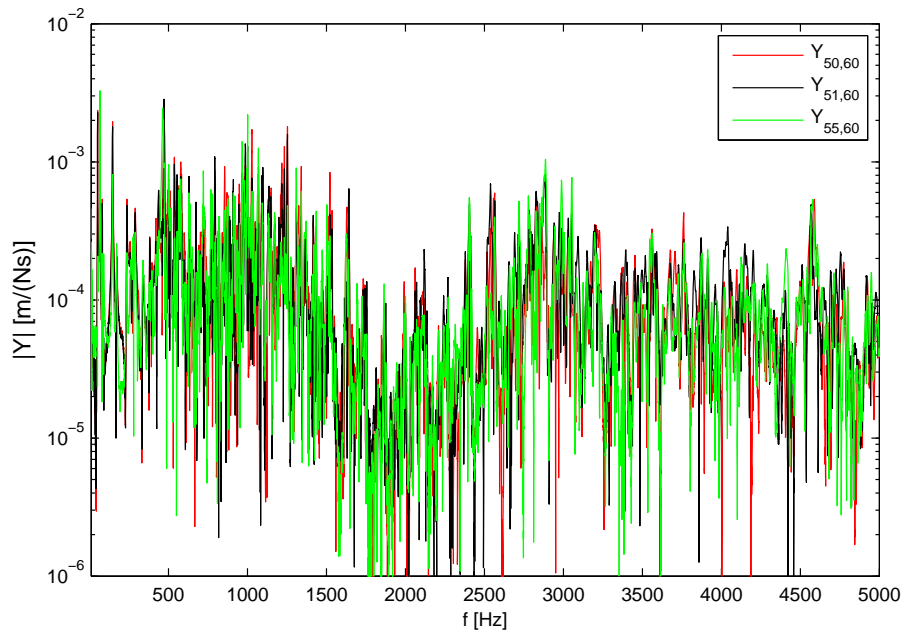


Figure F.48: Transfer mobilities, excitation at MP60, response at MP50, MP51 and MP55

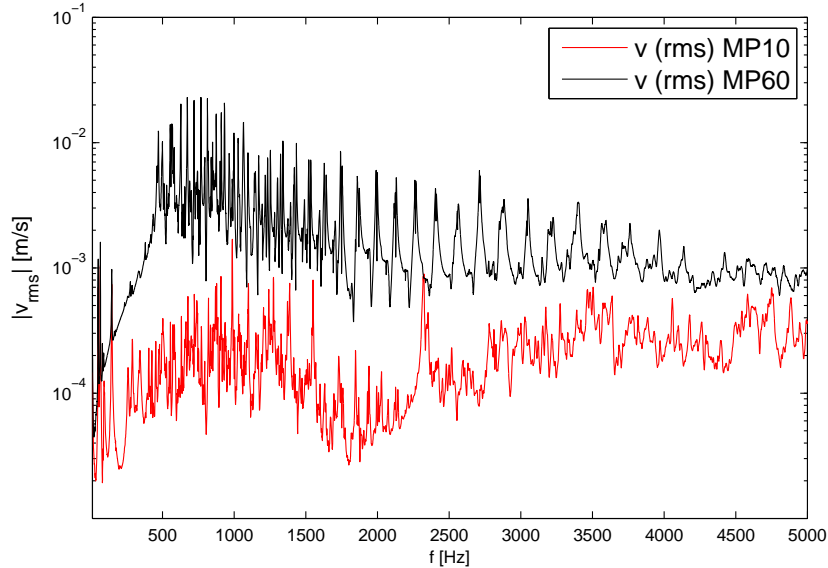


Figure F.49: Comparison of spatial mean rms-velocity for all measurement points that are consistently measured for both excitation cases, unit force excitation on stiffener (MP10) and in plate field (MP60)

F.4.8 Mean square velocity

In an attempt to establish an overview of the response for the plate strip and stiffener excitation cases, the root mean square velocity of selected response positions for a unit force excitation is used.

The first comparison includes all the measured points on the plate quarter that are consistently measured for both excitation cases, see Fig. F.49. It is obvious that for force excitation the stiffener excitation shows extremely lower average velocity levels, at least for frequencies above the global vibration region. Nonetheless, it should be pointed out that the plate field case (MP60) is dominated by the excitation point, where nearfields are also of major importance. Therefore a second comparison is performed including only remote points (distance more than 0.5 m) in order to exclude nearfield vibrations (see Fig. F.50). For farfield vibrations, the excitation point is not important in the low frequency regime up to about 200 Hz, where the plate vibrates globally. A last comparison includes only the points that are very remote, in this case only lateral points 30's-50's, see Fig. F.51. A significant difference for remote positions arises only between 400-1200 Hz, i.e. in the cut-on region of the first plate strip waves.

APPENDIX F. REGIONAL TRAIN FLOOR SECTION RESULTS

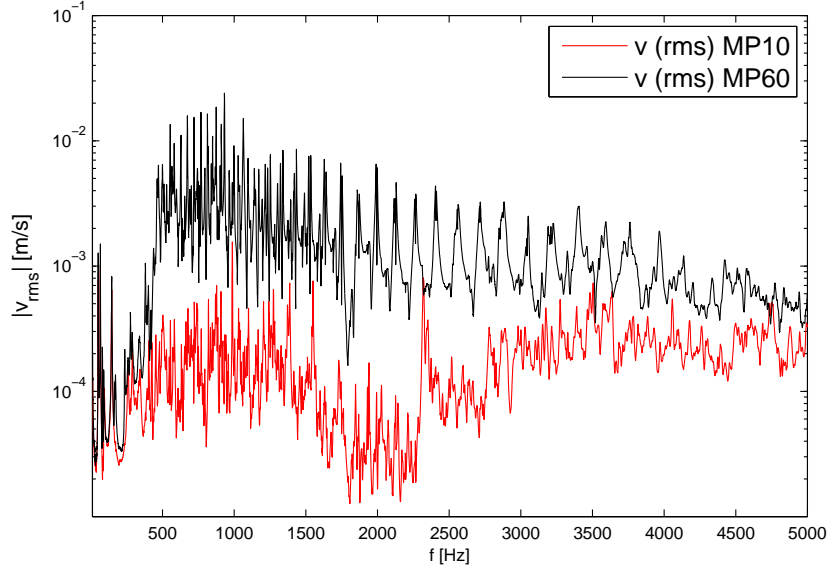


Figure F.50: Comparison of spatial mean rms-velocity for farfield measurement points (distance > 0.5 m), unit force excitation on stiffener (MP10) and in plate field (MP60)

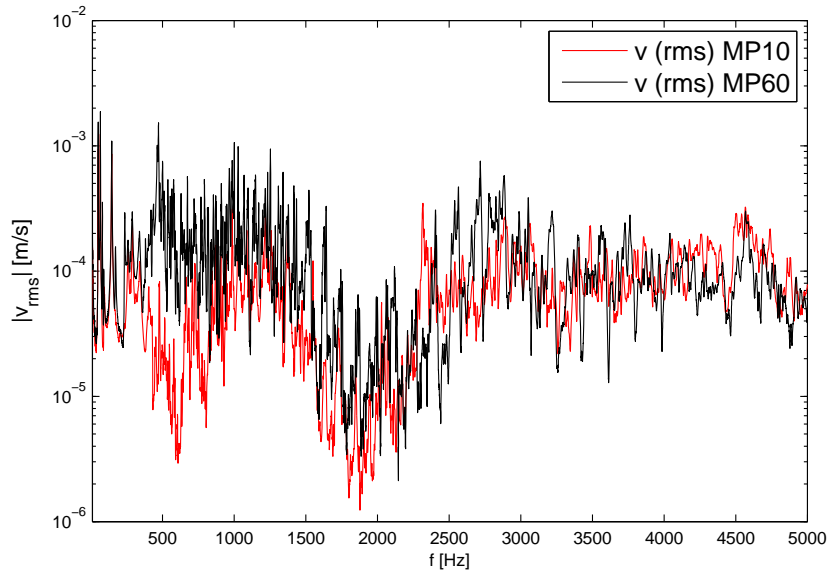


Figure F.51: Comparison of spatial mean rms-velocity for remote measurement points (MP 30's-50's), unit force excitation on stiffener (MP10) and in plate field (MP60)

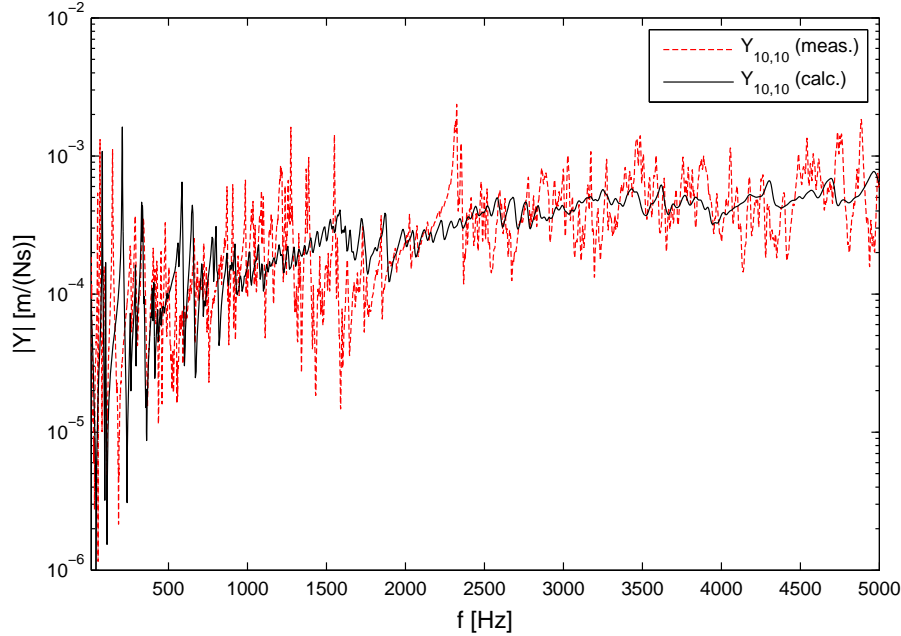


Figure F.52: Comparison of measured and FE-calculated input mobility on stiffener (MP10)

F.5 Comparison Calculation - Measurement

F.5.1 Stiffener Excitation

A standard FE-calculation using a quarter model of the light weight plate is performed and results are compared in this section with the measured ones.

The overall agreement between measured and calculated mobility for excitation on a stiffener is moderate. In analogy with the results of the two-dimensional profile strip investigation it is expected that there is a frequency shift in the calculated results because of the neglected fillets at the joints that stiffen the real test object. This stiffening effect is not easily implemented in a calculation model and so it is neglected here. In the case of a profile strip the frequency shift was about 10 % over nearly the whole frequency range. Such a constant factor frequency shift is not observed for the plate results here. The stop-band in the range 1600 – 2300 Hz is shifted as expected to lower frequencies in the calculation (see Fig. F.56). The overall level at high frequencies above 3000 Hz is similar for measurements and calculations, at least for response positions in the vicinity of the excitation point. The overall agreement of calculated and measured input mobility is satisfying for the stiffener excitation case.

APPENDIX F. REGIONAL TRAIN FLOOR SECTION RESULTS

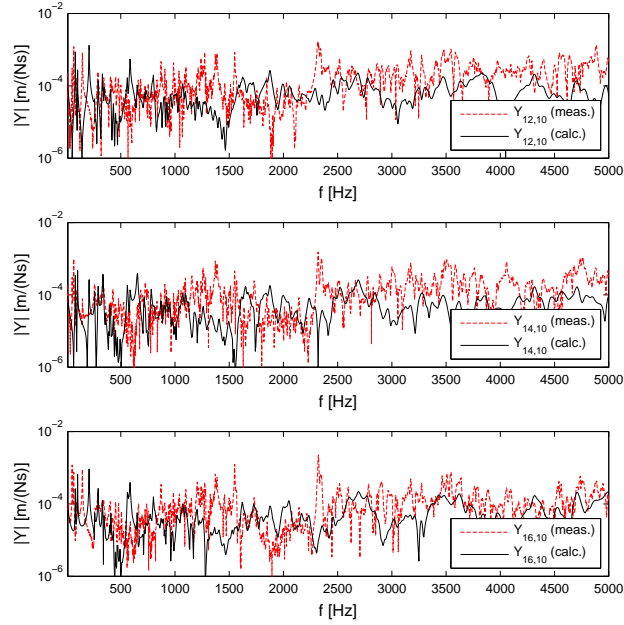


Figure F.53: Comparison of measured and FE-calculated transfer mobilities, stiffener excitation (MP10)

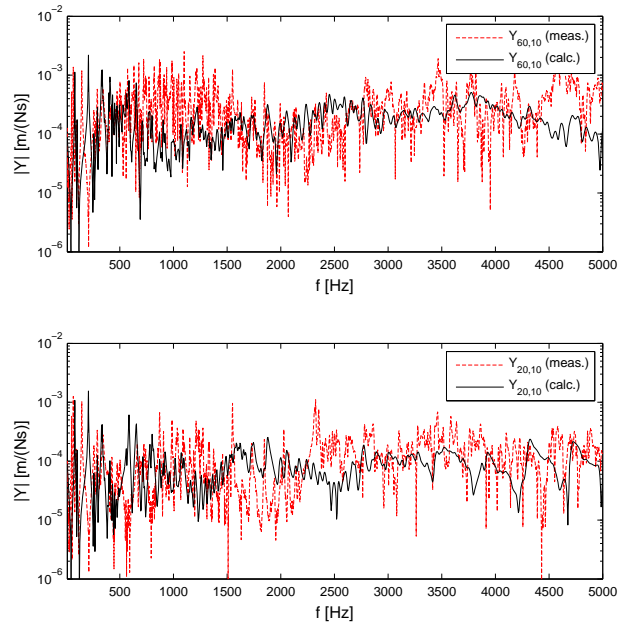


Figure F.54: Comparison of measured and FE-calculated transfer mobilities, stiffener excitation (MP10)

APPENDIX F. REGIONAL TRAIN FLOOR SECTION RESULTS

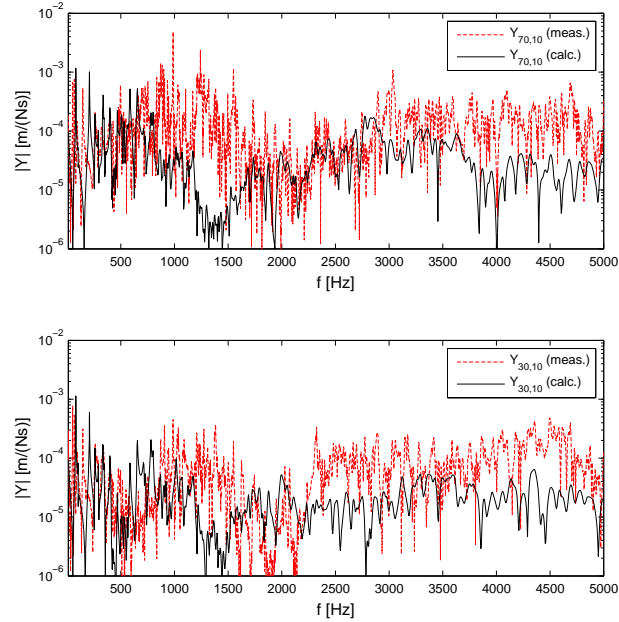


Figure F.55: Comparison of measured and FE-calculated transfer mobilities, stiffener excitation (MP10)

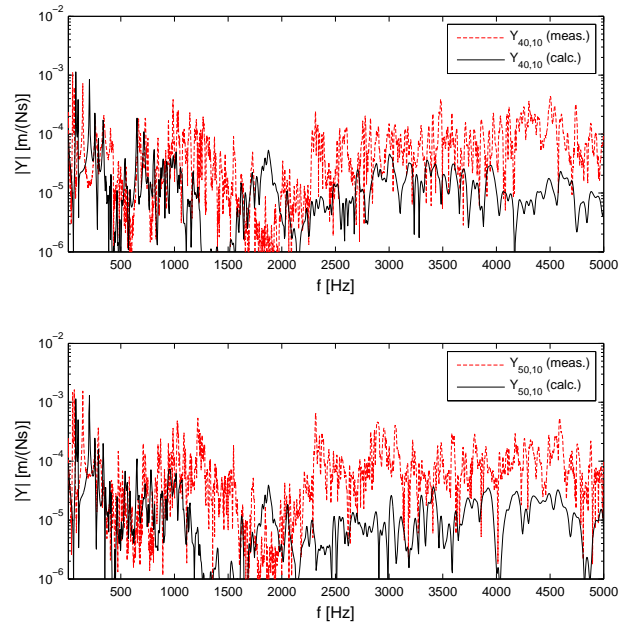


Figure F.56: Comparison of measured and FE-calculated transfer mobilities, stiffener excitation (MP10)

APPENDIX F. REGIONAL TRAIN FLOOR SECTION RESULTS

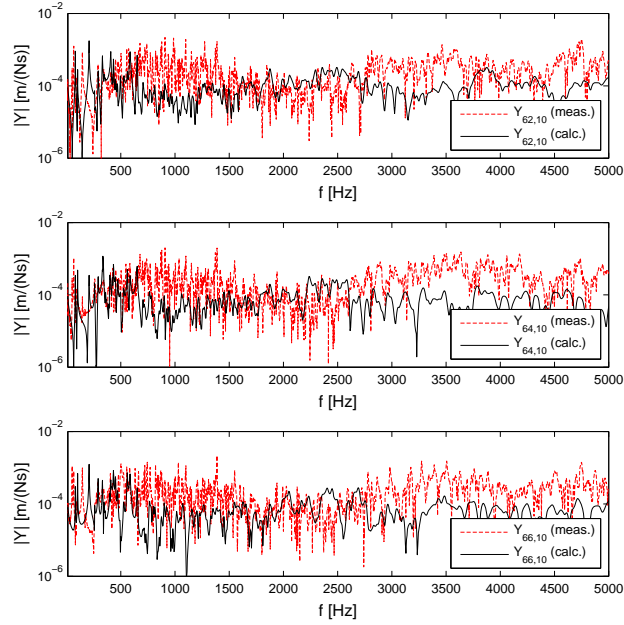


Figure F.57: Comparison of measured and FE-calculated transfer mobilities, stiffener excitation (MP10)

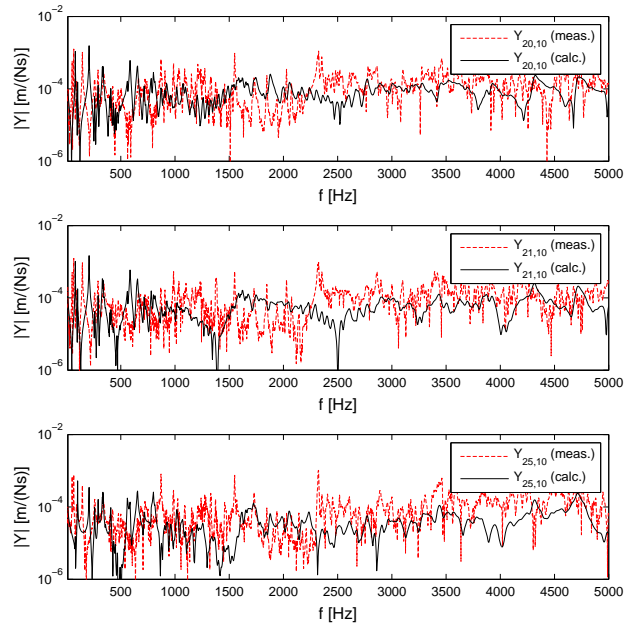


Figure F.58: Comparison of measured and FE-calculated transfer mobilities, stiffener excitation (MP10)

APPENDIX F. REGIONAL TRAIN FLOOR SECTION RESULTS

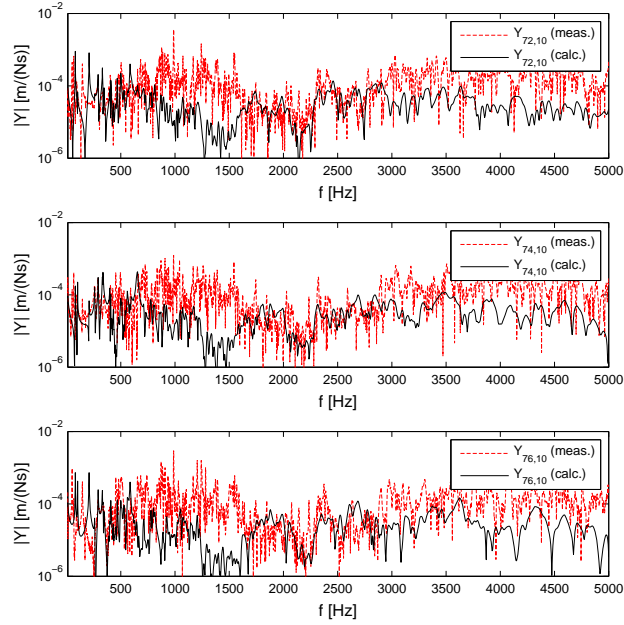


Figure F.59: Comparison of measured and FE-calculated transfer mobilities, stiffener excitation (MP10)

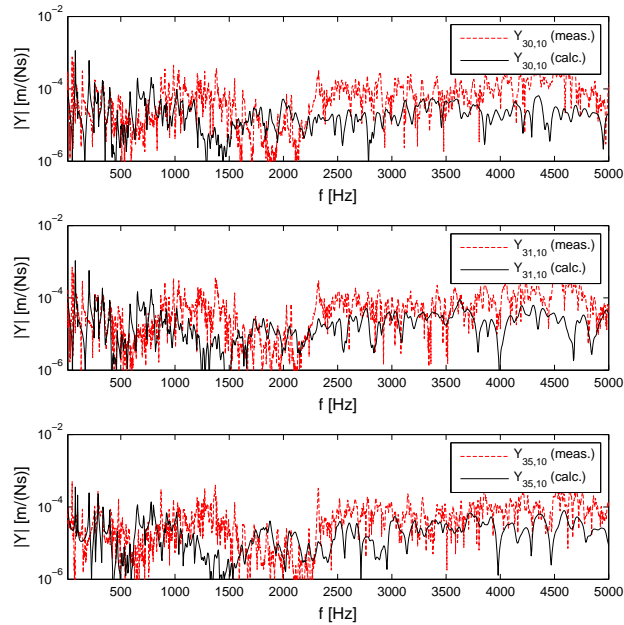


Figure F.60: Comparison of measured and FE-calculated transfer mobilities, stiffener excitation (MP10)

APPENDIX F. REGIONAL TRAIN FLOOR SECTION RESULTS

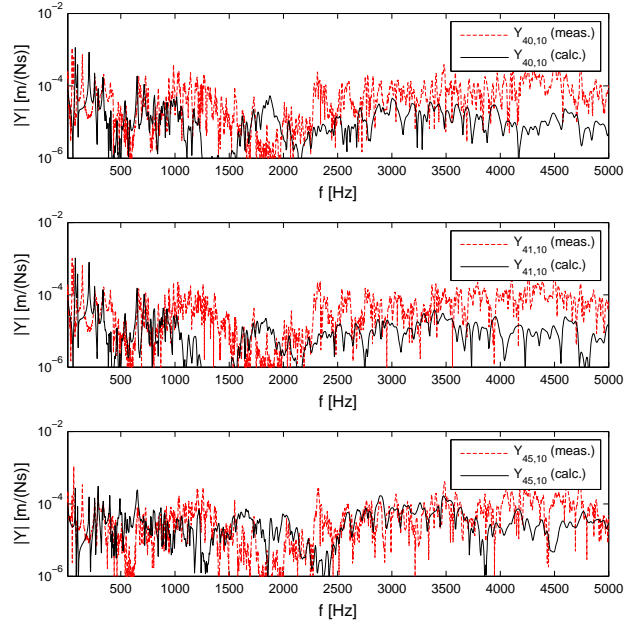


Figure F.61: Comparison of measured and FE-calculated transfer mobilities, stiffener excitation (MP10)

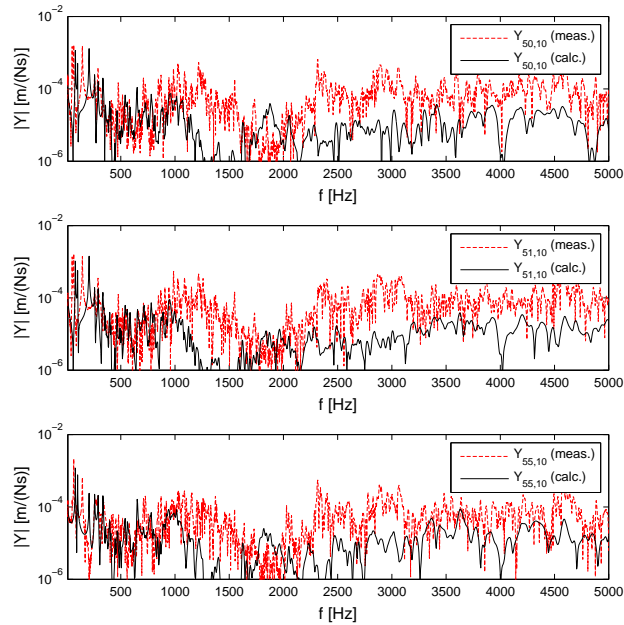


Figure F.62: Comparison of measured and FE-calculated transfer mobilities, stiffener excitation (MP10)

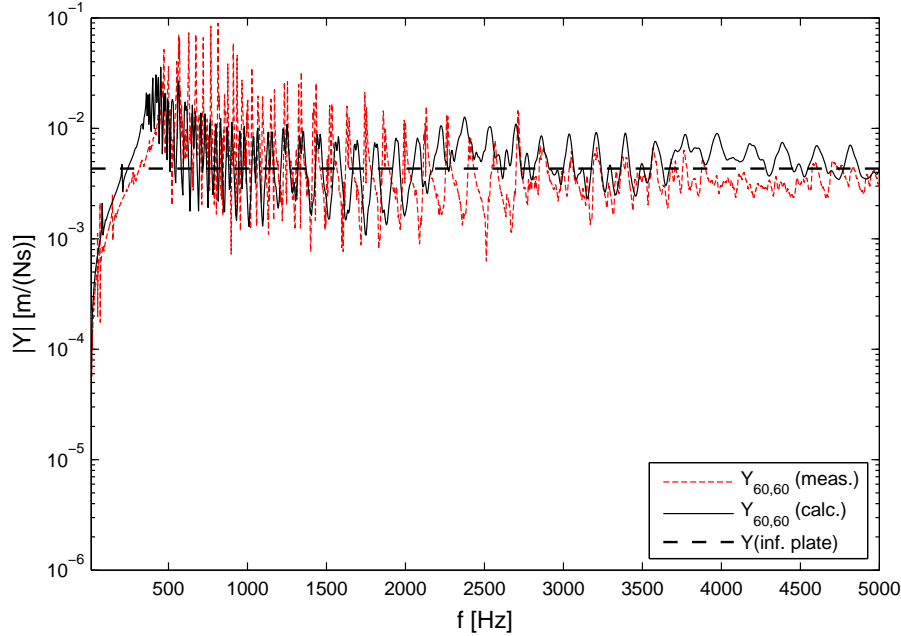


Figure F.63: Comparison of measured and FE-calculated input mobility in plate field (MP60)

What is obvious from the comparison of measured and calculated mobilities is that the loss factor in the calculations, which is chosen to be 0.01 is too high, at least in the higher frequency regime. In the measured results, the resonance peaks are much more pronounced than in the calculated results. This is in agreement with damping measurements performed on a profile strip, where the average loss factor is determined to be around 0.001 or even less. The reason for choosing the higher loss factor in the calculations is that this reduces the necessary frequency resolution in the calculations as the smoothness of the mobility curves is increased. For remote points and frequencies above 2000 Hz, the discrepancy between the measured and calculated results can be explained to some extent by the stronger damping in the calculations, reducing the amplitudes of the transfer mobilities.

F.5.2 Plate Field Excitation

For excitation directly at the centre of a plate field, the comparison of measured and FE-calculated results is included in this section. The input mobility is plotted in Fig. F.63.

The agreement between measured and calculated input mobility is good. In the global frequency regime below 400 Hz the mobility is stiffness-like,

APPENDIX F. REGIONAL TRAIN FLOOR SECTION RESULTS

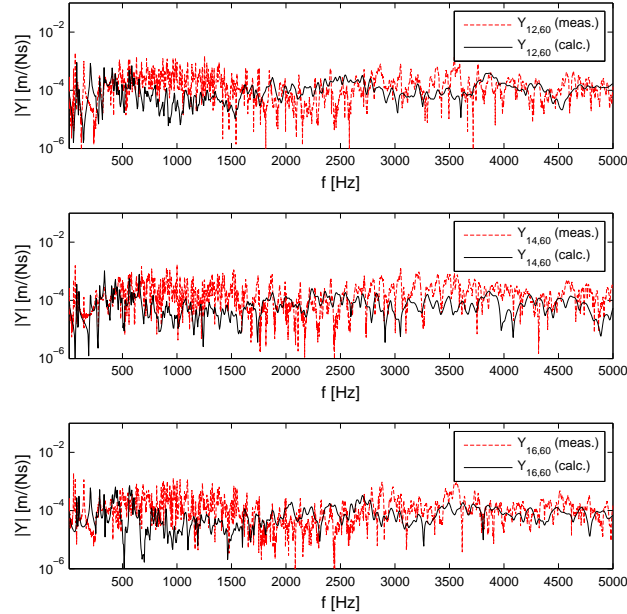


Figure F.64: Comparison of measured and FE-calculated transfer mobilities, plate field excitation (MP60)

interrupted only by minor global resonance peaks. This region ends with the cut-on of wave propagation in local waves, which is shifted slightly between measurement and calculation, lower in the calculated results, which can again be explained by the stiffening effects of the fillets at the joints. In the frequency regime between 400 Hz and about 2000 Hz the measured mobility indicates strong resonant behaviour with very sharp resonance peaks. These peaks are not well identified in the FE-calculation, partly because of the limited frequency resolution of 5 Hz and partly because of the high damping in the FE-model. At high frequencies the measured and calculated input mobility approach the input mobility of an infinite thin plate with a thickness of the plate strip.

The comparison of transfer mobilities is included in Figs. F.64 to F.73. The overall agreement for the transfer mobilities is moderate. Significant underestimations in the calculations arise mainly in the frequency range 500-2000 Hz. A matching representation can be achieved for the transfer mobilities in the excited plate strip (Fig. F.68), where the strong cut-on effects are obvious in calculation and measurement.

APPENDIX F. REGIONAL TRAIN FLOOR SECTION RESULTS

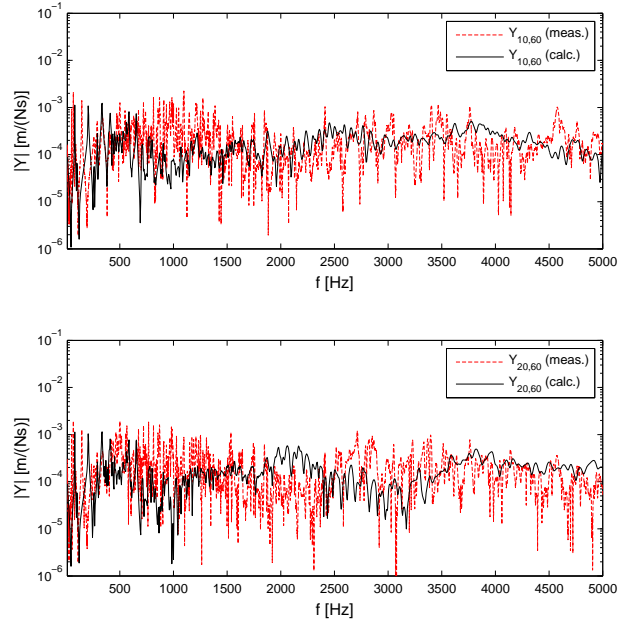


Figure F.65: Comparison of measured and FE-calculated transfer mobilities, plate field excitation (MP60)

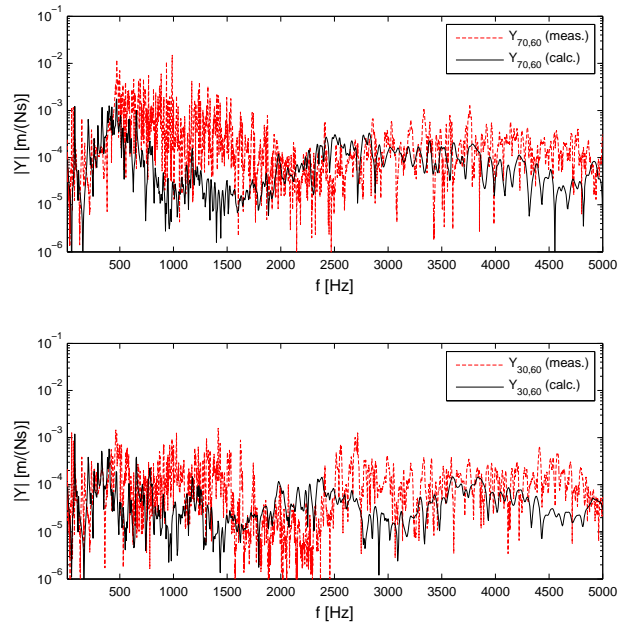


Figure F.66: Comparison of measured and FE-calculated transfer mobilities, plate field excitation (MP60)

APPENDIX F. REGIONAL TRAIN FLOOR SECTION RESULTS

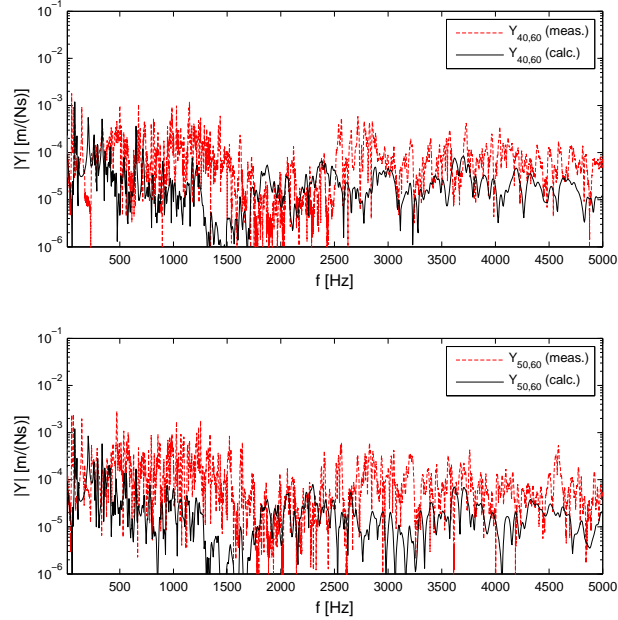


Figure F.67: Comparison of measured and FE-calculated transfer mobilities, plate field excitation (MP60)

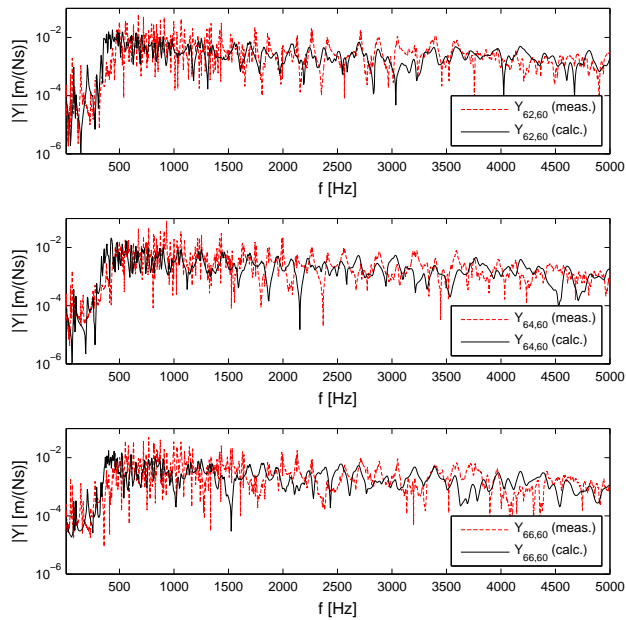


Figure F.68: Comparison of measured and FE-calculated transfer mobilities, plate field excitation (MP60)

APPENDIX F. REGIONAL TRAIN FLOOR SECTION RESULTS

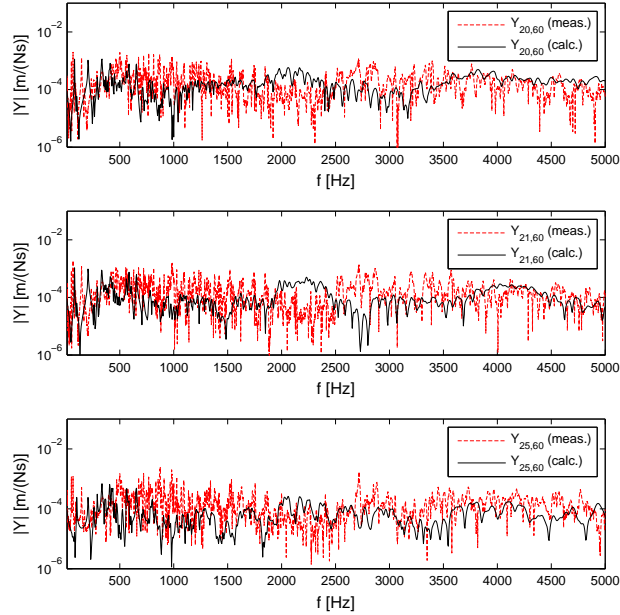


Figure F.69: Comparison of measured and FE-calculated transfer mobilities, plate field excitation (MP60)

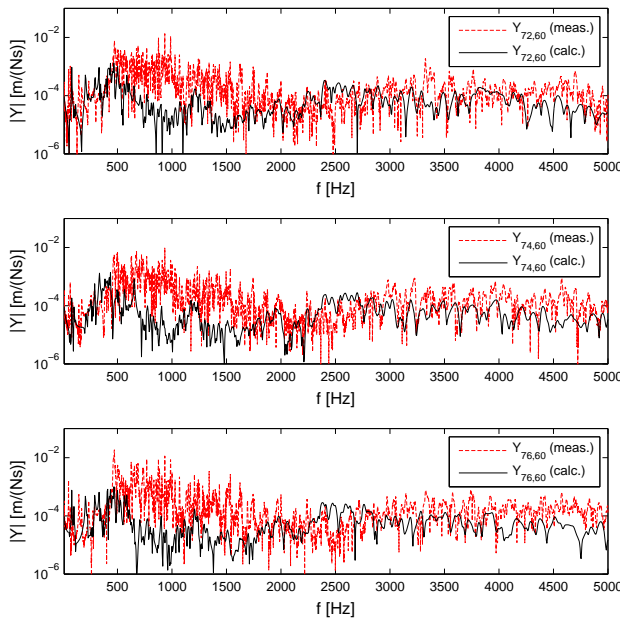


Figure F.70: Comparison of measured and FE-calculated transfer mobilities, plate field excitation (MP60)

APPENDIX F. REGIONAL TRAIN FLOOR SECTION RESULTS

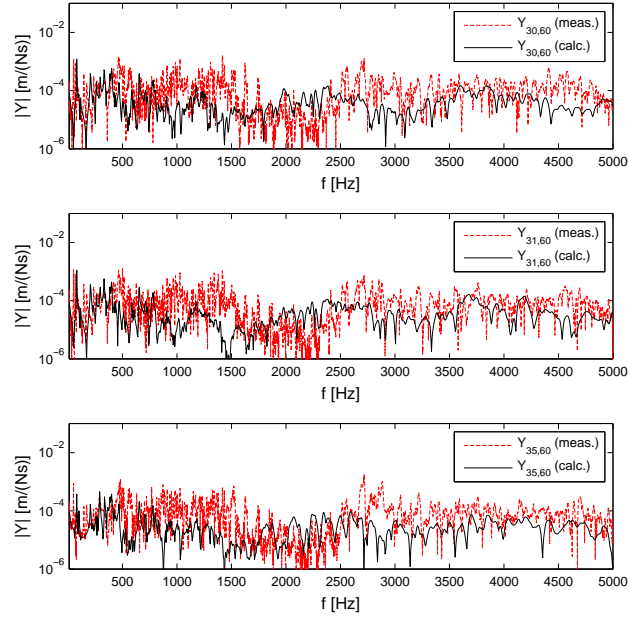


Figure F.71: Comparison of measured and FE-calculated transfer mobilities, plate field excitation (MP60)

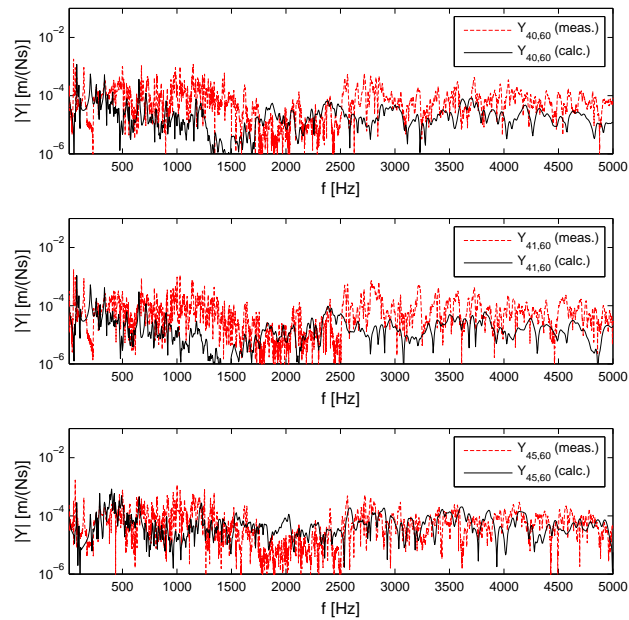


Figure F.72: Comparison of measured and FE-calculated transfer mobilities, plate field excitation (MP60)

APPENDIX F. REGIONAL TRAIN FLOOR SECTION RESULTS

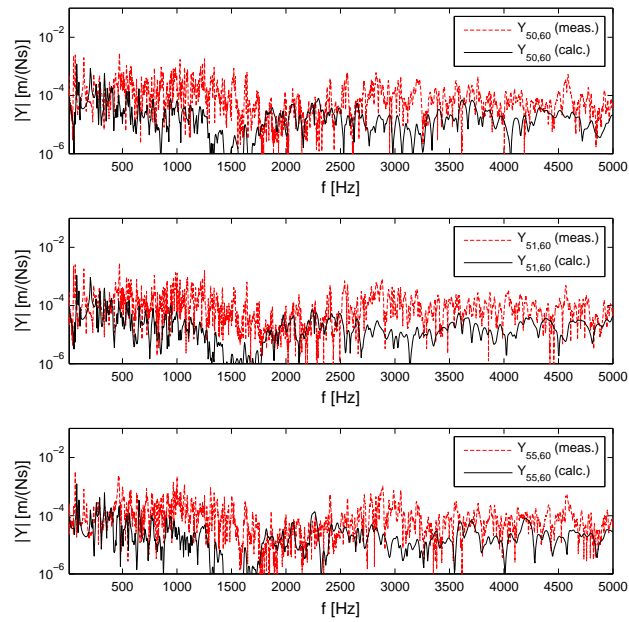


Figure F.73: Comparison of measured and FE-calculated transfer mobilities, plate field excitation (MP60)